Fault Tolerant Adaptive Control of an Unmanned Aerial Vehicle

by

Willem Albertus Basson

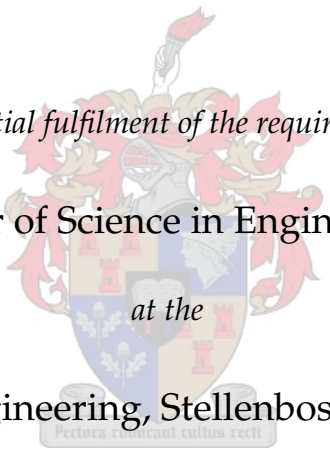

Thesis presented in partial fulfilment of the requirements for the degree of

Master of Science in Engineering

at the

Faculty of Engineering, Stellenbosch University

Supervisor: Mr J.A.A. Engelbrecht
Department of Electrical and Electronic Engineering

December 2011

Declaration

By submitting this thesis electronically, I declare that the entirety of the work contained therein is my own original work, that I am the sole author thereof (save to the extent explicitly otherwise stated), that reproduction and publication thereof by Stellenbosch University will not infringe any third party rights and that I have not previously in its entirety or in part submitted it for obtaining any qualification.

December 2011

Abstract

This thesis presents the development of an adaptive longitudinal control system for an unmanned aerial vehicle (UAV). The project forms part of a research effort at Stellenbosch University into different fault-tolerant control techniques for UAVs.

In order to demonstrate the usefulness of fault-tolerant adaptive control, the control system was designed to handle damage-induced longitudinal shifts in the centre of gravity (CG) of the aircraft, which are known to have a dramatic effect on the stability of a fixed-wing aircraft.

Using a simplified force and moment model, equations were derived which model the effect of longitudinal CG shifts on the behaviour of the aircraft. A linear analysis of the longitudinal dynamics using these equations showed that the short period mode can become unstable for backward CG shifts.

An adaptive pitch rate controller with the model reference adaptive control structure was designed to re-stabilise the short period mode when the CG shifts backwards. The adaptive law was designed using Lyapunov stability theory. Airspeed, climb rate and altitude controllers were designed around the pitch rate controller to allow full autonomous control of the longitudinal dynamics of the UAV. These outer loops were designed with constant parameters, since they would be unaffected by CG shifts if the adaptive pitch rate controller performed as desired.

Pure software simulations as well as hardware-in-the-loop simulations showed that the adaptive control system is able to handle instantaneous shifts in the centre of gravity which would destabilise a fixed-gain control system. These simulation results were validated in flight tests, where the aircraft was destabilised using positive feedback and re-stabilised by the adaptive control system.

Thus the simulation and flight test results showed that an adaptive control can re-stabilise an unstable aircraft without explicit knowledge of the change in the aircraft dynamics, and therefore could be effective as part of an integrated fault-tolerant control system.

Opsomming

Hierdie tesis bied die ontwikkeling aan van 'n aanpassende longitudinale beheerstelsel vir 'n onbemande vliegtuig. Die projek is deel van navorsing by die Universiteit van Stellenbosch oor verskillende fout-tolerante beheertegnieke vir onbemande vliegtuie.

Om die doeltreffendheid van aanpassende beheer te demonstreer, is die beheerstelsel ontwerp om situasies te kan hanteer waar die vliegtuig só beskadig word dat sy massamiddelpunt agtertoe skuif, wat 'n groot invloed op die stabiliteit van 'n vastevlerk-vliegtuig kan hê.

'n Vereenvoudigde model van die kragte en momente wat op die vliegtuig inwerk is gebruik om vergelykings af te lei wat beskryf hoe die gedrag van die vliegtuig verander as die massamiddelpunt agtertoe verskuif. Hierdie vergelykings is gebruik in 'n lineêre analise van die longitudinale dinamika van die vliegtuig, wat getoon het dat die kortperiode-modus onstabiel kan raak as die massamiddelpunt agtertoe verskuif.

'n Aanpassende heitempobeheerder met die modelverwysings-aanpassende beheerstruktuur is ontwerp om die kortperiode-modus weer te stabiliseer wanneer die massamiddelpunt agtertoe verskuif. Die aanpassingswet is ontwerp deur die gebruik van Lyapunov se stabiliteitsteorie. Lugspoed-, klimtempo- en hoogtebeheerders is rondom die aanpassende heitempobeheerder ontwerp sodat die longitudinale dinamika van die vliegtuig heeltemal outonoom beheer kan word. Hierdie buitelusse is ontwerp met vaste parameters, aangesien hulle nie geraak sal word deur verskuiwings in die massamiddelpunt as die aanpassende heitempobeheerder na wense werk nie.

Suiwer sagteware-simulasies, sowel as hardeware-in-die-lus-simulasies, het getoon dat die aanpassende beheerstelsel oombliklike verskuiwings in die massamiddelpunt goed kan hanteer, waar sulke verskuiwings 'n beheerstelsel met vaste parameters onstabiel sou maak. Hierdie simulasie-resultate is bevestig deur vlugtoetse te doen, waar die vliegtuig onstabiel gemaak is deur positiewe terugvoer, en weer deur die aanpassende beheerstelsel stabiel gemaak is.

Die simulasie- en vlugtoetsresultate wys dus dat aanpassende beheer 'n onstabiele vliegtuig weer kan stabiliseer sonder eksplisiete kennis van die veranderinge in die dinamika van die vliegtuig. Aanpassende beheer kan dus doeltreffend wees as deel van 'n geïntegreerde fout-tolerante beheerstelsel.

Acknowledgements

I, the author, would like to thank the following people:

- My study leader, Mr Japie Engelbrecht, for all your hard work, encouragement, guidance and patience throughout my project.
- Former ESL engineers Ruan de Hart and Rudi Gaum, for your help during the preparations for the flight tests in 2010 – your expertise was invaluable, and your work ethic inspiring.
- Current ESL engineers A.M. de Jager and Lionel Basson, as well as fellow-student Sampie Smit, for your assistance during the flight tests in 2011.
- Prof. Thomas Jones and Dr Iain Peddle, for your input and guidance during our project group meetings.
- Our safety pilot, Michael Basson – your experience and skill with RC aircraft has been an immense asset to the project.
- The technical staff at the E&E Department, including Wessel Croukamp, Wynand van Eeden and Johan Arendse.
- The CSIR DPSS, who funded the research, and the NRF, who also provided me with financial assistance.
- My fellow students at the ESL, for all the friendships that were made, for all the encouragement, and for making it a joy to come in to work every day.
- My family: Anton, Erina, Carin and Johan Basson, for all your love and support during the project.
- My friends at TBT/St. Paul's church, for all your spiritual support, encouragement and accountability during the project.
- My Lord and Saviour Jesus Christ – were it not for His help, my work would be useless; were it not for His hope, my life would be meaningless.

Contents

List of Figures

List of Tables

Nomenclature

Symbols used in aircraft modelling and control

Greek letters

α	Angle of attack
β	Angle of sideslip
δ_a	Aileron deflection
δ_e	Elevator deflection
δ_r	Rudder deflection
δ_t	Throttle command
ζ	Damping ratio
θ	Pitch angle
θ_w	Pitch angle of the wind axis system, i.e. the climb angle of the aircraft
ρ	Air density
τ_T	Engine time constant
ϕ	Roll angle
ψ	Heading angle
ω_d	Undamped natural frequency
ω_n	Natural frequency

Small letters

a_a	Axial specific acceleration
a_l	Lateral specific acceleration
a_n	Normal specific acceleration
b	Wing span
$\bar{c}$	Mean aerodynamic chord
e	Oswald efficiency factor
g	Gravitational acceleration
h	Altitude
j	Imaginary unit ($\sqrt{-1}$)
m	Mass
p	Roll rate
q	Pitch rate
$\bar{q}$	Dynamic pressure
r	Yaw rate
u	Axial velocity
v	Lateral velocity
w	Normal velocity
$x_{_G}$	Longitudinal CG shift distance

Capital letters

A	Aspect ratio
C_D	Aerodynamic drag coefficient
C_y	Aerodynamic side force coefficient
C_L	Aerodynamic lift coefficient
C_l	Aerodynamic roll moment coefficient
C_m	Aerodynamic pitching moment coefficient
C_n	Aerodynamic yaw moment coefficient
E	East position coordinate
F_L	Lift force
D	Down position coordinate
I_{xx}	Moment of inertia about the roll axis
I_{yy}	Moment of inertia about the pitch axis
I_{zz}	Moment of inertia about the yaw axis
I_{xy}	Roll and pitch product of inertia
I_{xz}	Roll and yaw product of inertia
I_{yz}	Pitch and yaw product of inertia
L	Roll moment
M	Pitching moment
N	Yaw moment, North position coordinate
S	Reference wing area
T	Thrust output
$\bar{V}$	Airspeed
X	Axial Force
Y	Lateral Force
Z	Normal Force

Vectors

$\mathbf{F}$	Force vector
$\mathbf{M}$	Moment vector
$\mathbf{P}$	Position vector
$\mathbf{V}$	Velocity vector
$\boldsymbol{\omega}$	Rotation rate vector

Superscripts

A	Aerodynamic forces and moments
B	Vector coordinated in body axes
E	Vector coordinated in inertial (earth) axes
G	Gravitational forces and moments
T	Engine forces and moments, Trim value of control input

Symbols used in adaptive control

Greek letters

$\boldsymbol{\alpha}(s)$	Numerator polynomial vector used to create the states of the filters in the MRC law
γ	Scalar adaptive gain
Γ	Adaptive gain matrix
$\boldsymbol{\theta}_c$ or $\boldsymbol{\theta}$	Estimate of the ideal controller parameter vector, which is used in the control law
$\boldsymbol{\theta}_c^*$ or $\boldsymbol{\theta}^*$	Ideal controller parameter vector
$\boldsymbol{\theta}_p$	Estimate of the plant parameter vector
$\boldsymbol{\theta}_p^*$	True plant parameter vector
λ	Pole frequency of the filters in the MRC law
$\Lambda(s)$	Denominator of the filters in the MRC law
$\boldsymbol{\omega}$	Vector of signals used by the MRC law

Small letters

$\mathbf{e}$	State error in an MRC system
e_1	Output error, i.e. the difference between the plant and model outputs
$k_m,\ k_p$	High-frequency gains of the reference model and plant
m_p	Number of plant zeroes
n	Upper bound on the order of the plant
n^*	Relative degree of the plant
n_m^*	Relative degree of the reference model
n_p	Order of the plant
p_m	Number of reference model zeroes
q_m	Order of the reference model
r	Reference command
u_p	Plant input
y_m	Reference model output
y_p	Plant output

Capital letters

$A_p,\ B_p,\ C_p$	State space representation of the plant
$F,\ g$	State space representation of the filters in the MRC law
$G_c(s)$	Closed-loop transfer function of the MRC system
$G_p(s)$	Plant transfer function
V	Lyapunov-like function used to design the adaptive law
$R_m(s),\ R_p(s)$	Denominators of the reference model and plant
$W_m(s)$	Reference model transfer function
Y_c	State vector of the whole closed-loop MRC system
$Z_m(s),\ Z_p(s)$	Numerators of the reference model and plant

Abbreviations and acronyms

ADC	Analog-to-Digital Converter/Conversion
AFTC	Active Fault-Tolerant Control
AVL	Athena Vortex Lattice, a numerical analysis software package for aerodynamic modelling
CAN	Controller-Area Network
CG	Centre of Gravity
DCM	Direction Cosine Matrix
EKF	Extended Kalman Filter
EPP	Expanded Polypropylene
ESL	Electronic Systems Lab at Stellenbosch University
GPS	Global Positioning System
HIL	Hardware-in-the-loop
IMU	Inertial Measurement Unit
ITEC	Integral Trim Elevator Control
LQR	Linear Quadratic Regulator
LTI	Linear Time-Invariant
MIMO	Multi-Input, Multi-Output
MKY	Meyer-Kalman-Yakubovich lemma
MRAC	Model Reference Adaptive Control
MRC	Model Reference Control
NED	North, East and Down inertial axis system
NP	Neutral Point
NSA	Normal Specific Acceleration
OBC	On-Board Computer
OPE	Online Parameter Estimator
PC	Personal Computer
PI	Proportional-Integral
PR	Positive Real
PWM	Pulse Width Modulation
RC	Remote Controlled
RF	Radio Frequency
RMS	Root-mean-square
SISO	Single Input, Single Output
SPR	Strictly Positive Real
SU	Stellenbosch University
UAV	Unmanned Aerial Vehicle
USB	Universal Serial Bus

Chapter 1

Introduction

Unmanned aerial vehicles (UAVs) are a fast-growing sector of the aviation industry. They have gained widespread use in performing tasks that are too dull, dirty or dangerous for aircraft with human pilots. Also, since they do not have to carry a human pilot, they can be made much smaller than manned aircraft, which makes them less expensive and more energy-efficient. However, most autopilots for UAVs cannot match the ability of a human pilot to adapt to different situations, such as in-flight damage or system failures.

Stellenbosch University has been active in UAV research for several years. This project forms part of a research effort into active fault tolerant control (AFTC) of UAVs, which was started at SU in 2009. Research is being done into various parts of the fault tolerant control problem, including stall prevention [1], system identification [2], control re-allocation [3], fault detection and isolation, and upset recovery, as well as the overall architecture of an integrated AFTC system.

The goal of this project within the AFTC research effort is to investigate the use of model reference adaptive control (MRAC) as part of the integrated AFTC system. An MRAC system consists of a plant to be controlled, a control law, a reference model and an adaptation mechanism, as shown in Figure 1.1. The control law generates an input signal for the plant in order to follow a command signal, using feedback of the plant output, just as it does in a conventional control system. The reference model represents the desired response of the plant output to commands.

In a non-adaptive or *fixed-gain* control system, the parameters of the control law are constant. In an MRAC system, however, the controller parameters are adjusted by the adaptation mechanism in an attempt to eliminate the error between the plant and model outputs. This will ensure that the response of the closed-loop system is as close as possible to the desired response, even if the plant behaviour changes.

The role of adaptive control within an AFTC system would be to provide a first line of defence against in-flight failures, quickly stabilising the aircraft and giving the other components of the AFTC system time to identify the problem and solve it in an optimal way. Robust

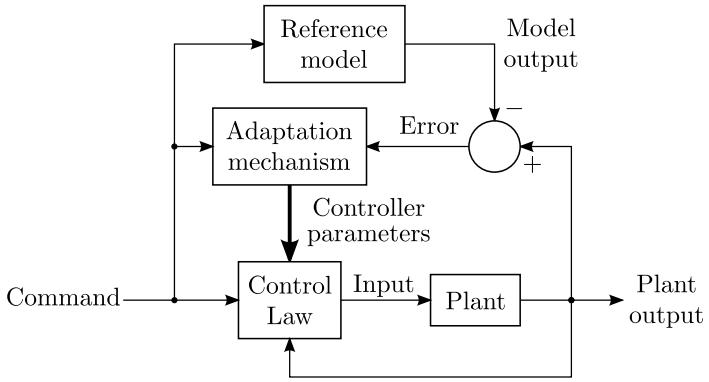

Figure 1.1: Structure of a model reference adaptive control system

control provides an alternative to adaptive control in performing this task – this thesis will evaluate adaptive control as a possible solution to the failure survival problem, which should allow future research to compare the performance of adaptive and robust control techniques.

If it could be shown that an adaptive flight control system can keep the aircraft flying safely in situations where a fixed-gain control system would be unable to, this would show that adaptive control can be an effective part of a fault tolerant control system. Specifically, the usefulness of adaptive control could be clearly demonstrated by finding a failure case which a fixed-gain control system cannot handle, and designing an adaptive control system to handle it.

A number of criteria were used to evaluate potential failure cases for this purpose. Firstly, the failure case should be serious enough to necessitate the use of adaptive control in order to keep the aircraft in the air. For instance, the failure could change the aircraft dynamics to such an extent that the aircraft will become unstable if a conventional control system is used. Secondly, the failure should allow an adaptive control system to be designed which is able to handle the failure. Finally, the failure case should ideally be one that can be replicated in a flight test without causing permanent damage to the aircraft, so that the real-life performance of the adaptive control system can be evaluated.

Initially, actuator failures were investigated as a possible failure case. It was found that most actuator failures fall into one of two categories: those that can be handled by adaptive control, but do not seriously affect the stability and controllability of the aircraft when a fixed-gain control system is used, and those which cannot be handled well by either fixed-gain or adaptive control systems. Therefore it was decided that actuator failures would not be the best situation to demonstrate the usefulness of adaptive control.

The next failure case considered was shifts in the centre of gravity (CG) of an aircraft. CG shifts can have a dramatic effect on the stability of the aircraft, as well as the closed-loop stability of a fixed-gain flight control system. Such shifts can be caused by something breaking off the aircraft, or by fuel or cargo shifting around inside it.

Figure 1.2: The Variable Stability UAV built at Stellenbosch University

In a previous project at Stellenbosch University [4], a control system was designed for a Variable Stability UAV – an aircraft with a CG that can be moved along its longitudinal axis. The control design was initially done for the Sekwa UAV, which was designed and built by the CSIR to investigate the concept of variable stability as a technique to decrease drag and extend the range of UAVs. Eventually, however, the control system was implemented and flight-tested using a Variable Stability UAV built at Stellenbosch University, shown in Figure 1.2. This Variable Stability UAV was still available for use in this project, and could allow the handling of CG shifts by an adaptive control system to be tested in practice.

Therefore it was decided to design an adaptive flight control system for this project, which can handle shifts in the centre of gravity an aircraft, and to test the control system in practice using the Variable Stability UAV. Since the lateral dynamics of an aircraft are not seriously affected by longitudinal CG shifts, it was decided to focus on the longitudinal control of the Variable Stability UAV.

If this control design could fulfil its goal, it would indicate that adaptive control can be useful as part of a fault-tolerant control system, and therefore a successful control design would provide a positive answer to the central research question of this project.

Since this project is part of the research into fault-tolerant control, the main goal of the adaptive control system is to handle CG shifts caused by in-flight damage. These shifts are likely to happen very fast, for instance if something breaks off the front of the aircraft. There-

fore the focus of the control design was on handling instantaneous shifts in the centre of gravity.

However, adaptive control could also potentially be a solution to the *variable stability problem*, where the CG is moved backwards gradually and intentionally to change the behaviour of the aircraft, as can be done with the Sekwa UAV. Therefore, as a secondary objective, the adaptive control system to be designed for fault tolerance would also be tested as a solution to the variable stability problem, which was the primary goal of the control design presented in [4].

A number of tools could be used to test the adaptive control system and evaluate its performance. Firstly, linear analysis could be used to investigate the effects of instantaneous CG shifts on a fixed-gain control system, providing a benchmark with which the adaptive control system can be compared.

However, linear analysis can not be used to analyse an adaptive control system, since such a control system is non-linear, nor can it be used to investigate the effects of gradual CG shifts, since these make the aircraft model time-varying. Therefore the performance of the adaptive control system and the effect of gradual CG shift would have to be investigated in non-linear simulation.

The simplest form of non-linear simulation is one where both the aircraft model and the control system are implemented on a PC. For this project, the aircraft model and control system were simulated using Matlab and Simulink. This pure software simulation approach has the advantage of great flexibility, and allows simulations to be run significantly faster than real-time.

If the pure software simulations are successful, the next step would be to implement the control system on the avionics of the aircraft and perform hardware-in-the-loop simulations, where the control system runs on the avionics but the aircraft model is still implemented on a PC in Matlab and Simulink. This provides an important intermediate phase between pure software simulations and practical tests, and allows the implementation of the control system on the avionics to be tested safely.

Finally, if both the software and hardware-in-the-loop simulations are successful, the adaptive control system can be tested in practice by performing flight tests with the Variable Stability UAV. Ideally, the control system would be tested by physically moving the CG of the aircraft in flight. However, if the aircraft is destabilised in any way, for instance through positive feedback, and the adaptive control system is able to re-stabilise it, this would serve as a real-life demonstration of the fault tolerance of the adaptive control system.

This thesis starts with an overview of relevant literature in Chapter 2. Chapter 3 describes the non-linear model of the aircraft that was used in analysis, control design and simulation. This chapter includes the derivation of equations which model the effects of shifts in the centre of gravity on the parameters of the aircraft. Chapter 4 gives a linear model of the

longitudinal dynamics of the aircraft, and investigates the effect of CG shifts on these dynamics using linear analysis tools. This analysis motivates the adaptive control strategy used to handle shifts in the centre of gravity.

Chapter 5 provides an overview of the adaptive control techniques used in this project. Chapter 6 describes the design of a longitudinal control system which can be combined with these adaptation techniques, and provides a linear analysis of the effect of CG shifts on this control system when adaptation is disabled. Chapter 7 investigates the response of the control system with different adaptive laws to CG shifts in non-linear simulation, and Chapter 8 gives the results of flight tests that were done to evaluate the performance of the control system in practice. Chapter 9 concludes the thesis with a summary and recommendations for future work.

Chapter 2

Literature survey

This chapter provides an overview of literature that is relevant to this thesis. Section 2.1 discusses the research into aircraft modelling and control done at Stellenbosch University, on which this thesis is built. Section 2.2 provides an overview of different adaptive control techniques, and Section 2.3 reviews different approaches to the modelling of variable stability aircraft.

2.1 Modelling and control of fixed-wing aircraft

This project builds on previous research into the modelling and control of UAVs at the Electronic Systems Lab (ESL) at Stellenbosch University. A standard non-linear and linearised model of a fixed-wing aircraft, and a discussion of the aircraft modes of motion, are given in [5], based on books such as [6] and [7]. This aircraft model assumes that the aircraft has a static centre of gravity.

In [8], an acceleration-based control strategy is proposed, and the aircraft model is given in a form which is convenient for the design of an acceleration-based control system. This strategy also is the basis of the control system designed in [4] for the Variable Stability UAV.

The modelling and control strategies presented in these sources could be modified for use in this project. This would greatly accelerate the modelling and design process, and also provide continuity with previous research at the ESL.

2.2 Adaptive control techniques

This section provides an overview of some of the many different adaptive control techniques that can be found in literature.

It would be useful to investigate a number of different adaptive control techniques in detail and compare them, but the time constraints on this project would not allow this approach. Instead, it was decided to choose one adaptive control technique, investigate it in detail in

theory and simulation, and to identify the key practical issues around implementing it on a UAV as part of an AFTC system.

Also, since this project is intended as a first exploration of the field of adaptive control for the UAV research at Stellenbosch University, the focus of the project is on applying existing techniques to the problem of fault-tolerant control of UAVs, rather than developing new techniques or making a new contribution to the field of adaptive control.

Therefore the purpose of this literature survey is to identify the different adaptive control techniques that exist and have been used for fault-tolerant flight control, to assess the advantages and disadvantages of each technique, and then to choose one adaptive control technique for a focused evaluation as a part of a fault tolerant control system for a UAV.

2.2.1 Stability-based adaptive control

A popular class of adaptive control techniques is those based on Lyapunov stability theory. These techniques are described in many books on adaptive control, such as [9], [10], and [11]. The book on robust adaptive control by Ioannou and Sun [12] is a particularly useful reference, since it provides adaptive control schemes which can be applied to a wide class of problems, giving detailed derivations and stability proofs, as well as summarising the algorithms in a way which makes them very easy to apply to a given control problem.

Stability-based adaptive control techniques have mostly been limited to SISO plants, but have also been expanded to the control of MIMO systems. Techniques to do this are discussed in [11], [12] and [13], and were applied to fault tolerant flight control in [14]. However, in this project, adaptive control techniques will only be applied to the SISO inner loops of the aircraft control system, and therefore such MIMO adaptive control techniques are not really applicable to this project.

Adaptive control schemes based on Lyapunov stability theory have the advantage that their stability can be proven mathematically under certain assumptions. These assumptions, however, may be very restrictive or even unrealistic if the simplest forms of the adaptive control schemes are used. These schemes may, for instance, require that the plant be free of disturbances and measurement noise. This assumption is typically far from true in the aircraft control industry.

Therefore much research has been done into improving the robustness of stability-based adaptive control systems to disturbances, noise and unmodelled dynamics. Books such as [10] and [12] suggest modifications to the adaptive laws they present to make them more robust. These include the use of a dead zone, leakage or dynamic normalisation in the adaptive law, and in [15] the adaptive control system was made robust to output disturbances by periodically resetting to zero the output error which drives adaptation.

Many papers present other robustness modifications, mostly filtering techniques, which are applied to a specific adaptive scheme or class of unmodelled phenomena, and therefore

are too specific to be applied in this project. Examples include [16], [17] and [18].

2.2.2 Simple Adaptive Control

Another adaptive control technique is the one presented by Kaufman et al. in [19], which the authors call *Simple Adaptive Control*. This control technique is based on concept of a command generator tracker (CGT), which in its simplest form allows the design of an adaptive control system to follow sinusoidal reference commands. This technique can then be expanded to follow any reference command.

An initial investigation into Simple Adaptive Control indicated that its control and adaptation algorithms are, ironically, much more complex than stability-based control schemes such as those presented in [12].

2.2.3 Adaptive robust control

As mentioned in the introduction to this thesis, robust control techniques such as $\mathcal{H}_\infty$ provide an alternative to adaptive control in ensuring stability of an aircraft immediately after a failure occurs. These techniques typically use fixed control parameters, which are chosen to ensure robust stability at the cost of performance.

Adaptive laws can be added to robust control schemes to create an adaptive robust control system. These systems are distinct from robust adaptive control systems, where a control system is first designed using adaptive control techniques, and then modified to improve its robustness

An adaptive robust control system can ensure both stability and performance if the aircraft suffers in-flight damage. Techniques for designing such control systems are presented in [20] and [21], and are applied to fault-tolerant flight control in [22].

Adaptive robust control schemes could be very useful as part of a fault-tolerant control system, but researching these techniques in this project would mean venturing simultaneously into two different fields which have not yet been used extensively in the ESL. Therefore it was decided to focus this project on adaptive control only, while later research could investigate robust control, and then possibly combine the two control design approaches.

2.2.4 Neural and fuzzy adaptive control systems

Much of the recent research into adaptive control systems has made use of neural networks and fuzzy logic, or a combination of the two techniques.

Neural networks are a statistical tool which can approximate complex non-linear functions to a high degree of accuracy. [23] contains numerous papers describing neural adaptive control techniques, and [24] provides a survey of the use of neural networks in adaptive flight

control. Example applications of neural networks to fault-tolerant flight control can be found in [25], [26] and [27].

Fuzzy control is an intuitively defined rule-based control technique, which has been used before in the ESL for the control of an airship [28]. Fuzzy logic can also be used in an adaptive control system, as was done for fault tolerant flight control in [29].

Neural networks and fuzzy logic can also be combined to create a neuro-fuzzy adaptive control system. Examples where neuro-fuzzy techniques were used for fault-tolerant flight control include [30] and [31].

As with adaptive robust control, investigating neural or fuzzy adaptive control for this project would imply that in one project, two large steps would be taken away from the classical control techniques in established use at the ESL. Research has been done into fuzzy control before, but it was decided that adaptive control techniques which are more easily compatible with current control systems should be investigated first, before combining adaptive control with other less established control techniques, such as fuzzy logic and neural networks.

2.2.5 Summary of adaptive control techniques

This section reviewed adaptive control techniques based on stability theory, the Simple Adaptive Control algorithms, adaptive robust control, and neural and fuzzy adaptive control systems.

The survey suggested that Simple Adaptive Control is unnecessarily complex, while adaptive robust control as well as neural and fuzzy adaptive control would be too large a leap away from the established control techniques in use at the ESL.

Therefore it was decided to focus on adaptive control techniques based on stability theory for this project. Specifically, it was decided to use the techniques presented in [12], since this source contains both the mathematical details and summaries of the different adaptive algorithms, as well as modifications to improve their robustness.

Chapter 5 gives the theory behind the design of an adaptive control system, summarised from [12], and derives a number of different adaptive laws. A fixed-gain control system is then designed Chapter 6 with the addition of these adaptive laws in mind, and in Chapter 7 the adaptive and control laws are combined to form an adaptive control system, which is then tested in non-linear simulation.

2.3 Modelling of variable stability aircraft

This section provides an overview of research into the modelling of aircraft where the position of the centre of gravity is uncertain or can change during flight. The purpose of this review is to show different approaches to modelling aircraft with moving centres of gravity, to evaluate the advantages and disadvantages of each approach, and then to choose a

modelling approach for this project.

Since this project will use CG shifts as an example situation to demonstrate the effectiveness of adaptive control, rather than specifically designing an adaptive control system to handle CG shifts, the focus of this review is more on the modelling of the effect of CG shifts than on the control techniques used in the various sources.

2.3.1 Numerical modelling in the aerodynamic parameters

As mentioned in the introduction, a previous project at Stellenbosch University (SU) [4] was concerned with the design of a flight control system for the Sekwa UAV, which was implemented and tested on the SU Variable Stability UAV. Both these aircraft had moveable centres of gravity. The effect of CG shifts was modelled by performing an analysis of the airframe with different CG positions using AVL, a vortex lattice analysis program. A second-order polynomial fit was performed on the AVL data to obtain equations for each aerodynamic parameter as a function of the CG position. These equations were then used to calculate the controller parameters in real time to yield the desired performance for all CG positions.

A similar modelling approach was used in [32], where a control system was designed for an aircraft with an uncertain but constant mass and CG position. Here the effects of both mass and CG variations on the aerodynamic parameters were modelled using a two-dimensional polynomial fit on data obtained using numerical analysis.

The advantage of numerically modelling the effect of CG shifts on the aerodynamics parameter is that it allows a linear analysis of the effect of CG shifts on the aircraft dynamics, since linear models are usually given in symbolic form in terms of these parameters. The disadvantage of this approach is that it requires multiple analyses of each aircraft to obtain its model for all CG positions, which can become cumbersome if different aircraft need to be analysed, or if the aircraft configuration changes. Ideally, a single numerical analysis of the aircraft should yield a model which is applicable for all possible CG positions.

2.3.2 Symbolic modelling in the equations of motion

An alternative to modelling the effects of CG shifts at an aerodynamics parameter level is to model these effects at an equations of motion level. This approach was used in [27] and [33]. Both sources used the same equations of motion which were defined symbolically in terms of the CG position in three dimensions. In the former, the CG was assumed to shift due to in-flight damage, while the latter designed an autopilot for an aircraft which uses active CG control, where fuel is moved around between different tanks in the aircraft to dynamically control the CG position.

This approach to modelling the effect of CG shifts has the advantage that it is based on symbolic equations, given in terms of the nominal aircraft parameters and the CG position.

This eliminates the need for multiple analyses of the same aircraft. However, these equations are not as easy to integrate with linear models of the aircraft dynamics, and therefore this approach would complicate the linear analysis of the effect of CG shifts on the aircraft dynamics.

2.3.3 Other approaches

Another approach to modelling aircraft with moving CGs can be found in [34], where a control system was designed to handle variations in the mass and CG of an aircraft, which could be caused by structural damage, active CG control or a heavy load airdrop. The aircraft was modelled as consisting of a rigid part and a moving part. CG shifts were modelled as changes in the position of the moving part relative to the rigid part, while changes in the mass of the aircraft were modelled as the moving part separating from the rigid part.

This modelling approach was not seriously considered for this project, since it would be difficult to combine with the standard models of a fixed-wing aircraft, which generally assume that the aircraft consists of one rigid body.

Another form of variable stability is the use of feedback to change the dynamics of an aircraft, in order to test the robustness of a control system in flight. This technique is used in the VISTA F-16 aircraft (Variable stability In-flight Simulator Test Aircraft), mentioned in [35] and [36], which uses feedback to simulate the flight characteristics of different aircraft.

This approach provides an alternative to CG shifts as a test situation to demonstrate the performance of an adaptive control situation. An aircraft could be made artificially unstable in flight using feedback, which would probably be easier and safer to implement practically than making the aircraft physically unstable by moving the CG.

2.3.4 Summary of variable stability modelling

The literature on the modelling of variable stability aircraft provides a number of approaches to modelling the effect of CG shifts on the aircraft dynamics. However, each of the methods in the sources mentioned above has its own disadvantages. The numerical curve-fits used by [4] and [32] require multiple analyses of the airframe, while the symbolic equations of motion in terms of the CG position from [27] and [33] complicate the linear analysis of the effect of CG shifts on the aircraft dynamics.

Therefore a new approach would be used for this project, which would combine the benefits of both methods mentioned above through a set of symbolic expressions for the aerodynamics parameters of the aircraft, in terms of the CG position and the nominal values of these parameters.

These nominal values could be calculated through a single AVL analysis of an airframe for one nominal CG position. Then the symbolic expressions would allow the parameters to

be calculated for any CG position, and used in a linear analysis of the aircraft dynamics with the CG in that position. The derivation of these equations is described in Section 3.4.

The concept of using feedback to simulate different flight characteristics, as can be done with the VISTA F-16, could also be useful in this project. This approach could be used to artificially destabilise an aircraft in flight, and so test whether the adaptive control system is able to re-stabilise an unstable system.

As mentioned in the introduction, demonstrating that adaptive control is able to re-stabilise and unstable aircraft would be sufficient to show the usefulness of adaptive control, but the handling of a practical failure case would be ideal. Therefore the focus of this thesis will be on CG shifts rather than on destabilisation through positive feedback, since a model of the effect of CG shifts could be used in the linear analysis of Chapters 4 and 6, and in the simulations of Chapter 7. Positive feedback would merely serve as a simple practical destabilisation technique for the flight tests described in Chapter 8.

Chapter 3

Aircraft model

In order to analyse the effect of in-flight damage on an aircraft, design a fault-tolerant adaptive control system and test this control system in simulation, a non-linear model of the aircraft is required, and this model must include the effects of in-flight damage on the aircraft behaviour.

Since this thesis focuses on shifts in the centre of gravity as a failure case to test the fault-tolerance of the adaptive control system, this chapter derives a non-linear model of a fixed-wing aircraft with a moving CG. This model is obtained by augmenting a standard fixed-wing aircraft model with a set of equations which model the effect of CG shifts on the aircraft parameters. The model is derived in symbolic form, and then applied to the Variable Stability UAV.

A block diagram of this aircraft model is shown in Figure 3.1, with the blocks in the diagram roughly corresponding to the sections of this chapter. Section 3.1 establishes all the conventions and definitions used in the aircraft model. Section 3.2 gives the six degrees of freedom equations of motion for the aircraft, and Section 3.3 gives the equations for the forces and moments acting on the aircraft. Section 3.4 concludes the chapter by deriving equations which model the effect of shifts in the centre of gravity in the aircraft parameters.

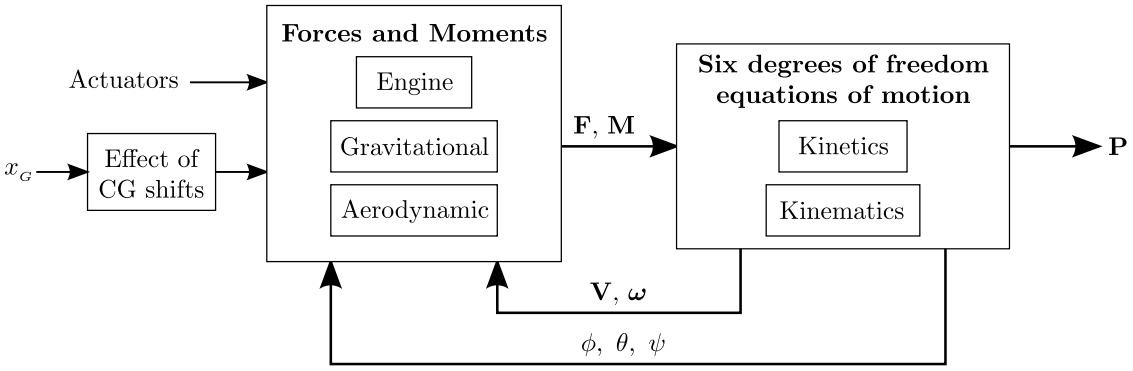

Figure 3.1: Structure of the aircraft model

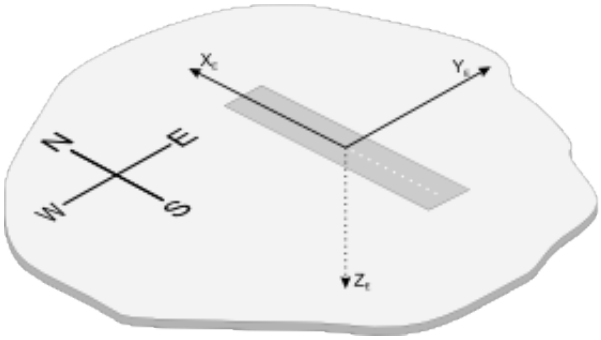

Figure 3.1.1: Definition of the inertial axis system [4]

3.1 Definitions and notations

3.1.1 Axis system definition

This section defines the different axis systems used in this project, and the relations between them. All vectors used to describe the motions of the aircraft are coordinated in these axis systems.

Inertial axes

In order to apply Newton's laws and obtain an aircraft model, an inertial axis system is required. A right-handed earth axis system is defined for this purpose, with its origin at a certain point on the runway, as shown in Figure 3.1.1. This point is typically chosen below the centre of gravity of the aircraft at the start of the motion studied. The X-axis of the inertial axis system is defined as pointing north, the Y-axis as pointing east, and the Z-axis as pointing downwards.

In order for this axis system to be considered inertial, the earth must be assumed flat and non-rotating. This assumption is reasonable for this project since the distances flown are small, and the rotation of the earth is insignificant compared to that of the aircraft.

The position and velocity of the aircraft are defined as the position and velocity of the aircraft's centre of gravity relative to this inertial axis system. The position of the aircraft in inertial axes is given by the north, east and down coordinates N, E and D, and the velocity vector in inertial axes consists of the time derivatives of the three position coordinates.

$$\mathbf{P}^E = \begin{bmatrix} N & E & D \end{bmatrix}^\mathsf{T} \tag{3.1.1}$$

$$\mathbf{V}^E = \begin{bmatrix} \dot{N} & \dot{E} & \dot{D} \end{bmatrix}^\mathsf{T} \tag{3.1.2}$$

Body axes

Having defined an earth-fixed inertial axis system so that Newton's laws can be applied to the aircraft motions, defining an axis system fixed to the aircraft, known as a body axis

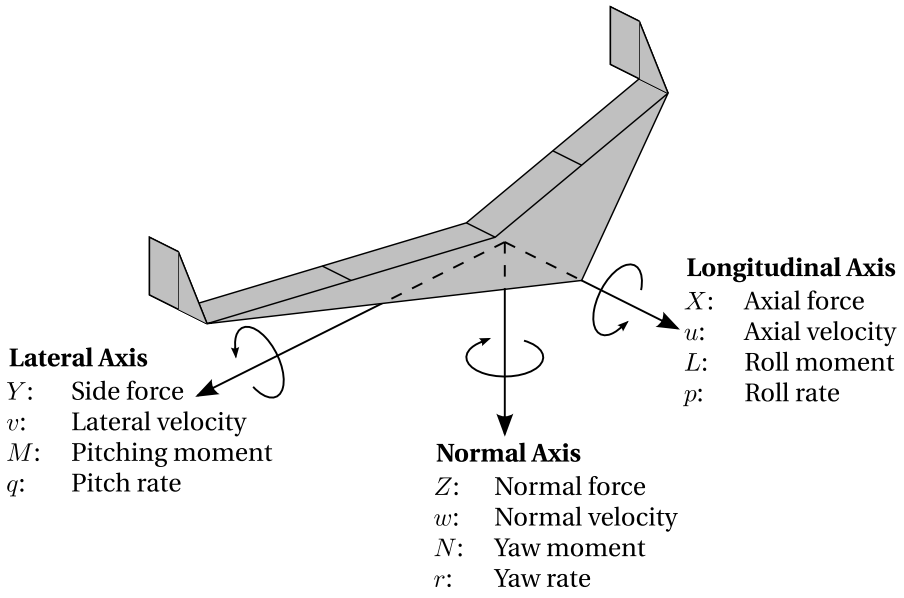

Figure 3.1.2: Definition of the body axis system

system, will greatly simplify the resulting aircraft model. It will also allow the attitude of the aircraft relative to the inertial axes to be represented, and is the axis system in which acceleration and angular rate sensor measurements are naturally coordinated. Such a body axis system is illustrated in Figure 3.1.2.

The origin of the axis system is at the centre of gravity. The X-axis, also known as the longitudinal or roll axis, lies in the aircraft's plane of symmetry, parallel to some reference line, typically the wing chord line, and points in the forward direction. The Z-axis, known as the normal or yaw axis, is also in the plane of symmetry, and is perpendicular to the X-axis in the down direction. The Y-axis, also known as the lateral or pitch axis, is perpendicular to the plane of symmetry, and points in the right-hand or starboard direction.

Figure 3.1.2 also shows the components of the force, moment, velocity and rotation rate vectors coordinated in body axes. X, Y and Z are the force components in the three body axes, u, v and w are the velocity components, L, M and N are the moments about each axis, and p, q and r are the rotation rates around each axis.

$$\mathbf{F}^B = \begin{bmatrix} X & Y & Z \end{bmatrix}^\mathsf{T} \tag{3.1.3}$$

$$\mathbf{V}^B = \begin{bmatrix} u & v & w \end{bmatrix}^\mathsf{T} \tag{3.1.4}$$

$$\mathbf{M}^B = \begin{bmatrix} L & M & N \end{bmatrix}^\mathsf{T} \tag{3.1.5}$$

$$\boldsymbol{\omega}^B = \begin{bmatrix} p & q & r \end{bmatrix}^\mathsf{T} \tag{3.1.6}$$

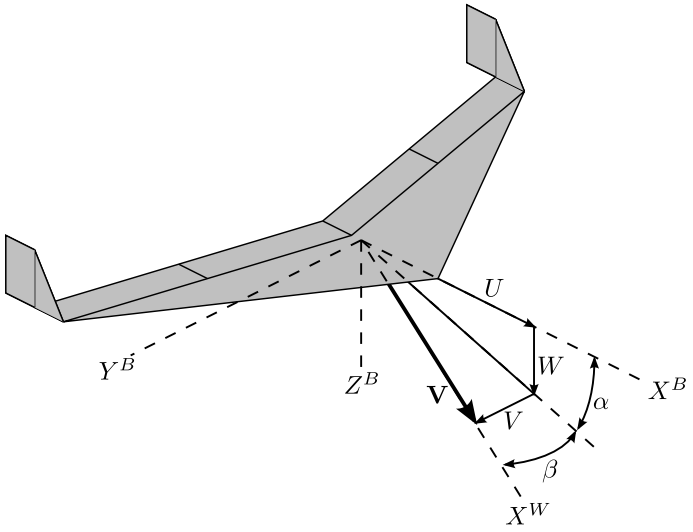

Figure 3.1.3: Definition of the wind axis system

Wind axes

The third axis system used in this thesis is the wind axis system, illustrated in Figure 3.1.3. The origin of this axis system is the centre of gravity, and the X^W-axis points in the direction of the velocity vector $\mathbf{V}$. The Z^W-axis points downwards in the aircraft's plane of symmetry, perpendicular to the velocity vector, and the Y^W-axis points to the right, perpendicular to the X^W and Z^W-axes.

The body axis system can be transformed into the wind axis system by first rotating it around the Y^B-axis through the angle of attack α, and then rotating it around the Z^B-axis through the sideslip angle β, as shown in Figure 3.1.3.

The rotation rate of the aircraft is usually expressed as that of the body axis system with respect to inertial space, coordinated in body axes. It can also be represented as the rotation of the wind axis system with respect to inertial space, coordinated in wind axes. These rotation rates represent a change in the direction of the velocity vector, rather than the attitude of the aircraft.

It can also be convenient to express the acceleration vector of the aircraft in wind axes, particularly the specific acceleration, which is the difference between the total acceleration and the gravitational acceleration of the aircraft [8]:

$$\mathbf{a}_s^w = \mathbf{a}^w - \mathbf{a}_G^w \tag{3.1.7}$$

The specific acceleration in wind axes consists of the axial, lateral and normal specific acceleration components:

$$\mathbf{a}_s^w = \begin{bmatrix} a_a \\ a_l \\ a_n \end{bmatrix} \tag{3.1.8}$$

Unless stated otherwise, these acceleration components will refer to the *specific* acceleration coordinated in *wind* axes.

3.1.2 Attitude representation

In order to describe the motions of the aircraft through inertial space, a representation is required of the orientation, or attitude, of the aircraft with respect to this space. This can be done using Euler angles, an ordered set of three rotation angles which can fully describe the orientation of one axis system with respect to another.

The Euler 3-2-1 attitude representation was used for this project. For this representation, the roll angle ϕ, pitch angle θ and yaw angle ψ were defined so that any attitude can be reconstructed by following these steps, starting with the aircraft wings-level and pointing north:

1. Rotate the aircraft around its Z-axis by the yaw angle ψ. Using the right-hand rule, a positive rotation around the axis pointing down is a rotation to the right.

2. Rotate the aircraft around its Y-axis by the pitch angle θ. A positive rotation around the axis pointing to the right is a upward pitching motion.

3. Rotate the aircraft around its X-axis by the roll angle ϕ. A positive rotation around the axis pointing forwards is a roll to the right.

It can be shown [5] that, for this attitude representation, a vector $\mathbf{V}$ can be transformed from inertial axes to body axes using the matrix $\mathbf{T}$, known as the Direction Cosine Matrix or DCM:

$$\mathbf{V}^B = \mathbf{T}\mathbf{V}^E \tag{3.1.9}$$

$$\mathbf{T} = \begin{bmatrix} C_\psi C_\theta & S_\psi C_\theta & -S_\theta \\ C_\psi S_\theta S_\phi - S_\psi C_\phi & S_\psi S_\theta S_\phi + C_\psi C_\phi & C_\theta S_\phi \\ C_\psi S_\theta C_\phi + S_\psi S_\phi & S_\psi S_\theta C_\phi - C_\psi S_\phi & C_\theta C_\phi \end{bmatrix} \tag{3.1.10}$$

where the following shorthand notation is used:

$$\begin{aligned} C_x &= \cos x \\ S_x &= \sin x \end{aligned} \tag{3.1.11}$$

The reverse transformation can be done using the inverse of the DCM, which equals its transpose, since the DCM is orthogonal.

Any aircraft attitude can be represented in this way, but this representation is not unique when the pitch angle is $\pm 90°$, i.e. when the aircraft points straight upwards or downwards. For instance, using rotation angles of $\psi = 0$, $\theta = 90°$ and $\phi = 90°$ will produce exactly the

same attitude as $\psi = -90°$, $\theta = 90°$ and $\phi = 0$. However, for non-aerobatic flight, the pitch angle will always be much less than 90 degrees, and therefore this Euler angle representation was deemed adequate for this project.

3.1.3 Shifts in the centre of gravity

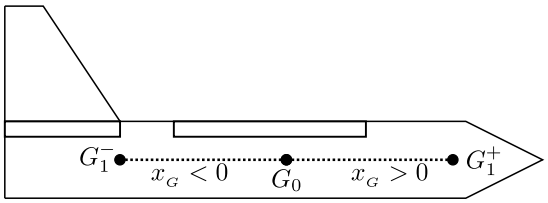

Figure 3.1.4: Notations used to describe shifts in the centre of gravity

For this project, it is assumed that the centre of gravity of the aircraft can shift along the X-axis of the body axis system. In Figure 3.1.4, point G_0 is the nominal CG position, G_1 is the actual location of the CG, and x_G is the distance by which the CG has shifted. The shift distance x_G is defined as positive for a forward shift (G_1^+), and negative for a backward shift (G_1^-).

Furthermore, the following assumptions are made regarding the shift in the centre of gravity:

- It is assumed that the CG shift is entirely internal, and that no external changes to the airframe take place. In reality, CG shifts due to in-flight damage are likely to coincide with damage to the airframe which would affect its aerodynamic properties. However, this thesis focuses on failures where the aerodynamic effects of structural damage are insignificant compared to that of the shift in the centre of gravity. This is assumption is also exactly true for tray movements in the Variable Stability UAV.

- It is assumed that the mass and moment of inertia of the aircraft are unaffected. Again, this assumption will not be valid for all possible practical failures, but the focus of this thesis is on in-flight damage which causes changes in mass and moment of inertia that are insignificant compared to the effect of the CG shift. Also, the mass of the Variable Stability UAV will not change when the tray moves, and the mass of the tray is small enough compared to that of the aircraft that its movement will not significantly affect the moment of inertia.

3.1.4 Angles of incidence

In the aerodynamic modelling of a fixed-wing aircraft, it is often useful to express the velocity vector of the aircraft, coordinated in body axes, in polar form. In stead of expressing it in

rectangular coordinates as three vector components u, v and w, it can be expressed in terms of the airspeed $\bar{V}$, the angle of attack α, and the sideslip angle β.

The airspeed is defined as the magnitude of the velocity vector, while the angle of attack and angle of sideslip are respectively defined as the normal and lateral angles between the velocity vector and the body axis system. These angles are also the angles incidence of the air flow onto the aircraft.

The following equations can be used to transform the velocity vector in body axes from rectangular to polar coordinates:

$$\bar{V} = \sqrt{u^2 + v^2 + w^2} \tag{3.1.12}$$

$$\tan\alpha = w/u \tag{3.1.13}$$

$$\sin\beta = v/\bar{V} \tag{3.1.14}$$

If the aircraft is rotating, then different points on the aircraft will have different angles of incidence. For instance, if the aircraft is pitching upwards, there will be a greater angle of incidence on the tailplane than on the wing, causing the tailplane to generate more lift and damp the pitching motion. This phenomenon is known as *induced angle of attack* and is responsible for many of the aerodynamic properties of fixed-wing aircraft.

The velocity vector of the aircraft, and therefore its angle of attack, is defined in a conventional aircraft as that of its centre of gravity. Therefore variations in the angle of incidence over the length of the aircraft can cause ambiguity in the definition of the aircraft's angle of attack when the centre of gravity moves around.

In the rest of this thesis, the term "angle of attack of the aircraft" and the corresponding symbol α with no subscript will refer to the angle of incidence on the actual CG. Subscripts will be used to distinguish between the angles of incidence on the nominal and actual centres of gravity (α_{G_0} and α_{G_1}, respectively). Therefore the following will always be true:

$$\alpha = \alpha_{G_1} \tag{3.1.15}$$

while the following will be true if the CG is in the nominal position:

$$\alpha_{G_0} = \alpha_{G_1} = \alpha \tag{3.1.16}$$

The angle of sideslip β is also defined as the angle of incidence on the actual centre of gravity, but CG shifts have much less effect on the lateral dynamics, as shown in Appendix C, and therefore the effect of CG shifts on the definition of angle of sideslip was not taken into account.

Figure 3.1.5 shows the velocities and angles of incidence of the nominal and actual centres of gravity for a forward (positive) CG shift. For small angles of attack and pitch rates, the forward velocity of each point will be approximately equal to the airspeed:

$$u_{G_1} \approx u_{G_0} \approx \bar{V} \tag{3.1.17}$$

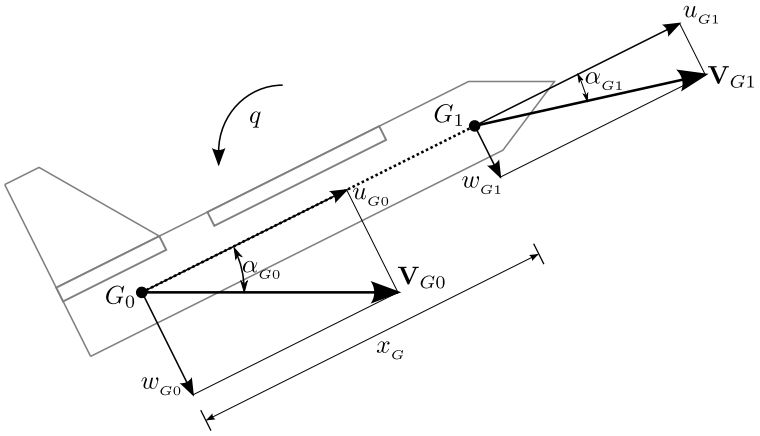

Figure 3.1.5: Angles of incidence at the nominal and actual centres of gravity

Also for small angles of attack, the downward velocities of the two points will be related as follows:

$$w_{G_1} = w_{G_0} - x_G q \tag{3.1.18}$$

The angle of incidence of the nominal CG is defined as the inverse tangent of the ratio between its downward and forward velocities, which for small angles of attack can be approximated by the ratio itself:

$$\alpha_{G_0} = \arctan\left(\frac{w_{G_0}}{u_{G_0}}\right) \approx \frac{w_{G_0}}{u_{G_0}} \tag{3.1.19}$$

Equation 3.1.18 can be substituted into a similar expression for the angle of incidence on the actual centre of gravity, yielding an equation relating α_{G_0} and α_{G_1}:

$$\begin{aligned} \alpha_{G_1} &\approx \frac{w_{G_1}}{u_{G_1}} \\ &= \frac{w_{G_0} - x_G q}{u_{G_0}} \\ &= \alpha_{G_0} - \frac{x_G q}{\bar{V}} \end{aligned} \tag{3.1.20}$$

Therefore the difference between the angles of incidence on the nominal and actual CGs is dependent on the CG shift distance, the pitch rate and the airspeed. This relation will be used in the analysis of the effect of CG shifts on the aerodynamic properties of the aircraft in Section 3.4.

3.1.5 Actuator definitions

The Variable Stability UAV has seven physical actuators which can be used to control the aircraft, shown in Figure 3.1.6. A throttle command can be sent to the motor through the speed controller, and on each wing there is a rudder and an inboard and outboard elevon.

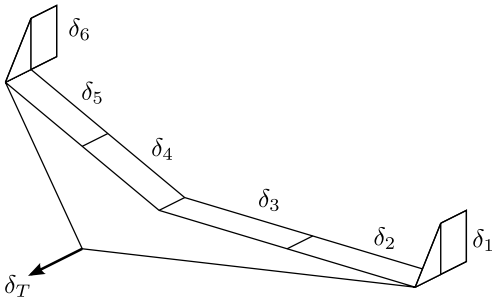

Figure 3.1.6: The physical actuators of the Variable Stability UAV

These physical actuators can be mixed together to create the four virtual actuators of a conventional fixed-wing aircraft: the throttle δ_T, which provides propulsion, the aileron δ_A, which control the rolling motions, the elevator δ_E, which controls the pitching motions, and the rudder δ_R, which controls the yawing motions.

Furthermore, the aerodynamic actuators were divided into three pairs: the two rudders, the two elevons on the left wing and the two elevons on the right wing. The physical actuators were constrained so that the deflection of two paired actuators would be identical at any time, effectively reducing the set of actuators to a rudder, a left elevon and a right elevon.

The virtual rudder actuator was defined as the average deflection of the two rudders, the virtual elevator as the average common-mode deflection of the left and right elevons, and the virtual aileron as the average differential deflection of the elevons.

The constraining of the physical actuators and the definitions of the virtual actuators imply the manner in which the physical actuators must be deflected to produce a given set of virtual actuator deflections. The physical rudders simply follow the virtual rudder command, the left elevons must be the difference between the virtual elevator and aileron commands, and the right elevons must be the sum of the virtual elevator and aileron commands.

The throttle actuator was defined so that a positive throttle command will produce a forward thrust force. The aerodynamic actuators were all defined so that a positive deflection will produce a negative moment around the corresponding axis. The virtual actuator limits were chosen so that the virtual aileron and elevator would both have a maximum deflection of $\pm 12^\circ$, and the virtual rudder would have a range of $\pm 15^\circ$. The virtual thrust actuator would have a maximum setting of 17 N.

The mathematical relationship between the physical and virtual actuators is discussed in detail in Appendix A.2, using the concept of a *mixing matrix*. For the rest of the body of this thesis, it will be assumed that the aircraft only has the four virtual actuators. The effect of each actuator is described by the force and moment equations of Section 3.3.

3.2 Six degrees of freedom equations of motion

This section describes the equations of motion for a rigid body moving and rotating in three dimensions, taken from [5].

3.2.1 Kinetics

The following equations describe the relation between the forces and moments acting on the aircraft and the velocity and angular rate components of the aircraft in body axes:

$$X = m(\dot{u} - vr + wq) \tag{3.2.1}$$

$$Y = m(\dot{v} + ur + wp) \tag{3.2.2}$$

$$Z = m(\dot{w} - uq + vp) \tag{3.2.3}$$

$$L = \dot{p}I_{xx} + qr(I_{zz} - I_{yy}) \tag{3.2.4}$$

$$M = \dot{q}I_{yy} + pr(I_{xx} - I_{zz}) \tag{3.2.5}$$

$$N = \dot{r}I_{zz} + pq(I_{yy} - I_{xx}) \tag{3.2.6}$$

3.2.2 Kinematics

The following matrix equation describes the relation between angular rates of the aircraft in body axes, and the time derivatives of the Euler angles which represent the attitude of the aircraft:

$$\begin{bmatrix} \dot{\phi} \\ \dot{\theta} \\ \dot{\psi} \end{bmatrix} = \begin{bmatrix} 1 & \sin\phi\tan\theta & \cos\phi\tan\theta \\ 0 & \cos\phi & -\sin\phi \\ 0 & \sin\phi\sec\theta & \cos\phi\sec\theta \end{bmatrix} \begin{bmatrix} p \\ q \\ r \end{bmatrix} \tag{3.2.7}$$

The rates of change of the position coordinates of the aircraft are related to the body axis velocity components through the inverse of the DCM given in Equation 3.1.10:

$$\begin{bmatrix} \dot{N} \\ \dot{E} \\ \dot{D} \end{bmatrix} = \begin{bmatrix} C_\psi C_\theta & C_\psi S_\theta S_\phi - S_\psi C_\phi & C_\psi S_\theta C_\phi + S_\psi S_\phi \\ S_\psi C_\theta & S_\psi S_\theta S_\phi + C_\psi C_\phi & S_\psi S_\theta C_\phi - C_\psi S_\phi \\ -S_\theta & C_\theta S_\phi & C_\theta C_\phi \end{bmatrix} \begin{bmatrix} u \\ v \\ w \end{bmatrix} \tag{3.2.8}$$

where the shorthand of Equation 3.1.11 is used again.

3.3 Forces and moments

This section gives equations for the forces and moments acting on the aircraft, coordinated in body axes unless stated otherwise. The total force and moment vectors acting on the aircraft in flight are the sum of the aerodynamic, thrust and gravitational forces:

$$\mathbf{F} = \mathbf{F}^A + \mathbf{F}^T + \mathbf{F}^G \tag{3.3.1}$$

$$\mathbf{M} = \mathbf{M}^A + \mathbf{M}^T + \mathbf{M}^G \tag{3.3.2}$$

where $\mathbf{F}^B$ is the body axis force vector consisting of the axial force X, the side force Y and the normal force Z, and $\mathbf{M}^B$ is the body axis moment vector consisting of the roll moment L, the pitching moment M and the yaw moment N:

$$\mathbf{F}^B = \begin{bmatrix} X \\ Y \\ Z \end{bmatrix} \qquad \mathbf{M}^B = \begin{bmatrix} L \\ M \\ N \end{bmatrix} \tag{3.3.3}$$

In order for the kinetic equations of Section 3.2.1 to apply to an aircraft with a moving centre of gravity, the force vector must act through the instantaneous CG, and the moment vector must act around it. Therefore the effect of CG shifts on the aerodynamic, thrust and gravitational forces and moments must be taken into account in order to model an aircraft with a moving CG. This section gives the standard force and moment equations for an aircraft with a static CG, while Section 3.4 discusses the effect of CG shifts on the forces and moments.

3.3.1 Gravitational forces and moments

The aircraft is assumed to be flying in a uniform gravitational field, with a gravitational acceleration of $g = 9.81\ \mathrm{m/s^2}$ in the direction of the Z-axis of the inertial axis system:

$$\mathbf{F}^{GE} = \begin{bmatrix} 0 \\ 0 \\ mg \end{bmatrix} \tag{3.3.4}$$

The gravitational force vector can be transformed from inertial axes to body axes using the DCM, yielding the following result:

$$\begin{bmatrix} X^G \\ Y^G \\ Z^G \end{bmatrix} = \begin{bmatrix} -\sin\theta \\ \cos\theta\sin\phi \\ \cos\theta\cos\phi \end{bmatrix} mg \tag{3.3.5}$$

The gravitational force acts through the aircraft's centre of gravity, and therefore creates no moments around any of the axes through it.

$$\mathbf{M}^G = \mathbf{0} \tag{3.3.6}$$

An implication of the assumption of a uniform gravitational field is that the aircraft's centre of gravity and its centre of mass are the same point, and the two terms can be used interchangeably. In this thesis, the point will generally be referred to as the centre of gravity.

Since the gravitational force by definition acts through the instantaneous centre of gravity of the aircraft, CG shifts will have no effect on the force, and will not cause it to create any moments around the CG.

3.3.2 Engine forces and moments

A simple first-order system with a time constant τ_T was used to model the engine dynamics:

$$\dot{T} = \frac{1}{\tau_T}(\delta_T - T) \tag{3.3.7}$$

where the thrust command δ_T and thrust force T are the input and output of the system respectively. The engine creates a force along the X-axis equal to the thrust output, and all other engine forces and moments are zero:

$$X^T = T \tag{3.3.8}$$

$$Y^T = Z^T = 0 \tag{3.3.9}$$

$$\mathbf{M}^T = \mathbf{0} \tag{3.3.10}$$

Since the thrust force acts along the X-axis of the body axis system, and this project only considers shifts in the centre of gravity along the same axis, the effect of the thrust force is not dependent on the CG position.

3.3.3 Aerodynamic forces and moments

The aerodynamic forces and moments acting on an aircraft are much more complex than the gravitational and thrust forces, and have a much greater effect on the aircraft dynamics. All the aerodynamic forces and moments are proportional to the dynamic pressure $\bar{q}$, which is a function of the air density ρ and the airspeed $\bar{V}$:

$$\bar{q} = \tfrac{1}{2}\rho\bar{V}^2 \tag{3.3.11}$$

The aerodynamic forces are products of the dynamic pressure, the wing reference area S, and the aerodynamic force coefficients:

$$X^A = \bar{q}SC_X \tag{3.3.12}$$

$$Y^A = \bar{q}SC_Y \tag{3.3.13}$$

$$Z^A = \bar{q}SC_Z \tag{3.3.14}$$

The aerodynamic moments are products of the dynamic pressure, the wing reference area, and the aerodynamic moment coefficients, as well as an appropriate reference moment arm, which in the case of the pitching moment is the mean aerodynamic chord $\bar{c}$, and in the case of the roll and yaw moments is the wing span b:

$$L^A = \bar{q}SbC_l \tag{3.3.15}$$

$$M^A = \bar{q}S\bar{c}C_m \tag{3.3.16}$$

$$N^A = \bar{q}SbC_n \tag{3.3.17}$$

The axial and normal force coefficients can expressed in terms of the lift and drag coefficients, where lift is defined as an upward force normal to the velocity vector in the plane of symmetry, and drag as a force in the opposite direction to the velocity vector. The lift and drag coefficients are related to the axial and normal force coefficients as follows:

$$C_X = -C_D \cos\alpha + C_L \sin\alpha \tag{3.3.18}$$

$$C_Z = -C_L \cos\alpha - C_D \sin\alpha \tag{3.3.19}$$

The force and moment coefficients depend on the airspeed, angles of incidence, rotation rates and actuator deflections. These dependencies are non-linear in general, but can be approximated with the following set of linear equations if the angles of incidence are small enough:

$$C_D = C_{D_0} + \frac{C_L^2}{\pi A e} \tag{3.3.20}$$

$$C_y = C_{y_\beta}\beta + \frac{b}{2\bar{V}}C_{y_p}p + \frac{b}{2\bar{V}}C_{y_r}r + C_{y_{\delta_a}}\delta_a + C_{y_{\delta_r}}\delta_r \tag{3.3.21}$$

$$C_L = C_{L_0} + C_{L_\alpha}\alpha + \frac{\bar{c}}{2\bar{V}}C_{L_q}q + C_{L_{\delta_e}}\delta_e \tag{3.3.22}$$

$$C_l = C_{l_\beta}\beta + \frac{b}{2\bar{V}}C_{l_p}p + \frac{b}{2\bar{V}}C_{l_r}r + C_{l_{\delta_a}}\delta_a + C_{l_{\delta_r}}\delta_r \tag{3.3.23}$$

$$C_m = C_{m_0} + C_{m_\alpha}\alpha + \frac{\bar{c}}{2\bar{V}}C_{m_q}q + C_{m_{\delta_e}}\delta_e \tag{3.3.24}$$

$$C_n = C_{n_\beta}\beta + \frac{b}{2\bar{V}}C_{n_p}p + \frac{b}{2\bar{V}}C_{n_r}r + C_{n_{\delta_a}}\delta_a + C_{n_{\delta_r}}\delta_r \tag{3.3.25}$$

The proportionality constants in the equations above are the non-dimensional stability and control derivatives. They are defined as the partial derivatives of the force and moment coefficients with respect to a particular aircraft state or actuator deflection, using the following notation:

$$C_{x_y} = \frac{\partial C_x}{\partial y} \tag{3.3.26}$$

These parameters can be determined by analysis software such as AVL. Given a geometric model of an aircraft, its inertial properties, including the CG position, and an operating point, AVL calculates the aerodynamic parameters of the aircraft around that operating point. The AVL analysis of the Variable Stability UAV is described in Appendix A.3.2.

The aerodynamic forces and moments can be seriously affected by shifts in the centre of gravity, and therefore these effects are investigated in Section 3.4.

3.4 Effect of CG shifts on the aircraft parameters

In the Sections 3.2 and 3.3, a model was given for an aircraft with a static centre of gravity. In order to design an adaptive control system to handle CG shifts and test it in simulation,

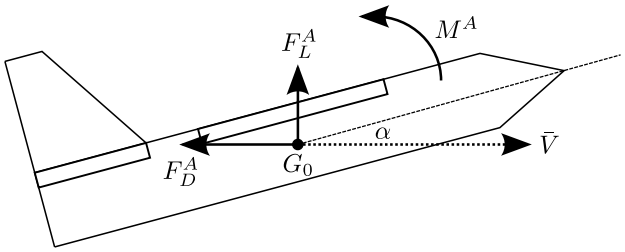

Figure 3.4.1: Longitudinal aerodynamic forces and moments

the aircraft model must be modified to include the effects of CG shifts. CG shifts should be modelled in a way that allows a simple linear analysis of their effect on the aircraft dynamics, and does not require a numerical analysis of the airframe for each CG position.

Therefore in this section, symbolic expressions are derived for the longitudinal stability and control derivatives of a general fixed-wing aircraft in terms of the nominal values of these parameters and the longitudinal position of the CG. These expressions are derived using a simplified force and moment model of the aircraft, and allow analysis and simulation of the longitudinal dynamics of any aircraft using the data from a single AVL analysis. The results are applied to the Variable Stability UAV and compared with those of AVL analyses for different CG positions.

This section only analyses the effect of CG shifts on the longitudinal dynamics. Appendix C gives an analysis of the effect of longitudinal CG shifts on the lateral dynamics, which shows that they are not seriously affected over the range of CG positions considered for this project.

3.4.1 Derivation

In Section 3.3.3, equations were given for three components of the longitudinal aerodynamic effects on the aircraft: a drag force, which acts through the CG in a direction opposite to the velocity vector, a lift force, which acts through the CG in a direction perpendicular to the velocity vector, and a pitching moment around the CG. These forces and moments are shown in Figure 3.4.1.

The drag force is typically much smaller than the lift force and does not have as much effect on the aircraft dynamics, and is therefore not included in the analysis of the effect of CG shifts. Also, it is assumed that the angle of attack is small enough that its cosine can be regarded as unity.

Using the equations of Section 3.3.3, expressions for the lift force and pitching moment

can be obtained that are linear in the longitudinal aircraft states and the elevator deflection:

$$F_L^A = (\bar{q}SC_{L_0}) + (\bar{q}SC_{L_\alpha})\alpha + \left(\frac{\bar{q}S\bar{c}C_{L_q}}{2\bar{V}}\right)q + (\bar{q}SC_{L_{\delta_e}})\delta_e \tag{3.4.1}$$

$$M^A = (\bar{q}S\bar{c}C_{m_0}) + (\bar{q}S\bar{c}C_{m_\alpha})\alpha + \left(\frac{\bar{q}S\bar{c}^2C_{m_q}}{2\bar{V}}\right)q + (\bar{q}S\bar{c}C_{m_{\delta_e}})\delta_e \tag{3.4.2}$$

In these two equations, the coefficients of the states and the elevator input, which contain the nominal *non-dimensional* stability and control derivatives, can be lumped together to form the nominal *dimensional* stability and control derivatives:

$$F_L^A = L_0 + L_\alpha\alpha + L_q q + L_{\delta_e}\delta_e \tag{3.4.3}$$

$$M^A = M_0 + M_\alpha\alpha + M_q q + M_{\delta_e}\delta_e \tag{3.4.4}$$

where the following notation is used for the non-dimensional and dimensional coefficients respectively:

$$C_{x_y} = \frac{\partial C_x}{\partial y} \tag{3.4.5}$$

$$X_y = \frac{\partial X}{\partial y} \tag{3.4.6}$$

Equations 3.4.3 and 3.4.4 are expressions for a lift force through the *nominal* CG, and a pitching moment around it. These expressions depend on the angle of incidence at the nominal CG. However, in order to combine the expressions for the forces and moments with the kinetic equations of Section 3.2.1 to obtain an aircraft model, expressions are required for the forces through and moments around the *actual* CG, which depend on the angle of incidence at this point.

That is, for a variable stability aircraft, Equations 3.4.3 and 3.4.4 must be written as:

$$F_{L_{G0}}^A = L_0 + L_\alpha\alpha_{G_0} + L_q q + L_{\delta_e}\delta_e \tag{3.4.7}$$

$$M_{G0}^A = M_0 + M_\alpha\alpha_{G_0} + M_q q + M_{\delta_e}\delta_e \tag{3.4.8}$$

where $F_{L_{G0}}^A$ is the lift force through the nominal centre of gravity G_0, M_{G0}^A is the pitching moment around G_0, and α_{G_0} is the angle of incidence at G_0. For the aircraft model, expressions are required for $F_{L_{G1}}^A$ and M_{G1}^A that depend α_{G_1}:

$$F_{L_{G1}}^A = L'_0 + L'_\alpha\alpha_{G_1} + L'_q q + L'_{\delta_e}\delta_e \tag{3.4.9}$$

$$M_{G1}^A = M'_0 + M'_\alpha\alpha_{G_1} + M'_q q + M'_{\delta_e}\delta_e \tag{3.4.10}$$

where the constants with the notation X'_y are the new dimensional stability and control derivatives with the CG shift taken into account.

$F_{L_{G0}}^A$ and M_{G0}^A can be treated as a force acting through G_0 and a couple moment acting on the aircraft, shown in Figure 3.4.2. These must be transformed to a couple moment and a force acting through G_1. The couple moment is independent of the CG position, while the

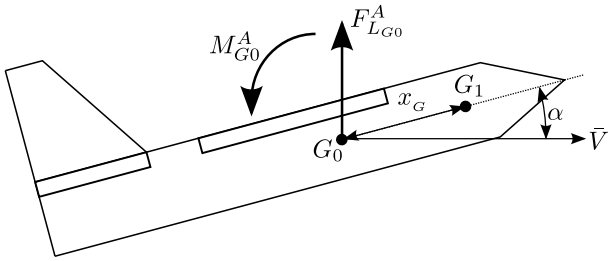

Figure 3.4.2: Lift force and pitching moment at the nominal and actual CGs

force through G_0 can be represented as the same force through G_1 and the pitching moment which it creates around G_1. Therefore the force and couple moment at G_1 can be written in terms of the force and couple moment at G_0 as follows:

$$F^A_{L_{G1}} = F^A_{L_{G0}} \tag{3.4.11}$$

$$\begin{aligned} M^A_{G1} &= M^A_{G0} - F^A_{L_{G0}} x_G \cos\alpha \\ &\approx M^A_{G0} - F^A_{L_{G0}} x_G \end{aligned} \tag{3.4.12}$$

From Section 3.1.4, the relation between the angles of incidence at the nominal and actual CGs is as follows:

$$\alpha_{G_1} = \alpha_{G_0} - \frac{x_G q}{\bar{V}} \tag{3.4.13}$$

$$\therefore \alpha_{G_0} = \alpha_{G_1} + \frac{x_G q}{\bar{V}} \tag{3.4.14}$$

Equations 3.4.11 to 3.4.14 can be substituted into Equations 3.4.7 and 3.4.8 and manipulated to yield the following expressions for the lift force and pitching moment at the actual CG:

$$F^A_{L_{G1}} = L_0 + L_\alpha \alpha_{G_1} + \left(L_q + \frac{L_\alpha}{\bar{V}} x_G \right) q + L_{\delta_e} \delta_e \tag{3.4.15}$$

$$\begin{aligned} M_{G_1} &= (M_0 - L_0 x_G) + (M_\alpha - L_\alpha x_G)\alpha_{G_1} \\ &\quad + \left(M_q + \left(\frac{M_\alpha}{\bar{V}} - L_q \right) x_G - \frac{L_\alpha x_G^2}{\bar{V}} \right) q \\ &\quad + (M_{\delta_e} - L_{\delta_e} x_G)\delta_e \end{aligned} \tag{3.4.16}$$

These equations have the form of Equations 3.4.9 and 3.4.10, and therefore the new dimensional stability and control derivatives can be taken from them. Three of the eight parameters are unaffected by the CG shift:

$$L'_0 = L_0 \tag{3.4.17}$$

$$L'_\alpha = L_\alpha \tag{3.4.18}$$

$$L'_{\delta_e} = L_{\delta_e} \tag{3.4.19}$$

Four parameters are linearly dependent on the CG shift distance x_G:

$$L'_q = L_q + \frac{L_\alpha}{\bar{V}} x_G \tag{3.4.20}$$

$$M'_0 = M_0 - L_0 x_G \tag{3.4.21}$$

$$M'_\alpha = M_\alpha - L_\alpha x_G \tag{3.4.22}$$

$$M'_{\delta_e} = M_{\delta_e} - L_{\delta_e} x_G \tag{3.4.23}$$

The change in L_q is due to the induced angle of attack at the nominal CG, while the three moment coefficients above are affected by the moment of the lift force at G_0 around the actual CG.

The last parameter is quadratically dependent on x_G:

$$M'_q = M_q + \left(\frac{M_\alpha}{\bar{V}} - L_q \right) x_G - \frac{L_\alpha}{\bar{V}} x_G^2 \tag{3.4.24}$$

M_q is affected by both the induced angle of attack and the pitching moment created by the lift force, hence the quadratic relation to the CG shift distance.

These new dimensional stability and control derivatives can in turn be transformed back to the non-dimensional coefficients:

$$C'_{L_0} = C_{L_0} \tag{3.4.25}$$

$$C'_{L_\alpha} = C_{L_\alpha} \tag{3.4.26}$$

$$C'_{L_{\delta_e}} = C_{L_{\delta_e}} \tag{3.4.27}$$

$$C'_{L_q} = C_{L_q} + 2C_{L_\alpha} \left(\frac{x_G}{\bar{c}} \right) \tag{3.4.28}$$

$$C'_{m_0} = C_{m_0} - C_{L_0} \left(\frac{x_G}{\bar{c}} \right) \tag{3.4.29}$$

$$C'_{m_\alpha} = C_{m_\alpha} - C_{L_\alpha} \left(\frac{x_G}{\bar{c}} \right) \tag{3.4.30}$$

$$C'_{m_{\delta_e}} = C_{m_{\delta_e}} - C_{L_{\delta_e}} \left(\frac{x_G}{\bar{c}} \right) \tag{3.4.31}$$

$$C'_{m_q} = C_{m_q} + \left(2C_{m_\alpha} - C_{L_q} \right) \left(\frac{x_G}{\bar{c}} \right) - 2C_{L_\alpha} \left(\frac{x_G}{\bar{c}} \right)^2 \tag{3.4.32}$$

These parameters can be used in the aerodynamic equations of Section 3.3.3 to obtain a non-linear model of a variable stability aircraft. This model can then be used in non-linear simulation, or for a linear analysis of the effect of CG shifts on the aircraft dynamics.

3.4.2 Analysis and comparison with AVL data

The nominal parameters of an aircraft can be substituted into Equations 3.4.25 to 3.4.32 to calculate its aerodynamic parameters for any CG position. Appendix A.3 gives the parameters of the Variable Stability UAV for a number of CG positions, starting at the nominal distance of 351 mm behind the nose of the aircraft.

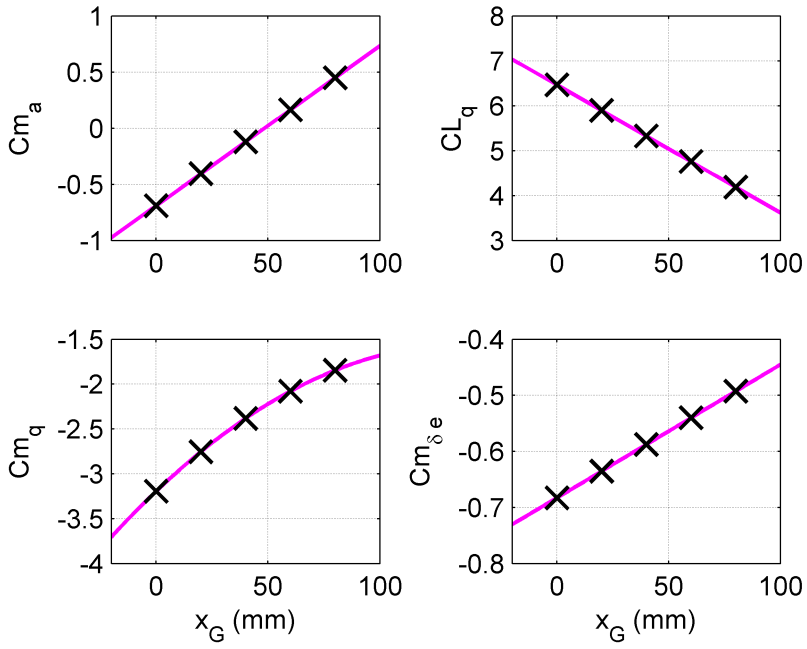

Figure 3.4.3: Changes in the aerodynamic parameters of the Variable Stability UAV over a range of backward CG shifts, calculated using the derived equations (solid line) and AVL (crosses)

In Figure 3.4.3, the crosses indicate the values of the parameters C_{m_α}, C_{L_q}, C_{m_q} and $C_{m_{\delta_e}}$ returned by AVL at five different CG positions. The solid lines represent the values of these parameters over a range of CG movement, calculated using the equations of the previous section. The values of these four parameters calculated by the equations are virtually identical to those returned by AVL, while C_{L_α} and $C_{L_{\delta_e}}$ remain constant according to both the equations and AVL. AVL does not return values for the static lift and pitching moment coefficients C_{L_0} and C_{m_0}.

Since AVL is a trusted tool the analysis of aircraft dynamics and in aircraft control design, the correspondence with AVL data adds considerable credibility to the derived equations for the effect of CG shifts on the aerodynamic parameters.

From Figure 3.4.3, it is clear that the parameter C_{m_α} is the most severely affected by shifts in the centre of gravity, changing its sign for a shift of 48 mm. According to the AVL analysis, the neutral point is 48 mm behind the nominal CG, and therefore C_{m_α} is negative when the CG is in front of the neutral point, and positive when the CG is behind the neutral point. This parameter determines the stability of the mode of motion known as the short period mode, which is discussed in Section 4.4.1.

3.5 Summary

In this chapter, equations were developed to model the flight behaviour of the Variable Stability UAV. After establishing the necessary notations and definitions, equations were given for the six degrees of freedom equations of motion, consisting of the kinetic and kinematic equations. Then equations were given for the gravitational, engine and aerodynamic forces and moments acting on the aircraft, and the chapter concluded with a set of equations which represent the effect of shifts in the centre of gravity on the aerodynamic parameters. These equations corresponded almost exactly with an analysis performed using AVL.

In Chapter 4, the non-linear aircraft model is linearised so that the effect of CG shifts on the longitudinal dynamics can be investigated using linear analysis. The aircraft model equations from this chapter can also be used to perform non-linear simulations of the effect of CG shifts on the Variable Stability UAV, in order to test the fault-tolerance of the adaptive control system designed in Chapters 5 and 6. Such simulations are done in Chapter 7.

Chapter 4

Linear longitudinal analysis

In Chapter 3, a non-linear, cross-coupled model of the aircraft dynamics was developed. Since many tools exist for the analysis of linear time-invariant (LTI) systems and for the design of control systems for such plants, it is desirable to obtain an LTI approximation of the aircraft dynamics. This chapter is concerned with deriving a linear model of the longitudinal aircraft dynamics, which should allow a linear analysis of the effect of CG shifts. This analysis should in turn provide useful insight for the design of a fault tolerant adaptive longitudinal control system.

Section 4.1 states the assumptions that were used to linearise the aircraft model, and Section 4.2 defines the trim condition around which the longitudinal aircraft dynamics were linearised. Section 4.3 derives a linear model of the longitudinal dynamics of the aircraft, and Section 4.4 analyses the longitudinal modes of motion. Section 4.5 discusses the decoupling of the longitudinal dynamics into rotational dynamics and kinematics, and Section 4.6 analyses the effect of CG shifts on the longitudinal dynamics.

This chapter focuses on the linear analysis of the *longitudinal* dynamics of the Variable Stability UAV, since these are seriously affected by longitudinal shifts in the centre of gravity. Appendix C gives a linear analysis which shows that longitudinal CG shifts do not have much effect on the lateral dynamics, and Section 4.4.1 contains a brief explanation of why this is the case.

4.1 Linearising assumptions

The linear analysis of the aircraft dynamics is limited to two-dimensional, subsonic, incompressible airflow. Since the maximum airspeed of the Variable Stability UAV is much less than the speed of sound, these assumptions are reasonable for the analysis of its dynamics [6].

The dynamics of the aircraft are analysed by separating its aerodynamic properties under symmetric and asymmetric flow. During symmetric flow, the lateral aerodynamic coefficients

(C_y, C_l and C_n) are exactly zero for a symmetrical aircraft, and therefore symmetric flow only affects the longitudinal dynamics of the aircraft. Asymmetric flow does have some effect on the longitudinal aerodynamic coefficients (C_L, C_D and C_m), but this effect is typically very small compared to that of symmetric flow, and therefore it is assumed that asymmetric flow only affects the lateral dynamics.

This separation between symmetric and asymmetric flow decouples the longitudinal and lateral dynamics, and allows them to be analysed separately. This chapter focuses on the linear analysis of the longitudinal dynamics.

Also, the linear analysis of the aircraft makes use of small disturbance theory. This theory assumes that the deviations of all angles from their trim values will be small enough that their cosines can be regarded as unity, and their sines and tangents as equal to the angles themselves, expressed in radians. For non-aerobatic flight this is a reasonable assumption, since the roll and pitch angles and angles of incidence will remain relatively small.

4.2 Definition of the trim condition

A trim condition is a point in the space of state and control vectors where the time derivative of the state vector is zero:

$$\mathbf{X}_t,\ \mathbf{U}_t \Rightarrow \dot{\mathbf{X}} = 0 \tag{4.2.1}$$

where $\mathbf{X}$ is a vector containing the total values of all the aircraft states, and $\mathbf{U}$ is a vector containing the total values of all actuators. The calculation of the state and control values at the trim point is discussed in [7].

In this section, the total values of state variables will be denoted using capital letters for vectors (e.g. $\mathbf{X}$), and the subscript tot for scalars (e.g. α_{tot}). The subscript t will be used to indicate the trim values of variables (e.g. $\mathbf{X}_t$, α_t), while vectors with lowercase letters (e.g. $\mathbf{x}$) and scalars without subscripts (e.g. α) will be used for the deviations of variables from their trim values.

The total values of actuators will be denoted using capital subscripts (e.g. δ_E), trim values using the subscript t (e.g. δ_{E_t}), and deflections from trim using small letter subscripts (δ_e).

The longitudinal state and control vectors are defined as follows:

$$\mathbf{X} = \begin{bmatrix} \bar{V}_{tot} & \alpha_{tot} & q_{tot} & \theta_{tot} & T_{tot} \end{bmatrix}^\mathsf{T} \tag{4.2.2}$$

$$\mathbf{U} = \begin{bmatrix} \delta_E & \delta_T \end{bmatrix}^\mathsf{T} \tag{4.2.3}$$

Since the aircraft flies at a low altitude (less than 100 metres), the variation in air pressure with altitude has a negligible effect on the aircraft dynamics, and therefore the altitude is not included in the longitudinal state vector for the trim analysis.

If the aircraft is trimmed in level flight, then the pitch rate will have a trim value of zero, and the trim values of the angle of attack and pitch angle will be the same, as will the trim values of the thrust command and the thrust state. Therefore the elements of the trim state and control vectors will be as follows:

$$\mathbf{X}_t = \begin{bmatrix} \bar{V}_t & \alpha_t & 0 & \alpha_t & T_t \end{bmatrix}^\mathsf{T} \tag{4.2.4}$$

$$\mathbf{U}_t = \begin{bmatrix} \delta_{E_t} & T_t \end{bmatrix}^\mathsf{T} \tag{4.2.5}$$

The vectors $\mathbf{x}$ and $\mathbf{u}$ are defined as the deflections of the total state and control vectors $\mathbf{X}$ and $\mathbf{U}$ from their trim values $\mathbf{X}_t$ and $\mathbf{U}_t$:

$$\mathbf{x} = \mathbf{X} - \mathbf{X}_t \tag{4.2.6}$$

$$\mathbf{u} = \mathbf{U} - \mathbf{U}_t \tag{4.2.7}$$

The elements of these vectors are as follows:

$$\begin{bmatrix} \bar{V} \\ \alpha \\ q \\ \theta \\ T \end{bmatrix} = \begin{bmatrix} \bar{V}_{tot} - \bar{V}_t \\ \alpha_{tot} - \alpha_t \\ q_{tot} \\ \theta_{tot} - \alpha_t \\ T_{tot} - T_t \end{bmatrix} \tag{4.2.8}$$

$$\begin{bmatrix} \delta_e \\ \delta_t \end{bmatrix} = \begin{bmatrix} \delta_E - \delta_{E_t} \\ \delta_T - T_t \end{bmatrix} \tag{4.2.9}$$

4.3 Linear longitudinal model

In this section, a linear model of the longitudinal dynamics of the aircraft is obtained. As argued in Section 4.1, the longitudinal dynamics of the aircraft can be decoupled from the lateral dynamics. They can expressed as a differential equation of the following form, where the time derivative of the state vector is a function of the state and control vectors:

$$\dot{\mathbf{X}} = \mathbf{f}(\mathbf{X}, \mathbf{U}) \tag{4.3.1}$$

This equation describes the dynamics of the longitudinal state and control vectors defined in Equations 4.2.2 and 4.2.3.

Since the thrust state is unaffected by the other aircraft states, and since it has already been argued that the aircraft states are unaffected by the altitude, these two states can be decoupled from the aircraft model. A block diagram of this representation of the longitudinal dynamics is shown in Figure 4.3.1. This leaves a four-dimensional state vector containing the aerodynamic states of the aircraft:

$$\mathbf{X} = \begin{bmatrix} \bar{V}_{tot} & \alpha_{tot} & q_{tot} & \theta_{tot} \end{bmatrix}^\mathsf{T} \tag{4.3.2}$$

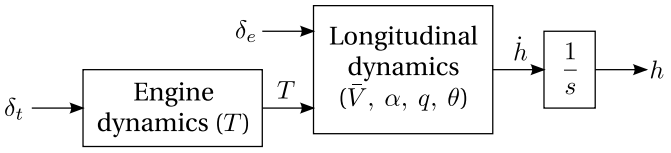

Figure 4.3.1: Longitudinal dynamics with the engine and altitude dynamics decoupled

The inputs affecting these states are the elevator deflection and the thrust state:

$$\mathbf{U} = \begin{bmatrix} \delta_E & T_{tot} \end{bmatrix}^{\mathsf{T}} \tag{4.3.3}$$

and the climb rate is an output dependent on these states:

$$\dot{h} = \bar{V}_{tot} \sin(\theta_{tot} - \alpha_{tot}) \tag{4.3.4}$$

If the state of this non-linear system is close to the trim condition $\mathbf{X}_t$, then its behaviour can be approximated by a linear differential equation:

$$\dot{\mathbf{x}} = A\mathbf{x} + B\mathbf{u} \tag{4.3.5}$$

where lowercase is used for the deflections of the state and control vectors from their trim values.

The parameter matrices in Equation 4.3.5 are the Jacobians of the state derivative function with respect to the state and control vectors, evaluated at the trim condition:

$$A = \left[\frac{\partial \mathbf{f}(\mathbf{X}, \mathbf{U})}{\partial \mathbf{X}}\right]_{\mathbf{X}_t,\, \mathbf{U}_t} \tag{4.3.6}$$

$$B = \left[\frac{\partial \mathbf{f}(\mathbf{X}, \mathbf{U})}{\partial \mathbf{U}}\right]_{\mathbf{X}_t,\, \mathbf{U}_t} \tag{4.3.7}$$

The parameters of the Variable Stability UAV, given in Appendix A.3, can be substituted into the non-linear model, which allows these Jacobians to be calculated numerically. With the CG in the most forward position and at a trim airspeed of 18 m/s, this will yield the following result:

$$\begin{bmatrix} \dot{\bar{V}} \\ \dot{\alpha} \\ \dot{q} \\ \dot{\theta} \end{bmatrix} = \begin{bmatrix} -0.285 & 4.26 & -0.0687 & -9.81 \\ -0.0602 & -11.71 & 0.854 & 0 \\ 0 & -209.4 & -8.89 & 0 \\ 0 & 0 & 1 & 0 \end{bmatrix} \begin{bmatrix} \bar{V} \\ \alpha \\ q \\ \theta \end{bmatrix} + \begin{bmatrix} -0.910 & 0.256 \\ -1.93 & -5.76 \times 10^{-4} \\ -207.2 & 0 \\ 0 & 0 \end{bmatrix} \begin{bmatrix} \delta_e \\ T \end{bmatrix} \tag{4.3.8}$$

The throttle dynamics of Section 3.3.2 are already linear:

$$\dot{T} = -\tfrac{1}{\tau} T + \tfrac{1}{\tau} \delta_t \tag{4.3.9}$$

$$\tau = 0.2 \text{ s}$$

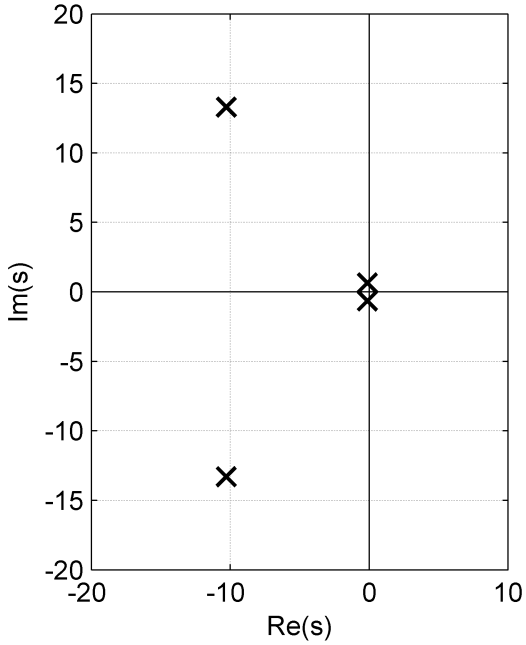

Figure 4.4.1: Longitudinal open-loop poles of the Variable Stability UAV

and the altitude dynamics can be linearised into the following output equation for the fourth-order state-space of Equation 4.3.8:

$$\dot{h} = \begin{bmatrix} 0 & -\bar{V}_t & 0 & \bar{V}_t \end{bmatrix} \begin{bmatrix} \bar{V} \\ \alpha \\ q \\ \theta \end{bmatrix} \tag{4.3.10}$$

$$\bar{V}_t = 18 \text{ m/s}$$

4.4 Longitudinal modes of motion

The A-matrix of Equation 4.3.8 has the following eigenvalues, which are the longitudinal open-loop poles of the aircraft, shown in Figure 4.4.1:

$$\begin{aligned} s_{1,2} &= -10.3 \pm 13.3j \\ s_{3,4} &= -0.132 + 0.647j \end{aligned} \tag{4.4.1}$$

These two complex pole pairs correspond to the two classical longitudinal modes of motion for a fixed-wing aircraft: the short period mode and the phugoid mode. These two modes of motion will now be described qualitatively, and the expected effect of shifts in the centre of gravity on each mode will be discussed briefly. A more detailed quantitative analysis of the two modes can be found in [5].

4.4.1 Short-period mode

The higher-frequency pole pair in Equation 4.4.1 corresponds to the short-period mode. This mode of motion is generated by a mass-spring-damper effect associated with perturbations in the angle of attack of the aircraft. The "mass" in the system is the moment of inertia of the aircraft around its pitch axis (I_{yy}).

The pitching moment due to a perturbation in angle of attack (C_{m_α}) is equivalent to a position-dependent spring force in the system. A perturbation in angle of attack causes a lift force centred at the longitudinal neutral point (NP), which in turn will cause a pitching moment around the centre of gravity. If the CG is in front of the NP, this pitching moment will counteract the perturbation in angle of attack, and therefore the parameter C_{m_α} will be negative and the short period mode will be stable. If the CG is behind the NP, the pitching moment will amplify the perturbation, C_{m_α} will be positive, and the short period mode will be unstable.

The pitching moment due to pitch rate (C_{m_q}) acts as a velocity-dependent damping force in the system. A pitching motion creates an induced angle of attack on the tailplane of a conventional aircraft, or on the rear of a flying wing. This creates a lift force on the rear of the aircraft, which counteracts the pitching motion.

As shown in Section 3.4, the three parameters which dominate the short period mode are all significantly affected by shifts in the centre of gravity, and therefore it is to be expected that this mode of motion will be seriously affected by CG shifts. The parameter C_{m_α} is affected the most, and can even change its sign, which indicates that sufficiently large CG shifts can cause the short period mode to become unstable.

The short-period mode has a lateral counterpart in the *dutch roll mode*, where the sideslip angle and yaw rate interact in a similar fashion to the angle of attack and the pitch rate in the short-period motion. The roll rate and roll angle also couple into the dutch roll mode, but this mode of motion is still similar to the short-period mode in that its stability is dependent on the relative positions of the centre of gravity and the *lateral* neutral point.

However, the lateral NP is typically much further backward than the longitudinal NP, since the only lifting surfaces which have a significant effect on the yaw dynamics are the rudders, which are typically located at the rear of the aircraft. By contrast, the pitching dynamics are dependent on the tailplane (if the particular aircraft has one) as well as the wings, which have a centre of pressure much further forward than that of the rudders.

Therefore the nominal centre of gravity is typically far in front of the lateral neutral point, and the dutch roll mode is not as nearly as severely affected by CG shifts as the short-period mode is. This qualitative argument is confirmed quantitatively for the Variable Stability UAV in Appendix C, where the effect of CG shifts on the lateral parameters is determined with AVL, and used in a linear analysis of the effect of CG shifts on the lateral dynamics.

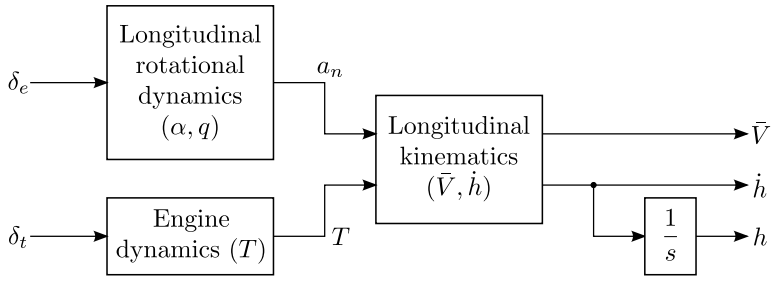

Figure 4.5.1: Longitudinal aircraft model with the rotational dynamics decoupled from the kinematics

4.4.2 Phugoid mode

The lower-frequency pole pair in Equation 4.4.1 corresponds to the phugoid mode. This mode of motion is caused by an exchange between kinetic and potential energy, damped by aerodynamic drag [5], and is mostly manifested in the airspeed and the pitch angle θ_w of the wind axis system, also known as the climb angle, which is the difference between the pitch angle and angle of attack.

If the aircraft experiences a negative perturbation in climb angle, it will start to descend and gain airspeed. The angle of attack remains more or less constant during the motion, and therefore the increase in airspeed leads to an increase in lift, counteracting and eventually reversing the perturbation in climb angle. This creates a slow up-and-down oscillation. This mode of motion is usually visible in the open-loop system as a pair of lightly damped poles with a low frequency, such as the lower-frequency pair in Equation 4.4.1.

The main aerodynamic effect on this mode of motion is the change in lift associated with a change in airspeed. This effect does not have an aerodynamic parameter associated with it; rather, all aerodynamic forces and moments are affected by changes in the airspeed. However, the greatest contributions to the total lift force come from the zero-angle of attack lift force and the lift force due to angle of attack, represented by the parameters C_{L_0} and C_{L_α} respectively. Neither of these parameters is affected by shifts in the centre of gravity, and therefore it is expected that CG shifts will not have such a great effect on the phugoid mode.

4.5 Decoupling of the rotational dynamics and kinematics

In [8], the linear longitudinal model of Equation 4.3.8 was divided into the longitudinal rigid-body rotational dynamics and the longitudinal point mass kinematics. A block diagram of this model structure, including the engine and altitude dynamics, is shown in Figure 4.5.1.

The longitudinal rotational dynamics can be represented as a state-space model with the angle of attack and the pitch rate as states, the elevator deflection as an input, and the normal specific acceleration (NSA) as an output. The longitudinal kinematics has the airspeed and

climb rate as states, and its inputs are the normal specific acceleration and the thrust state, which for small angles of attack is proportional to the axial specific acceleration. The longitudinal rotational dynamics then represent the short-period mode of the aircraft, while the longitudinal kinematics represent the phugoid mode.

This model structure is the basis for the control strategy used in [4] and [8], where an NSA controller is used in the inner loop to control the short-period mode, and reduce the aircraft to a point mass with a controllable acceleration vector. An airspeed and climb rate controller, which generates NSA and throttle commands, is used around the NSA loop.

In reality, the airspeed couples back from the kinematics to the rotational dynamics, and therefore this representation of the aircraft model is not exact. However, as argued in [8], this coupling can be ignored, and this model representation used in the control design, if there is sufficient timescale separation between the two sets of dynamics. Since the bandwidth of the short-period mode of the Variable Stability UAV is about 25 times faster than that of its phugoid mode, this representation is valid for this aircraft.

4.5.1 Longitudinal rigid-body rotational dynamics

The rotational dynamics can be expressed in the following state-space form using the dimensional stability and control derivatives [8]:

$$\begin{bmatrix}\dot{\alpha}\\ \dot{q}\end{bmatrix} = \begin{bmatrix}-\dfrac{L_a}{m\bar{V}_t} & 1-\dfrac{L_q}{m\bar{V}_t}\\ \dfrac{M_\alpha}{I_{yy}} & \dfrac{M_q}{I_{yy}}\end{bmatrix}\begin{bmatrix}\alpha\\ q\end{bmatrix} + \begin{bmatrix}-\dfrac{L_{\delta_e}}{m\bar{V}_t}\\ \dfrac{M_{\delta_e}}{I_{yy}}\end{bmatrix}\delta_e$$

$$a_n = \begin{bmatrix}-\dfrac{L_\alpha}{m} & -\dfrac{L_q}{m}\end{bmatrix}\begin{bmatrix}\alpha\\ q\end{bmatrix} + \begin{bmatrix}-\dfrac{L_{\delta_e}}{m}\end{bmatrix}\delta_e \tag{4.5.1}$$

The derivatives of the angle of attack and pitch rate are essentially the same as in Equation 4.3.8, except that the effects of variations in the airspeed and pitch angle are ignored. The deviation of the normal specific acceleration from trim is simply the deviation of lift force from its trim value, divided by the mass of the aircraft.

For the Variable Stability UAV flying at 18 m/s, the numerical values of this state-space model are as follows:

$$\begin{bmatrix}\dot{\alpha}\\ \dot{q}\end{bmatrix} = \begin{bmatrix}-11.57 & 0.854\\ -209.4 & -8.89\end{bmatrix}\begin{bmatrix}\alpha\\ q\end{bmatrix} + \begin{bmatrix}-1.93\\ -207.2\end{bmatrix}\delta_e \tag{4.5.2}$$

$$a_n = \begin{bmatrix}-208.2 & -2.63\end{bmatrix}\begin{bmatrix}\alpha\\ q\end{bmatrix} + \begin{bmatrix}-34.8\end{bmatrix}\delta_e \tag{4.5.3}$$

Transfer functions from elevator to NSA and from elevator to pitch rate can be obtained from

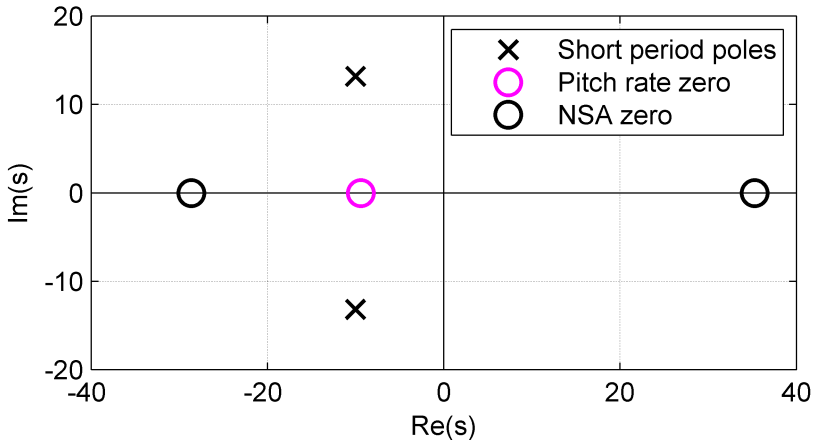

Figure 4.5.2: Poles and zeroes of the transfer functions from elevator to NSA and pitch rate

this state space:

$$\frac{a_n(s)}{\delta_e(s)} = \frac{-34.8(s-35.7)(s+28.9)}{s^2+20.45s+281.6} \tag{4.5.4}$$

$$\frac{q(s)}{\delta_e(s)} = \frac{-207.2(s+9.61)}{s^2+20.45s+281.6} \tag{4.5.5}$$

The poles and zeroes of these transfer functions are shown in Figure 4.5.2. The poles of this model of the rotational dynamics are nearly identical to the short period mode poles of the full longitudinal model. The transfer function from elevator to NSA has two zeroes, one of which is in the right half-plane, which means that the transfer function is non-minimum phase. The transfer function to pitch rate, however, is minimum phase, since its one zero is in the left half-plane.

The non-minimum phase nature of the NSA response is caused by the lift force due to an elevator deflection ($C_{L_{\delta_e}}$). If the elevator is deflected upwards, the aircraft will first accelerate downwards due to this lift force. Then it will start pitching up because of the pitching moment due to the elevator deflection ($C_{m_{\delta_e}}$). This will cause an increase in angle of attack, which will in turn generate an upward lift force (C_{L_α}), causing the aircraft to accelerate upwards. This behaviour can be seen in the NSA response of the Variable Stability UAV to a step in the elevator deflection, shown in Figure 4.5.3.

On a conventional aircraft with a separate wing and tailplane, the moment arm of the elevator around the centre of gravity is long enough that the lift force generated by the elevator is not very significant compared to the pitching moment. Then the zero in the right half-plane will be at a high frequency, and the undershoot in the step response will be small and will quickly fade away. In this case, the non-minimum phase behaviour can often be ignored when designing the control system.

For a flying wing such as the Variable Stability UAV, however, the elevator moment arm is short, and the lift force due to an elevator deflection is significant compared to the pitching

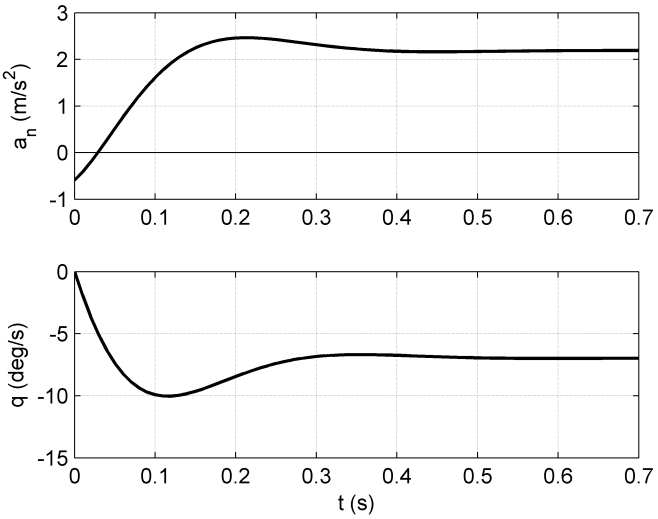

Figure 4.5.3: NSA and pitch rate responses to a 1° step in elevator deflection

moment. Therefore the zero in the right half plane is in the same frequency range as the short period poles, and the non-minimum phase behaviour of the Variable Stability UAV must be taken into account in designing the control system for the aircraft.

4.5.2 Longitudinal point mass kinematics

This section derives a model of the longitudinal kinematics of the aircraft, with the airspeed and climb rate used as state variables. The dynamic equations are first given in terms of the airspeed and the climb angle θ_w, and then transformed to give the dynamics of the climb rate.

This model does not include any drag effects, since drag is difficult to model, and if it is treated as an unmodelled disturbance, it can easily be removed by using integral control. Neglecting drag, the forces affecting the airspeed of the aircraft are the components of the thrust force and gravity in the direction of the velocity vector, shown in Figure 4.5.4.

$$\dot{\bar{V}} = \frac{T}{m}\cos\alpha - g\sin\theta_w \tag{4.5.6}$$

The time derivative of the climb angle can be obtained from the kinematic relationship between speed, normal acceleration and rotation rate for a circular motion:

$$a_n = -\bar{V}\dot{\theta}_w \tag{4.5.7}$$

$$\therefore \dot{\theta}_w = -\frac{a_n}{\bar{V}} \tag{4.5.8}$$

To linearise the differential equations, it is assumed that the angle of attack and climb angle are small, so that $\cos\alpha \approx 1$ and $\sin\theta_w \approx \theta_w$. Then the equations reduce to:

$$\dot{\bar{V}} = \tfrac{1}{m}T - g\theta_w \tag{4.5.9}$$

$$\dot{\theta}_w = -\frac{1}{\bar{V}_t}a_n \tag{4.5.10}$$

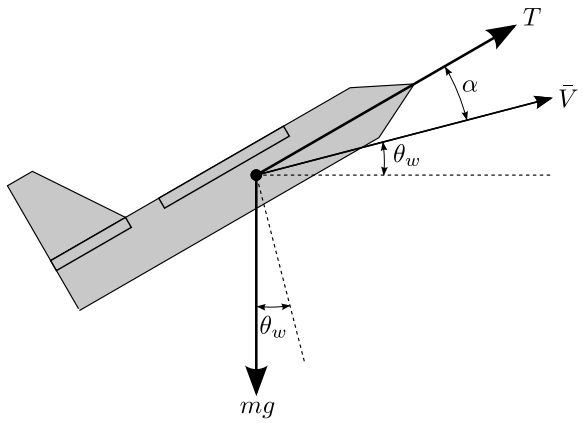

Figure 4.5.4: Forces affecting the airspeed of the aircraft, neglecting drag

where $\bar{V}_t$ is the trim airspeed.

The climb angle can be replaced by the climb rate using the following relation:

$$\dot{h} = \bar{V} \sin\theta_w \approx \bar{V}_t \theta_w \tag{4.5.11}$$

Then the differential equations can be written as:

$$\dot{\bar{V}} = \frac{1}{m}T - \frac{g}{\bar{V}_t}\dot{h} \tag{4.5.12}$$

$$\ddot{h} = -a_n \tag{4.5.13}$$

which can be expressed in state-space form as follows:

$$\begin{bmatrix} \dot{\bar{V}} \\ \ddot{h} \end{bmatrix} = \begin{bmatrix} 0 & -\frac{g}{\bar{V}_t} \\ 0 & 0 \end{bmatrix} \begin{bmatrix} \bar{V} \\ \dot{h} \end{bmatrix} + \begin{bmatrix} 0 & \frac{1}{m} \\ -1 & 0 \end{bmatrix} \begin{bmatrix} a_n \\ T \end{bmatrix} \tag{4.5.14}$$

This state-space model represents the phugoid mode of the aircraft. However, the poles of Equation 4.5.14 are both at the origin of the s-plane, while the actual phugoid poles are lightly damped at a low frequency. If unmodelled effects such as the coupling of the airspeed back into the rotational dynamics were taken into account, the resulting feedback would move the poles from the origin to their true locations.

Therefore this decoupled model is not an exact representation of the aircraft dynamics, but due to the timescale separation between the rotational dynamics and the kinematics, it should be adequate for control design purposes. However, the linear analysis of the control system should be done with the full longitudinal model of Equation 4.3.8 to obtain a better representation of what its behaviour would be in practice.

4.6 Effect of CG shifts on the longitudinal dynamics

The linear aircraft model of this chapter can be used together with the equations of Section 3.4 to investigate the effect of shifts in the centre of gravity on the dynamics of the aircraft. If

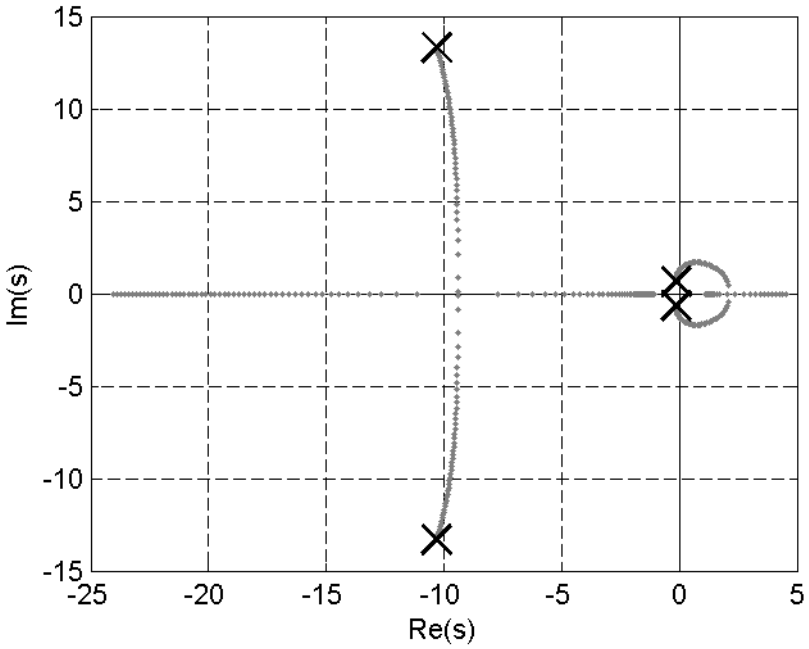

Figure 4.6.1: Effect of CG shifts on the open-loop longitudinal poles

such an analysis could show which mode of motion is most affected by CG shifts, this would indicate where adaptation should be added to the control system to keep the aircraft stable, since the inner control loops typically control the short period mode, and the outer loops control the phugoid mode.

The equations describing the effect of CG shifts on the aircraft parameters can be substituted into the full aircraft model and the model re-linearised, as was done for the nominal case in Section 4.3, to investigate the effect of CG shifts on the full longitudinal dynamics. Alternatively, the expressions for the shifted parameters can be substituted into the model of the rotational dynamics given in Section 4.5.1, to investigate the effect of CG shifts on the short period mode. In this section, both approaches will be used, and their results will be compared.

Figure 4.6.1 shows the effect of backward CG shifts on the poles of the full longitudinal dynamics. As the CG move backwards, the short period poles converge towards the real axis, where they eventually meet and diverge. One pole moves along the real axis towards negative infinity, while the other moves towards the right half-plane. The phugoid mode poles circle to the right, cross the imaginary axis to become unstable, and also converge towards the real axis where they meet and diverge, one to positive infinity and the other to the origin.

At a first glance, it seems as though the phugoid mode poles are the most affected by the CG shifts, since they are the first to become unstable. However, the distinction between the two modes of motion becomes unclear when the short period poles become real and move into the same frequency range as the phugoid mode poles.

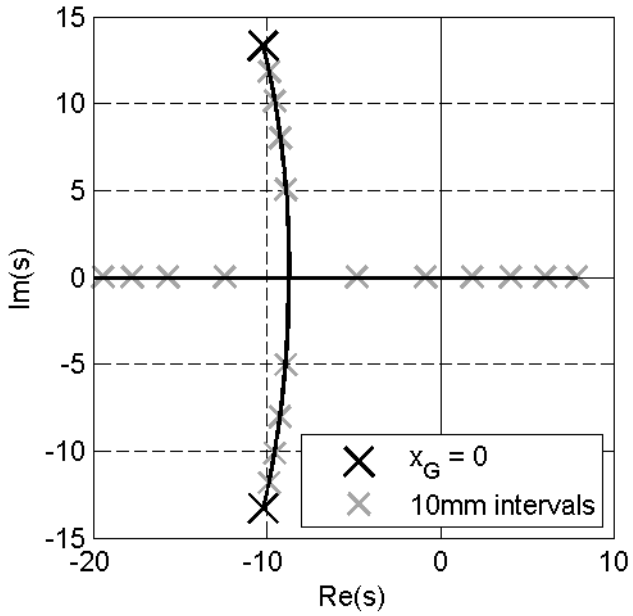

Figure 4.6.2: Effect of CG shifts on the poles of the longitudinal rotational dynamics

Figure 4.6.2 shows the effect of a CG shift on the short period poles when the longitudinal rotational dynamics of Section 4.5.1 are used to model this mode of motion. In a similar fashion to the short period poles of the full longitudinal dynamics, the poles of this second-order system converge towards the real axis where they meet and diverge. In this case, however, one of the short period poles crosses the imaginary axis and becomes unstable for a CG shift of about 63 mm.

Figure 4.6.3 shows the movements of the poles of both systems for backward CG shifts. The real and imaginary parts of the poles are plotted separately against the backward CG shift distance. In both cases the short period poles meet at the real axis for a shift of about 47 mm, but as they diverge along the real axis the unstable pole of the rotational dynamics moves closer to the phugoid mode poles than the short-period poles of the full longitudinal dynamics.

Therefore the analysis of the full longitudinal model does not clearly indicate which mode of motion will be the most affected if the CG moves backwards, but the analysis of the rotational dynamics clearly suggests that the short period mode will become unstable. Therefore this analysis suggests that adaptation should be used in the inner loop which controls the short period mode, but does not provide a conclusive answer.

4.7 Summary

In this chapter, a linear longitudinal model of the Variable Stability UAV was obtained by linearising the longitudinal dynamics of Chapter 3 around a trim condition. From this lin-

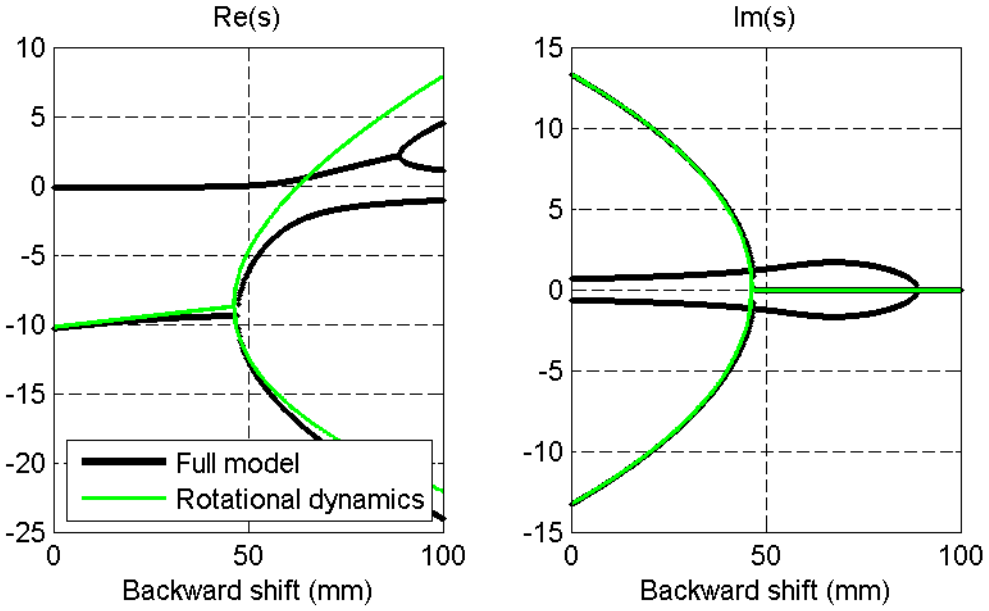

Figure 4.6.3: Changes in the real and imaginary parts of the longitudinal open-loop poles as the CG shifts backwards

ear model, the short period and phugoid modes of motion could be identified. The model was then divided into the longitudinal rigid-body rotational dynamics, which describes the behaviour of the pitch rate and angle of attack, and the longitudinal point mass kinematics, which describes the behaviour of the airspeed and climb rate.

The effect of CG shifts on the longitudinal dynamics was investigated using the expressions for the aerodynamic parameters in terms of the CG position. This analysis clearly showed that sufficiently large CG shifts can destabilise the longitudinal dynamics, but did not clearly show which mode of motion would be destabilised. The analysis of the rotational dynamics indicated that the short period mode is most affected, but the analysis of the full longitudinal dynamics was slightly ambiguous in that regard, and could even be interpreted to suggest that the phugoid mode is more seriously affected.

However, the physical discussion of both longitudinal modes of motion in Section 4.4 also indicates that the short period mode should be more severely affected by CG shifts, and CG shifts were successfully handled in the inner-loop controller for the short period mode in [4]. Therefore the balance of evidence suggests that CG shifts will predominantly affect the short period mode, and therefore it was decided to design an adaptive inner-loop controller to control this mode of motion.

Once the control system has been designed, a closed-loop analysis of the effect of CG shifts may provide more insight into which control loops should account for the change in the aircraft dynamics. Such an analysis is done in Section 6.6, and should indicate whether the choice of an adaptive inner loop was correct.

The use of adaptive inner loops is likely to be appropriate for any fault-tolerant flight

control system, since almost all the uncertainty in the aircraft model and the possible effects of in-flight damage are encapsulated at a rotational dynamics level. Therefore, if an adaptive inner-loop controller can control the rotational dynamics even if the aircraft suffers damage, the outer loops will be able to control the kinematics of the aircraft without making any special provision for in-flight damage.

The longitudinal rotational dynamics and kinematics can now be used to design inner-loop and outer-loop controllers respectively. Then the full linear longitudinal model will allow the closed-loop behaviour of the control system and the Variable Stability UAV to be investigated.

The control system will initially be designed as a fixed-gain control system, so that the effect of CG shifts on a control system without adaptation can be investigated. However, the control system must be designed in such a way that an adaptation mechanism can be added to adjust its parameters and keep the aircraft stable when the CG shifts backwards, and therefore an adaptive control approach must be chosen before the control system is designed. This is the subject of Chapter 5, where the theory behind the fault-tolerant adaptive control system is discussed.

Chapter 5

Adaptive control theory

This chapter provides the mathematical background to the fault-tolerant adaptive control system that was designed for the Variable Stability UAV. The adaptive control design approach was largely taken from [12], which offers thorough treatment of the standard adaptive control concepts and techniques.

This chapter only gives the adaptive control concepts which are necessary for understanding the design of the adaptive control system for this project. Some of the mathematical detail can be found in Appendix B, or in any book on stability theory and adaptive control.

Section 5.1 introduces the concept of adaptive control, and briefly discusses the different basic types of adaptive control. Section 5.2 summarises the derivation of an adaptive control system from [12], and Section 5.3 investigates the robustness of this adaptive control scheme. Section 5.4 concludes the chapter with a number of ways in which the adaptive law can be modified to improve its robustness.

This chapter may seem to lean heavily on [12] as a single source. Techniques from other sources were investigated, such as the MIT rule and the MRAC for a general linear system from [9], as well as the Simple Adaptive Control techniques from [19], but it was found that these techniques would be much more difficult to implement effectively than those given in [12].

5.1 Basic concepts of adaptive control

An adaptive control system is, in general, one where the control law is adjusted by some adaptive law to account for changes in the plant dynamics. This thesis focuses on the class of adaptive control systems where the parameters of the control law, rather than its structure, are adjusted to account for changes in the parameters of the plant to be controlled.

The basic structure of such a system is shown in Figure 5.1.1, where a plant with parameters contained in a vector $\boldsymbol{\theta}_p^*$ is controlled using a control law with parameters contained in a vector $\boldsymbol{\theta}_c$. This controller parameter vector is adjusted by an adaptive law, which can in

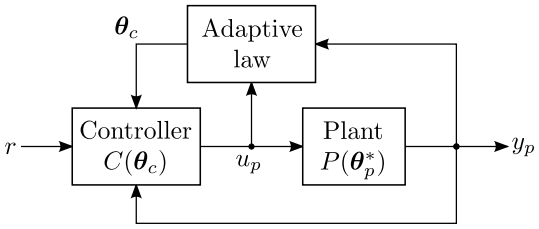

Figure 5.1.1: Basic structure of an adaptive control system

general make use of any available measurement or controller-generated signal to update the controller parameters.

5.1.1 Direct and indirect adaptive control

A large number of techniques exist for designing the adaptive law which updates the controller parameters. A basic distinction can be made between direct or implicit adaptive control, and indirect or explicit adaptive control.

In an *indirect* adaptive control system, the adaptive law includes a parameter estimator which provides an estimate $\boldsymbol{\theta}_p$ of the true *plant* parameter vector $\boldsymbol{\theta}_p^*$. This estimate is used to calculate the controller parameter vector $\boldsymbol{\theta}_c$ using an automated control design algorithm. This system is also known as an *explicit* adaptive control system, since the plant parameters are estimated explicitly in the adaptive law. The general structure of an indirect adaptive control system is shown in Figure 5.1.2.

In a *direct* adaptive control system, the plant parameters are not estimated explicitly. Instead, the adaptive law consists of a parameter estimator which generates an estimate $\boldsymbol{\theta}_c$ of the ideal *controller* parameter vector $\boldsymbol{\theta}_c^*$. Since this vector is a function of the true plant parameters, an estimate of the plant parameters is implicit in the estimate of the ideal controller parameters, which is why this system is also known as an *implicit* adaptive control system. The structure of a direct adaptive control system is essentially the same as that of the general adaptive control system shown in Figure 5.1.1.

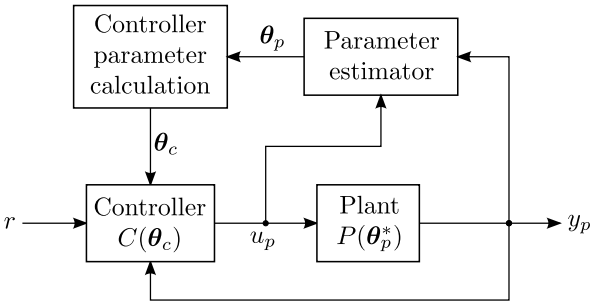

Figure 5.1.2: Indirect adaptive control system

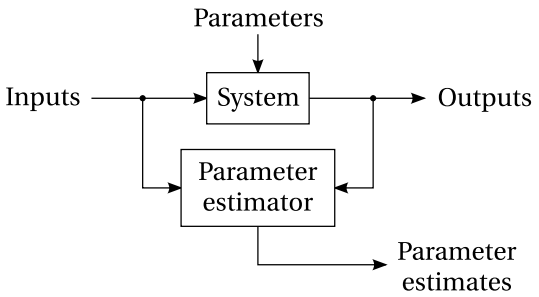

Figure 5.1.3: Structure of a general online parameter estimator

In both these methods, the adaptive law can be designed using an online parameter estimator (OPE), which in general has the structure shown in Figure 5.1.3. An OPE generates estimates of the parameters of a system in real time by monitoring the inputs and outputs of the system. The goal of an OPE is usually that the parameter estimates converge asymptotically towards their true values, but it can also be designed to achieve some other goal within a control system.

The design of an indirect adaptive control system requires a model of the open-loop plant in a form which is convenient for the design of an OPE to estimate the plant parameters. A direct adaptive control system typically requires a model of the closed-loop system in a form which allows the design of an OPE to estimate the ideal controller parameters.

As stated in the introduction, the goal of this project is to evaluate the use of adaptive control as part of a fault-tolerant flight control system for a UAV. This could, in principle, include both direct and indirect adaptive control techniques. However, indirect adaptive control can also be included under the scope of system identification, which is being investigated as another component of the fault tolerant control system. Therefore it was decided to focus on direct adaptive control algorithms in this project.

5.1.2 Model reference adaptive control

This project focuses on the class of adaptive control systems known as Model Reference Adaptive Control (MRAC) systems. These systems include a reference model, which represents the desired closed-loop behaviour of the plant and controller. In an MRAC system, the adaptive law is designed to minimise the output error e_1, which is defined as the difference between the outputs of the plant and the reference model.

MRAC systems can also be divided into direct and indirect MRAC systems. The two configurations are shown in Figure 5.1.4. In a direct MRAC, the ideal controller parameters are estimated directly by an adaptive law which makes use of the output error e_1. An indirect MRAC uses the output error in a parameter estimator which generates an estimate of the plant parameters, which is then used to calculate the controller parameters.

In this project, a direct MRAC was used to improve the fault tolerance of a longitudinal

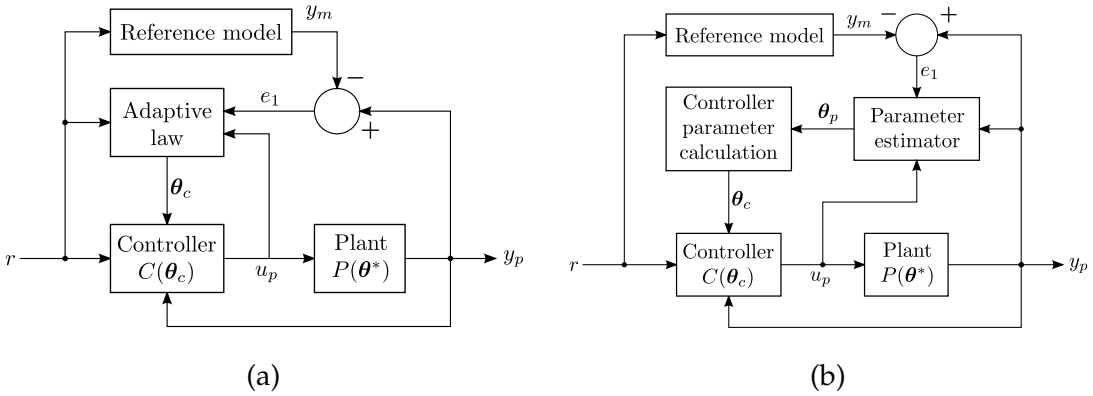

Figure 5.1.4: Two types of model reference adaptive control: (a) Direct MRAC, (b) Indirect MRAC

control system for the Variable Stability UAV. The rest of this chapter describes the derivation of the control law and the adaptive law which were used in this MRAC system.

5.2 Derivation of an adaptive control system

This section summarises the derivation of the algorithm for a model reference adaptive control system given in [12]. The algorithm is initially derived for an ideal plant which is free of disturbances, noise and unmodelled dynamics. The effect of such phenomena is discussed in Section 5.3, and Section 5.4 proposes modifications to the MRAC system to improve its robustness to them.

5.2.1 The model reference control problem

The MRAC system is designed as a solution to the general *model reference control problem*, or MRC problem, which is illustrated in Figure 5.2.1.

Given a linear time-invariant plant with input u_p and output y_p, and a reference model with input r and output y_m, the MRC objective is to generate a plant input so that, for any reference input $r(t)$ which is bounded and piecewise continuous, all signals in the system are bounded, and the plant output tracks the model output as closely as possible, i.e. that the

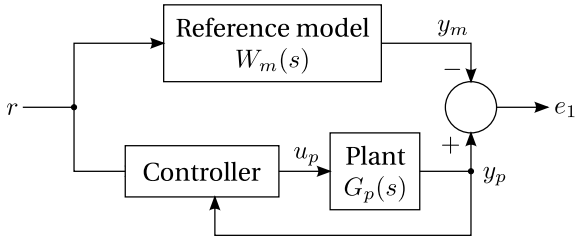

Figure 5.2.1: The model reference control problem

output error $e_1 = y_p - y_m$ is as close as possible to zero.

The plant is described by a state space model, relating the plant state $\mathbf{x}_p$, input u_p and output y_p:

$$\begin{aligned} \dot{\mathbf{x}}_p &= A_p \mathbf{x}_p + B_p u_p \\ y_p &= C_p^{\mathsf{T}} \mathbf{x}_p \end{aligned} \tag{5.2.1}$$

This state space can also be represented as a transfer function $G_p(s)$ of the following form:

$$y_p = G_p(s) u_p \tag{5.2.2}$$

$$G_p = k_p \frac{Z_p(s)}{R_p(s)} \tag{5.2.3}$$

$$= C_p^{\mathsf{T}} \left(s\mathrm{I} - A_p\right)^{-1} B_p \tag{5.2.4}$$

where Z_p and R_p are monic polynomials, and k_p is a constant known as the high frequency gain. A monic polynomial is one where the coefficient of the highest power of the variable is unity.

The reference model is given as a transfer function $W_m(s)$, which represents the desired response of the plant output to reference inputs:

$$y_m = W_m(s) r \tag{5.2.5}$$

$$W_m = k_m \frac{Z_m(s)}{R_m(s)} \tag{5.2.6}$$

where Z_m and R_m are monic polynomials, and k_m is a constant.

5.2.2 Model reference control law for a SISO plant

This section describes a control law which is suitable for use in a direct MRAC system. Subsequent sections will show that using this control law allows a convenient parametric model of the closed-loop system to be obtained, and an adaptive law to be designed which guarantees stability and convergence.

If the parameters of the plant are known, then the MRC problem can be solved using a certain control law, called the *model reference control law* in [12], with fixed parameters. This control law can only be used if certain assumptions hold regarding the plant and reference model.

The following assumptions must hold regarding the plant transfer function $G_p(s)$:

1. The numerator $Z_p(s)$ is a monic polynomial of degree m_p which has all its roots in the left half-plane

2. An upper bound n of the degree n_p of the denominator $R_p(s)$ is known

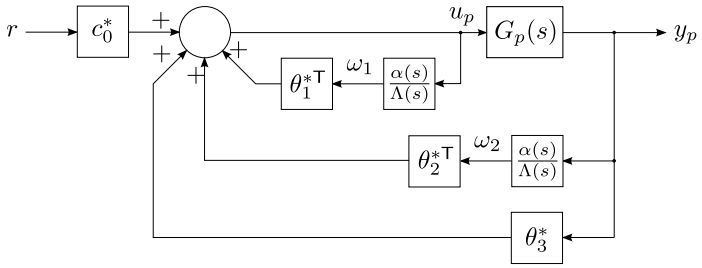

Figure 5.2.2: Block diagram of the model reference control law

3. The relative degree $n^* = n_p - m_p$ of the plant is known

4. The sign of the high frequency gain k_p is known

The first plant assumption implies a limitation of the MRC law: it can not be applied to non-minimum phase plants. It can, however, be applied to unstable minimum-phase plants.

The following assumptions must hold regarding the reference model transfer function $W_m(s)$:

1. The numerator $Z_m(s)$ and the denominator $R_m(s)$ are monic polynomials of degree q_m and p_m respectively, where $p_m \leq n$, and both have all their roots in the left half-plane

2. The relative degree $n_m^* = p_m - q_m$ of the reference model is the same as that of the plant, i.e. $n_m^* = n^*$

The first reference model assumption implies that the reference model must be both stable and minimum phase. The desired closed-loop response of the control system will almost always be stable, and can be chosen to be minimum phase in most situations, and therefore these restrictions on the reference model are not unreasonable.

The model reference control law, illustrated in Figure 5.2.2, is as follows:

$$u_p = \boldsymbol{\theta}_1^{*\mathsf{T}} \frac{\boldsymbol{\alpha}(s)}{\Lambda(s)} u_p + \boldsymbol{\theta}_2^{*\mathsf{T}} \frac{\boldsymbol{\alpha}(s)}{\Lambda(s)} y_p + \theta_3^* y_p + c_0^* r \tag{5.2.7}$$

where $\alpha(s)$ is a vector of descending powers of s:

$$\boldsymbol{\alpha}(s) = \begin{cases} \left[s^{n-2},\ s^{n-1},\ \ldots\ ,\ s,\ 1\right]^{\mathsf{T}} & \text{for } n \geq 2 \\ 0 & \text{for } n = 1 \end{cases} \tag{5.2.8}$$

The parameters $c_0^*,\ \theta_3^* \in \mathcal{R}^1$ and $\boldsymbol{\theta}_1^*,\ \boldsymbol{\theta}_2^* \in \mathcal{R}^{n-1}$ are constants to be designed, and $\Lambda(s)$ is an arbitrary monic stable polynomial of degree $n-1$ that contains $Z_m(s)$ as a factor:

$$\Lambda(s) = \Lambda_0(s) Z_m(s) = s^{n-1} + \lambda_{n-2} s^{n-2} + \ldots + \lambda_1 s + \lambda_0 \tag{5.2.9}$$

which implies that $\Lambda_0(s)$ is monic, stable and of degree $n - q_m - 1$. Therefore the factors

$$\boldsymbol{\theta}_1^{*\mathsf{T}} \frac{\boldsymbol{\alpha}(s)}{\Lambda(s)} \quad \text{and} \quad \boldsymbol{\theta}_2^{*\mathsf{T}} \frac{\boldsymbol{\alpha}(s)}{\Lambda(s)} \tag{5.2.10}$$

are filters of order $n-1$ with the same poles, which include the desired closed-loop zeroes, and different numerator polynomials, the coefficients of which are the elements of the parameter vectors $\boldsymbol{\theta}_1^*$ and $\boldsymbol{\theta}_2^*$.

The control law can also be represented in state-space form as follows:

$$\dot{\boldsymbol{\omega}}_1 = F\boldsymbol{\omega}_1 + gu_p \tag{5.2.11}$$

$$\dot{\boldsymbol{\omega}}_2 = F\boldsymbol{\omega}_2 + gy_p \tag{5.2.12}$$

$$u_p = \boldsymbol{\theta}^{*\mathsf{T}}\boldsymbol{\omega} \tag{5.2.13}$$

where $\boldsymbol{\theta}^*$ is the full controller parameter vector, and $\boldsymbol{\omega}$ is the vector of signals used in the control law:

$$\boldsymbol{\theta}^* = [\boldsymbol{\theta}_1^{*\mathsf{T}} \;\; \boldsymbol{\theta}_2^{*\mathsf{T}} \;\; \theta_3^* \;\; c_0^*]^{\mathsf{T}} \tag{5.2.14}$$

$$\boldsymbol{\omega} = [\boldsymbol{\omega}_1^{\mathsf{T}} \;\; \boldsymbol{\omega}_2^{\mathsf{T}} \;\; y_p \;\; r]^{\mathsf{T}} \tag{5.2.15}$$

The matrices F and g form a state-space representation of the filter $\alpha(s)/\Lambda(s)$, so that

$$\boldsymbol{\omega}_1 = \frac{\boldsymbol{\alpha}(s)}{\Lambda(s)}u_p \;\text{ and }\; \boldsymbol{\omega}_2 = \frac{\boldsymbol{\alpha}(s)}{\Lambda(s)}y_p \tag{5.2.16}$$

are the state vectors of the two filters in Equation 5.2.10.

With this control law, the closed-loop transfer function of the plant and controller will be:

$$G_c(s) = \frac{y_p(s)}{r(s)} = \frac{c_0^* k_p Z_p \Lambda^2}{\Lambda[(\Lambda - \boldsymbol{\theta}_1^{*\mathsf{T}}\boldsymbol{\alpha})R_p - k_p Z_p(\boldsymbol{\theta}_2^{*\mathsf{T}}\boldsymbol{\alpha} + \theta_3^*\Lambda)]} \tag{5.2.17}$$

For the case where the plant parameters are known and the controller parameters are fixed, the MRC objective is to choose the controller parameters so that $G_c(s) = W_m(s)$. This can be achieved by solving the following matching equations:

$$(\Lambda - \boldsymbol{\theta}_1^{*\mathsf{T}}\boldsymbol{\alpha})R_p - k_p Z_p(\boldsymbol{\theta}_2^{*\mathsf{T}}\boldsymbol{\alpha} + \theta_3^*\Lambda) = Z_p\Lambda_0 R_m \tag{5.2.18}$$

$$c_0^* k_p = k_m \tag{5.2.19}$$

Using these matching equations with the MRC law will cancel the open-loop zeroes of the plant with closed-loop poles, which is why it can only be used for minimum-phase plants, since non-minimum phase plants would require pole-zero cancellations in the right half plane. The control law furthermore creates the desired closed-loop zeroes, and moves the remaining closed-loop poles to the desired locations.

If the plant parameters are known exactly, Equations 5.2.18 and 5.2.19 can be solved numerically to obtain $\boldsymbol{\theta}^*$, which is the ideal value of the controller parameter vector. Using this parameter vector in the control law of Equation 5.2.7 will ensure that the closed-loop transfer function of the plant and controller is exactly equal to the reference model.

However, if the plant parameters are unknown, then the ideal controller parameter vector $\boldsymbol{\theta}^*$ can not be determined exactly. The plant parameters can be assumed to have some

nominal values, which will allow an approximation of $\boldsymbol{\theta}^*$ to be calculated, but if the plant parameters differ significantly from their assumed values, the closed-loop response of the system will deviate significantly from the desired response, and can even be unstable.

In this case, $\boldsymbol{\theta}^*$ must be replaced in the control law by $\boldsymbol{\theta}(t)$, an estimate of the ideal controller parameter vector, which is generated online by an adaptive law. The adaptive law is in the form of an expression for $\dot{\boldsymbol{\theta}}$, the rate at which the parameter estimate is updated. The initial value of the parameter vector is determined by solving the matching equations (5.2.18 and 5.2.19) for the nominal values of the plant parameters.

Section 5.2.3 summarises the derivation of a parametric model of the closed-loop system – that is, a model of the closed-loop system where the only unknown parameters are the ideal controller parameters $\boldsymbol{\theta}^*$. An online parameter estimator is then designed around this model in Section 5.2.4. This OPE generates the estimate $\boldsymbol{\theta}(t)$ of the unknown parameter vector $\boldsymbol{\theta}^*$, and so functions as an adaptive law for the MRAC system.

5.2.3 Parametric model of a model reference control system

A state-space representation of the whole closed-loop system can be obtained from the state equation of the plant and the control law:

$$\begin{aligned} \dot{\mathbf{Y}}_c &= A_0 \mathbf{Y}_c + B_c u_p \\ y_p &= C_c^{\mathsf{T}} \mathbf{Y}_c \end{aligned} \tag{5.2.20}$$

where $\mathbf{Y}_c = [\mathbf{x}_p^{\mathsf{T}} \;\; \boldsymbol{\omega}_1^{\mathsf{T}} \;\; \boldsymbol{\omega}_2{}^{\mathsf{T}}]^{\mathsf{T}}$ is the combined state vector of the plant and the controller. If $\mathbf{Y}_m$ is the state of a non-minimal representation of the reference model, and the *state error* is defined as $\mathbf{e} = \mathbf{Y}_c - \mathbf{Y}_m$, then the following state equation for the error dynamics can be obtained through algebraic manipulation:

$$\begin{aligned} \dot{\mathbf{e}} &= A_c \mathbf{e} + B_c \left(u_p - \boldsymbol{\theta}^{*\mathsf{T}} \boldsymbol{\omega} \right) \\ e_1 &= C_c^{\mathsf{T}} \mathbf{e} \end{aligned} \tag{5.2.21}$$

where A_c, $B_c c_0^*$ and C_c^{T} form a non-minimal state-space representation of the reference model. The values of these matrices are given in [12]. The error state equation can be written in transfer function form:

$$e_1 = C_c^{\mathsf{T}} \left(sI - A_c \right)^{-1} B_c \left(u_p - \boldsymbol{\theta}^{*\mathsf{T}} \boldsymbol{\omega} \right) \tag{5.2.22}$$

$$= W_m(s) \rho^* \left(u_p - \boldsymbol{\theta}^{*\mathsf{T}} \boldsymbol{\omega} \right) \tag{5.2.23}$$

$$\rho^* \triangleq \frac{1}{c_0^*} \tag{5.2.24}$$

Equation 5.2.23 represents a system with the plant input u_p and the controller signal vector $\boldsymbol{\omega}$ as inputs, and the output error e_1 as an output. The unknown parameters of this system

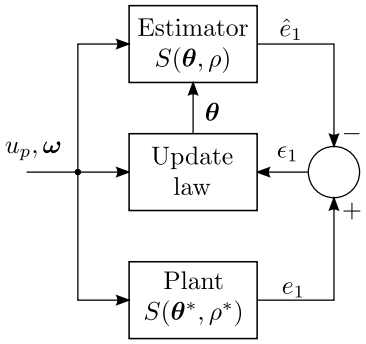

Figure 5.2.3: Online parameter estimator for the parametric model of a model reference control system

are the ideal controller parameter vector $\boldsymbol{\theta}^*$ and the additional parameter ρ^*. The unknown parameters of this system are contained in two linear factors, and therefore Equation 5.2.23 is called a *bilinear parametric model* of the closed-loop MRC system.

5.2.4 Adaptive law derivation

Using the parametric model of the MRC system in terms of the ideal controller parameters, an adaptive law can now be derived in the form of an OPE to estimate the ideal parameter vector $\boldsymbol{\theta}^*$. The structure of such an OPE is shown in Figure 5.2.3.

The OPE consists of an estimator and an update law, where the estimator is essentially a model of the system of Equation 5.2.23, with the unknown ideal parameters $\boldsymbol{\theta}^*$ and ρ^* replaced by their estimates $\boldsymbol{\theta}$ and ρ. It generates an estimate $\hat{e}_1(t)$ of the output error $e_1(t)$:

$$\hat{e}_1 = W_m(s)\rho\left(u_p - \boldsymbol{\theta}^\mathsf{T}\boldsymbol{\omega}\right) \tag{5.2.25}$$

This estimate is subtracted from the actual output error to generate the estimation error ϵ_1:

$$\epsilon_1 = e_1 - \hat{e}_1 \tag{5.2.26}$$

which is used by the update law to update the estimates of $\boldsymbol{\theta}^*$ and ρ^*.

However, since the control input is $u_p = \boldsymbol{\theta}^\mathsf{T}\boldsymbol{\omega}$, the estimator equation and the estimation error reduce to:

$$\hat{e}_1 = W_m(s)\rho\,(0) = 0 \tag{5.2.27}$$

$$\therefore \epsilon_1 = e_1 \tag{5.2.28}$$

That is, the estimation error is equal to the output error itself, which eliminates the need for an estimator in the adaptive law, and also the need to generate an estimate of ρ^*. All that remains in the adaptive law design is to find an update law for $\boldsymbol{\theta}$ which will ensure that the

output error e_1 tends asymptotically towards zero, and that all signals in the control system are bounded.

This can be done using Lyapunov stability theory, the mathematical details of which will not be discussed in this thesis, but can be found on any book on adaptive control or stability, such as [9], [10] and [11]. The definitions of concepts used here, as well as a first-order illustrative example, can be found in Appendix B.2.

The problem essentially reduces to finding a positive definite function V of the signals in the system, known as a *Lyapunov-like* function, which has a negative semidefinite time derivative. The classes of functions known as positive and negative definite and semidefinite are also defined in Appendix B.2.

To obtain such a Lyapunov-like function, the control law is substituted into the error state equation (5.2.21) to write it in the following form:

$$\begin{aligned} \dot{\mathbf{e}} &= A_c\mathbf{e} + B_c\tilde{\boldsymbol{\theta}}^{\mathsf{T}}\boldsymbol{\omega}, \qquad \mathbf{e}(0) = \mathbf{e}_0 \\ e_1 &= C_c^{\mathsf{T}}\mathbf{e} \end{aligned} \tag{5.2.29}$$

$$\therefore e_1 = W_m(s)\rho^*\tilde{\boldsymbol{\theta}}^{\mathsf{T}}\boldsymbol{\omega} \tag{5.2.30}$$

where the parameter error $\tilde{\boldsymbol{\theta}}$ is defined as the difference between the estimated and ideal controller parameter vectors:

$$\tilde{\boldsymbol{\theta}} = \boldsymbol{\theta}(t) - \boldsymbol{\theta}^* \tag{5.2.31}$$

From this point, obtaining a Lyapunov-like function which satisfies the requirements above can be made much easier if the reference model can be chosen to be a *strictly positive real* (SPR) transfer function. The definition of this class of transfer function, and necessary and sufficient conditions for a transfer function to be SPR, are given briefly in Appendix B.1, and discussed in detail in [19] and [37].

For the reference model to be SPR, it must be stable and minimum phase, and the relative locations of its poles and zeroes must fulfil certain requirements which are not excessively restrictive, but it must have a relative degree of 1. Therefore an SPR reference model can only be used if the plant also has a relative degree of 1. More complex design techniques are given in [12] for plants with other relative degrees, but in this derivation it will be assumed that the plant has a relative degree of 1.

If $W_m(s)$ is chosen to be SPR, then the MKY Lemma (Lemma B.1) implies the existence of two symmetrical positive definite matrices P_c and L_c, a vector q and a positive scalar ν_c, which satisfy the following algebraic equations:

$$\begin{aligned} P_cA_c + A_c^{\mathsf{T}}P_c &= -qq^{\mathsf{T}} - \nu_cL_c \\ P_c\bar{B}_c &= C_c \end{aligned} \tag{5.2.32}$$

The following positive definite Lyapunov-like function is proposed, which uses the matrix P_c and another symmetrical positive definite matrix Γ:

$$V\left(\tilde{\boldsymbol{\theta}}, \mathbf{e}\right) = \frac{\mathbf{e}^{\mathsf{T}} P_c \mathbf{e}}{2} + \frac{\tilde{\boldsymbol{\theta}}^{\mathsf{T}} \Gamma^{-1} \tilde{\boldsymbol{\theta}}}{2} |\rho^*| \tag{5.2.33}$$

Using Equations 5.2.29 and 5.2.32, it can be shown that the time derivative of V will be:

$$\dot{V} = -\frac{\mathbf{e}^{\mathsf{T}} q q^{\mathsf{T}} \mathbf{e}}{2} - \frac{\nu_c}{2} \mathbf{e}^{\mathsf{T}} L_c \mathbf{e} + \tilde{\boldsymbol{\theta}}^{\mathsf{T}} |\rho^*| \left(e_1 \boldsymbol{\omega} \operatorname{sgn}(\rho^*) + \Gamma^{-1} \dot{\tilde{\boldsymbol{\theta}}} \right) \tag{5.2.34}$$

Since $\dot{\tilde{\boldsymbol{\theta}}} = \dot{\boldsymbol{\theta}}$, the last term in Equation 5.2.34 can be made zero by choosing the following adaptive law:

$$\dot{\boldsymbol{\theta}} = -\Gamma e_1 \boldsymbol{\omega} \operatorname{sgn}(\rho^*) \tag{5.2.35}$$

which reduces the derivative of the Lyapunov-like function to:

$$\dot{V} = -\frac{\mathbf{e}^{\mathsf{T}} q q^{\mathsf{T}} \mathbf{e}}{2} - \frac{\nu_c}{2} \mathbf{e}^{\mathsf{T}} L_c \mathbf{e} \tag{5.2.36}$$

which is negative semidefinite.

From Equation 5.2.33, it is clear that the Lyapunov-like function V cannot be negative, and from Equation 5.2.36 that it cannot increase. This implies that V must eventually settle at some non-negative value. If the V settles, its derivative, and therefore the state error, must tend asymptotically towards zero over time, which implies that the output error also tends towards zero, which is the first objective of the adaptive control design.

Also, the fact that the Lyapunov-like function cannot increase, and is positive definite in the parameter error, places an upper bound on the magnitude of the parameter error, which implies that the parameters themselves are all bounded. Using the state equations of the closed-loop system, it can be shown that the boundedness of the state and parameter errors implies that all signals in the closed-loop system are bounded [12], which is the second objective of the adaptive control design.

Therefore the adaptive law of Equation 5.2.35 will ensure that all signals in the adaptive control system are bounded, and that the output error e_1 will tend asymptotically towards zero.

A number of things can be noted about this adaptive law. Firstly, it requires the sign of the unknown parameter ρ^* to be known. From Equations 5.2.19 and 5.2.24, it can be seen that:

$$\rho^* = \frac{1}{c_0^*} = \frac{k_p}{k_m} \tag{5.2.37}$$

Since the high-frequency gain of the reference model is chosen by the designer, the adaptive law requires knowledge of the sign of the high-frequency gain of the plant.

Control law	$u_p = \boldsymbol{\theta}^\mathsf{T}\boldsymbol{\omega}$ $\boldsymbol{\theta} = [\boldsymbol{\theta}_1^\mathsf{T} \;\; \boldsymbol{\theta}_2^\mathsf{T} \;\; \theta_3 \;\; c_0]^\mathsf{T}$ $\boldsymbol{\omega} = [\boldsymbol{\omega}_1^\mathsf{T} \;\; \boldsymbol{\omega}_2^\mathsf{T} \;\; y_p \;\; r]^\mathsf{T}$ $\omega_1 = \frac{\boldsymbol{\alpha}(s)}{\Lambda(s)}u_p; \qquad \omega_2 = \frac{\boldsymbol{\alpha}(s)}{\Lambda(s)}y_p$ $\boldsymbol{\alpha}(s)$ and $\Lambda(s)$ defined in Section 5.2.2
Initial control gains	Solve Equations 5.2.18 and 5.2.19
Adaptive law	$\dot{\boldsymbol{\theta}} = -\Gamma e_1 \boldsymbol{\omega}\,\mathrm{sgn}(k_p/k_m)$ Γ is a symmetric positive definite matrix

Table 5.1: MRAC scheme with an unnormalised adaptive law for a SISO plant of relative degree 1

Secondly, the adaptive law of Equation 5.2.35 does not guarantee that the controller parameters will converge towards their ideal values. It only guarantees that the parameters will be bounded, and that the output error will converge towards zero. However, in a direct adaptive control system, the convergence of the controller parameters to some ideal value is usually not required, as long as the closed-loop performance of the controller is satisfactory, which should be the case if $e_1 \to 0$.

Thirdly, the matrix Γ in the adaptive law, known as the *adaptive gain matrix*, is a square parameter matrix with as many rows and columns as there are adapted controller parameters. It can be chosen by the designer to be any symmetrical positive definite matrix. A simple option is to choose it as a multiple of the identity matrix:

$$\Gamma = \gamma \mathrm{I} \tag{5.2.38}$$

where γ is a positive scalar constant known as the *adaptive gain*. In this case, the adaptive law reduces to:

$$\dot{\boldsymbol{\theta}} = -\gamma e_1 \boldsymbol{\omega}\,\mathrm{sgn}(\rho^*) \tag{5.2.39}$$

Then the update rate of each controller parameter will be proportional to the signal by which it is multiplied in the control law.

The MRAC scheme with this adaptive law is summarised in Table 5.1.

5.3 Robustness of the adaptive control system

The adaptive control system derived in the previous sections guarantees that the output of a plant described by Equation 5.2.1 will asymptotically track the reference model output with zero error. However, this guarantee is only valid if the plant is described exactly by the ideal plant equation that was used, which will never be the case for a practical system. Practical systems are affected by disturbances, measurement noise, non-linearities and unmodelled

dynamics, and therefore can not be described exactly by a state space representation. These phenomena can easily be handled by a well-designed fixed-gain control system, but can have serious effects on an adaptive control system.

The sensors used by the Variable Stability UAV are all affected by measurement noise. The aircraft will also be affected by constant disturbances in flight, such as the pitching moment disturbance caused by a longitudinal CG shift. Therefore the effect of these two phenomena on an adaptive control system will be discussed briefly.

5.3.1 Noise

The plant output, which is fed back to the control and adaptive laws, will usually be affected by measurement noise in practice. Suppose the MRAC system is given a zero reference command, i.e. $r = y_m = 0$, that k_p/k_m is positive, and that a scalar adaptive gain is used. Then the update law for θ_3 reduces to:

$$\begin{aligned} \dot{\theta}_3 &= -\gamma e_1 y_p \\ &= -\gamma(y_p - y_m)y_p \\ &= -\gamma y_p^2 \end{aligned} \tag{5.3.1}$$

Therefore the noise will be squared and integrated in the adaptive law, which in this case will cause the parameter θ_3 to drift in the negative direction at a rate proportional to the noise variance. This adaptation is not required, since the control system can be designed to have good noise tolerance with fixed parameters, nor is it desired, since excessive drifting of the parameters can destabilise the closed-loop system.

This appears to be a fundamental problem with this adaptive law, since most control systems are designed so that zero-mean noise will have no net effect over a long period of time. Therefore it is essential that this adaptive law be modified to improve its noise tolerance if it is to be used in practice.

5.3.2 Constant disturbances

In any control system, there can be a steady-state error between the reference command and the plant output if the plant parameters deviate from their nominal values, or if the plant is affected by constant disturbances. In a fixed-gain control system, integral control can be used to eliminate steady-state errors in both these cases.

The MRC law used in the adaptive control system does not use integral control, but the controller parameters can be adapted to ensure that there are no steady-state errors due to incorrect plant parameters. However, adaptation cannot remove steady-state output errors that are caused by constant disturbances. If, for instance, the MRAC system is given a zero reference command, and the plant is affected by a constant disturbance, the plant output will be nonzero regardless of the MRC parameters.

This is not a serious problem in itself if there are outer loops around the MRAC system which use integral control, since these loops will simply bias the reference command of the MRAC to achieve the control objective. However, if the output error $e_1 = y_m - y_p$ is nonzero, it implies that at least one of the plant output and the model output, and therefore the reference command, must be nonzero. Since these signals are multiplied by the output error and then integrated in the adaptive law, adaptation will always take place if there is an output error due to a disturbance.

Once again this adaptation is unwanted, since the outer loops should be able to meet the control objective without adaptation taking place in the inner loop.

5.3.3 Summary of robustness

Both measurement noise and constant disturbances will cause the controller parameters to drift if the adaptive law of Equation 5.2.35 is used. This is due to the fact that the adaptive control system cannot distinguish between output errors caused by changes to the plant parameters, for which adaptation is desired, and errors due to noise and disturbances, for which adaptation is not desired.

This seems to be a general problem with adaptive control systems designed using stability theory. According to [22], adaptive control systems are sensitive to disturbances if the reference command is not persistently exciting. Signals could be superimposed on the reference command to excite the system dynamics and drive the adapted parameters to their correct values, but these signals would have to be chosen carefully to provide information to the adaptive law while not seriously affecting the performance of the control system. This approach was considered to be beyond the scope of this project.

Instead, different techniques were considered to modify the adaptive law to improve its tolerance of disturbances and noise. Section 5.4 investigates a number of these techniques.

5.4 Modifications for robustness

A number of modifications to the adaptive law of Equation 5.2.35 are suggested in [12] to improve the robustness of the MRAC system to phenomena such as disturbances, noise and unmodelled dynamics. This section briefly discusses some of these modifications and evaluates their usefulness for solving some of the practical issues surrounding the control of the Variable Stability UAV.

5.4.1 Normalisation

In the unnormalised adaptive law of Equation 5.2.35, restated below for convenience, the update rate of the controller parameters is proportional to the product of the output error e_1

and the signal vector $\boldsymbol{\omega}$:

$$\dot{\boldsymbol{\theta}} = -\Gamma e_1 \boldsymbol{\omega} \operatorname{sgn}(\rho^*) \tag{5.4.1}$$

The magnitudes of both e_1 and the elements of $\boldsymbol{\omega}$ are dependent on that of the reference command r. Therefore, if an unnormalised adaptive law is used, the rate at which the parameters are updated, and therefore the rate at which the response of the closed-loop system converges towards that of the reference model, will be dependent on the magnitude of the reference input.

In some applications, it may be desirable that the convergence rate of the controller parameters be independent of the input signal magnitude. In these cases, a normalised adaptive law can be used, where the signals are divided by a normalising signal to decrease the dependence of their magnitudes on that of the input signal. The derivation and stability proofs for such adaptive law can be found in [12] – only the resulting algorithm is given here, with simplifications applied which can be made if the reference model is SPR.

This adaptive law is derived from the same bilinear parametric model of the MRC system that was used for the unnormalised adaptive law:

$$e_1 = W_m(s)\rho^* \left(u_p - \boldsymbol{\theta}^{*\mathsf{T}} \boldsymbol{\omega} \right) \tag{5.4.2}$$

The two inputs u_p and $\boldsymbol{\omega}$ to this parametric model are filtered through the reference model to create two new inputs, u_f and $\boldsymbol{\phi}$:

$$u_f = W_m(s) u_p \tag{5.4.3}$$

$$\boldsymbol{\phi} = W_m(s) \boldsymbol{\omega} \tag{5.4.4}$$

These two filtered inputs are used to create a normalising signal:

$$n_s^2 = \boldsymbol{\phi}^{\mathsf{T}} \boldsymbol{\phi} + u_f^2 \tag{5.4.5}$$

This normalising signal will always be positive, except that it will be zero when both $\boldsymbol{\phi}$ and u_f are zero. Since other signals will be divided by the normalising signal, n_s^2 is used to create a new normalising signal m^2, which will never be zero:

$$m^2 = 1 + n_s^2 \tag{5.4.6}$$

The two filtered input signals are also used to generate an estimate $\hat{e}_1$ of the output error e_1:

$$\hat{e}_1 = \rho(u_f - \boldsymbol{\theta}^{\mathsf{T}} \boldsymbol{\phi}) \tag{5.4.7}$$

where ρ is the estimate of the additional unknown parameter $\rho^* = 1/c_0^*$, which appears in the bilinear parametric model but did not need to be estimated for the unnormalised adaptive law.

The estimate $\hat{e}_1$ and the normalising signal m^2 are used to generate the normalised estimation error ϵ:

$$\epsilon = \frac{e_1 - \hat{e}_1}{m^2} \tag{5.4.8}$$

Then the controller parameters can be adjusted using the following normalised adaptive law:

$$\dot{\boldsymbol{\theta}} = -\Gamma \epsilon \boldsymbol{\phi} \operatorname{sgn}(k_p/k_m) \tag{5.4.9}$$

while the estimate of ρ^* can be generated by the following update law:

$$\dot{\rho} = \gamma \epsilon (u_f - \boldsymbol{\theta}^\mathsf{T} \boldsymbol{\phi}) \tag{5.4.10}$$

The normalised adaptive law of Equation 5.4.9 is very similar to the unnormalised law of Equation 5.2.35, with the output error being replaced by the normalised estimation error and the signal vector $\boldsymbol{\omega}$ being replaced by its filtered equivalent $\boldsymbol{\phi}$. However, the procedure required to generate the normalised estimation error means that the normalised adaptation algorithm is much more complex than the unnormalised adaptive law.

Dynamic normalisation

According to [12], the normalised adaptive law can be made robust to unmodelled dynamics by using a technique known as *dynamic normalisation*, where the normalising signal is effectively low-pass filtered. The bandwidth δ_0 of this low-pass filter must be chosen so that it is slower than any unmodelled dynamics.

The following equations show how the dynamic normalising signal is generated, and can replace Equations 5.4.5 and 5.4.6 in the adaptive algorithm:

$$\dot{m}_s = -\delta_0 m_s + u_p^2 + y_p^2 \tag{5.4.11}$$

$$m_s(0) = 0 \tag{5.4.12}$$

$$m^2 = 1 + m_s \tag{5.4.13}$$

5.4.2 Leakage

Phenomena such as disturbances and noise can cause unwanted drift in the adapted parameters. This can be prevented using a technique known as *leakage*, which will cause the parameters to drift back to their initial values or to zero in the absence of an output error. This technique can be applied to both normalised and unnormalised adaptive laws.

The unnormalised adaptive law can be modified as follows to include leakage:

$$\dot{\boldsymbol{\theta}} = -\Gamma e_1 \boldsymbol{\omega} \operatorname{sgn}(\rho^*) - w\boldsymbol{\theta} \tag{5.4.14}$$

and leakage can be added to the normalised adaptive law as follows [12]:

$$\dot{\boldsymbol{\theta}} = \Gamma(\epsilon \boldsymbol{\phi} - w\boldsymbol{\theta}) \tag{5.4.15}$$

Both these adaptive laws will cause the parameters to drift to zero in the absence of an output error, which may not be ideal. They can be modified by replacing $\boldsymbol{\theta}$ in the leakage term with $(\boldsymbol{\theta} - \boldsymbol{\theta}_0)$, so that the parameters will drift back to their initial values $\boldsymbol{\theta}_0$ instead of zero.

The leakage variable w can be chosen in a number of different ways. The simplest way is to make it a positive constant σ – this technique is known as *fixed σ-modification*. Alternatively, a technique known as *switching σ-modification* can be used, where w is chosen as a function of $\boldsymbol{\theta}$, so that leakage only takes place if the parameter vector exceeds a certain bound. Finally, the leakage variable can be made dependent on the output error e_1 or the normalised estimation error ϵ, so that leakage will only take place if the error is large. This technique is known as *ϵ-modification*.

The use of leakage can prevent parameter drift due to disturbances and noise. The output error due to these phenomena will act as a force pushing the parameters away from their initial values, while the leakage will act as a force pushing them back to their initial values, which grows stronger as the parameters move further away. This system should eventually reach equilibrium, causing the parameters to settle at some value.

5.4.3 Dead zone

Another simple way in which the robustness of the adaptive control system can be improved is to introduce a dead zone in the error signal for which no adaptation takes place. The basic principle behind the use of a dead zone is that the parameters should not be adjusted when the signal-to-noise ratio in the system is low, in which case the adaptive law would not be able to distinguish between the signals and the noise [10].

In [12], this principle is applied to the normalised adaptive law shown in Section 5.4.1, with the width of the dead zone depending on the normalising signal m^2. In this thesis, however, the dead zone modification is only applied to the unnormalised adaptive law of Section 5.2.4, and the width of the dead zone is kept constant.

In the adaptive law of Equation 5.2.35, the output error e_1 is replaced by the error signal e_1':

$$\dot{\boldsymbol{\theta}} = -\Gamma e_1' \boldsymbol{\omega} \operatorname{sgn}(\rho^*) \tag{5.4.16}$$

where e_1' is defined as

$$e_1' = \begin{cases} e_1 + g_0 & ; \quad e_1 < -g_0 \\ 0 & ; \quad |e_1| \leq g_0 \\ e_1 - g_0 & ; \quad e_1 > g_0 \end{cases} \tag{5.4.17}$$

The dead zone relation from e_1 to e_1' is shown in Figure 5.4.1. Clearly, no adaptation will take place if the magnitude of the output error is less than the dead zone width g_0.

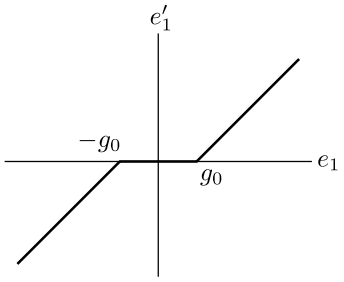

Figure 5.4.1: Output error dead zone used to improve the robustness of the unnormalised adaptive law

The dead zone could also be defined such that $e_1' = e_1$ when e_1 is outside the dead zone – then adaptation will suddenly take place at a significant rate as soon as the error leaves the dead zone. This would make the adaptive law discontinuous, which may affect the existence and uniqueness of solutions to the adaptive law, and create computational problems at the switching surface [38]. Therefore the dead zone is defined continuously as in Equation 5.4.17.

In the choice of the dead zone width, a trade-off must be made. Increasing the dead zone width will improve the robustness of the adaptive law to disturbances and noise, for which adaptation is not wanted, but will decrease its sensitivity to changes in the plant dynamics, for which adaptation is wanted.

Knowledge of the typical magnitudes of disturbances and noise that the plant will experience can be used to choose a dead zone width which will prevent unwanted adaptation [10]. Also, the fixed-gain portion of the control system can be designed to have good disturbance rejection, which will decrease the dead zone width required to handle these disturbances.

The use of a dead zone can also provide robustness against unmodelled dynamics. If the aircraft is modelled well, unmodelled dynamics will cause small output errors, and if these output errors are smaller than the dead zone width, they will have no effect on adaptation.

5.4.4 Evaluation of robustness modifications

The three robustness modifications proposed in this section all have different effects on the performance of the adaptive control system. Their expected effects can be evaluated against the goals of the adaptive control system for the Variable Stability UAV to determine which techniques would be appropriate for this design.

The purpose of the normalised adaptive law is to reduce the sensitivity of the adaptation rate to the magnitude of the input signal to the MRAC system. However, the focus of the adaptive control system for the Variable Stability UAV will not be on following commands accurately; instead, it is simply meant to keep the aircraft stable when it suffers in-flight damage. Therefore it would seem that a normalised adaptive law is not particularly suitable for this project.

The addition of leakage to the adaptive law will cause the controller parameters to drift back to their initial values, or to zero, when there is no output error. After the parameters have been adapted to account for a change in dynamics such as a CG shift, they would be expected to settle at new values where the closed-loop system is stable and the output error is small. However, leakage would cause them to drift back to their initial values, which could decrease the stability of the system again. Therefore leakage also does not intuitively seem to be a good solution to the problem of parameter drift in this application. However, the effect of this unwanted drift back to the initial values may not be significant in practice, and therefore leakage was considered worth investigating in simulation.

The use of a dead zone in the adaptive law will decrease its sensitivity to output errors, which could mean that the control system takes longer to react to damage than it would without the dead zone. However, the level of noise to be expected can easily be determined through flight tests, and the dead zone can be chosen just wide enough to prevent adaptation due to measurement noise. Then it should have little effect on the response of the adaptive control system to changes in the aircraft dynamics, such as those caused by CG shifts.

5.5 Summary

In this chapter, the basic concepts of adaptive control were defined, and the adaptive control problem was stated in terms of the more general Model Reference Control (MRC) problem. The MRC law with fixed parameters was presented as a solution to the MRC problem in the case where the plant parameters are known. An unnormalised adaptive law was derived from a parametric model of the closed-loop MRC system to adjust the parameters of the MRC law in the case of plant parameter variations.

An inspection of the adaptive control system indicated that phenomena such as disturbances and measurement noise could cause the adapted parameters to drift. A number of techniques were given which could improve its robustness to these phenomena, including a normalised adaptive law, dynamic normalisation, leakage, and the use of a dead zone.

The MRC law and the adaptive laws discussed in this chapter can now be used in a fault-tolerant adaptive control system for the Variable Stability UAV. The restrictions on which plants an MRC system can be designed for – particularly the requirement that the plant be minimum-phase – will determine which control loops can be made adaptive.

In Chapter 6, the control laws comprising the control system will be designed and analysed using linear tools. In Chapter 7 they will be combined with adaptive laws from this chapter, and tested in non-linear simulation to evaluate the fault tolerance of the adaptive control system.

Chapter 6

Longitudinal control system design

This chapter describes the design and linear analysis of a longitudinal control system for the Variable Stability UAV. The goal of the control design is to allow full autonomous control of the longitudinal dynamics of the aircraft, and to allow the integration of an adaptive law which can re-stabilise the aircraft when it is destabilised by in-flight damage. As mentioned in the introduction, it was decided to focus on damage-induced shifts in the centre of gravity to demonstrate the fault tolerance of the adaptive control system.

In Chapter 4, a linear analysis of the longitudinal dynamics of the aircraft showed that backward CG shifts can dramatically affect the stability of its short period mode. Therefore the control system must be designed so that the inner loop which controls the short period mode can be made adaptive in order to keep this mode of motion stable for all CG positions. To this end, the MRC law introduced in Chapter 5 can be used in the inner loop, so that one of the adaptive laws from that chapter can be used to adjust its parameters.

In this chapter, the control system is designed with fixed parameters, so that the effect of CG shifts on its closed-loop behaviour can be analysed using linear tools. The addition of an adaptive law will make the control system non-linear, and therefore the behaviour of the adaptive control system is investigated in non-linear simulation in Chapter 7.

Section 6.1 describes the architecture of the longitudinal control system and the different control loops it consists of, and Sections 6.2 to 6.5 describe the design of each of these control loops. Section 6.6 analyses the effect of shifts in the centre of gravity of the aircraft on the longitudinal closed-loop dynamics when adaptation is not used. Section 6.7 analyses the effect of varying the MRC parameters on the closed-loop dynamics when the CG is in the backward position, which should indicate how the adaptive law would have to adjust the parameters in order to re-stabilise the aircraft.

6.1 Longitudinal control system architecture

In Section 4.6 it was shown that the short period mode dynamics of an aircraft are the most

affected by shifts in its centre of gravity. In general, the rotational dynamics of an aircraft are likely to be much more affected by in-flight damage than the kinematics are [8]. Therefore, if the control loops responsible for controlling the rotational dynamics are made robust to CG shifts and other damage, and can present an invariant response to the outer loops, then the damage does not need to be taken into account in the design of the other control loops.

For this reason, a normal specific acceleration (NSA) controller was designed in [4], where knowledge of the CG position was used to calculate the required control gains to keep the aircraft stable. For this project, this NSA controller had to be replaced by an adaptive controller which can keep the aircraft stable without prior knowledge of the CG position or the exact nature of any other in-flight damage.

However, as shown in Section 4.5.1, the transfer function from elevator deflection to NSA is non-minimum phase, and therefore the MRC law cannot be used to control it, since it would have to perform pole-zero cancellations in the right half-plane. Therefore, instead of designing an adaptive NSA controller, an adaptive pitch rate controller was designed to control the short-period mode of the Variable Stability UAV, since the transfer function from elevator to pitch rate is minimum phase. The design of the pitch rate controller is discussed in Section 6.2.

This pitch rate controller was designed to operate at an airspeed of 18 m/s. It was found that changes in the airspeed have a significant effect on the behaviour of the pitch rate controller. One way to address this would be to adjust the parameters of the pitch rate controller using the airspeed measurement, to ensure that the pitch rate controller performs as desired at any possible airspeed. However, combining this gain scheduling technique with the adaptive law would be very complicated, and therefore this approach was not considered for this project.

Instead, an airspeed controller was designed to regulate the airspeed with zero steady-state error while the pitch rate controller is armed. The design of the airspeed controller is discussed in Section 6.3.

With a SISO airspeed controller already in place, a SISO climb rate controller was designed to complete the kinematic control of the aircraft. This controller was designed to generate pitch rate commands for the pitch rate controller in order to follow climb rate commands with zero steady-state error. The design of the climb rate controller is discussed in Section 6.4. Finally, an altitude loop was closed around the climb rate controller, the design of which is discussed in Section 6.5.

The two SISO controllers for the airspeed and climb rate could be replaced by a MIMO controller which controls both the airspeed and the climb rate. This controller could then be designed using techniques such as LQR to deliver better performance than the two SISO controllers. However, since the focus of this project was on the adaptive inner-loop controller, the performance of the outer loops was not seen as crucial, and the two SISO controllers were

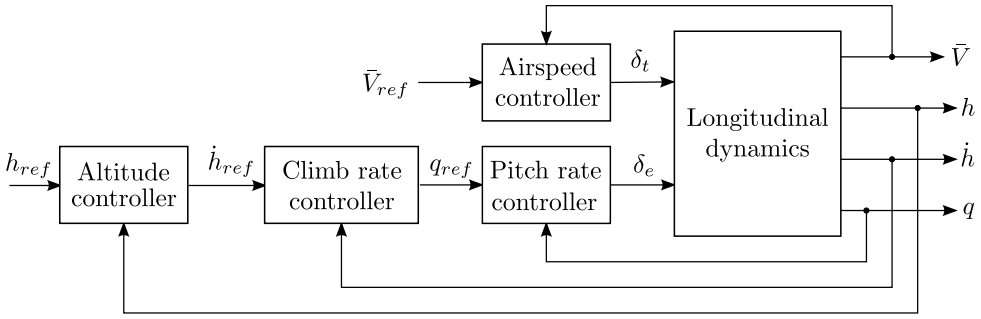

Figure 6.1.1: Longitudinal control system

considered adequate.

The structure of the longitudinal control system, with the pitch rate, airspeed, climb rate and altitude controllers, is shown in Figure 6.1.1.

6.2 Pitch rate controller

An adaptive pitch rate controller was designed to keep the short period mode stable when the aircraft is damaged in flight, and to allow it to follow pitch rate commands. These commands could either be generated by the outer control loops during autonomous flight, or by a human pilot during fly-by-wire operation, where the elevator commands from the remote control are translated into reference commands for the pitch rate controller.

A model reference adaptive control (MRAC) system, as described in Chapter 5, was designed to ensure stability of the closed-loop system when the aircraft dynamics changes. Figure 6.2.1 shows the MRAC structure applied to the control of the pitch rate of the aircraft. In this application, the reference command is the pitch rate reference command q_{ref}, the plant input is the elevator deflection δ_e, and the plant output is the pitch rate q. The output error e_1 can also be called the pitch rate error.

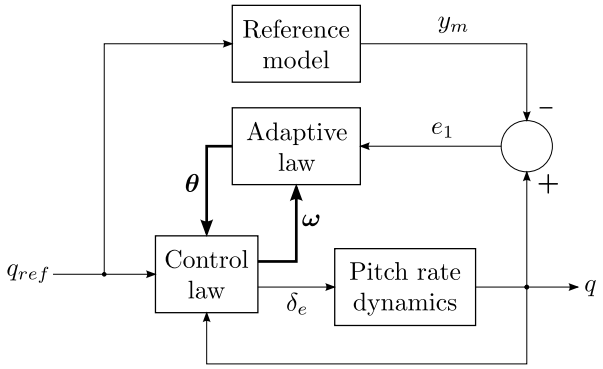

Figure 6.2.1: Pitch rate MRAC structure

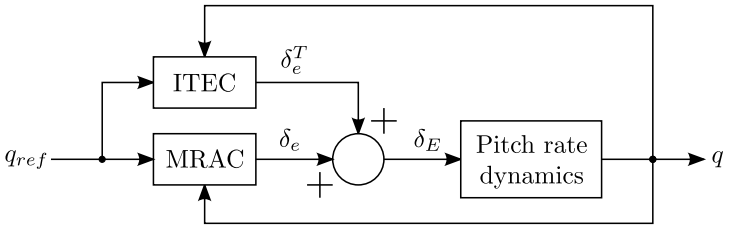

Figure 6.2.2: Pitch rate controller structure with MRAC and ITEC

If the aircraft is to follow pitch rate commands, it is natural to choose the reference model to have unity DC gain. Then the model output y_m will be equal to the pitch rate command q_{ref} in the steady state, and the two symbols can be used interchangeably in the steady-state analysis.

The MRC law used in the MRAC system does not use integral control, and therefore will not allow pitch rate commands to be tracked with zero steady-state error in the presence of pitching moment disturbances – that is, $q \neq q_{ref}$ in the steady state if disturbances are present. A shift in the centre of gravity will cause such a disturbance, since the lift vector will no longer be aligned with the CG.

If the aircraft experiences a constant pitching moment disturbance, it can be kept in trim ($q = 0$) using a constant pitch rate command ($q_{ref} \neq 0$) from the outer control loops or the human pilot. Then there will be a nonzero steady-state pitch rate error ($e_1 = q - q_{ref}$), which will cause the adapted parameters to drift. This may cause instability if the parameters are allowed to drift indefinitely.

A constant pitching moment disturbance will effectively change the elevator deflection required to keep the aircraft trimmed. If there are no disturbances, a constant trim elevator setting δ_{E_t} can be added to the elevator command δ_e generated by the MRAC to obtain the total elevator command δ_E. Then a zero elevator command from the MRAC will lead to a zero steady-state pitch rate. This is assumed in the design of the MRAC system, and the parameters will drift if it is not the case. Therefore the trim elevator setting must be adjusted to compensate for constant pitching moment disturbances.

This can be done by adding an integral trim elevator controller (ITEC) in parallel with the MRAC, which uses an integral control law to adjust the trim elevator setting and ensure that $q = q_{ref}$, and therefore $e_1 = 0$, in the steady state. The resulting structure of the pitch rate controller is shown in Figure 6.2.2. The MRAC block in this figure includes the control law, the adaptive law and the reference model. The design of the MRC law in the MRAC system is described in Section 6.2.1, and the addition of ITEC in Section 6.2.2.

6.2.1 Model-reference control

This section applies the MRC law given in Section 5.2.2 for a general SISO system to the control of the pitch rate of the Variable Stability UAV. In this chapter, the controller is designed with fixed parameters, chosen to yield the desired closed-loop response for the nominal plant parameters. The constant control gains can then be replaced by adapted parameters which are adjusted by one of the adaptive laws from Chapter 5.

Plant and reference model restrictions

In order to use the MRC law to control the pitch rate, the pitch rate dynamics must satisfy the plant assumptions given in Section 5.2.2. In Section 4.5.1 it was shown that the transfer function from elevator to pitch rate is a second-order system ($n_p = 2$) with one zero ($m_p = 1$), which therefore has a relative degree of $n^* = 1$. It is assumed that a positive elevator deflection will always produce a negative pitching moment, which means that the sign of the high-frequency gain of this transfer function is known to be negative. Also, this transfer function is minimum phase, since its only zero is in the left half-plane.

Therefore this transfer function satisfies the plant assumptions given in Section 5.2.2, and an MRC law can be designed for this plant. By contrast, the transfer function from elevator to normal specific acceleration has a zero in the right half-plane, and therefore the MRC law can not be used for an NSA controller.

As stated in Chapter 5, an upper bound on the plant order is required for the MRC law, i.e. an integer $n \geq n_p$. Since the plant is known to be a second order system, we can choose $n = n_p = 2$. There may well be unmodelled dynamics in the system which would increase its order, but the adaptive control system can be made robust to these using the techniques discussed in Section 5.4.

The reference model $W_m(s)$ of the MRAC system, which represents the desired closed-loop response of the MRC law, must be chosen to satisfy the reference model assumptions of Section 5.2.2. Therefore $W_m(s)$ must be stable, minimum phase, of relative degree 1, and of order $p_m \leq 2$. This means that the reference model must have two poles and one zero ($p_m = 2$, $q_m = 1$), or one pole and no zeroes ($p_m = 1$, $q_m = 0$).

The first-order reference model is actually a special case of the second-order reference model, where the zero and one of the poles are both located at $s = -\lambda_0$, the location of the MRC filter pole. Therefore it will be assumed from this point that the reference model has two poles and one zero, and the first-order reference model will not be treated separately.

In addition to the reference model assumptions of Section 5.2.2, $W_m(s)$ must also be chosen to be SPR if the adaptive law derived in Section 5.2.4 is to be used. As shown in Appendix B.1.2, this means that it should be stable and minimum-phase, that the frequency of the reference model zero must be less than the coefficient of the linear term in the denominator, and that the phase of $W_m(j\omega)$ should not exceed $\pm 90^\circ$ for any frequency.

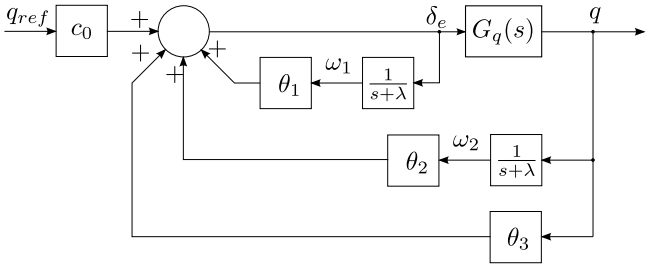

Figure 6.2.3: MRC law in the pitch rate controller

In general, the plant and the reference model will have the following forms:

$$G_p(s) = \frac{q(s)}{\delta_e(s)} = \frac{k_p(s+b_p)}{s^2 + a_{p1}s + a_{p2}} \tag{6.2.1}$$

$$W_m(s) = \frac{y_m(s)}{q_{ref}(s)} = \frac{k_m(s+b_m)}{s^2 + a_{m1}s + a_{m2}} \tag{6.2.2}$$

where $b_m < a_{m1}$ is necessary for $W_m(s)$ to be SPR.

Control law

The MRC law of Section 5.2.2, applied as a pitch rate controller, is as follows:

$$\delta_e = \boldsymbol{\theta}_1{}^{\mathsf{T}} \frac{\alpha(s)}{\Lambda(s)}\delta_e + \boldsymbol{\theta}_2{}^{\mathsf{T}} \frac{\alpha(s)}{\Lambda(s)} q + \theta_3 q + c_0 q_{ref} \tag{6.2.3}$$

For $n = 2$, the polynomial vector $\alpha(s)$ is unity, and all the controller parameters are scalars:

$$\alpha(s) = 1 \tag{6.2.4}$$

$$\theta_1,\ \theta_2,\ \theta_3,\ c_0 \in \mathcal{R}^1 \tag{6.2.5}$$

The filter denominator $\Lambda(s) = \Lambda_0(s)Z_m(s)$ must be monic and of order $n-1 = 1$. Therefore, for a second-order reference model, we have:

$$\Lambda(s) = Z_m(s) = s + \lambda \tag{6.2.6}$$

$$\lambda = z_m \tag{6.2.7}$$

$$\Lambda_0(s) = 1 \tag{6.2.8}$$

Then the MRC law used in the pitch rate controller reduces to:

$$\delta_e = \frac{\theta_1}{s+\lambda}\delta_e + \frac{\theta_2}{s+\lambda} q + \theta_3 q + c_0 q_{ref} \tag{6.2.9}$$

The control law is shown in block diagram form in Figure 6.2.3, and can also be written in vector form:

$$\delta_e = \boldsymbol{\theta}^{\mathsf{T}} \boldsymbol{\omega} \tag{6.2.10}$$

where

$$\boldsymbol{\theta} = \begin{bmatrix} \theta_1 & \theta_2 & \theta_3 & c_0 \end{bmatrix}^T \tag{6.2.11}$$

$$\boldsymbol{\omega} = \begin{bmatrix} \omega_1 & \omega_2 & q & q_{ref} \end{bmatrix}^T \tag{6.2.12}$$

and ω_1 and ω_2 are the states of the two first-order filters:

$$\dot{\omega}_1 = -\lambda\omega_1 + \delta_e \tag{6.2.13}$$

$$\dot{\omega}_2 = -\lambda\omega_2 + q \tag{6.2.14}$$

Parameter design

The values of the controller parameter vector $\boldsymbol{\theta}$ which will yield the desired closed-loop transfer function for the nominal plant can be determined using Equations 5.2.18 and 5.2.19. When the simplifications of Equations 6.2.4 to 6.2.8 are applied, these matching equations reduce to:

$$(Z_m - \theta_1)R_p - k_p Z_p(\theta_2 + \theta_3 Z_m) = Z_p R_m \tag{6.2.15}$$

$$c_0 k_p = k_m \tag{6.2.16}$$

If the plant and the reference model are in the form of Equations 6.2.1 and 6.2.2, then the matching equations can be solved symbolically to obtain the following expressions for the controller parameters:

$$\theta_1 = b_m - b_p \tag{6.2.17}$$

$$\theta_2 = \frac{a_{p2} - a_{m2} + b_m(a_{m1} - a_{p1})}{k_p} \tag{6.2.18}$$

$$\theta_3 = \frac{a_{p1} - a_{m1}}{k_p} \tag{6.2.19}$$

$$c_0 = k_m/k_p \tag{6.2.20}$$

$$\lambda = b_m \tag{6.2.21}$$

Equations 6.2.17 to 6.2.21 can be used to calculate the controller parameters which will yield any desired closed-loop transfer function. However, they do not provide much insight into the effect of each of these parameters. Such insight can be obtained by analysing the different feedback loops using root locus methods.

The feedback loop through θ_1 effectively creates a compensator in series with the plant, as shown in Figure 6.2.4:

$$\delta_e = u + \frac{\theta_1}{s+\lambda}\delta_e \tag{6.2.22}$$

$$\therefore \frac{\delta_e(s)}{u(s)} = \frac{1}{1 - \frac{\theta_1}{s+\lambda}}$$

$$= \frac{s+\lambda}{s+\lambda-\theta_1} \tag{6.2.23}$$

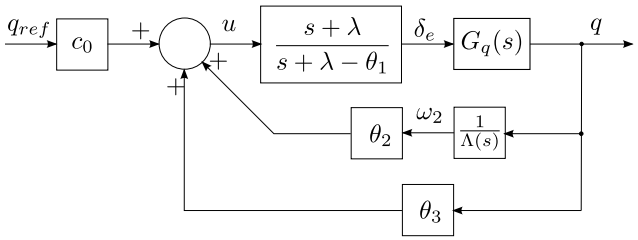

Figure 6.2.4: MRC law with the feedback loop through θ_1 replaced by a compensator in series with the plant

where

$$u = \theta_2\omega_2 + \theta_3 q + c_0 q_{ref} \tag{6.2.24}$$

Then, if Equation 6.2.17 and 6.2.21 are substituted into the compensator transfer function, it becomes:

$$\frac{\delta_e(s)}{u(s)} = \frac{s+b_m}{s+b_p} \tag{6.2.25}$$

which will cancel the plant zero with a pole and create the desired closed-loop zero. Then the minimal transfer function of the plant and compensator will be:

$$\frac{q(s)}{u(s)} = \frac{k_p(s+b_m)}{s^2+a_{p1}s+a_{p2}} \tag{6.2.26}$$

The control loops through θ_2 and θ_3 are closed around this transfer function. Since the loops are in parallel, they can be closed and analysed using root locus methods in any order. Whichever order is used, the zero at $s=-\lambda$ will be present in the root locus of θ_3, but will be cancelled by the filter pole in the root locus of θ_2.

Therefore, assuming that the short period poles are complex, varying θ_2 will cause the poles to move parallel to the imaginary axis. With negative feedback ($\theta_2 > 0$) they will diverge from the real axis, and with positive feedback ($\theta_2 < 0$) they will converge towards the real axis. Varying θ_3 will cause the poles to circle around the zero at $s=-b_m$; they will circle to the left for negative feedback ($\theta_3 > 0$), and to the right for positive feedback ($\theta_3 < 0$).

The effect of the controller parameters on the closed-loop response can best be understood using a number of examples.

Example 1: Reference model chosen for arbitrary response

Suppose that the plant is the pitch rate transfer function of Equation 4.5.5:

$$G_p(s) = \frac{-207.2(s+9.61)}{s^2+20.45s+281.6} \tag{6.2.27}$$

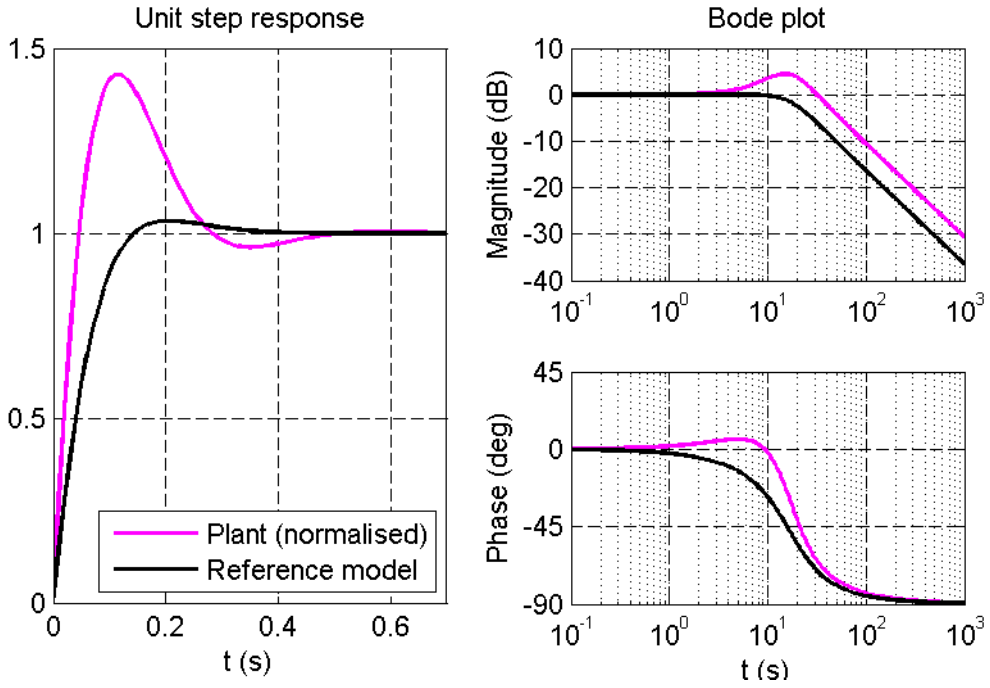

Figure 6.2.5: Step response and Bode plot of the example reference model

and the reference model is chosen to have well-damped poles ($\zeta = 0.8$) with about the same natural frequency as the open-loop poles, a zero at a higher frequency to ensure a small overshoot, and unity DC gain:

$$W_m(s) = \frac{15(s+20)}{s^2 + 28s + 300} \tag{6.2.28}$$

The unit step response and bode plot of this reference model are shown in Figure 6.2.5, along with those of the plant, normalised to have unity DC gain, for comparison.

The frequency of the zero is less than the linear term of the denominator ($20 < 28$), and the Bode plot shows that the phase of $W_m(j\omega)$ never exceeds $\pm 90°$. Therefore this choice of reference model satisfies the requirements for a second-order transfer function to be SPR, given in Appendix B.1.2.

Using Equations 6.2.17 to 6.2.21, the controller parameters can be calculated as:

$$\boldsymbol{\theta} = \begin{bmatrix} \theta_1 \\ \theta_2 \\ \theta_3 \\ c_0 \end{bmatrix} = \begin{bmatrix} 10.39 \\ -0.64 \\ 0.0364 \\ -0.0724 \end{bmatrix}$$

$$\lambda = 20$$

Note that θ_2 is negative, which implies positive feedback, and θ_3 is positive, which implies negative feedback.

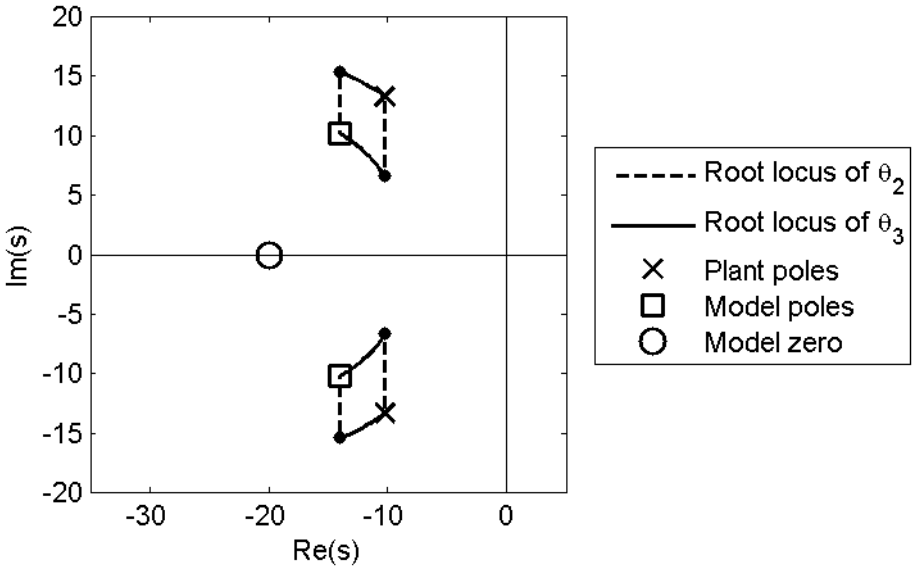

Figure 6.2.6: Root loci of the successively closed loops through θ_2 and θ_3 for the example control design

This combination of θ_1 and λ cancels the plant zero with a pole at $s = -9.61$, and creates the model zero at $s = -20$, so that the plant and compensator transfer function will be:

$$\frac{q(s)}{u(s)} = \frac{-207.2(s+20)}{s^2 + 20.45s + 281.6} \tag{6.2.29}$$

Figure 6.2.6 shows the root loci of θ_2 and θ_3 around the plant and the compensator. The positive feedback of θ_2 moves the poles towards the real axis, while the negative feedback of θ_3 causes them to circle to the left around the closed-loop zero. Whichever loop is closed first, the total effect of the feedback is to move the poles to the desired location.

This example shows that choosing a closed-loop response and then using the matching equations to calculate the controller parameters can result in a control system which uses positive feedback, which may cause instability in practice.

Example 2: Pure pitch rate feedback

A special case of the MRC pitch rate controller is where $\theta_1 = \theta_2 = 0$. This reduces the MRC law to a pitch rate damper which uses pure pitch rate feedback to damp the short period mode, with a feed-forward gain c_0 chosen for unity DC gain to pitch rate commands. In this case the choice of the filter pole λ has no effect as long as the two filter gains remain zero.

The root locus of the pitch rate damper is shown in Figure 6.2.7, with the closed-loop poles and step response if a feedback gain $\theta_3 = 0.026$ is used. This feedback gain will yield optimally damped closed-loop poles, and a feed-forward gain $c_0 = -0.167$ will ensure unity

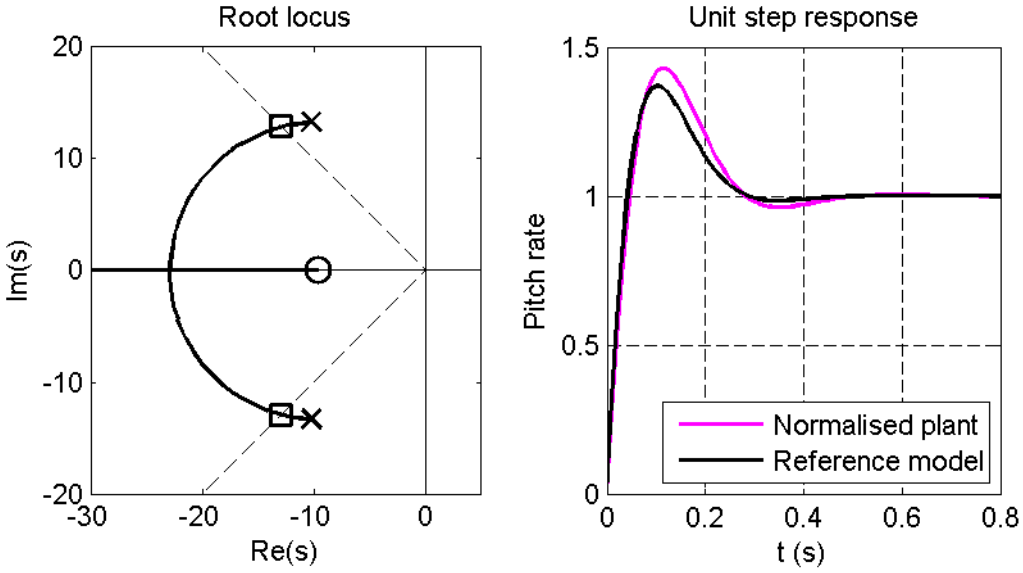

Figure 6.2.7: Root locus of the pitch rate controller with pure pitch rate feedback

DC gain. Then closed-loop transfer function will be:

$$W_m(s) = \frac{34.7s + 333.4}{s^2 + 25.8s + 333.4} \tag{6.2.30}$$

which can be shown to fulfil the SPR requirements of Appendix B.1.2.

The step response of this pitch rate damper has a large overshoot of 37%, but it does not require any positive feedback, which should make it more robust than the MRC system designed from a choice of reference model in the previous example.

Also, if this pitch rate damper is used in an MRAC system and the parameters θ_1 and θ_2 are not adapted from zero, then the adaptation will not necessarily be able to yield a closed-loop transfer function which is exactly equal to the reference model. It should, however, be able to adapt the two non-zero parameters to yield a closed loop system with acceptable performance – that is, good damping and sufficient bandwidth.

6.2.2 Integral trim elevator control

Normally, a constant trim elevator deflection will be added to the elevator command generated by the MRC law to obtain the total elevator deflection command, which will be sent to the servos:

$$\delta_E = \delta_e + \delta_{E_t} \tag{6.2.31}$$

Since the MRC law does not use integral control, a constant pitching moment disturbance will cause a steady-state error between q and q_{ref}, which can in turn cause undesired adaptation if the MRC law is used as part of an MRAC system.

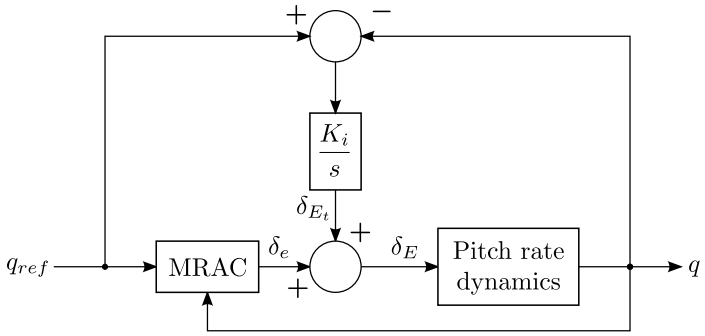

Figure 6.2.8: MRAC with integral trim elevator control (ITEC)

In order to ensure that $q = q_{ref}$ in the steady state when disturbances are present, an integral control law is used to adjust the trim elevator deflection:

$$\dot{\delta}_{E_t} = K_i(q_{ref} - q) \tag{6.2.32}$$

This control technique, which will be referred to as *integral trim elevator control* (ITEC), is shown in block diagram form in Figure 6.2.8.

If the actual pitch rate is less than the pitch rate command, then a positive pitching moment, and therefore a negative elevator deflection, is required to increase the pitch rate. Therefore the integrator gain K_i must be negative.

If $K_i = 0$, then the ITEC will have no effect. If K_i is chosen as a negative number with a small magnitude, then the trim elevator setting will be adjusted slowly to account for pitching moment disturbances, and the response of the aircraft to pitch rate commands will be very similar to the closed-loop response of the MRC law. Increasing the magnitude of K_i will cause the trim elevator setting to converge more quickly towards a new value, but will have a greater effect on the closed-loop response of the pitch rate controller.

The total pitch rate control law, combining the MRC and ITEC laws, will be as follows:

$$u = \left(c_0 + \frac{K_i}{s}\right) q_{ref} + \left(\frac{\theta_2}{s+\lambda} + \theta_3 - \frac{K_i}{s}\right) q \tag{6.2.33}$$

$$\delta_E = \left(\frac{s+\lambda}{s+\lambda-\theta_1}\right) u \tag{6.2.34}$$

In order to analyse the effect of the ITEC gain quantitatively, it is assumed that the ITEC is used in conjunction with an MRC law using pure pitch rate feedback:

$$\boldsymbol{\theta} = \begin{bmatrix} \theta_1 \\ \theta_2 \\ \theta_3 \\ c_0 \end{bmatrix} = \begin{bmatrix} 0 \\ 0 \\ 0.026 \\ -0.167 \end{bmatrix} \tag{6.2.35}$$

Without θ_1 and θ_2, the pitch rate control law reduces to:

$$\delta_E = \left(c_0 + \frac{K_i}{s}\right) q_{ref} + \left(\theta_3 - \frac{K_i}{s}\right) q \tag{6.2.36}$$

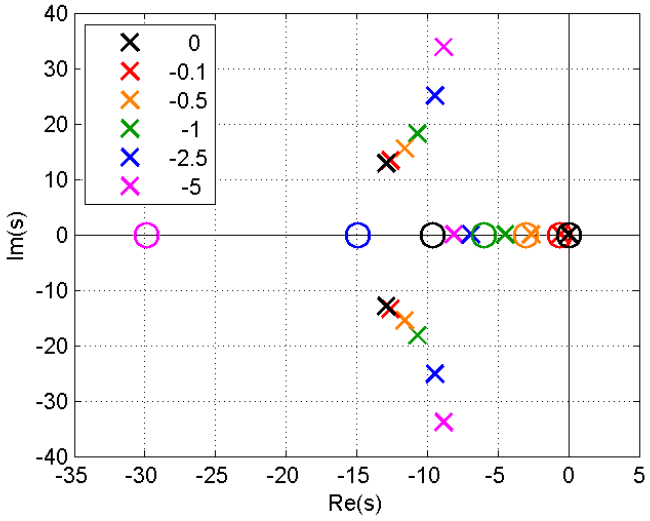

Figure 6.2.9: Closed-loop poles and zeroes of the pitch rate controller for different values of K_i

This control law and the plant transfer function can be used to obtain the closed-loop transfer function from q_{ref} to q when both the MRC and ITEC laws are used. The poles and zeroes of this transfer function are shown in Figure 6.2.9 for a number of values of K_i.

As K_i increases, the short-period poles placed by the MRC law become less damped, which will increase the overshoot experienced in response to a pitch rate command. The zero of the pitch rate transfer function at $s = -9.62$ is unaffected by the increase in K_i.

The use of ITEC also adds an integrator pole and a zero. For small values of K_i, the pole and the zero are close to each other at a low frequency, and therefore they will largely cancel each other out and have little effect on the response to a pitch rate command. As K_i increases, the pole and the zero increase in frequency, and move further away from each other, which implies that they could have a greater effect on the closed-loop response; however, the response should be dominated by the lightly damped short-period poles if K_i is large.

A similar analysis can be performed on the transfer function from a pitching moment disturbance M_d to the pitch rate. This disturbance enters the system as an additional input to the plant state space:

$$\begin{bmatrix} \dot{\alpha} \\ \dot{q} \end{bmatrix} = A \begin{bmatrix} \alpha \\ q \end{bmatrix} + B\delta_e + \begin{bmatrix} 0 \\ 1/I_{yy} \end{bmatrix} M_d \tag{6.2.37}$$

where A and B are the state-space matrices defined in Section 4.5.1.

The transfer function from M_d to q has the same poles as the one from q_{ref} to q, but it has zeroes located at $s = -11.57$ and $s = 0$ for all values of K_i. The zero at the origin means that the pitch rate will return to zero after a disturbance step, except when $K_i = 0$, in which case the zero will be cancelled by a pole at the origin. Furthermore, the lack of a zero near the

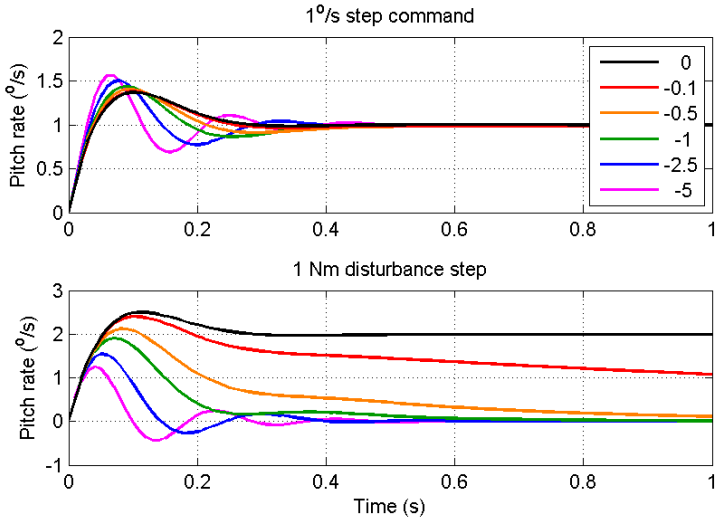

Figure 6.2.10: Closed-loop responses to unit steps in the pitch rate command and a pitching moment disturbance for different values of K_i

integrator pole implies that it will have a significant effect on the response of the controller to pitching moment disturbances.

Figure 6.2.10 shows the response of the system to unit steps in the pitch rate command and a pitching moment disturbance. When $K_i = 0$, the ITEC has no effect and the constant disturbance causes a steady-state pitch rate error. As K_i increases in magnitude, the response to a pitch rate command becomes more lightly damped, while the pitch rate returns to zero more quickly in response to a pitching moment disturbance.

These results indicate that a trade-off must be made in the choice of K_i between the quality of the response to a pitch rate command, and the time it takes to reject a pitching moment disturbance. In this case, it would seem that a value between -0.1 and -1 would be a good choice, since this would ensure quick disturbance rejection without seriously affecting the response to a step command.

Also, when the ITEC is implemented in practice, it would probably be necessary to limit the trim elevator state to prevent the integrator from running away. For instance, the elevators of the Variable Stability UAV have a maximum deflection of $\pm 12°$, and therefore the trim elevator deflection could be limited to a value such as $\pm 7°$ to ensure that the trim setting is not adjusted to a point where there elevator does not have enough authority to control the aircraft.

6.3 Airspeed controller

This section describes the design of a SISO airspeed controller for the Variable Stability UAV. The primary purpose of the controller is to regulate the airspeed at the nominal value of

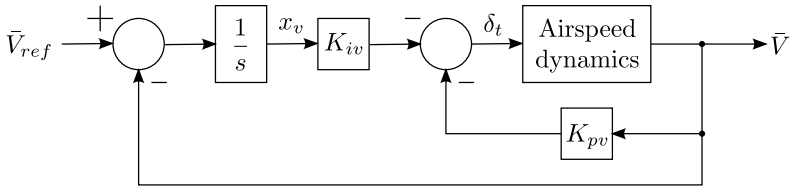

Figure 6.3.1: PI Airspeed controller

18 m/s, but it can easily be designed to allow airspeed step commands as well.

In Chapter 4, it was shown that, if drag is treated as an unmodelled disturbance, the airspeed dynamics are given by the following equation:

$$\dot{\bar{V}} = \frac{1}{m}T - \frac{g}{\bar{V}_t}\dot{h} \tag{6.3.1}$$

In the design of the airspeed controller, the gravity term through which climb rate couples into airspeed can also be treated as an unmodelled disturbance. Then the dynamics from thrust to airspeed reduce to a pure integral system:

$$\dot{\bar{V}} = \frac{1}{m}T \tag{6.3.2}$$

If the closed-loop bandwidth of the airspeed controller is chosen to be much less than that of the throttle dynamics, then the throttle dynamics can be neglected, and it can be assumed that $T = \delta_t$.

The following proportional-integral (PI) control law, shown in Figure 6.3.1, was used for the airspeed controller to ensure that there would be no steady-state errors to constant commands or disturbances, such as those caused by drag and gravity:

$$\delta_t = -K_{pv}\bar{V} - K_{iv}x_v \tag{6.3.3}$$

$$\dot{x}_v = \bar{V}_{ref} - \bar{V} \tag{6.3.4}$$

An augmented state space model can be obtained of the airspeed dynamics and the integrator:

$$\begin{bmatrix}\dot{\bar{V}}\\ \dot{x}_v\end{bmatrix} = \begin{bmatrix}0 & 0\\ -1 & 0\end{bmatrix}\begin{bmatrix}\bar{V}\\ x_v\end{bmatrix} + \begin{bmatrix}\frac{1}{m}\\ 0\end{bmatrix}T + \begin{bmatrix}0\\ 1\end{bmatrix}\bar{V}_{ref} \tag{6.3.5}$$

$$\dot{\mathbf{x}}_v = A_v\mathbf{x}_v + B_v\delta_t + B_{v_{cl}}\bar{V}_{ref} \tag{6.3.6}$$

The control law of Equation 6.3.3 can be substituted into this state equation to obtain the closed-loop characteristic polynomial of this system:

$$\mathrm{CP}_v = |sI - A_v + B_vK_v| \tag{6.3.7}$$

$$= s^2 + \tfrac{1}{m}K_{pv}s - \tfrac{1}{m}K_{iv} \tag{6.3.8}$$

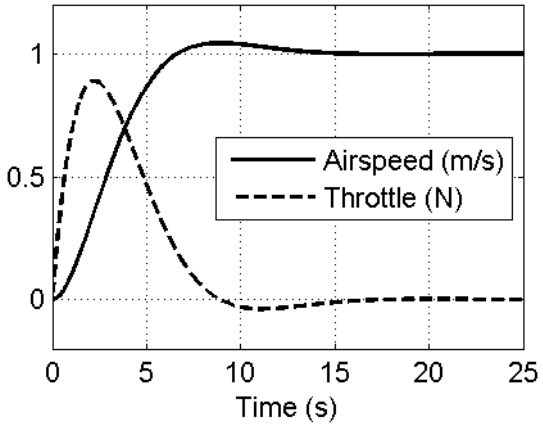

Figure 6.3.2: Response of the ideal kinematic model to an airspeed step command with thrust controlled directly

If the desired closed-loop natural frequency for the airspeed controller is ω_{nv} and the damping ratio is ζ_v, then the desired characteristic polynomial will be:

$$\mathrm{CP}_v = s^2 + 2\zeta_v\omega_{nv}s + \omega_{nv}^2 \tag{6.3.9}$$

By equating the coefficients of the two polynomials, the following expressions can be obtained for the controller parameters which will yield the desired behaviour:

$$K_{pv} = 2m\zeta_v\omega_{nv} \tag{6.3.10}$$

$$K_{iv} = -m\omega_{nv}^2 \tag{6.3.11}$$

These equations allow the airspeed controller to be designed for any desired closed-loop behaviour. A bandwidth of 0.5 rad/s for the airspeed controller was deemed sufficient, and the controller was designed to have the optimal damping ratio of 0.707. From these specifications, and from the mass of 3.9 kg, the following controller parameters were calculated to give the desired response:

$$K_v = \begin{bmatrix} K_{pv} & K_{iv} \end{bmatrix} = \begin{bmatrix} 2.76 & -0.975 \end{bmatrix} \tag{6.3.12}$$

The response of this controller with the plant of Equation 6.3.2 is shown in Figure 6.3.2. Since drag is neglected, no increase in steady-state thrust is required to maintain the higher airspeed. An increased steady-state thrust would be visible in the response if the full longitudinal model were used, but the exact response of the airspeed controller would depend on which other control loops are armed, and therefore the response of the airspeed controller with the full model is investigated in the analysis of the other control loops.

6.4 Climb rate controller

This section describes the design of a climb rate controller which generates pitch rates commands for the adaptive pitch rate controller, in order to follow climb rate commands with zero steady-state error.

6.4.1 Design

In [4], the airspeed and climb rate controller generated NSA reference commands for the NSA controller. Since the climb rate controller for this project had to be designed to generate pitch rate commands, the climb rate dynamics had to be written in a form which has the pitch rate as an input.

The climb rate can be defined in terms of the airspeed and climb angle, and then linearised for small climb angles:

$$\dot{h} = \bar{V} \sin \theta_w \tag{6.4.1}$$

$$\approx \bar{V}_t \theta_w \tag{6.4.2}$$

The time derivative of the climb rate can be approximated by assuming that the airspeed is constant ($\bar{V} = \bar{V}_t$), and that the pitch rates of the body axis and wind axis systems are the same ($\dot{\theta}_w = q$):

$$\therefore \ddot{h} \approx \bar{V}_t q \tag{6.4.3}$$

The latter assumption is equivalent to assuming that the angle of attack dynamics are much faster than the climb rate dynamics, since $\theta_w = \theta - \alpha$.

Furthermore, if the closed-loop climb rate dynamics are much slower than the pitch rate dynamics, then it can be assumed that $q = q_{ref}$ in the climb rate controller design. Then the transfer function from pitch rate command to climb rate can be modelled as a pure integrator, just like the transfer function from throttle to airspeed:

$$\frac{\dot{h}(s)}{q_{ref}(s)} = \frac{\bar{V}_t}{s} \tag{6.4.4}$$

The PI control law shown in Figure 6.4.1 was used for the climb rate controller:

$$q_{ref} = -K_{p\dot{h}} \dot{h} - K_{i\dot{h}} x_{\dot{h}} \tag{6.4.5}$$

$$\dot{x}_{\dot{h}} = \dot{h}_{ref} - \dot{h} \tag{6.4.6}$$

In the same way as the for the airspeed controller, expressions can be obtained for the climb rate controller parameters which will yield a desired closed-loop natural frequency $\omega_{n\dot{h}}$ and damping ratio $\zeta_{\dot{h}}$:

$$K_{p\dot{h}} = \frac{2\zeta_{\dot{h}} \omega_{n\dot{h}}}{\bar{V}_t} \tag{6.4.7}$$

$$K_{i\dot{h}} = -\frac{\omega^2_{n\dot{h}}}{\bar{V}_t} \tag{6.4.8}$$

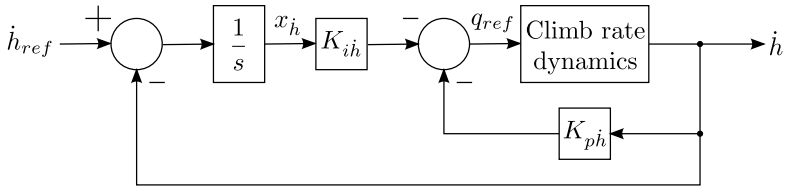

Figure 6.4.1: PI climb rate controller

A natural frequency of 1 rad/s was deemed sufficient for the climb rate controller, and the optimal damping ratio of 0.707 was chosen. These specifications can be achieved for a trim airspeed of 18 m/s by using the following control gains:

$$K_{\dot{h}} = \begin{bmatrix} K_{p\dot{h}} & K_{i\dot{h}} \end{bmatrix} = \begin{bmatrix} 0.079 & -0.056 \end{bmatrix} \tag{6.4.9}$$

6.4.2 Ideal response

Equations 6.3.1 and 6.4.3 together comprise a state-space representation of the kinematics of the aircraft, with thrust and pitch rate as inputs, neglecting the effects of drag and the dynamics from the pitch rate command q_{ref} to the wind axis pitch rate $\dot{\theta}_w$. Figure 6.4.2 shows the response of this system to airspeed and climb rate step commands when the airspeed and climb rate controllers are used.

The responses show an overshoot and response time as would be expected from the chosen closed-loop poles. Since the effect of changes in airspeed on the lift force and pitching moment are neglected, an airspeed step has no effect on the pitch rate command or the climb rate, and since drag is neglected, no steady-state throttle increase is required to maintain a higher airspeed. However, since gravity is included in the model, a climb rate step creates a disturbance to the airspeed dynamics, which causes a transient drop in airspeed until the airspeed controller increases the throttle to maintain the initial airspeed.

6.4.3 Response with full aircraft model and inner loops included

Figure 6.4.3 shows the response of the airspeed and climb rate controllers to step commands when controlling the full longitudinal model of Section 4.3, using the same MRC pitch rate controller as in Section 6.2.2, but with ITEC disabled.

The airspeed and climb rate step responses are close to the ideal responses shown in Figure 6.4.2, indicating that the assumptions made in the kinematic modelling and the control design were valid. The major difference is in the input response to an airspeed step command. A non-zero steady-state thrust command is required to overcome the increased drag and maintain the new airspeed.

Also, a negative steady-state pitch rate command is required to keep the aircraft flying straight and level at this airspeed, even though the actual pitch rate settles at zero. This is

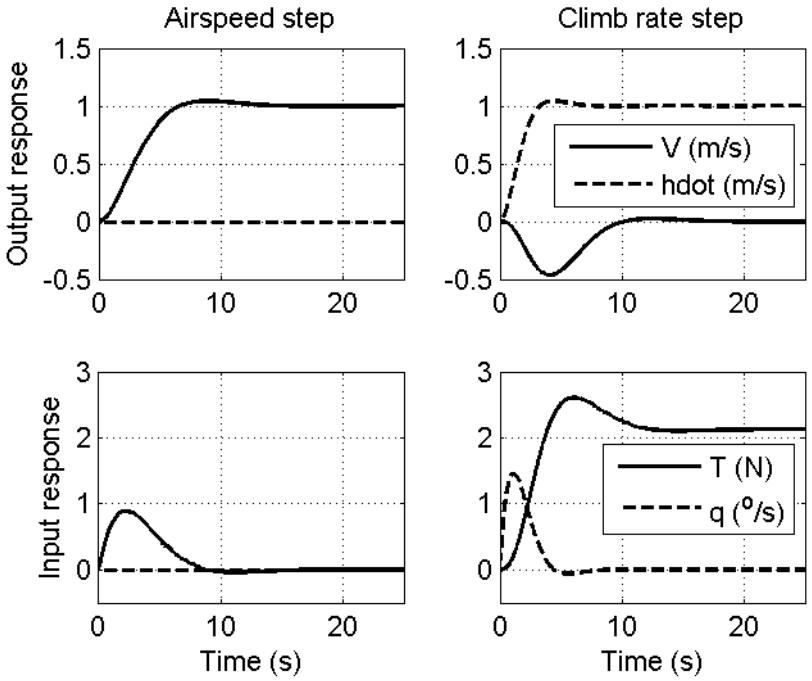

Figure 6.4.2: Response of the ideal kinematic model to airspeed and climb rate commands with thrust and pitch rate controlled directly

due to the fact that less negative elevator is required to trim the aircraft at the higher airspeed, effectively creating a positive pitching moment disturbance, which the climb rate controller counteracts with a negative pitch rate command. This creates a steady-state output error in the pitch rate controller, which could cause unwanted adaptation of the MRC parameters if an adaptive law were added to the control system.

Figure 6.4.4 shows the response to airspeed and climb rate step commands if ITEC is used in conjunction with the MRC law to counter the pitching moment disturbance caused by changes in the airspeed. The ITEC system increases the trim elevator setting and so eliminates the need for a steady-state pitch rate command to trim the aircraft at the higher airspeed, which would also prevent unnecessary adaptation of the MRC parameters.

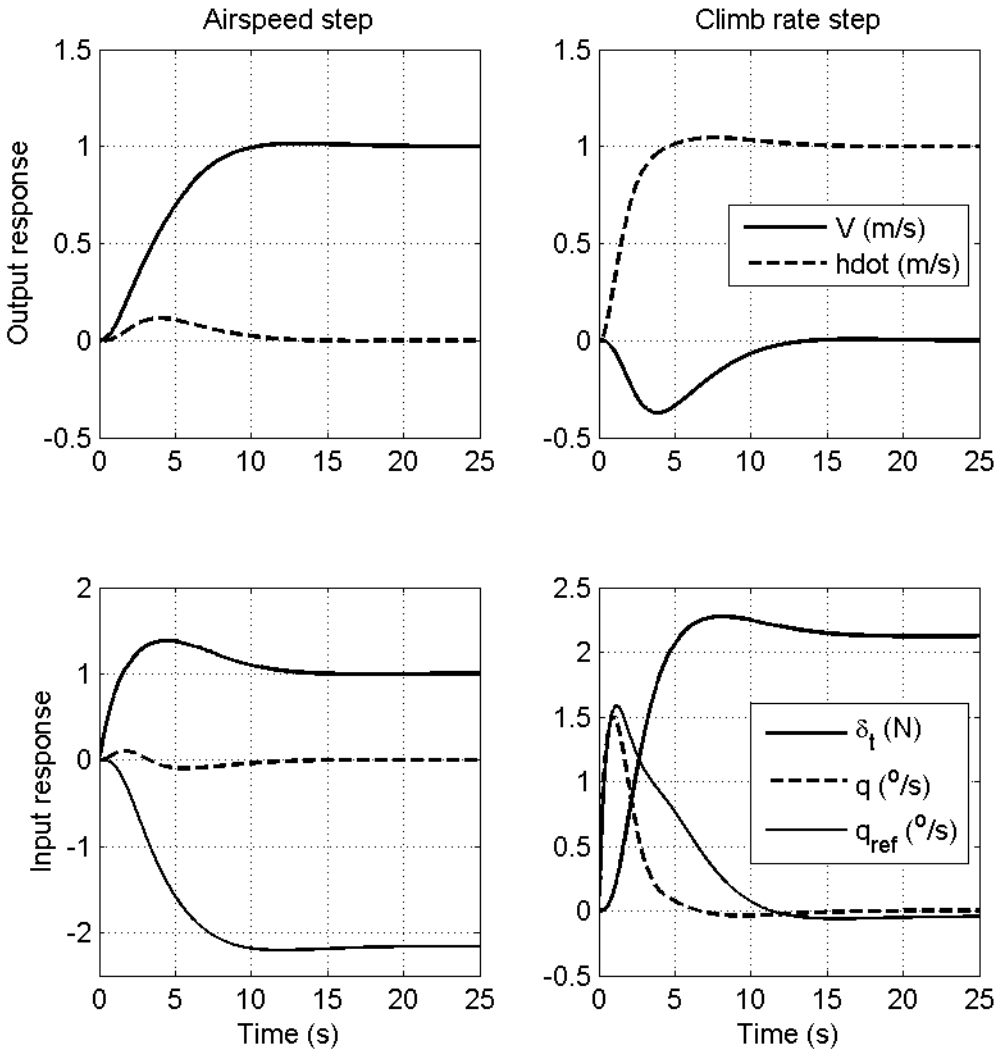

Figure 6.4.3: Response to airspeed and climb rate steps with the full aircraft dynamics and the pitch rate controller without ITEC

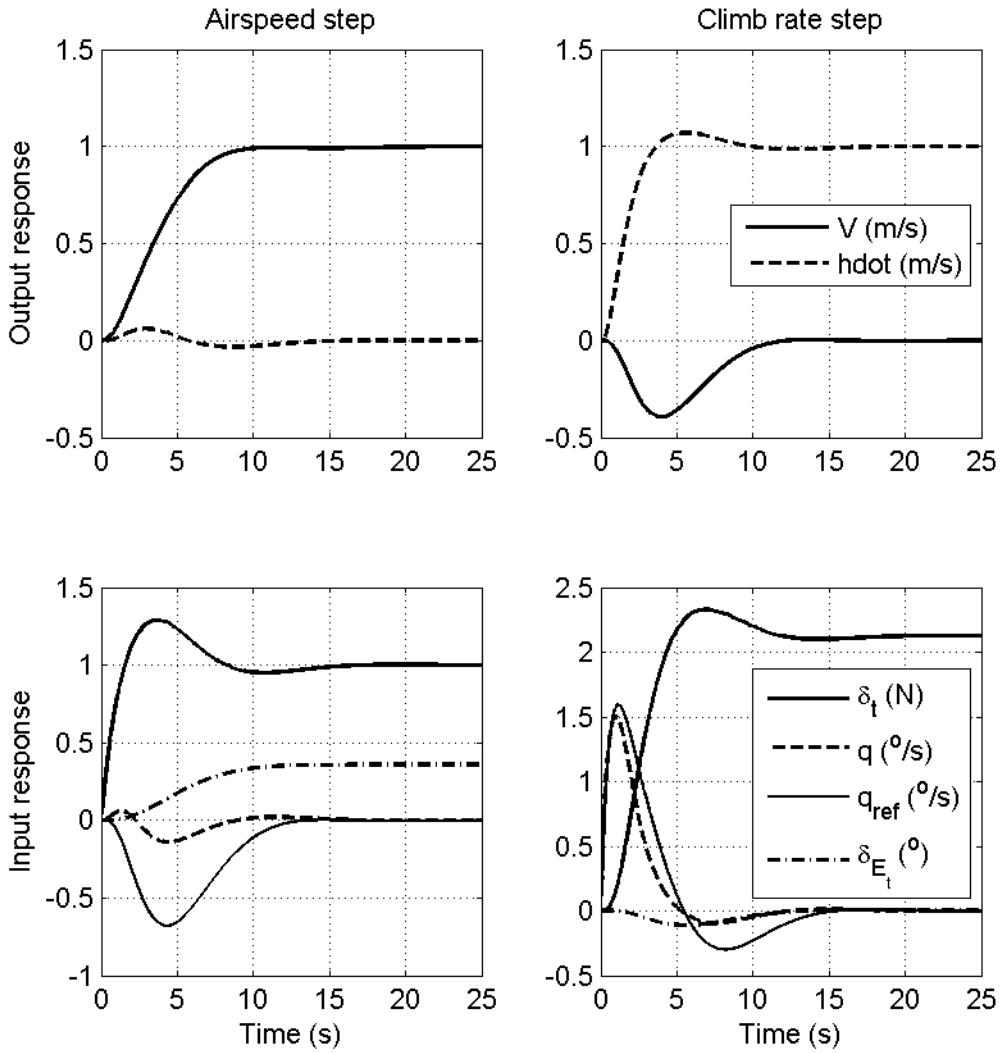

Figure 6.4.4: Response to airspeed and climb rate steps with the full aircraft dynamics and the pitch rate controller with ITEC

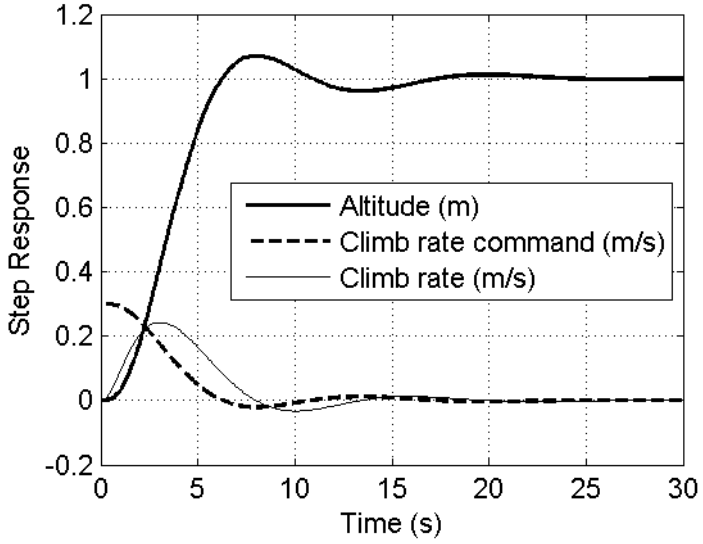

Figure 6.5.1: Response to an altitude step command

6.5 Altitude controller

A simple proportional control loop was added around the climb rate controller to allow the aircraft to follow and altitude command h_{ref}. Essentially, the control law consists of proportional altitude feedback to the climb rate command:

$$\dot{h}_{ref} = K_h(h_{ref} - h) \tag{6.5.1}$$

It was found that $K_h = 0.3$ produced an acceptable response, shown in Figure 6.5.1.

However, for a large altitude step command, this control law could command a larger climb rate than the aircraft can perform. Therefore the control law was modified using a saturation operator to enter the aircraft into a constant climb rate for large altitude step commands:

$$\dot{h}_{ref} = \text{sat}\Big(K_h(h_{ref} - h),\ \dot{h}_{max}\Big) \tag{6.5.2}$$

The saturation operator is defined as follows:

$$\text{sat}(x,\ a) = \begin{cases} -a & ; \quad x < a \\ x & ; \quad |x| \leq a \\ a & ; \quad x > a \end{cases} \tag{6.5.3}$$

It was found that the aircraft is able to climb or descend at 2 metres per second, and therefore this was used for the maximum climb rate. The saturation is a non-linearity in the control law, and therefore its effect on the response of the altitude controller is investigated in non-linear simulation in Chapter 7.

6.6 Effect of CG shifts on the closed-loop dynamics

This section analyses the effect of shifts in the centre of gravity on the closed-loop dynamics of the Variable Stability UAV with the control system designed in this chapter. The control system will be analysed with fixed parameters to provide a benchmark against which the adaptive control system can be compared to assess the effect of adaptation on fault tolerance.

The effect of CG shifts on the closed-loop behaviour will be analysed with different control loops enabled, using the CG shift equations of Section 3.4. For each control configuration, the effect of the CG position on the closed-loop poles and the responses to step commands and pitching moment disturbances are shown and discussed.

Pitching moment disturbances are included in the analysis since a shift in the CG will cause the aircraft to experience such a disturbance. These disturbances will act as an extra input to the time derivative of the pitch rate:

$$\begin{bmatrix} \dot{\hat{V}} \\ \dot{\alpha} \\ \dot{q} \\ \dot{\theta} \end{bmatrix} = A\mathbf{x} + B\mathbf{u} + \begin{bmatrix} 0 \\ 0 \\ \frac{1}{I_{yy}} \\ 0 \end{bmatrix} M_{dist} \tag{6.6.1}$$

where A, B, $\mathbf{x}$ and $\mathbf{u}$ are defined in Section 4.3.

Section 6.6.1 investigates the effect of CG shifts on the pitch rate controller, using the longitudinal rotational dynamics as the plant model, and Section 6.6.2 investigates the effect of CG shifts if the airspeed and climb rate controllers are armed, using the full longitudinal aircraft model. The analysis of these two configurations should indicate what effect CG shifts will have during fly-by-wire operation and autonomous flight respectively, if adaptation is not used.

The effects of CG shifts on the climb rate and altitude controllers are very similar, and therefore the altitude controller is not analysed in this section.

6.6.1 Effect on pitch rate control

The same pitch rate controller used in Section 6.2.2 was used in the analysis of CG shifts on the closed-loop dynamics. This controller uses pure pitch rate feedback in the MRC law, and an ITEC gain of 0.1.

Figure 6.6.1 shows the effect of CG shifts on the closed-loop poles of the pitch rate controller with ITEC. As the CG moves backwards, the complex poles converge towards the real axis. The frequency of the integrator pole increases until it meets the short period pole moving to the left on the real axis. Then these two poles break away and circle to the right, becoming unstable for a shift of about 75 mm.

Figure 6.6.2 shows the response of this pitch rate controller to step commands for a number of CG positions. As the CG moves backwards, the overshoot increases dramatically.

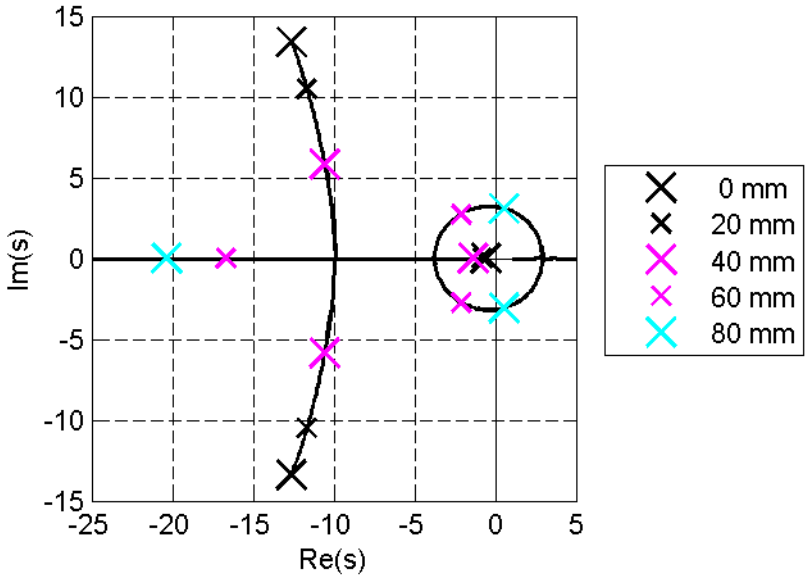

Figure 6.6.1: Effect of CG shifts on the closed-loop poles of the pitch rate controller with MRC and ITEC

Eventually the response becomes unstable, as would be expected from the pole movements of Figure 6.6.1.

Figure 6.6.3 shows how the rejection of a 1 Nm pitching moment disturbance by the ITEC law is affected by CG shifts. The use of integral control ensures that the constant disturbance does not cause a steady-state error in the stable responses. Once again the backward CG shift increases the magnitude of the transient response, until it destabilises the system.

These results show that sufficiently large CG shifts can destabilise the closed-loop system when a fixed-gain pitch rate controller is used.

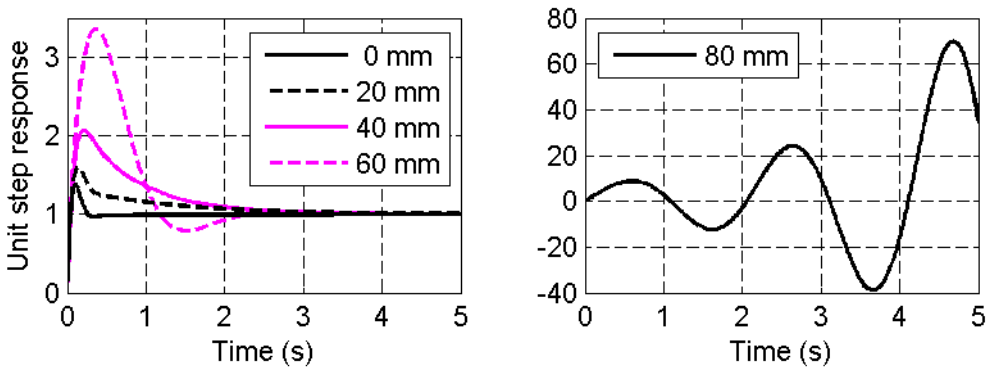

Figure 6.6.2: Effect of CG shifts on the step response of the pitch rate controller with MRC and ITEC

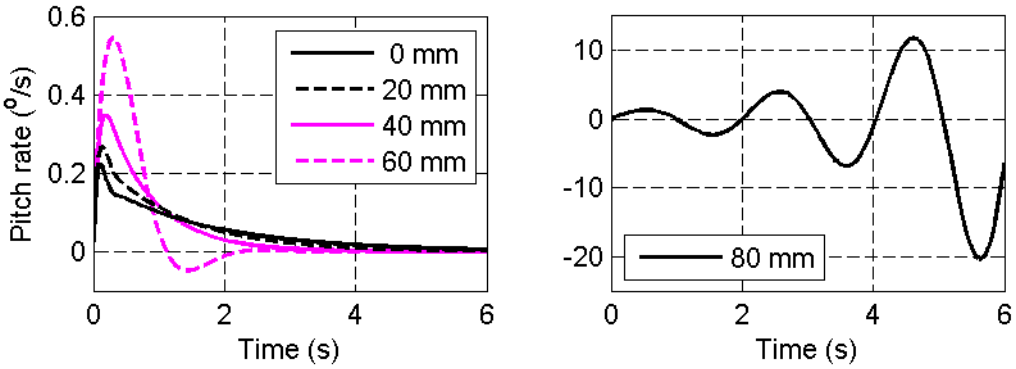

Figure 6.6.3: Effect of CG shifts on the response of the pitch rate controller with MRC and ITEC to a pitching moment disturbance of 1 Nm

6.6.2 Effect on airspeed and climb rate control

This section investigates the effect of shifts in the centre of gravity if the climb rate controller of Section 6.4 is used around the pitch rate controller of Section 6.2, along with the airspeed controller of Section 6.3. Since the airspeed dynamics are not seriously affected by CG shifts, only the climb rate response of the controller will be addressed in this section.

Figure 6.6.4 shows the effect of CG shifts on the closed-loop poles of the airspeed and climb rate controllers. The low-frequency poles of the kinematic controllers remain stable for all CG positions, but the short period poles move to the right from the locations where they were placed by the pitch rate controller, and become unstable for a backward shift of about 66 mm.

This confirms the tentative conclusion drawn from the linear analysis of the open-loop dynamics in Section 4.6. Clearly, the closed-loop poles of the short period mode and the pitch rate controller become unstable, while the fixed-gain kinematic controllers are able to keep the kinematics stable, and therefore the pitch rate controller should be made adaptive to keep the aircraft stable when the CG moves backwards.

Figures 6.6.5 and 6.6.6 show the climb rate responses of the control system to step commands and pitching moment disturbance steps for different CG positions. The damping of the disturbance response decreases dramatically as the CG shifts backwards, while the response to climb rate commands seems largely unaffected by CG shifts until the system becomes unstable.

The difference between the responses can be explained by investigating the closed-loop transfer function $G_{cl}(s)$ from climb rate command to climb rate, and the transfer function

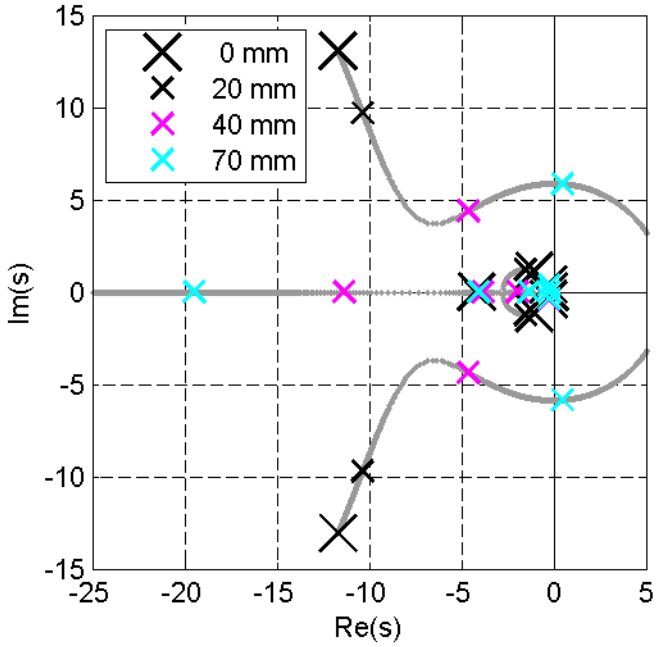

Figure 6.6.4: Effect of CG shifts on the closed-loop poles of the airspeed and climb rate controllers

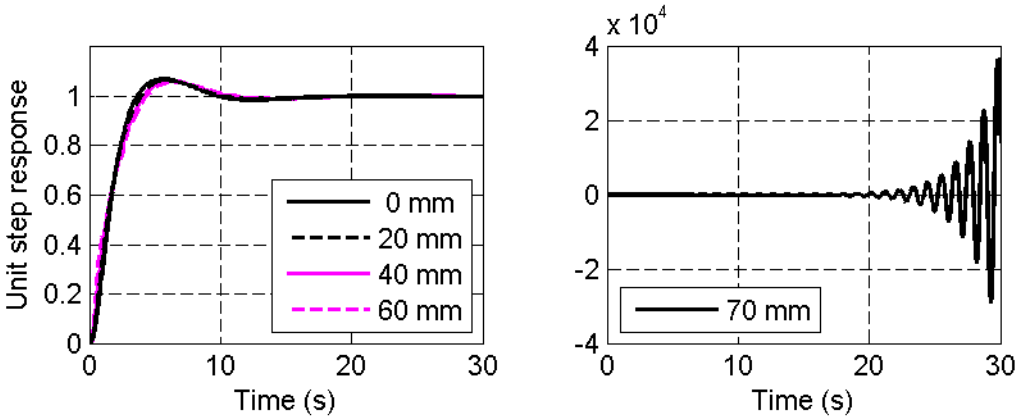

Figure 6.6.5: Effect of CG shifts on the response of the system to a climb rate step command

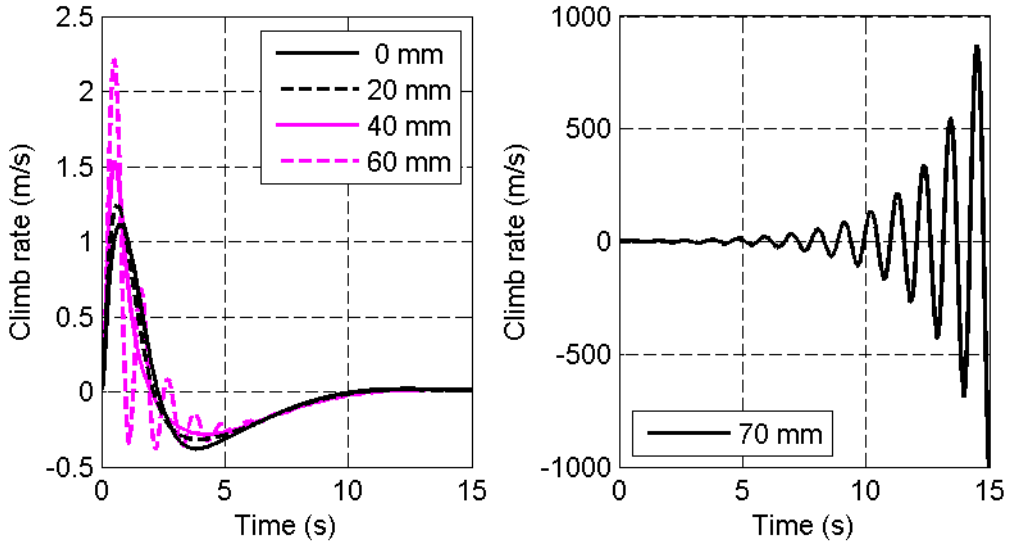

Figure 6.6.6: Effect of CG shifts on the climb rate response of the closed-loop system to a 1 Nm pitching moment disturbance step

$G_{dist}(s)$ from a pitching moment disturbance to climb rate:

$$G_{cl}(s) = \frac{\dot{h}(s)}{\dot{h}_{ref}(s)} \tag{6.6.2}$$

$$G_{dist}(s) = \frac{\dot{h}(s)}{M_{dist}(s)} \tag{6.6.3}$$

Figure 6.6.7 shows the low-frequency poles and zeroes of both these transfer functions for a 60 mm backward shift, which clearly displays poorly damped behaviour in response to a disturbance step, but not in response to a step command. The poorly damped behaviour is to be expected as a result of a pole pair at $s = -0.77 + 5.8j$, which is not visible in Figure 6.6.7.

Both transfer functions have the same four low-frequency poles, as well as a pair of complex zeroes at a low frequency. However, the transfer function from $\dot{h}_{ref}$ has only one other low-frequency zero, while the transfer function from M_d has two more zeroes at the origin.

The three zeroes in the transfer function from $\dot{h}_{ref}$ will largely cancel out three of the low-frequency poles of the first transfer function, which means that the net effect of the low-frequency poles and zeroes will be similar to a first-order low-pass filter, which will create significant cutoff at the frequency of the poorly damped poles, and therefore attenuate their contribution to the response to a step command.

However, in the transfer function from a pitching moment disturbance, the four low-frequency zeroes will largely cancel out all four low-frequency poles, and no such low-pass filtering effect will exist. The response of the lightly damped poles will not be attenuated, and therefore they will make a significant contribution to the response to a pitching moment disturbance step.

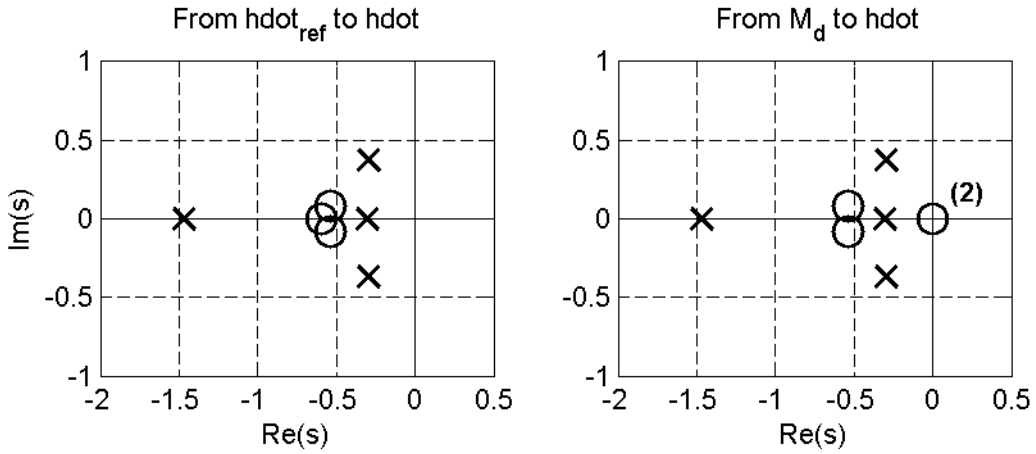

Figure 6.6.7: Low-frequency poles and zeroes of the transfer functions from climb rate command to climb rate and from pitching moment disturbance to climb rate with the CG shifted backwards by 60 mm

Figure 6.6.8 shows the magnitude plots of the Bode diagrams of both transfer functions. The transfer function from the pitching moment disturbance has a large peak at the frequency of the lightly damped poles, while this peak is attenuated by the low-pass filter behaviour at a lower frequency in the transfer function from a climb rate command.

These results show that backwards shifts in the centre of gravity can seriously affect the behaviour of a fixed-gain longitudinal control system, with the closed-loop dynamics becoming poorly damped or even unstable for sufficiently large shifts, even if the reduced stability is not immediately visible in the response of the aircraft to commands. Therefore the controller parameters would need to be adjusted to keep the closed loop system stable if the CG were to move due to in-flight damage.

6.7 Effect of adjusting the MRC parameters when the aircraft is unstable

Section 6.6 investigated the behaviour of the control system with constant parameters and the CG in different positions. In this section, the CG will be assumed to be in the unstable backward position, and the response of the system with different MRC parameters will be investigated using linear tools. This should indicate how the adaptive laws of Chapter 5 would have to adjust the MRC parameters to re-stabilise the aircraft after a CG shift.

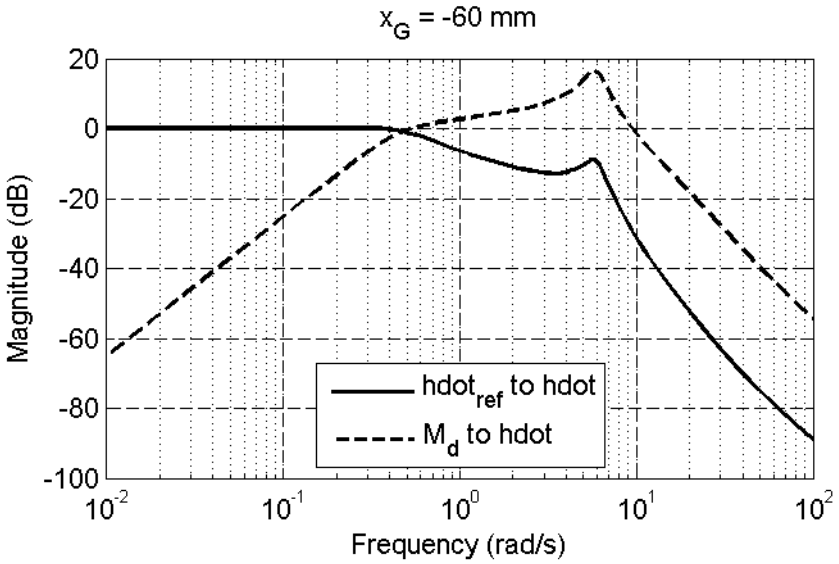

Figure 6.6.8: Bode magnitude plots of the transfer functions from climb rate command to climb rate and from pitching moment disturbance to climb rate with the CG shifted backwards by 60 mm

6.7.1 Effect on pitch rate control

Figure 6.7.1 shows the movements of the closed-loop poles of the rotational dynamics and the pitch rate controller when the CG is in the backward position ($x_{_G} = -80$ mm) and the feedback gain θ_3 is changed. The same nominal pitch rate controller is used as in Section 6.6.

If θ_3 has the nominal value of 0.026 or less, the system is unstable. Increasing θ_3 moves the unstable poles to the left, and the system becomes stable if a feedback gain of $\theta_3 = 0.037$ is used. The feed-forward gain c_0 has no effect on the closed-loop poles of the pitch rate controller – it only affects the gain in response to pitch rate commands.

6.7.2 Effect on airspeed and climb rate control

Figures 6.7.2 and 6.7.3 show the root loci of the loops through θ_3 and c_0 when the airspeed and climb rate control loops are closed around the pitch rate controller with the CG at $x_{_G} = -80$ mm.

Once again, the short period poles are unstable if θ_3 has its nominal value or less, but move to the left if θ_3 is increased. A feedback gain $\theta_3 = 0.058$ will stabilise the system, while $\theta_3 = 0.145$ will give the short period poles optimal damping. However, the system cannot be stabilised by adjusting c_0 positively or negatively.

These results seem to indicate that, in order for the adaptive control system to re-stabilise the aircraft when the CG moves backwards, the adaptive law must increase the feedback gain θ_3. The actual behaviour of the adaptive control system must be tested in non-linear simulation to determine if this is what it will do.

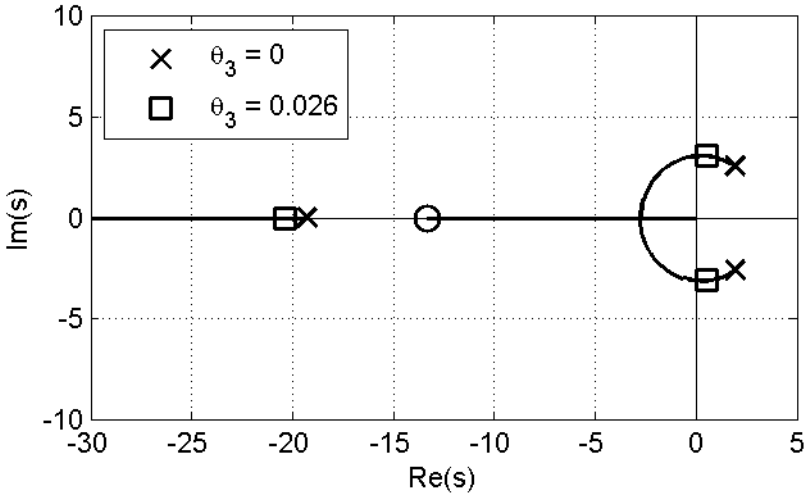

Figure 6.7.1: Root locus of θ_3 when the pitch rate controller with ITEC is used, and the CG is at $x_G = -80$ mm

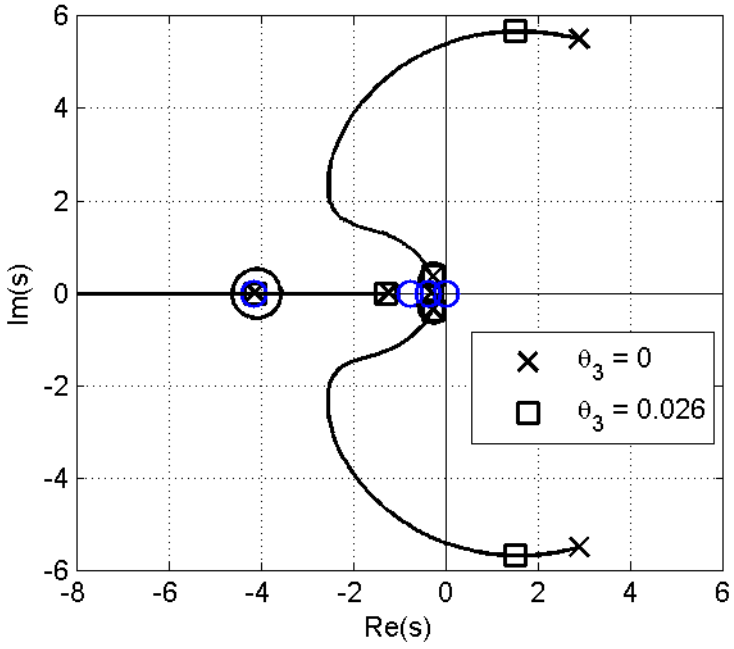

Figure 6.7.2: Root locus of θ_3 with the climb rate controller armed and the CG at $x_G = -80$ mm

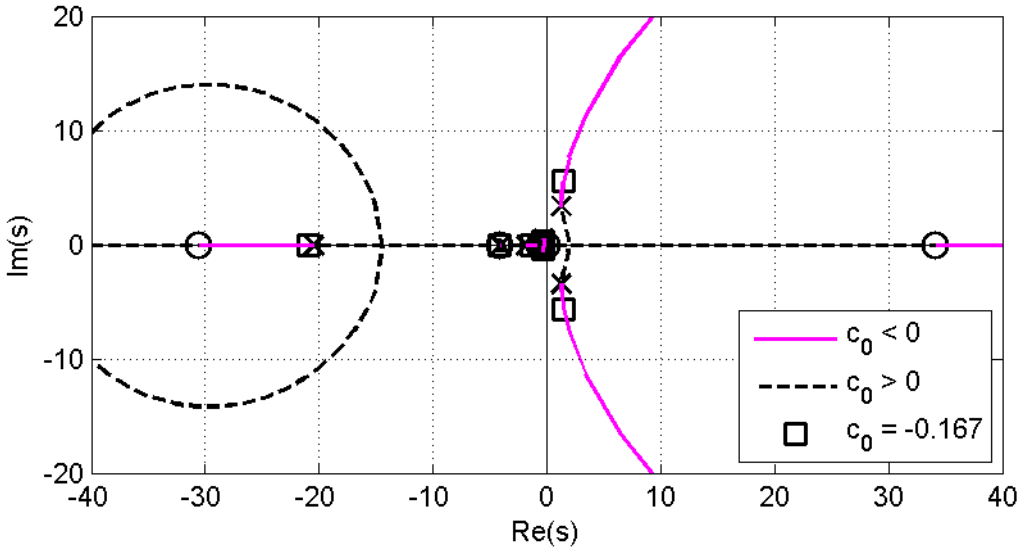

Figure 6.7.3: Root locus of c_0 with the climb rate controller armed and the CG at $x_G = -80$ mm

However, if a control system is stable for some range of a constant parameter, it does not imply that an adaptive control system will be stable if that parameter varies within the same range [39]. Therefore, even if the adaptive law increases the feedback gain, non-linear simulation must show if this does in fact stabilise the system.

6.8 Summary

This chapter described the design of a fixed-gain control system for the Variable Stability UAV, on which an adaptive control system can be based. A pitch rate controller was designed in the inner loop to control the short period mode of the aircraft dynamics. This controller consists of a model reference control (MRC) law, which can be used with fixed parameters or as part of a model reference adaptive control (MRAC) system, and an integral trim elevator control (ITEC) law, which was added to eliminate steady-state errors due to pitching moment disturbances. Airspeed, climb rate and altitude controllers were designed around the pitch rate controller to control the longitudinal kinematics of the aircraft. The control laws comprising the control system are summarised in Table 6.1.

The equations of Section 3.4 were used to investigate the effect of shifts in the centre of gravity on the closed-loop dynamics of the aircraft in both fly-by-wire operation and autonomous flight. In both cases it was found that CG shifts can seriously affect the response of the control system to commands and disturbances, and that sufficiently large shifts will

Airspeed controller	$\dot{x}_v$	=	$\bar{V}_{ref} - \bar{V}$
	δ_t	=	$-K_{pv}\bar{V} - K_{iv}x_v$
Pitch rate controller	δ_e	=	$\frac{\theta_1}{s+\lambda}\delta_e + \frac{\theta_2}{s+\lambda}q + \theta_3 q + c_0 q_{ref}$
	$\dot{\delta}_{E_t}$	=	$K_i(q_{ref} - q)$
	δ_E	=	$\delta_e + \delta_{E_t}$
Climb rate controller	$\dot{x}_{\dot{h}}$	=	$\dot{h}_{ref} - \dot{h}$
	q_{ref}	=	$-K_{p\dot{h}}\dot{h} - K_{i\dot{h}}x_{\dot{h}}$
Altitude controller	$\dot{h}_{ref}$	=	$\text{sat}\Big(K_h(h_{ref} - h),\ \dot{h}_{max}\Big)$

Table 6.1: Summary of the longitudinal control system

destabilise the closed-loop system if adaptation is not used. The effect of varying the MRC parameters when the aircraft is unstable was also investigated, and this indicated that increasing the feedback gain of the pitch rate controller should be able to re-stabilise the closed-loop system in both modes of operation.

In Chapter 7, the control system which was designed and analysed using linear tools in this chapter is investigated further in non-linear simulation, which includes the effect of CG shifts, as well as adjusting the parameters of the pitch rate controller using the adaptive laws of Chapter 5 in an MRAC system. This will allow the handling of shifts in the centre of gravity by the adaptive control system to be investigated, which should provide insight into the effect of adaptation on the fault tolerance of the control system.

Chapter 7

Non-linear simulation

In Chapter 6, a fixed-gain longitudinal control system was designed around the linear model of the Variable Stability UAV which was given in Chapter 4. The aircraft and control system were analysed using linear tools to determine how the closed-loop dynamics will be affected by shifts in the centre of gravity, as an example of a failure case which can seriously affect the aircraft dynamics.

This control system includes an MRC law in the pitch rate controller, which can be combined with a reference model and one of the adaptive laws of Chapter 5 to form a model reference adaptive control system. This would make the control system non-linear, and therefore the behaviour of the adaptive control system cannot be analysed using linear tools. Also, linear analysis cannot be used to investigate the effect of gradual CG shifts, since these make the aircraft model time-varying.

This chapter describes non-linear simulations that were done using the non-linear aircraft model of Chapter 3, the longitudinal control system of Chapter 6 and the adaptive laws of Chapter 5. The primary goal of the simulations is to investigate the fault tolerance of the adaptive control system, particularly its handling of instantaneous damage-induced shifts in the centre of gravity of the aircraft. A secondary goal is to evaluate the adaptive control system as a solution to the variable stability problem by simulating gradual CG shifts.

Section 7.1 describes the simulation environment that was used, including the implementation of the aircraft model and the control system, as well as the controller parameters that were used, and Section 7.2 discusses the different variations of the adaptive law that were used.

Section 7.3 shows the response of the non-linear aircraft model and control system in normal operating conditions, and Section 7.4 investigates the response of the control system to instant shifts in the centre of gravity. Section 7.5 analyses the effect of measurement noise on the adaptive control system, and evaluates techniques to improve its noise tolerance. Finally, Section 7.6 investigates the response of the adaptive control system to gradual shifts in the centre of gravity.

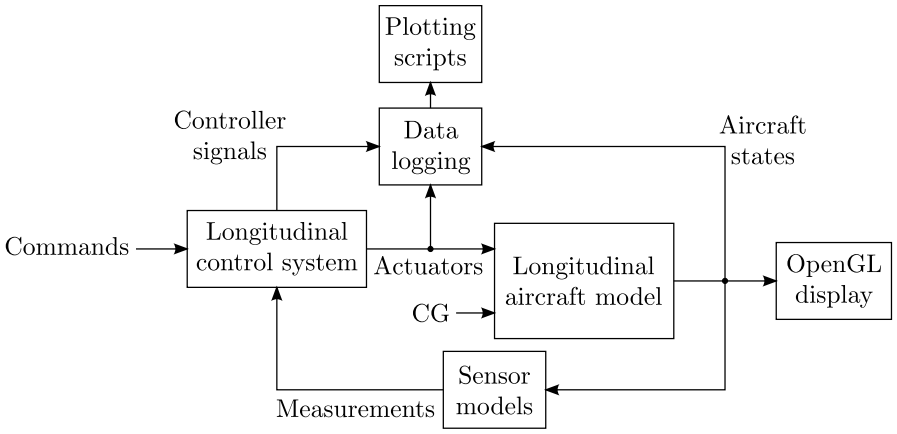

Figure 7.1.1: Block diagram of the pure software simulation

7.1 Simulation environment

7.1.1 Software and HIL simulation environments

Two different simulation environments were used to test the adaptive control system. Firstly, a pure software simulation was used, where the longitudinal control system and the non-linear longitudinal aircraft model were both implemented in Simulink. This simulation also included sensor models, data logging and an OpenGL interface which allowed simulations to be displayed using 3D graphics. A block diagram of this simulation is shown in Figure 7.1.1.

Secondly, a hardware-in-the-loop (HIL) simulation was used, where the control system was implemented on the avionics of the Variable Stability UAV, and a Simulink model of the full non-linear aircraft model was used. The avionics were connected to the PC through HIL interface hardware, which connected to the PC through USB and to the avionics through a CAN bus. The ground station hardware and software and a remote control (RC) transmitter, which were used for flight tests, were also used for these simulations. A block diagram of this simulation is shown in Figure 7.1.2.

The 3D graphics software was developed at Stellenbosch University, and allows flight tests to be simulated visually, which is a vital step in the preparation for a flight test, since it allows an intuitive assessment of the behaviour of a controller. A screen shot of the software is shown in Figure 7.1.3.

In both simulation environments, the equations of Section 3.4 were used to model the effect of CG shifts on the aircraft parameters. The results of the HIL simulations were very similar to those of the pure software simulations, and therefore only the latter are shown in this chapter. The HIL simulations were only used in preparation for the flight tests, as described in Section 8.1. The rest of this section describes the software simulation environment in further detail.

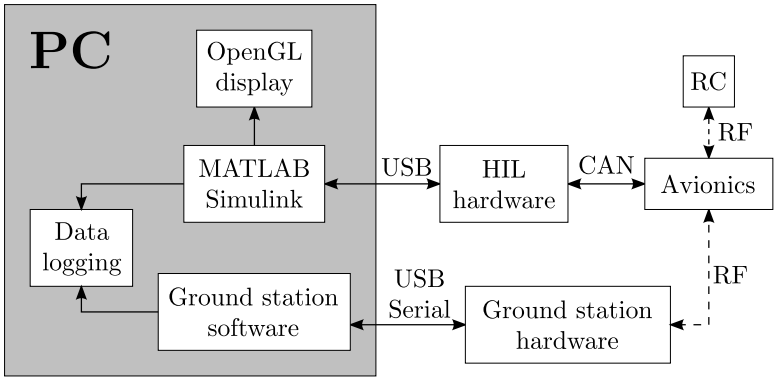

Figure 7.1.2: Block diagram of the HIL simulation

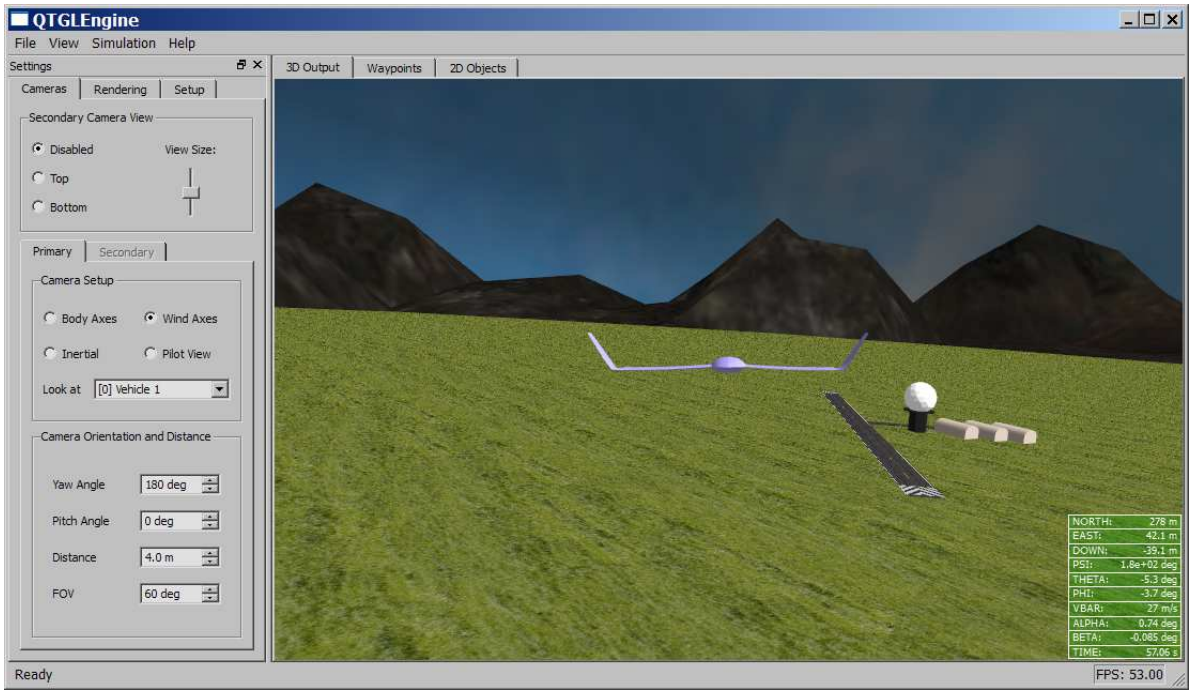

Figure 7.1.3: The OpenGL engine displaying a HIL simulation

7.1.2 Aircraft model and control system implementation

The non-linear aircraft model of Chapter 3 was implemented in Simulink using two continuous-time S-functions – one for the six degrees of freedom equations of motion of Section 3.2, and one for the force and moment model described in Section 3.3. The force and moment model also includes the effect of shifts in the centre of gravity, using the equations derived in Section 3.4.

The control system was implemented using Simulink blocks. Since the control system was designed in continuous time, but was meant to be implemented discretely on the avionics of the Variable Stability UAV, all continuous integrators were replaced by discrete Euler integrators with a sample time of 20 milliseconds:

$$\frac{1}{s} \Rightarrow \frac{0.02}{z-1} \tag{7.1.1}$$

7.1.3 Controller parameters

The non-linear simulations used the same controller parameters that were used in the linear analysis of the effect of CG shifts in Section 6.6. Only proportional pitch rate feedback was used for the MRC law, with the parameters initialised to the following values:

$$\boldsymbol{\theta}_0 = \begin{bmatrix} \theta_1 \\ \theta_2 \\ \theta_3 \\ c_0 \end{bmatrix} = \begin{bmatrix} 0 \\ 0 \\ 0.026 \\ -0.167 \end{bmatrix} \tag{7.1.2}$$

Using these parameters with the plant transfer function of Equation 4.5.5 yields the following closed-loop transfer function, which was used as the reference model for the MRAC system:

$$W_m(s) = \frac{34.7s + 333.4}{s^2 + 25.8s + 333.4} \tag{7.1.3}$$

In simulations where ITEC was enabled, the value $K_i = -0.1$ was used for the ITEC gain, since this value was found to adjust the trim elevator setting at a sufficient rate without seriously affecting the transient response of the pitch rate controller, as shown in Section 6.2.2.

The following parameters were used for the outer loop controllers in all simulations:

$$[K_{pv} \;\; K_{iv}] = [2.76 \;\; -0.975] \tag{7.1.4}$$

$$[K_{p\dot{h}} \;\; K_{i\dot{h}}] = [0.079 \;\; -0.056] \tag{7.1.5}$$

$$K_h = 0.3 \tag{7.1.6}$$

$$\dot{h}_{max} = 2 \text{ m/s} \tag{7.1.7}$$

7.2 Adaptive laws

This section shows how the adaptive laws of Chapter 5 were applied to the pitch rate control problem, and describes the different variations of the adaptive law that were used for the simulations in this chapter.

Simulations were done with both the normalised and unnormalised adaptive laws of Chapter 5. However it was found that, in simulations with normalised adaptive law, the normalising signal stayed very close to unity, and therefore the results of these simulations were nearly identical to those of simulations with the corresponding unnormalised adaptive laws.

Since normalisation seemed to have very little effect, and as argued in Section 5.4.4 was not expected to be very effective for this project, the normalised adaptive laws are not described in this section, and their simulation results are not shown in this chapter. Techniques to increase the effect of normalisation could be investigated, but it was decided to focus on a thorough investigation of the unnormalised adaptive laws instead.

7.2.1 Basic adaptive law

In Chapter 5, it was shown that the following adaptive law will yield a stable closed-loop system when used to adjust the parameters of an MRC law:

$$\dot{\boldsymbol{\theta}} = -\Gamma e_1 \boldsymbol{\omega} \operatorname{sgn}(k_p/k_m) \tag{7.2.1}$$

Since $k_p < 0$ and $k_m > 0$ for the pitch rate controller, the adaptive law becomes:

$$\dot{\boldsymbol{\theta}} = \Gamma e_1 \boldsymbol{\omega} \tag{7.2.2}$$

$$\begin{bmatrix} \dot{\theta}_1 \\ \dot{\theta}_2 \\ \dot{\theta}_3 \\ \dot{c}_0 \end{bmatrix} = \Gamma e_1 \begin{bmatrix} \theta_1 \\ \theta_2 \\ \theta_3 \\ c_0 \end{bmatrix} \tag{7.2.3}$$

The adaptive gain matrix Γ was chosen so that θ_1 and θ_2 will not be adapted from zero:

$$\Gamma = \begin{bmatrix} 0 & 0 & 0 & 0 \\ 0 & 0 & 0 & 0 \\ 0 & 0 & \gamma & 0 \\ 0 & 0 & 0 & \gamma \end{bmatrix} \tag{7.2.4}$$

Then the adaptive law reduces to:

$$\begin{aligned} \dot{\theta}_3 &= \gamma e_1 q \\ \dot{c}_0 &= \gamma e_1 q_{ref} \end{aligned} \tag{7.2.5}$$

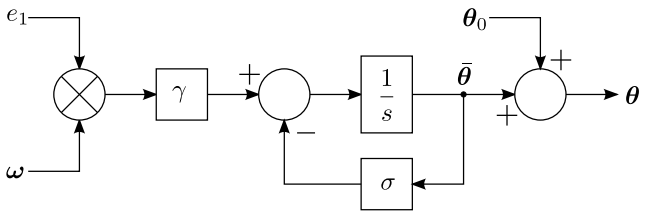

Figure 7.2.1: Unnormalised adaptive law with leakage

where $\gamma > 0$ is the scalar adaptive gain.

This adaptive law forms the basis for two variations which will also be used in this chapter: an adaptive law with leakage and an adaptive law with a dead zone. These two variations will be described in the following sections.

7.2.2 Leakage

The leakage modification described in Section 5.4.2 was applied to the unnormalised adaptive law for some simulations in this chapter, so that the controller parameters are drawn back to their initial values in order to prevent parameter drift. The fixed-σ modification technique was used in the adaptive law for the pitch rate controller:

$$\dot{\boldsymbol{\theta}} = \gamma e_1 \boldsymbol{\omega} - \sigma(\boldsymbol{\theta} - \boldsymbol{\theta}_0) \tag{7.2.6}$$

where $\sigma > 0$ is a constant called the *leakage gain*. If $\sigma = 0$, this adaptive law reduces to the basic adaptive law of Equation 7.2.5.

If $\bar{\boldsymbol{\theta}}$ is defined as the deviation of the adapted parameter vector from its initial value, then the adaptive law can be rewritten in the following form, shown as a block diagram in Figure 7.2.1:

$$\bar{\boldsymbol{\theta}} = \boldsymbol{\theta} - \boldsymbol{\theta}_0 \tag{7.2.7}$$

$$\dot{\bar{\boldsymbol{\theta}}} = \gamma e_1 \boldsymbol{\omega} - \sigma \bar{\boldsymbol{\theta}} \tag{7.2.8}$$

Then the adaptive law can be written as a transfer function from the product $e_1\boldsymbol{\omega}$ to $\boldsymbol{\theta}$:

$$\therefore \boldsymbol{\theta} = \boldsymbol{\theta}_0 + \frac{\gamma}{s+\sigma}(e_1\boldsymbol{\omega}) \tag{7.2.9}$$

where the adaptive law without leakage can be written as:

$$\boldsymbol{\theta} = \boldsymbol{\theta}_0 + \frac{\gamma}{s}(e_1\boldsymbol{\omega}) \tag{7.2.10}$$

Using leakage in this way, the integrator in the unnormalised adaptive law is replaced by a first-order low-pass filter. If the bandwidth of this filter is low compared to the error bandwidth, i.e. if the leakage gain is small, then a persistent pitch rate error will cause the parameters to drift from their initial values to a new steady-state value, with the distance that they drift proportional to the average of the product $e_1\boldsymbol{\omega}$.

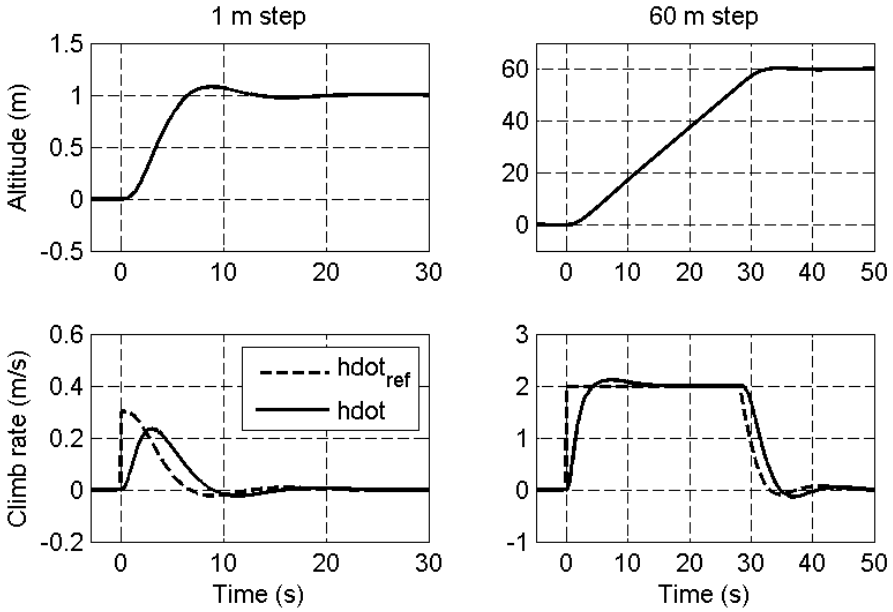

Figure 7.3.1: Response of the altitude controller to step commands in non-linear simulation

7.2.3 Dead zone

An adaptive law with a dead zone, as described in Section 5.4.3, was also used for simulations in this chapter. The two nonzero MRC parameters are adjusted as follows:

$$\begin{aligned} \dot{\theta}_3 &= \gamma e_1' q \\ \dot{c}_0 &= \gamma e_1' q_{ref} \end{aligned} \tag{7.2.11}$$

where e_1' is defined as

$$e_1' = \begin{cases} e_1 + g_0 & ; \quad e_1 < -g_0 \\ 0 & ; \quad |e_1| \leq g_0 \\ e_1 - g_0 & ; \quad e_1 > g_0 \end{cases} \tag{7.2.12}$$

Then the two parameters will only be adapted if $|e_1| > g_0$.

7.3 Nominal response

As mentioned in Section 6.5, the limiting of the climb rate command generated by the altitude controller makes this controller non-linear, and therefore its response must be investigated in non-linear simulation. Figure 7.3.1 shows the response of the altitude controller to altitude step commands of 1 metre and 60 metres when the full non-linear aircraft model is used.

For a 1 metre step, the climb rate command never reaches the 2 m/s limit, and the response is very similar to the linear response shown in Section 6.5. For a 60 metre step, the climb rate command is limited at 2 m/s for a period long enough that the climb rate settles

there, and so the aircraft performs most of the altitude step at a constant climb rate. Therefore the altitude controller performs as designed in non-linear simulation.

7.4 Response to instant CG shifts

The adaptive control system was primarily designed to handle shifts in the centre of gravity of the aircraft. If this shift is caused by in-flight damage, then it is likely to happen very quickly, and therefore this section investigates the effect of adaptation on the response of the control system to instantaneous CG shifts.

The purpose of the adaptive control system is to prevent the loss of the aircraft when a failure occurs. To do this, the adaptive controller must firstly re-stabilise the aircraft if it becomes unstable, and secondly it must prevent the aircraft from entering an unsafe flight condition, such as a high angle of attack which would stall the aircraft. The linearised aerodynamic model of Section 3.3.3 does not include any stall effects, but the aircraft is likely to stall if the angle of attack exceeds about 10 degrees.

Another factor to be considered in evaluating the performance of the adaptive control system is the response of the adapted controller parameters. Ideally, the parameters should adapt to the change in the aircraft dynamics and then settle at new values, which should yield a closed-loop behaviour as close as possible to the behaviour of the system prior to the CG shift and adaptation. At the very least, the parameters should settle at values where all the closed-loop poles are stable and well damped, in which case the closed-loop behaviour should be acceptable.

7.4.1 Response without adaptation

In order to investigate the effect of adaptation on the response of the control system to CG shifts, the control system must first be tested in simulation without adaptation, which means that the MRC parameters will be constant.

Figure 7.4.1 shows the pitch angle and angle of attack responses of the fixed-gain control system to instantaneous backward CG shifts of various distances. The system remains stable for shifts up to 60 mm, but for a 60 mm shift the response is very poorly damped. The angle of attack peaks just over 6 degrees for this shift, which is unlikely to stall the aircraft.

For a shift of 67 mm, the system is unstable, and the aircraft oscillates with a slowly growing magnitude. The angle of attack reaches a value which would probably stall the aircraft within seconds of the shift. For larger shifts, the system becomes violently unstable as soon as the shift takes place.

These results are consistent with the linear analysis done in Section 6.6.2, where the poles of the closed-loop system became unstable for shifts greater than 66 mm.

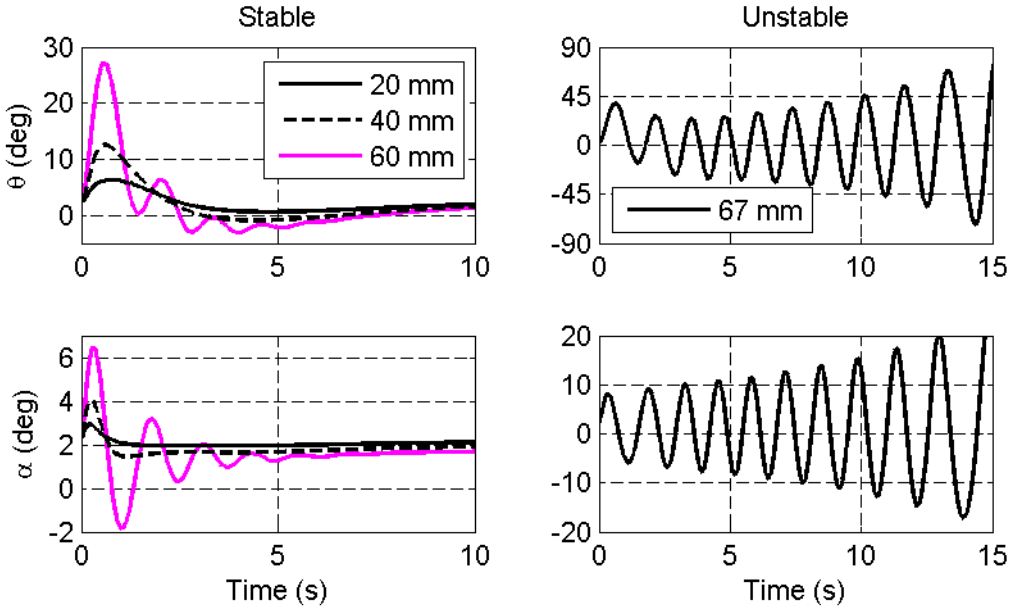

Figure 7.4.1: Response of the altitude controller to CG shifts of various distances with adaptation disabled

7.4.2 Response with adaptation enabled and ITEC disabled

This section investigates the effect of adaptation on the response of the control system to instant CG shifts. Since the ITEC law was added to the pitch rate controller with adaptation in mind, the system will be simulated with and without ITEC to investigate its effect on the adaptive control system.

Figure 7.4.2 shows the response of the adaptive control system to an 80 mm backward CG shift, which would make the fixed-gain control system unstable. The adaptive law of Equation 7.2.5 was used with different adaptive gains, and ITEC was disabled for these simulations.

The CG shift causes a pitching moment disturbance, which excites the unstable dynamics and causes the aircraft to oscillate. The resulting pitch rate error causes the controller parameters to be adapted, which re-stabilises the aircraft, and the oscillations fade away. Increasing the adaptive gain increases the rate at which the parameters are adapted, and decreases the amount of transient oscillation caused by the CG shift.

When an adaptive gain of $\gamma = 0.01$ is used, the aircraft experiences quite a large oscillation before stabilising. The angle of attack peaks at about 12 degrees, which would probably stall the aircraft in practice. However, using values of $\gamma = 10$, $\gamma = 1$ and possibly $\gamma = 0.1$ will keep the angle of attack small enough and prevent the aircraft from stalling.

From Figure 7.4.2 it seems that increasing the adaptive gain improves the performance of the adaptive control system in handling CG shifts. However, there is an upper limit on the adaptive gain. Figure 7.4.3 shows the response of the system to a 40 mm shift, which does

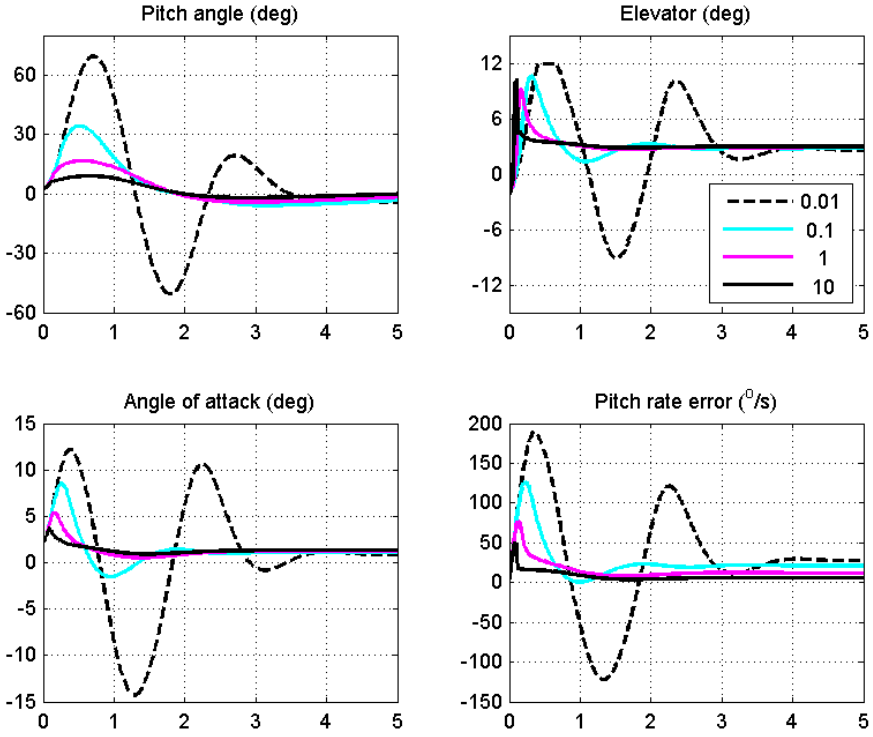

Figure 7.4.2: Response of the adaptive control system without ITEC to an 80 mm backward CG shift with different values of the adaptive gain γ

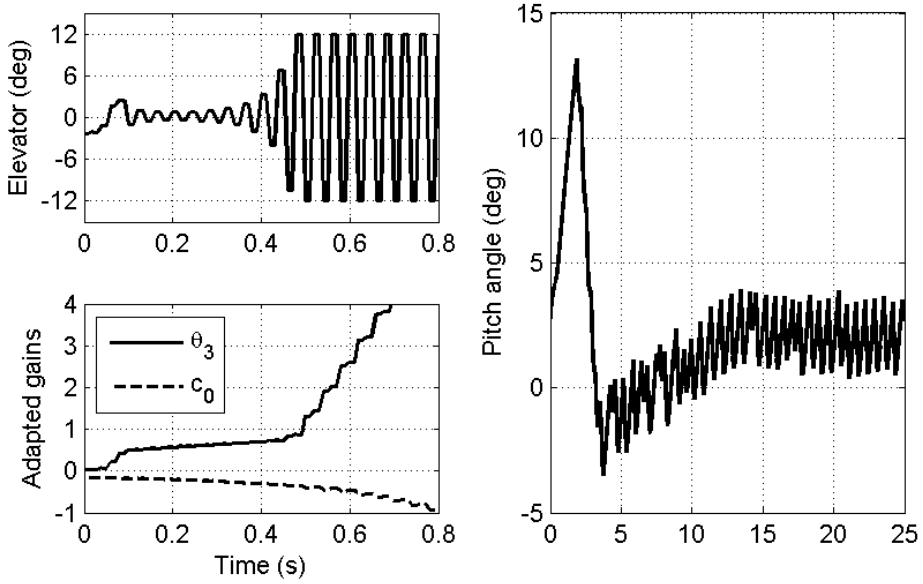

Figure 7.4.3: Response of the adaptive control system without ITEC to a 40 mm backward CG shift with an adaptive gain $\gamma = 100$

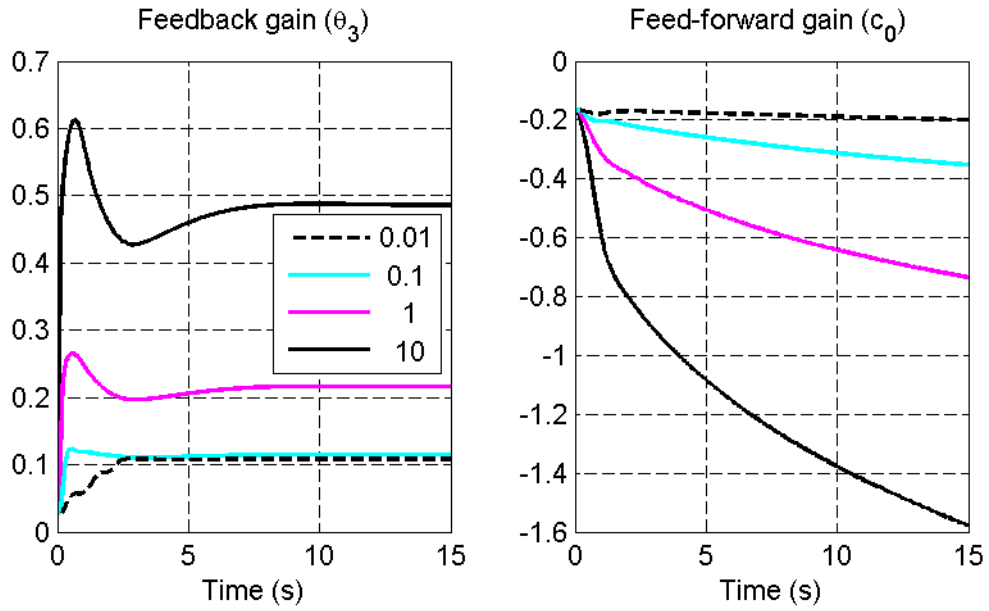

Figure 7.4.4: Response of the adaptive control system without ITEC to an 80 mm backward CG shift with different values of the adaptive gain γ

not destabilise the fixed-gain control system, if an adaptive gain of $\gamma = 100$ is used.

In this case, it can be seen from the elevator response that the system becomes unstable after about 0.2 seconds. The elevator oscillates with a growing amplitude until it saturates at 12 degrees and the system enters a limit cycle.

This unstable behaviour is caused by a phenomenon known as *stiffness*. When a differential equation is solved through numerical integration, it can become stiff if the derivative in the equation depends strongly on the solution, and the sample rate is slow compared to the system dynamics. In this case, if the adaptive gain is large, the derivatives of the controller parameters depend strongly on the signals in the control system (q, q_{ref}, e_1 etc.), which in turn depend strongly on the controller parameters themselves. The concept of stiffness is discussed in more detail in Appendix B.3.

The simulation results in this section show that adapting the parameters of the MRC pitch rate controller with an appropriate adaptive gain can stabilise the response of the aircraft if the closed-loop system is destabilised by a backward CG shift. However, the effect of the CG shift on the adapted parameters must also be investigated.

Figure 7.4.4 shows the effect of the different adaptive gains on the adapted parameters of the pitch rate controller for the same 80 mm shift. In each case, the feedback gain θ_3 settles at a new value, but the feed-forward gain c_0 keeps drifting. This can be explained though an inspection of the adaptive law:

$$\begin{bmatrix} \dot{\theta}_3 \\ \dot{c}_0 \end{bmatrix} = \gamma e_1 \begin{bmatrix} q \\ q_{ref} \end{bmatrix} \tag{7.4.1}$$

In the steady-state, the climb rate controller uses a non-zero pitch rate command Q_0 to counter the pitching moment disturbance caused by the CG shift and maintain a zero pitch rate. Therefore, in the steady state:

$$q = 0 \tag{7.4.2}$$

$$q_{ref} = y_m = Q_0 \tag{7.4.3}$$

$$e_1 = q - y_m = -Q_0 \tag{7.4.4}$$

and therefore

$$\dot{\theta}_3 = \gamma e_1 q = 0 \tag{7.4.5}$$

$$\dot{c}_0 = \gamma e_1 q_{ref} = -\gamma Q_0^2 \tag{7.4.6}$$

Therefore θ_3 will settle at a new value after a shift, while c_0 will continue to grow more negative. As the magnitude of c_0 increases, that of the required pitch rate command will decrease. Over time, the command will very slowly tend towards zero, while c_0 will keep drifting towards negative infinity.

The values of the controller parameters and the position of the CG at any point in time can be used in a linear analysis of the closed-loop system, similar to what was done in Chapter 6. Since the adaptive control system is non-linear and time-varying, this will not yield a true representation of the system while the parameters are changing. However, if the rate of change of the parameters is slow compared to the bandwidth of the pitch rate controller, then they can be assumed constant over small time intervals, and the resulting linear system will provide a reasonable approximation of the true system behaviour. Then this linear analysis can provide insight into the effect of adaptation on the system dynamics.

This analysis was done using the time-varying controller parameters for an 80 mm shift with an adaptive gain of $\gamma = 10$, and the resulting movements of the closed-loop poles in the first 100 seconds after the shift are shown in Figure 7.4.5. The CG shift moves the short period poles into the right half-plane, but they are stabilised by the adaptive law within two 20 ms integration time steps. As θ_3 settles and c_0 increases in magnitude, the poles move away from the real axis, which will lead to poorly damped behaviour.

These results show that, even though the adaptive control system is able to stabilise the aircraft when the CG shifts backwards, it suffers from parameter drift due to the pitching moment disturbance. This confirms the need for some form of integral control to ensure a zero steady-state pitch rate error, and therefore Section 7.4.3 investigates the effect of adding an ITEC law to the adaptive pitch rate controller in order to eliminate parameter drift

7.4.3 Response with adaptation and ITEC enabled

Figure 7.4.6 shows the response of the control system to instantaneous CG shifts of various distances if ITEC is enabled with a gain of $K_i = -0.1$, and adaptation is enabled with an

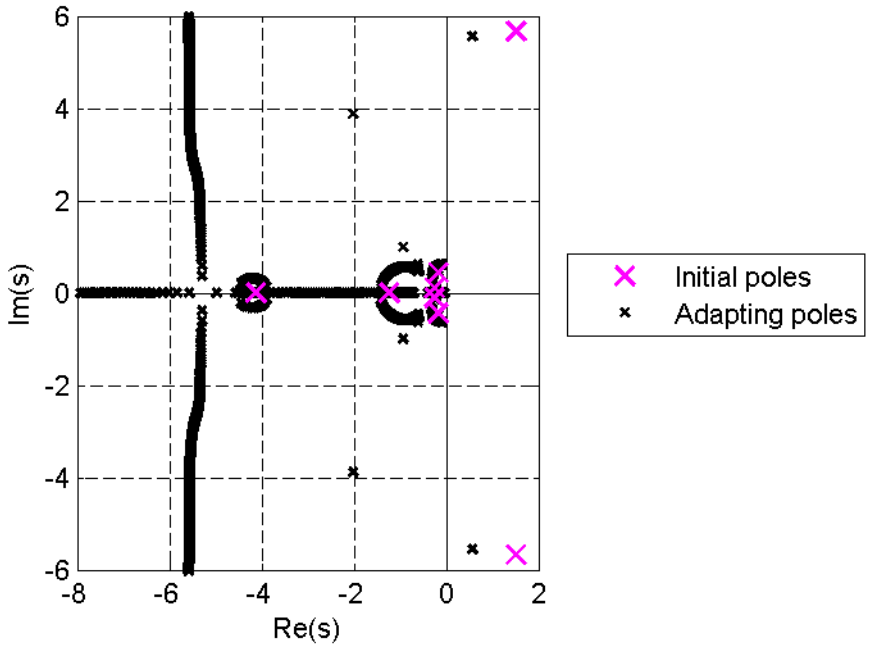

Figure 7.4.5: Movement of closed-loop poles as the MRC parameters are adapted for an 80 mm shift if ITEC is not used

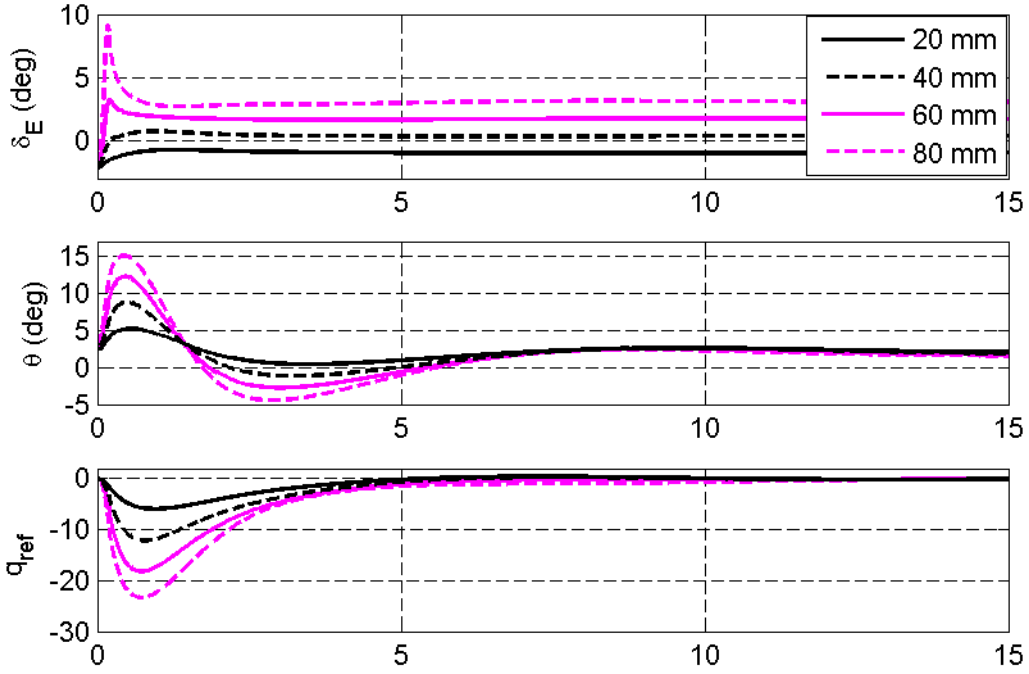

Figure 7.4.6: Response to different CG shifts with adaptation and ITEC enabled

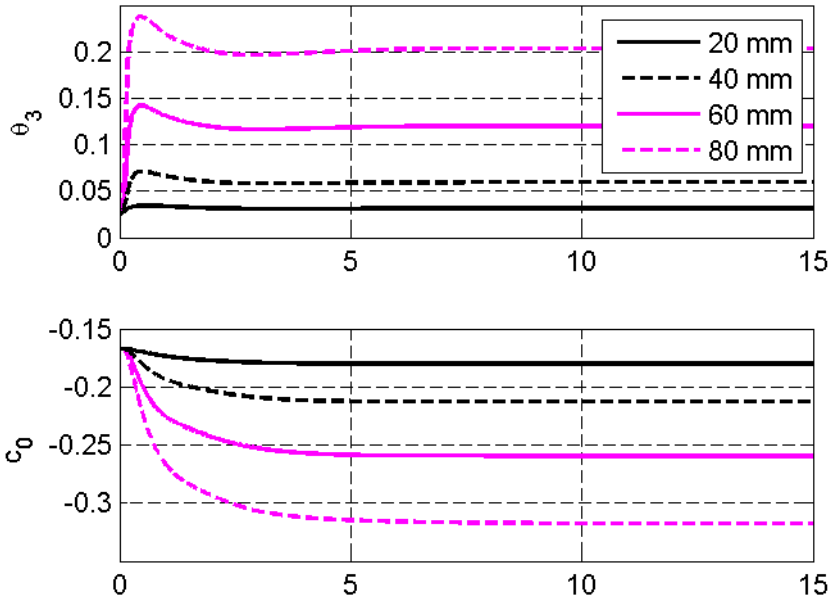

Figure 7.4.7: Response of the adapted control gains to different CG shifts with ITEC enabled

adaptive gain of $\gamma = 1$. In each case, the aircraft experiences a transient response due to the pitching moment disturbance, and the adaptive controller ensures that the response is stable and well damped, as was the case when ITEC was disabled. However, the use of ITEC ensures that no steady-state pitch rate command is required to keep the aircraft in trim.

Figure 7.4.7 shows the response of the adapted MRC parameters for these CG shifts. With ITEC enabled, both parameters settle at new values within a few seconds, since the use of integral control eliminates the steady-state pitch rate error which caused parameter drift when ITEC was disabled.

When the controller parameters reach their steady-state values, the control system becomes LTI again, and linear techniques can be used to analyse the system behaviour after adaptation has taken place. Figure 7.4.8 shows the locations of the closed-loop poles after adaptation has finished for each of the CG shifts. The adaptive controller does not return the poles to the locations they had before the shift, but it does ensure that all poles are stable and well damped.

The results in this section show that the addition of the ITEC law to the pitch rate controller prevents the parameter drift caused by the pitching moment disturbance, and allows the controller parameters to settle at values where the closed-loop system is stable.

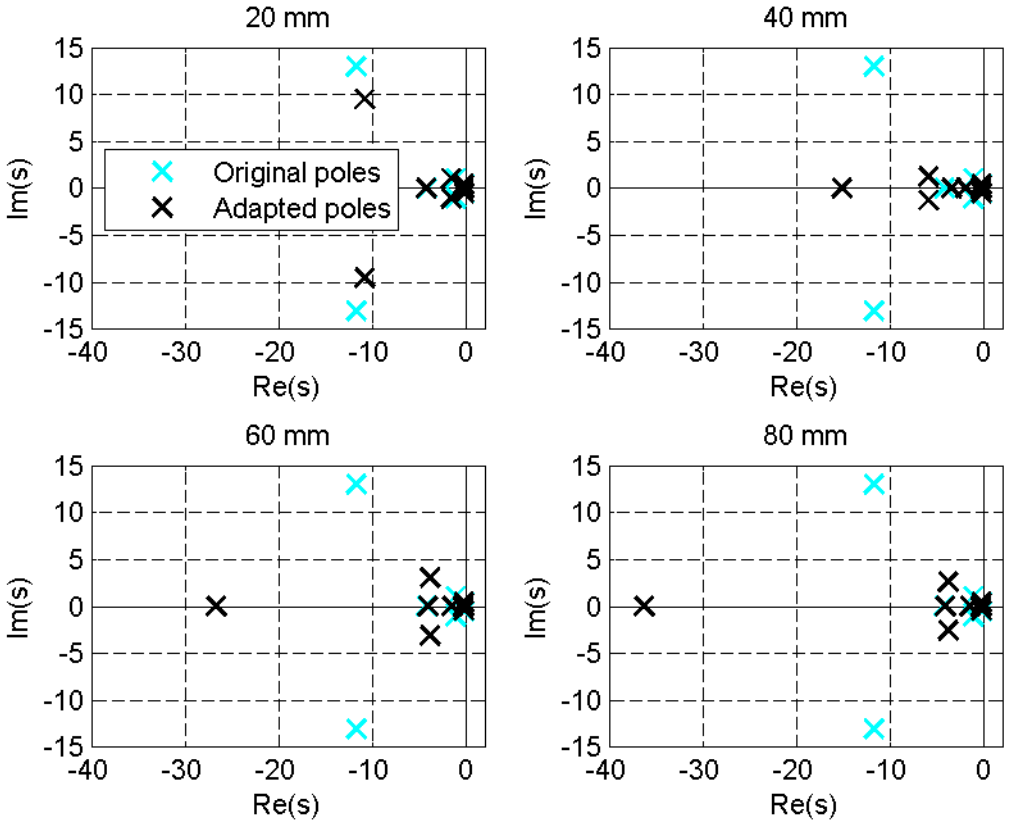

Figure 7.4.8: Locations of the closed-loop poles after the CG has shifted and the adapted parameters have settled

7.5 Effect of measurement noise on the adaptive control system

In the simulations of Section 7.4, it was assumed that the control system is not affected by measurement noise. However, all practical system suffer from measurement noise, and therefore the effect of noise on the adaptive control system must be investigated.

Figure 7.5.1 shows the response of the control system to noise in the pitch rate measurement with an RMS value of 2 degrees per second if adaptation is disabled. The pitch rate measurement q_{mez} is the sum of the true pitch rate and a white noise signal. The fixed-gain control system has good noise tolerance, as both the pitch angle and the elevator deflection mostly stay within 0.2 degrees of their trim values.

Figure 7.5.2 shows the response of the adaptive control system to the same measurement noise if an adaptive gain of $\gamma = 1$ is used in the basic adaptive law of Equation 7.2.5. The magnitude of the noise in both the elevator deflection and the pitch rate slowly increases over time.

Figure 7.5.3 shows the response of the adapted control gains in this situation. The noise causes both adapted parameters to drift, with the feedback gain θ_3 drifting much more than

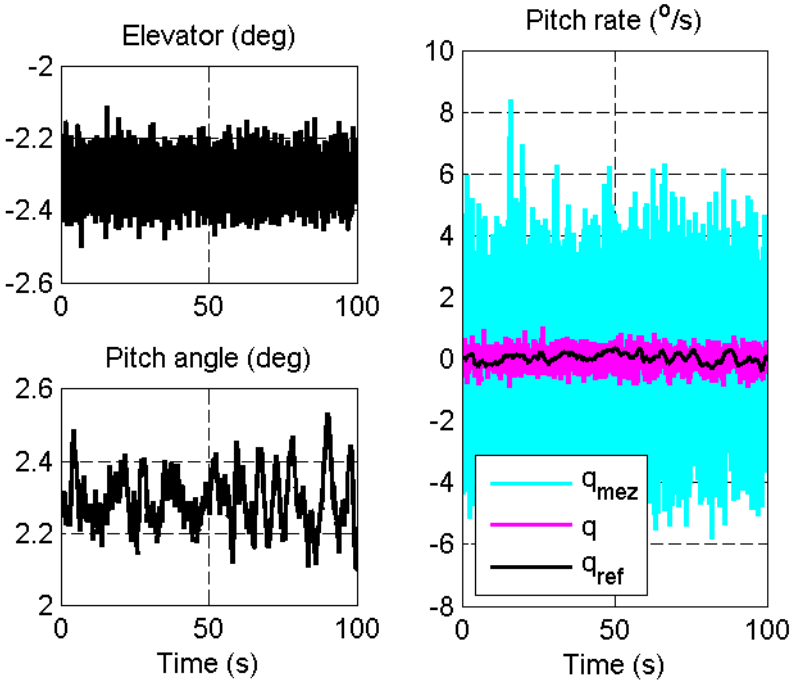

Figure 7.5.1: Response of the control system to pitch rate measurement noise with adaptation disabled

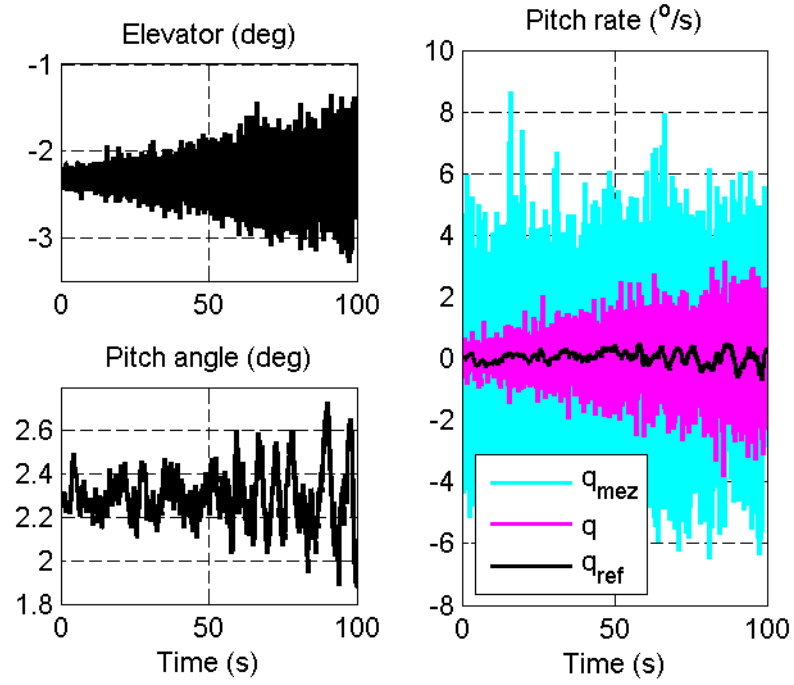

Figure 7.5.2: Response of the control system to pitch rate measurement noise with adaptation enabled

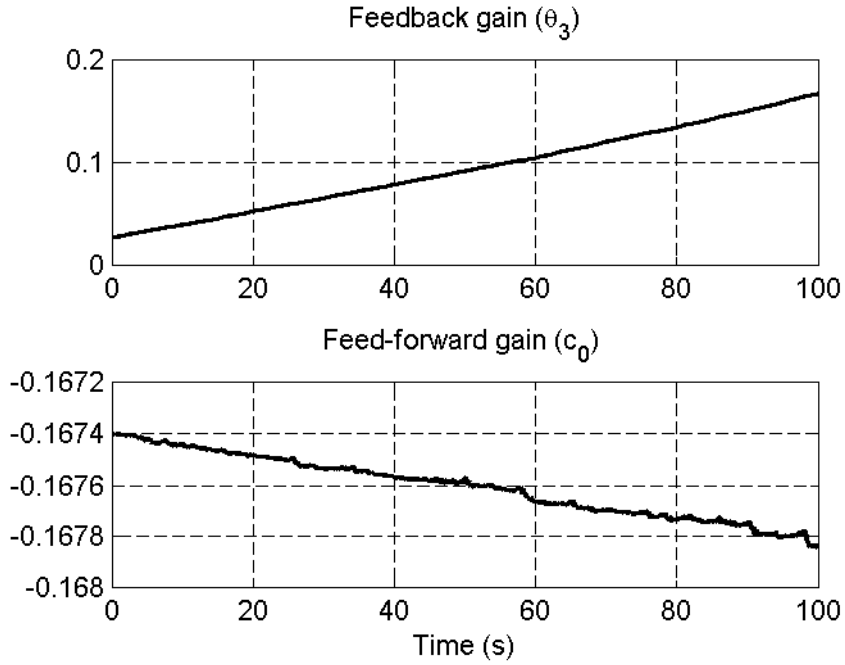

Figure 7.5.3: Response of the adapted control gains to pitch rate measurement noise

the feed-forward gain c_0 due to the relative magnitudes of the noise in the pitch rate measurement and command. The growing feedback gain feeds back an increasing amount the noise to the elevator, which causes the response shown in Figure 7.5.2.

These results show that measurement noise can cause parameter drift in the adaptive control system. This parameter drift is unwanted because the control system is able to handle measurement noise very well without adaptation, and the stability of the system could be affected if the gains keep on drifting.

Therefore the adaptive law must be modified to improve its noise tolerance. The following sections investigate the effect of leakage, discussed in Section 7.2.2, and a dead zone, discussed in Section 7.2.3, on the noise tolerance of the adaptive control system.

7.5.1 Effect of leakage in the adaptive law

The control system was simulated with the adaptive law of Equation 7.2.6, which includes leakage. An adaptive gain of $\gamma = 1$ was used, and values of 0.1, 0.2 and 1 were used for the leakage gain σ.

Figure 7.5.4 shows the response of the aircraft to measurement noise with leakage enabled. It was found that the three leakage gains produced nearly identical responses in the elevator, pitch angle and pitch rate. The use of leakage improves the noise tolerance of the adaptive control system, with the elevator deflection and pitch angle mostly staying within 0.2 degrees of their trim values, as was the case without adaptation.

Figure 7.5.5 shows the response of the adapted parameters to measurement noise with the

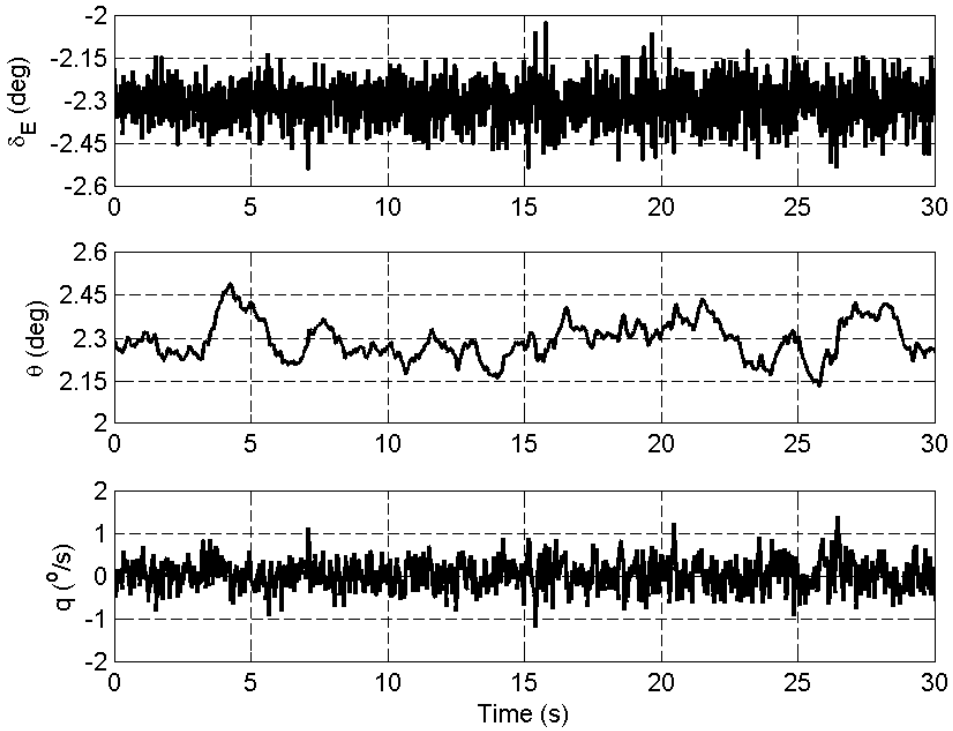

Figure 7.5.4: Response of the adaptive control system with leakage to pitch rate measurement noise

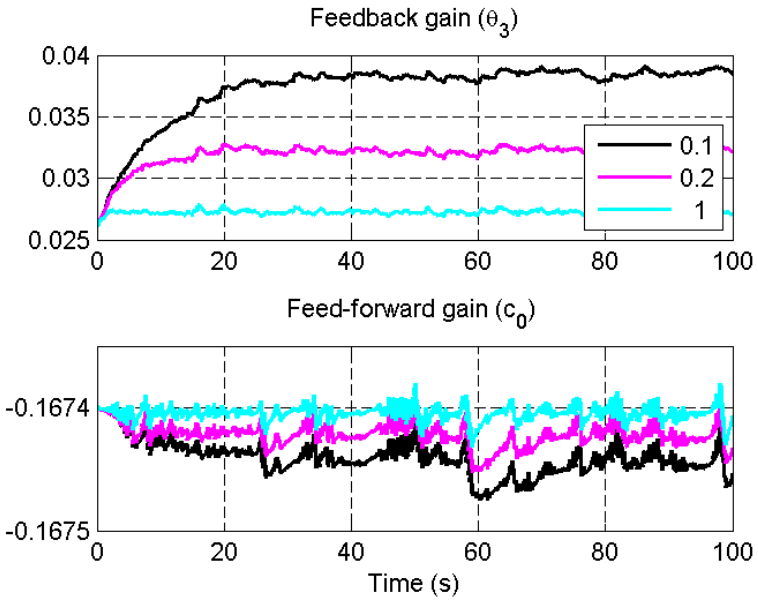

Figure 7.5.5: Response of the adapted control gains to pitch rate measurement noise with different values of the leakage gain σ

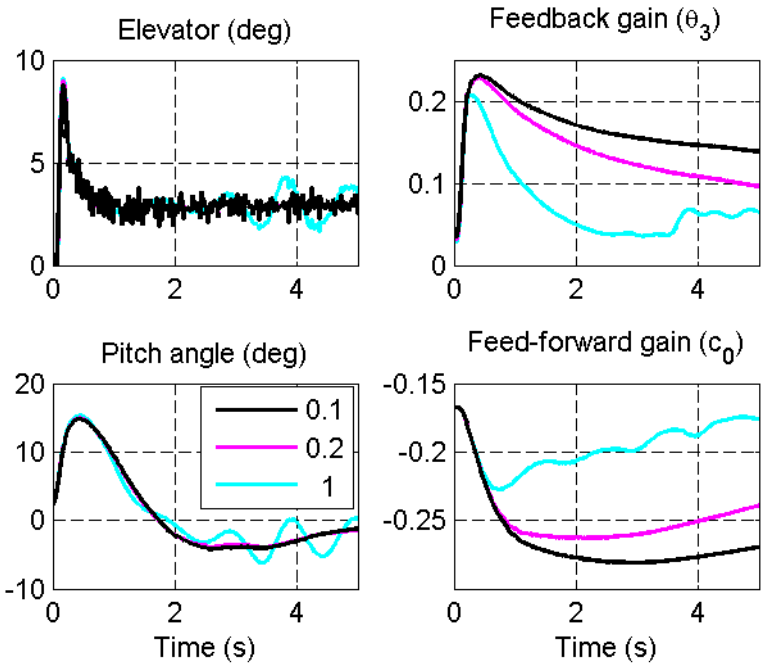

Figure 7.5.6: Initial response to an 80 mm CG shift with different values of the leakage gain σ

different leakage gains. In each case, the parameters drift away from their initial values, but eventually settle around a steady-state value. Once again the feedback gain drifts much more than the feed-forward gain, but it still remains reasonably close to its initial value. Increasing the leakage gain decreases the amount by which the parameters drift from their initial values.

These results show that the use of leakage can prevent excessive parameter drift due to measurement noise, but the effect of leakage on the ability of the adaptive control system to handle CG shifts must also be investigated. Figures 7.5.6 and 7.5.7 show the response of the adaptive control system with leakage to an instantaneous 80 mm CG shift.

Figure 7.5.6 shows that the controller parameters quickly jump to new values after the CG shift, and then start drifting back towards their initial values. With a leakage gain of $\sigma = 1$, the adaptation is soon nullified by this drift, and instability is visible within the first 5 seconds.

Figure 7.5.7 shows the long-term response of the system with leakage to the CG shift. The adapted parameters drift back to steady-state values close to their initial values, and the aircraft experiences continued small oscillations.

After adaptation has taken place, the closed-loop system is stable, and the output error goes to zero. This causes the controller parameters to drift back towards their initial values. As they approach their initial values, the closed-loop system becomes unstable again, the output error grows, and adaptation takes place again. This adaptation re-stabilises the system, the output error returns to zero and the cycle repeats itself. This causes small oscillations which continually appear, grow and fade away, as can be seen most clearly for $\sigma = 0.2$

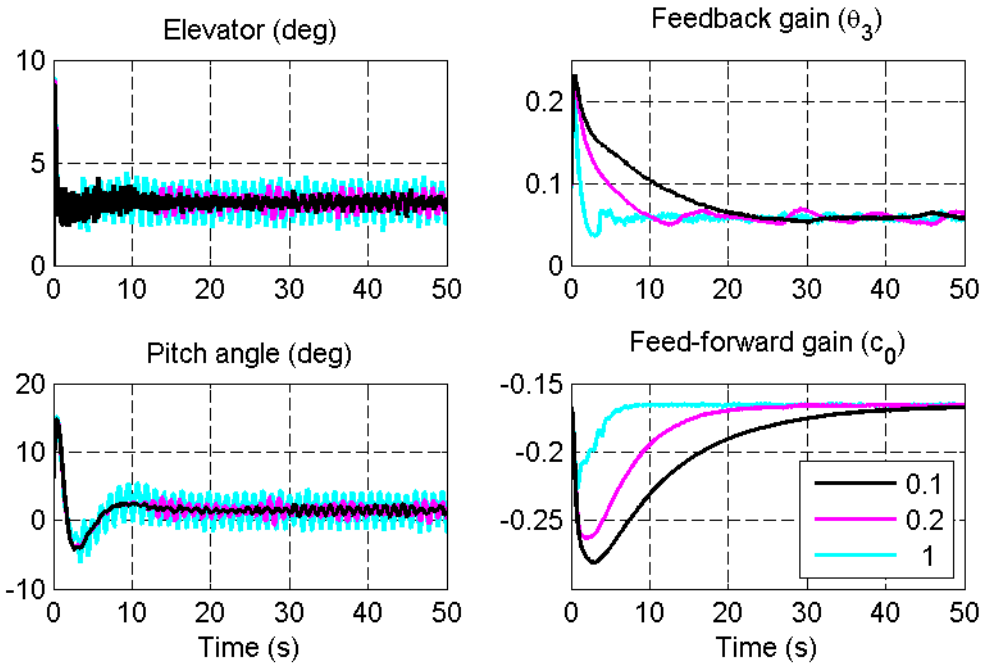

Figure 7.5.7: Long-term response to an 80 mm CG shift with different values of the leakage gain σ

in Figure 7.5.7.

These results show that, even though the use of leakage can improve the noise tolerance of the adaptive control system, it has a negative effect on its ability to handle CG shifts.

7.5.2 Effect of a dead zone in the adaptive law

Another technique which could improve the noise tolerance of the adaptive control system is to use an adaptive law with a dead zone, as given in Equations 7.2.11 and 7.2.12.

If the magnitude of the noise is known, the dead zone width g_0 can be chosen so that no adaptation will take place because of the noise on its own. Then the response of the adaptive control system to the noise will be identical to that of the system without adaptation, shown in Figure 7.5.1. It was found that a dead zone width of 10 degrees per second will prevent adaptation due to the noise used in these simulations.

Figure 7.5.8 shows the response of the adaptive control system with this dead zone and an adaptive gain of $\gamma = 1$ to CG shifts of various distances when there is noise in the pitch rate measurement. In each case, the aircraft experiences a transient which is well damped by the adaptive control system.

Figure 7.5.9 shows the response of the adapted parameters as well as the pitch rate error to these shifts. The pitch rate error shoots up when the CG shifts, but as the parameters are adapted it quickly decreases and enters the 10°/s dead zone, after which no further adaptation takes place, and the gains settle at new values within seconds.

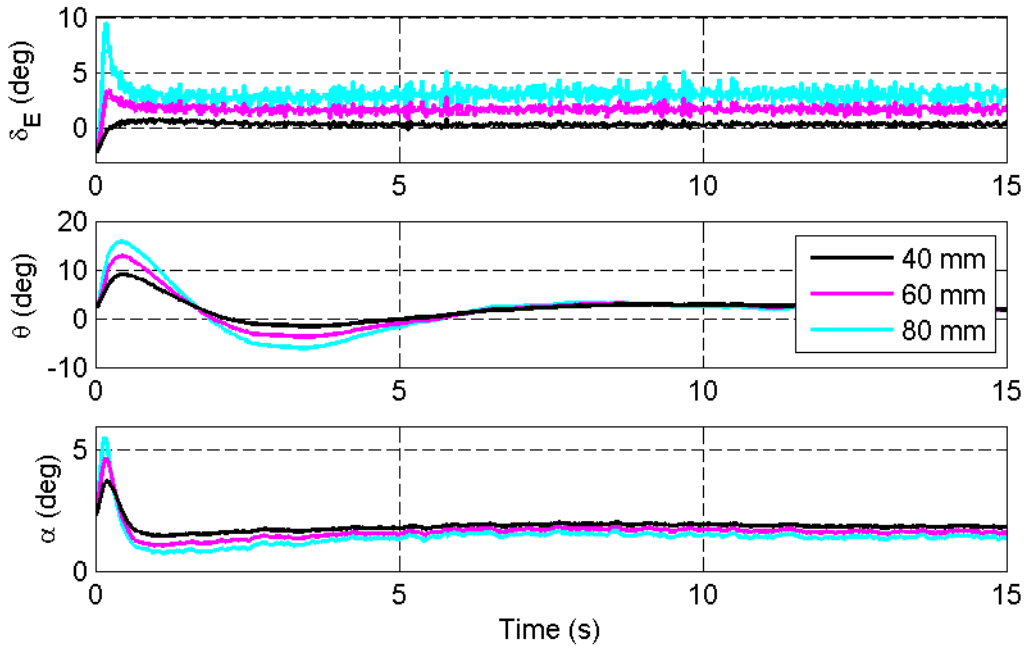

Figure 7.5.8: Response to instant CG shifts with pitch rate measurement noise and a 10°/s dead zone

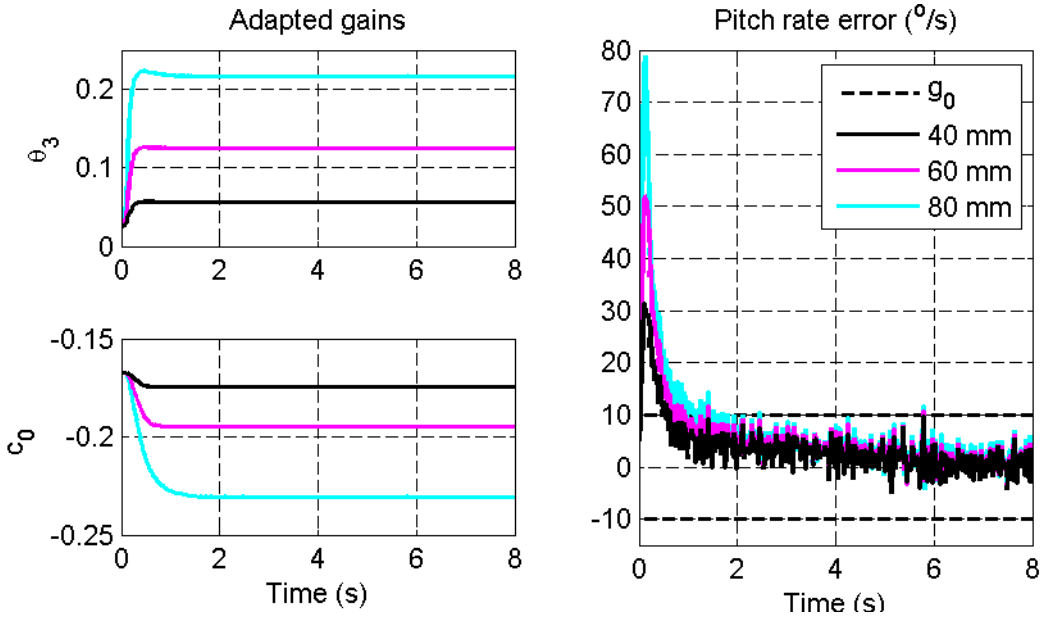

Figure 7.5.9: Response of the pitch rate error and the adapted gains to instant shifts with pitch rate measurement noise and a 10°/s dead zone

The steady-state values of the control gains in this case are very similar to their values when there is no noise and no dead zone is used, as shown in Figure 7.4.7. The closed-loop poles after adaptation are also very similar, with the poles not returning to their original positions, but all settling in stable and well-damped locations.

These results indicate that the adaptive pitch rate controller system which uses ITEC in parallel with the MRAC, and an unnormalised adaptive law with a dead zone, is able to re-stabilise the aircraft after an instantaneous backward CG shift, and is robust to both constant pitching moment disturbances and measurement noise.

7.6 Response to gradual CG shifts

In Sections 7.4 and 7.5, the response of the adaptive control system to instantaneous shifts in the centre of gravity was investigated. These shifts are likely to be the result of in-flight damage, which could cause mass to break off the front of the aircraft or suddenly move around inside it.

However, the CG of an aircraft can also be moved intentionally. In [4], a control system was designed to solve the *variable stability problem*, where the aircraft is intentionally made unstable by moving mass backwards to decrease the drag of the aircraft. This control system was implemented and tested on the Variable Stability UAV built at Stellenbosch University. This aircraft has its avionics and batteries mounted on a tray which can move backwards to destabilise the aircraft.

The tray could only move at a finite speed, and therefore the effect of destabilising the aircraft in this way could be very different from the simulated instantaneous CG shifts of the previous sections. A control system was designed for the tray in [4] so that it would have a first-order response to position step commands, with a time constant of 2 seconds.

This section investigates the response of the adaptive control system to this type of gradual shift in the centre of gravity. This will allow adaptive control to be investigated as a possible solution to the variable stability problem, which is not the focus of this thesis, but could be a useful secondary application of the adaptive control system.

7.6.1 Response without adaptation

Figure 7.6.1 shows the effect of gradual CG shifts of various distances on the control system when adaptation is disabled. For all the distances shown, the response initially seems stable and well damped. For a 70 mm shift, the response eventually becomes visibly unstable, but remains very small for several seconds after the CG has settled in an unstable position. By contrast, an instant CG shift of 60 mm led to very poorly damped behaviour, while a 70 mm instant shift would make the system violently unstable.

This difference in response is due to the fact that the fixed-gain control system can counter

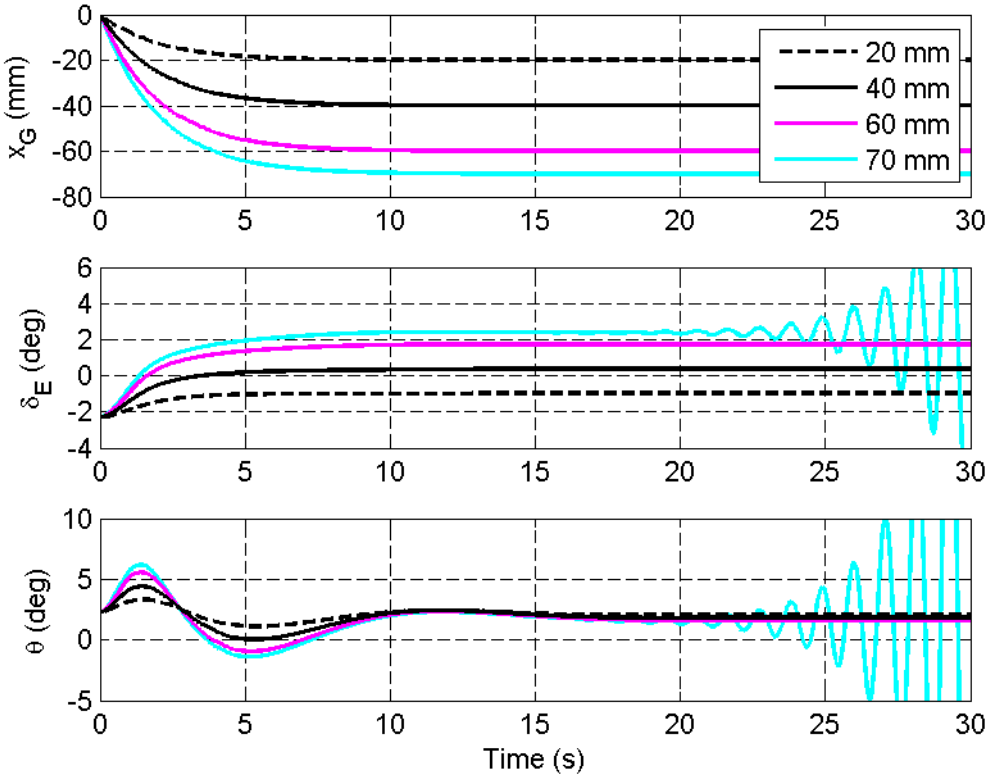

Figure 7.6.1: Response of the control system without adaptation to gradual CG shifts of various distances

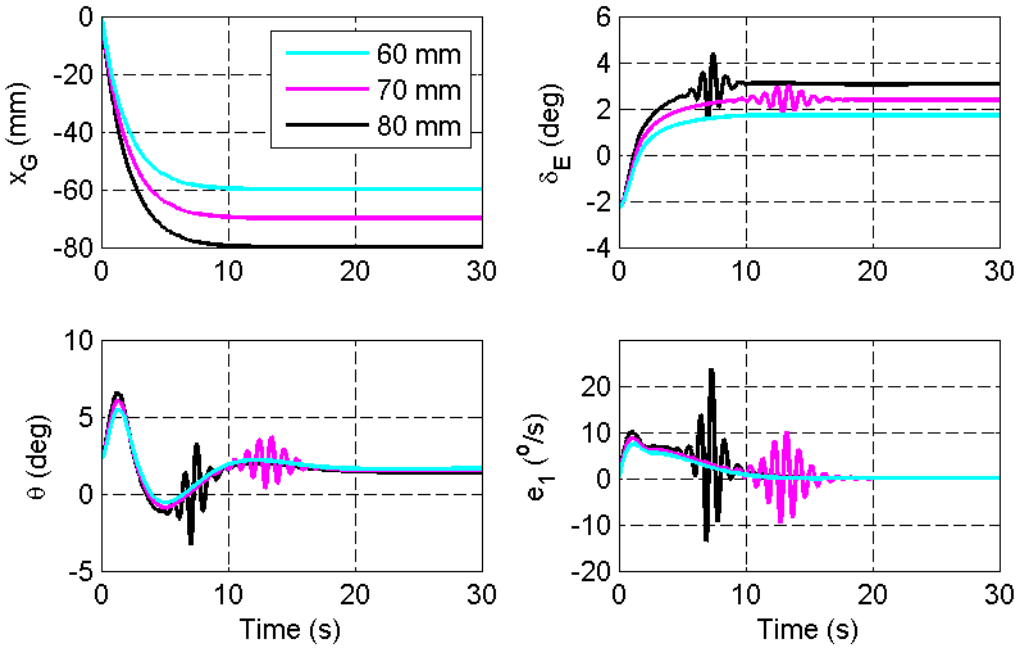

Figure 7.6.2: Response of the adaptive control system to gradual CG shifts

the slowly growing pitching moment disturbance caused by the gradual CG shift much more easily than it can counter the disturbance step created by an instant shift. The outer loops ensure that the underdamped or unstable dynamics are not significantly excited, and therefore the underdamped stable dynamics are not visible in the response, and the unstable oscillations take a long time to grow to a significant magnitude.

7.6.2 Response with adaptation

Figures 7.6.2 and 7.6.3 show the response of the adaptive control system to gradual CG shifts of various distances. An adaptive gain of $\gamma = 1$ was used, but no dead zone was used in the adaptive law, and no noise was added in this simulation.

For a 60 mm shift, which does not destabilise the closed-loop system, the controller parameters are not adjusted very much, and the response of the aircraft is very similar to the shift without adaptation, shown in Figure 7.6.1. For a 70 or 80 mm shift, the aircraft experiences an oscillation which initially grows in magnitude, and then starts fading away as the parameters are adjusted.

This behaviour can be explained by examining the closed-loop poles of the system before and after adaptation has taken place, shown in Figure 7.6.4 for both a 70 and 80 mm shift. In both cases, the short period poles are located just to the right of the imaginary axis before adaptation, indicating that the closed-loop system is barely unstable, which corresponds to the slowly growing oscillations seen in both cases. The adaptation moves the short period poles to positions just left of the imaginary axis, indicating that the system is barely stable,

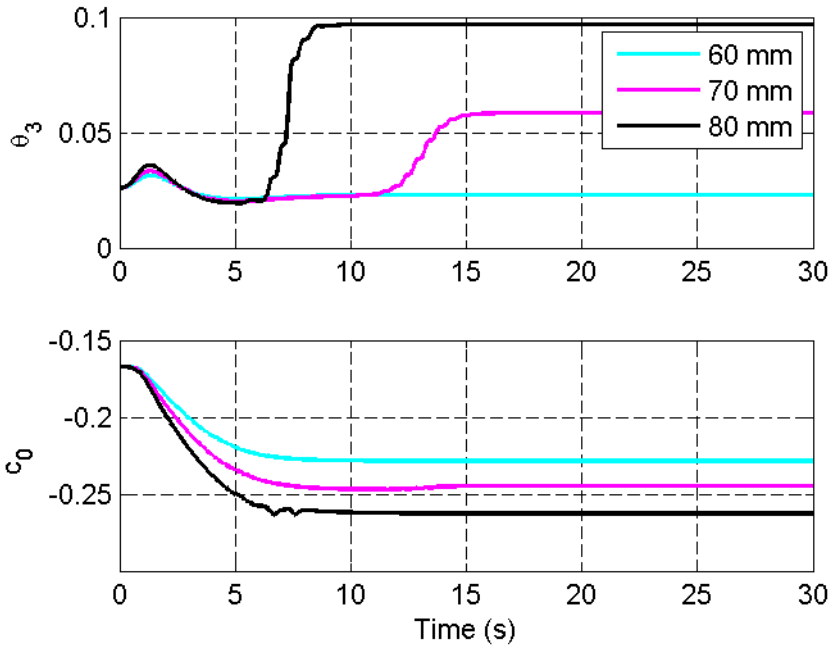

Figure 7.6.3: Response of the adapted gains to gradual CG shifts

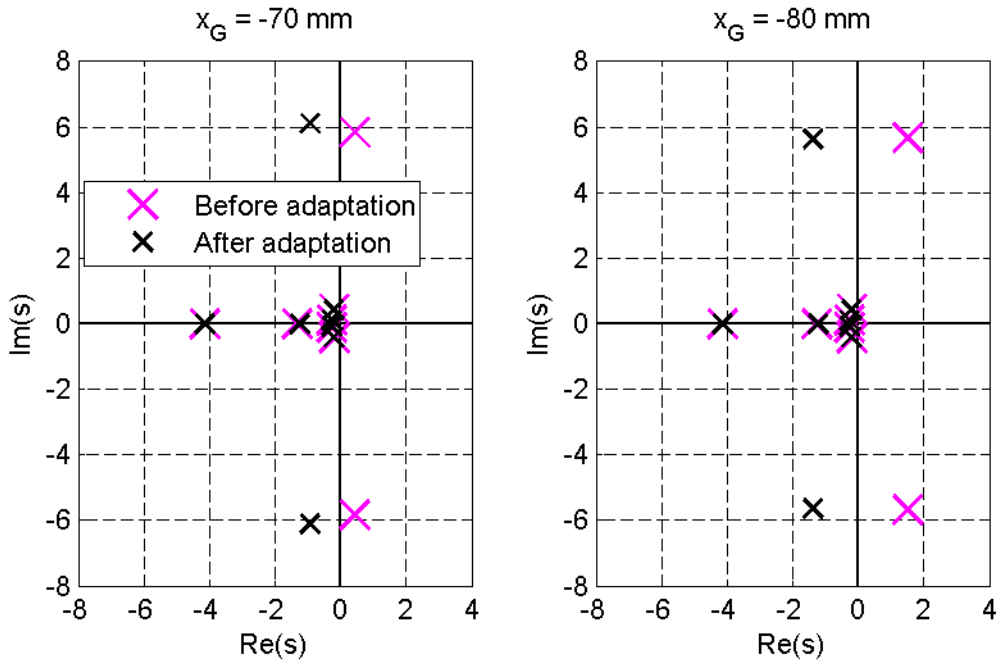

Figure 7.6.4: Closed-loop poles before and after adaptation for a gradual CG shift

which corresponds to the slowly decaying oscillations seen after adaptation.

These simulations show that the adaptive control system is able to re-stabilise the closed-loop system if it is destabilised by a gradual shift in the centre of gravity. However, the response after adaptation is still very poorly damped, since the controller parameters are not adapted sufficiently to provide acceptable damping.

The adaptation of the controller parameters is driven by the output error. The adaptive controller is designed so that the controller parameters will come close to their ideal values, or at least acceptable values, as the output error goes to zero. However, the fixed-gain control loops of the longitudinal control system are also designed to eliminate the output error. This causes the output error to go to zero before the controller parameters have been adjusted sufficiently to ensure adequate closed-loop performance.

In the case of an instantaneous CG shift, the output error shoots up quickly, exciting the unstable dynamics and providing information for the adaptive law. This causes significant adaptation before the outer control loops can react to the disturbance. The controller parameters are adjusted sufficiently that the closed-loop behaviour becomes acceptable before the output error is eliminated.

However, the outer loops are able to account for the slowly growing pitching moment disturbance caused by a gradual CG shift and keep the aircraft trimmed until the closed-loop system becomes unstable. This prevents the unstable dynamics from being excited significantly. Once the system becomes unstable, the output error starts growing, but the fixed-gain control loops reduce its magnitude, depriving the adaptive law of information and preventing the controller parameters from being adapted sufficiently.

The inclusion of a dead zone in the adaptive law, which will be necessary if there is noise in the pitch rate measurement, will further decrease its responsiveness to gradual CG shifts. The outer loops will ensure that the output error initially stays within the dead zone. The oscillations will increase in magnitude until the output error leaves the dead zone, causing the controller parameters to be adapted just enough to stabilise the closed-loop system. The oscillations will start fading away, the output error will enter the dead zone and no further adaptation will take place.

Because of these factors, the adaptive control system does not perform as well in handling gradual shifts in the centre of gravity as it does with instantaneous CG shifts.

7.7 Summary

In this chapter, it was confirmed in non-linear simulations that instantaneous backward shifts in the centre of gravity of the Variable Stability UAV can destabilise the fixed-gain control system, as was seen in the linear analysis of Chapter 6. It was found that the basic adaptive law of Equation 7.2.5 can re-stabilise the aircraft if an appropriate adaptive gain is chosen,

but that an adaptive gain which is too small will not be able to react fast enough to save the aircraft, while an adaptive gain which is too large can cause instability due to stiffness in the adaptive law.

It was found that the pitching moment disturbance due to a CG shift creates a steady-state error between the pitch rate and the pitch rate command if ITEC is not used, which causes the adapted parameters to drift. The addition of ITEC eliminates this parameter drift, and allows the parameters to settle at values where all the closed-loop poles of the system are stable and well damped.

The addition of noise in the pitch rate measurement was also found to cause parameter drift if the basic adaptive law is used. Leakage and a dead zone were investigated as possible techniques to improve the noise tolerance of the adaptive control system. It was found that both techniques could significantly decrease the parameter drift due to noise, but only the dead zone did so without compromising the performance of the adaptive control system in handling CG shifts.

Finally, it was found that the adaptive control system is able to re-stabilise the aircraft if the CG moves backwards gradually, but that it does not perform as well in this case as it does with instantaneous CG shifts, with the system barely stable after adaptation has taken place.

This indicates that the adaptive control system developed for this project is not a viable solution for the variable stability problem, which was the focus of [4]. However, if the CG is moved back intentionally to change the aircraft dynamics, this information could be made available to the autopilot, and therefore it would be unnecessary to design a system which can keep the aircraft stable without knowledge of the CG position.

By contrast, the adaptive control system performs very well in handling simulated instant shifts in the centre of gravity, which was its primary design goal. This indicates that adaptive control systems could probably be designed to handle a wide range of in-flight damage situations which could seriously affect the stability of a UAV. Therefore these simulations results suggest that adaptive control could be an effective part of an active fault-tolerant control system.

The software simulations of this chapter were repeated in HIL simulation in preparation for flight tests of the adaptive control system using the Variable Stability UAV. Chapter 8 gives the results of these flight tests, which were done to test if the adaptive control system is able to re-stabilise an unstable aircraft in practice. These tests could provide further insight into the effect of adaptation on the fault tolerance of the control system.

Chapter 8

Flight tests

In Chapter 7, it was shown in non-linear simulation that the control system designed in Chapter 6 can be combined with an adaptive law from Chapter 5 to create a fault-tolerant adaptive control system which is able to handle shifts in the centre of gravity of an aircraft. The control system performed well in simulation, but successful practical tests would give validation to the simulation results.

Initially, the intention was that the fault tolerance of the adaptive control system would be tested in flight by moving the avionics tray of the Variable Stability UAV backwards to simulate a damage-induced shift in the centre of gravity. However, simulations showed the effects of such gradual CG shifts and damage-induced instantaneous CG shifts can be very different, and that the adaptive control system handles the latter much better than the former.

Furthermore, as will be shown in this chapter, structural modifications had to be made to the aircraft, which prevented the tray from being moved all the way backwards. Therefore another way of destabilising the aircraft in flight had to be found, and it was decided that applying positive feedback of the pitch rate to the elevators would be an acceptable alternative method.

Section 8.1 describes the preparations that had to be done before flight tests could be performed with the Variable Stability UAV. Section 8.2 describes a remote controlled flight to test the aircraft system. In Section 8.3, the fixed-gain pitch rate controller was tested and found to be unstable. Section 8.4 analyses this instability, proposes possible causes, and describes measures that were taken to address it. These measures prevented the aircraft from being made physically unstable, and therefore Section 8.5 introduces positive pitch rate feedback as an alternative method of destabilising the aircraft. Section 8.6 and 8.7 describe flight tests of the adaptive pitch rate controller in fly-by-wire mode and with the full longitudinal control system.

The full aircraft system used in the flight tests, including the hardware and software of the aircraft, ground station and hardware-in-the-loop simulation interface, is described in Appendix A.1.

8.1 Preparation

This section summarises the preparations that had to be done before flight tests of the adaptive control system could be performed with the Variable Stability UAV. For a more detailed description of the systems mentioned here, see Appendix A.1.

The aircraft had crashed into a tree in its last flight for the previous project, and the damage had to be assessed and repaired. Fortunately, there was no major damage. The right wing had been bent slightly and lost some rigidity, but this could be restored by removing the fibre tape covering the wing and then re-taping the wing. The servo for the right rudder had also been damaged in the crash, and was replaced.

Next, the avionics had to be restored to working order. New power and CAN bus cables were made to replace the old ones, which greatly improved the tidiness of the avionics. Cables were also made to measure the current and voltage of the motor battery using the ADC channels of the OBC. This was necessary for the thrust test, and to check the battery usage in flight. The RC receiver from the previous project was now obsolete and had to be replaced, and the new receiver required a level translator board to be added to the servo board.

The servos of the six aerodynamic actuators had to be calibrated to ensure that they would always have the commanded deflection. This was done by programming the correct offset, gain and mixing matrix values onto both the OBC and the servo board. A thrust test was also done to determine the maximum thrust, and to determine the mapping of PWM commands for the speed controller to the thrust output. The thrust test procedure is described in Appendix A.3.3.

The sensors of the Variable Stability UAV also had to be calibrated to have the correct offsets and gains. The accelerometers were calibrated by rotating the IMU to 90° angles and ensuring that it always measures 9.81 $\mathrm{m/s^2}$ in the correct direction. The rate gyroscopes were calibrated using a rate table which can turn at a specified angular rate. The accelerometers and gyroscopes were also temperature-calibrated using a temperature sensor on the IMU, to ensure that their measurements do not drift with temperature.

The magnetometer was calibrated by logging data during a series of 360° rotations around the NED axes. An automated script then performed a least-squares fit on the data to determine the calibration offsets and gains.

Finally, before any control loops could be armed in flight, they had to be implemented on the avionics of the Variable Stability UAV and tested in hardware-in-the-loop (HIL) simulation. This allowed the control loops to be tested safely, to ensure that they are stable and robust, and also that the transition between manual control and the autopilot, or from one control configuration to another, would not cause any dangerous transient responses.

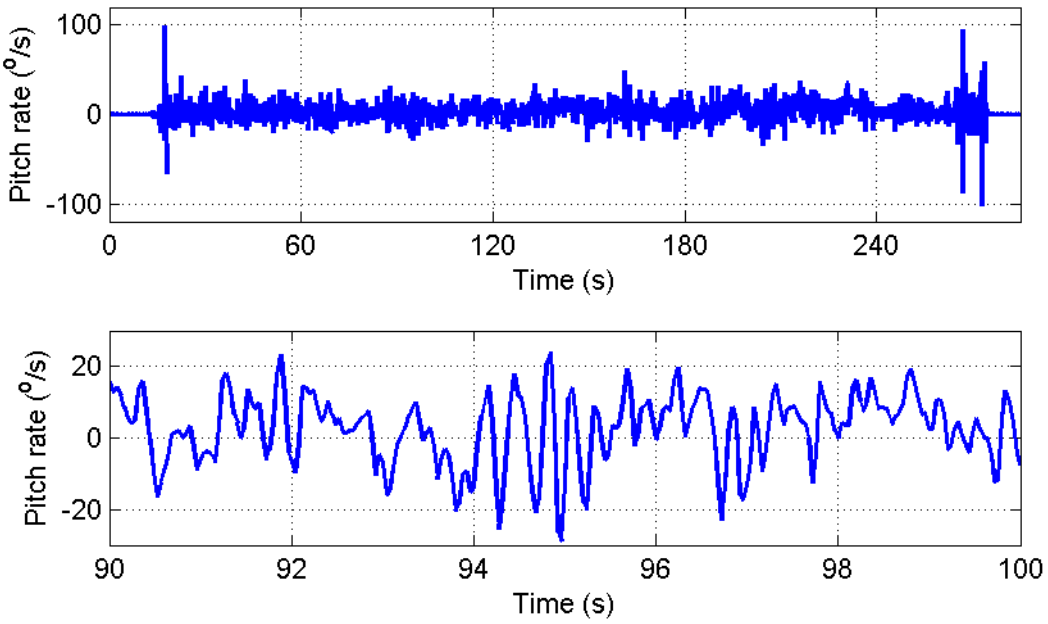

Figure 8.2.1: Pitch rate measurement from the first RC flight

8.2 Remote controlled flight

A first test flight was done to test the airworthiness of the Variable Stability UAV, and to ensure that all the sensors and the estimator worked correctly. The safety pilot took off and flew circuits around the airfield for about four minutes before landing. The aircraft could maintain an airspeed of about 18 m/s without using full throttle, and therefore this was chosen as the trim airspeed for the control design.

Figure 8.2.1 shows the logged pitch rate measurement from the RC flight. Apart from when the aircraft was on the ground, the pitch rate measurement seemed to be affected by noise with an amplitude of about 20 degrees per second. However, zooming in on the data reveals sinusoidal content with a frequency of about 3 Hz in the pitch rate measurement. This is clearly visible around the 95-second mark, but can be seen in the pitch rate measurement as long as the aircraft is airborne.

The periodic output disturbance in the pitch rate measurement was not noticed at this stage, and the flight test campaign proceeded without any effort to address it.

8.3 Fixed-gain pitch rate controller test

After the RC flight, the next step was to test the pitch rate and airspeed controllers in flight. The autopilot would have full control of the throttle to follow an airspeed reference, and the pitch rate controller would be armed in fly-by-wire mode – that is, the safety pilot would use

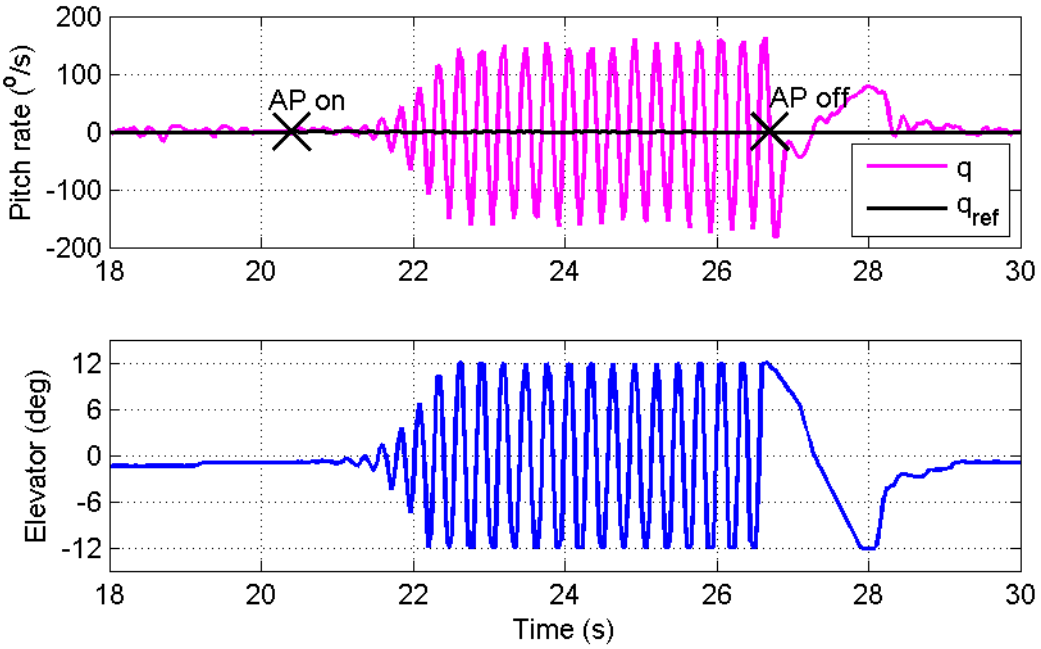

Figure 8.3.1: Unstable response of the pitch rate controller with $\theta_3 = 0.1$

his elevator stick to generate pitch rate commands for the pitch rate controller, which would generate an elevator deflection to follow the command. ITEC was enabled for this flight, but adaptation was not. The safety pilot retained full control of the aileron and rudder actuators.

Since the pitch rate dynamics are dependent on the airspeed, the airspeed controller was armed along with the pitch rate controller to keep the airspeed close to the nominal value. The airspeed and pitch rate controllers were designed so that they performed well in simulation, with the pitch rate controller adding some damping to the short period mode, and the airspeed controller regulating the airspeed without actuating the throttle too aggressively.

A feedback gain of $\theta_3 = 0.1$ for the pitch rate controller had produced good results in early simulations. However, the pitch rate controller with this gain proved unstable in practice, as can be seen from the response in Figure 8.3.1. When the autopilot was switched on, the aircraft started oscillating with a growing magnitude until the elevator saturated and the system entered a limit cycle, forcing the safety pilot to retake manual control to save the aircraft.

The feedback gain was decreased to $\theta_3 = 0.05$, and the autopilot was engaged again. Figure 8.3.2 shows the response of the system with this feedback gain. Initially, the system was much more stable, and the pitch rate seemed to follow the command, but the response still became unstable at times. This happened especially when the airspeed increased, since this increased the effect of the elevators and therefore the effective feedback gain.

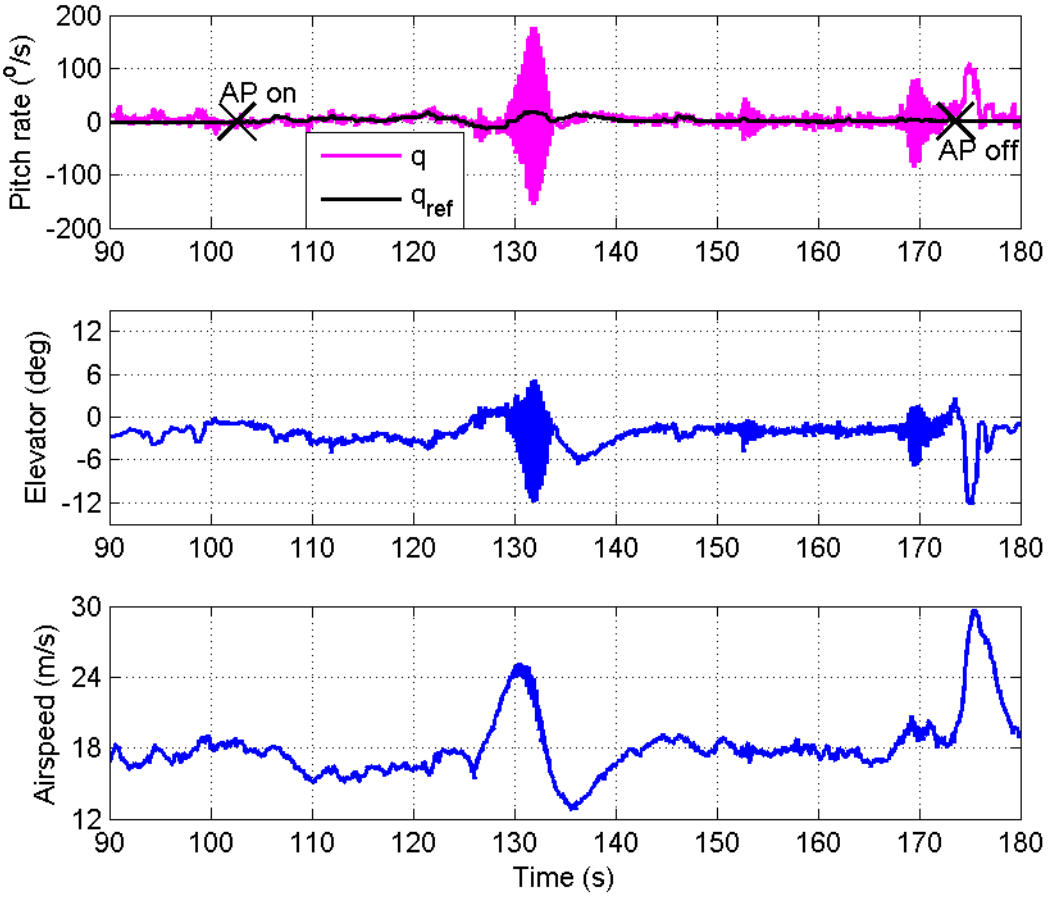

Figure 8.3.2: Response of the pitch rate controller with $\theta_3 = 0.05$, showing instability at higher airspeed

8.4 Analysis of instability

This large discrepancy between simulation and practical results forced an investigation into the flight test results and the aircraft model. Firstly, it was discovered that the aircraft parameters taken from [4], which had been used in the control design, were incorrect. The mean aerodynamic chord $\bar{c}$ was given there as 0.33 metres, along with stability and control derivatives that were calculated in AVL assuming a value of $\bar{c} = 0.508$ m. This led to a significant difference between the behaviour of the aircraft model and that of the actual aircraft, which contributed to the instability seen in this flight test.

Furthermore, an incorrect assumption regarding the value of $\bar{c}$ will affect the modelling of the effect of CG shifts on the aircraft parameters. The effect of a CG shift is dependent on the ratio of the shift distance to $\bar{c}$, and therefore if the true value of $\bar{c}$ is less than its assumed value, then CG shifts will have more effect than expected.

This was possibly the cause of the crash which occurred during the last flight test doc-

umented in [4]. In this flight, the autopilot was disengaged while the CG was in a position where calculations indicated that the aircraft would be stable. However, the aircraft turned out to be unstable with the CG in that position. The safety pilot lost control of the aircraft and it crashed.

Once the modelling error was discovered, the pitch rate controller was re-designed using the correct aircraft parameters, resulting in a feedback gain of $\theta_3 = 0.03$ or less, as was used in Chapters 6 and 7. However, even with the decreased feedback gain, some oscillation was still experienced in subsequent flight tests.

This prompted further investigation of the flight data, which led to the discovery of the sinusoidal output disturbance. If the sinusoidal pitch rate measurement is fed back to the elevator with a large feedback gain, it could amplify the disturbance and cause the instability seen in the flight data.

A number of explanations for the output disturbance were considered. Firstly, it was thought that vibrations from the motor might have caused the oscillation. However, the oscillation was not visible during take-off, when the motor turns at full speed, and therefore this explanation was considered unlikely.

An alternative explanation was that the inertial measurement unit (IMU), which includes the pitch rate gyroscope, was vibrating relative to the airframe. The IMU was mounted on the flexible metal plate of the avionics tray, which in turn was mounted on rails which could allow it to slide backwards and forwards to move the CG of the aircraft. The way that the IMU was mounted on the plate allowed it to move considerably relative to the rest of aircraft.

The movement of the IMU could not be modelled exactly, but a rough estimate of its dynamics can provide insight into a possible cause of the instability. Suppose that the response of the IMU to a change in the pitch rate of the aircraft can be modelled using a transfer function from the actual pitch rate q to the pitch rate measurement q_{mez}, which has two lightly damped poles:

$$\frac{q_{mez}(s)}{q(s)} = \frac{\omega_n^2}{s^2 + 2\zeta\omega_n s + \omega_n^2} \tag{8.4.1}$$

From the flight data it seems that w_n is approximately 3 Hz or 20 rad/s, and the damping ratio could be around $\zeta = 0.1$. Furthermore, the IMU includes an analog second-order Butterworth filter with a frequency of 8 Hz, which is about 50 rad/s. Then the sensor transfer function for the pitch rate will be

$$\frac{q_{mez}(s)}{q(s)} = \frac{400}{s^2 + 4s + 400} \times \frac{2500}{s^2 + 70s + 2500} \tag{8.4.2}$$

This sensor transfer function can be included in the analysis of the pitch rate controller, yielding the root locus shown in Figure 8.4.1, which shows the closed-loop poles for a feedback gain of $\theta_3 = 0.1$. In this case, the pitch rate feedback makes the poles of the IMU unstable. This is by no means an exact representation of the response of the pitch rate controller,

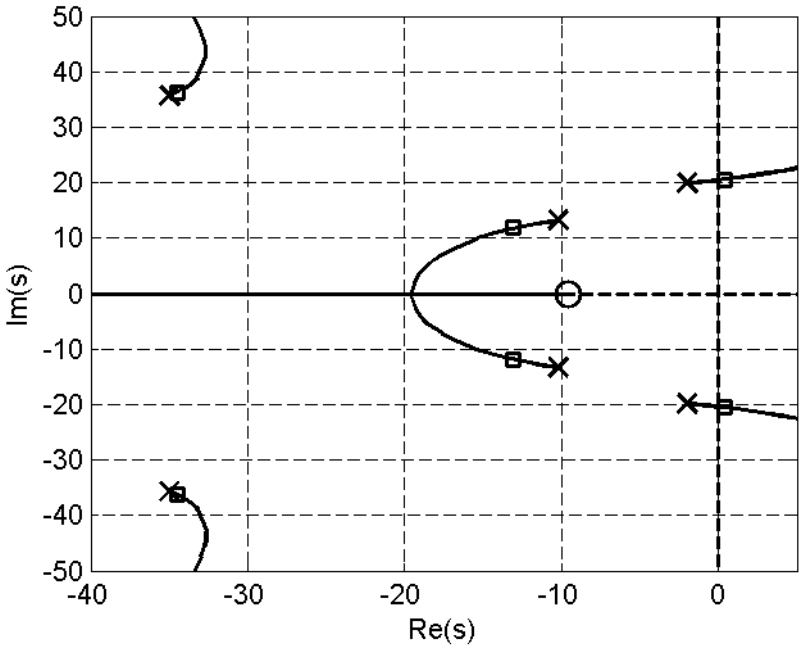

Figure 8.4.1: Root locus of the pitch rate controller with estimated IMU dynamics and Butterworth filter included

but it does indicate that this type of unmodelled dynamics could have caused the instability seen in the test flight.

Another possible contributing factor to the unstable behaviour is that the shell covering the avionics was quite flexible. The rear of the cover in particular could have been buffeting in the wind, acting as an unmodelled elevator and causing the sinusoidal pitch rate response. Feeding these unmodelled dynamics back to the elevator could also have caused the instability of the pitch rate controller.

In order to eliminate the buffeting of the shell, pieces of plywood were glued in to increase the rigidity of the cover. The IMU was also vibration-mounted in an attempt to reduce its motion relative to the airframe. Both these modifications, however, made it impossible for the tray to move backwards, and therefore a complete rebuild of the top cover would be required before the aircraft could be made physically unstable again.

8.5 Alternative destabilisation technique: Positive feedback

After the structural modifications discussed in Section 8.4, the response of the adaptive control system to CG shifts could no longer be tested by moving the tray of the Variable Stability UAV backwards, and therefore another technique had to be found to alter the aircraft dynamics in flight.

This was done using positive feedback of the pitch rate to the elevator. The pitch rate

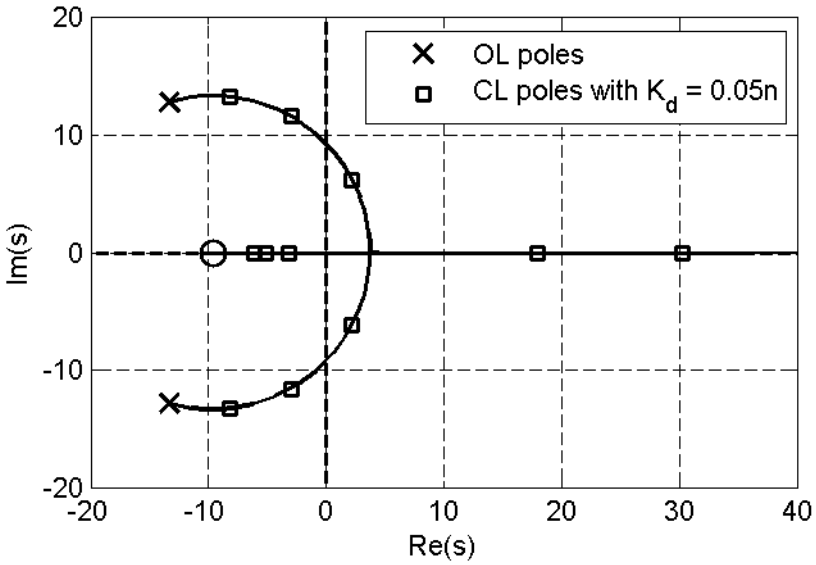

Figure 8.5.1: Root locus of the positive feedback loop through the destabilising gain K_d

control law was modified so that the elevator deflection would be the sum of the trim elevator setting generated by the ITEC law (δ_{E_t}), the deviation from trim generated by the MRC law (δ_e), and a positive feedback term:

$$\delta_E = \delta_{E_t} + \delta_e - K_d q \tag{8.5.1}$$

where $K_d > 0$ is the *destabilising gain*. Since a positive elevator deflection creates a negative pitching moment, commanding a negative elevator deflection for a positive pitch rate constitutes positive feedback.

Figure 8.5.1 shows the root locus of the positive feedback loop if it is closed around the negative feedback loop with a gain of $\theta_3 = 0.03$, which was used in these flight tests. According to the root locus, the system will be unstable for a destabilising gain of $K_d = 0.15$ or greater.

The root locus of Figure 8.5.1 differs significantly from the movements of the short-period poles due to CG shifts, shown in Section 4.6. Therefore, destabilising the aircraft in this way does not provide direct insight into the handling of CG shifts by the adaptive control system, but could show that the adaptive control system is able to re-stabilise an unstable system, and so demonstrate its fault tolerance in practice.

Also, this destabilisation technique has the advantage that it can be enabled and disabled instantly, while the tray can only move at a finite speed. If the autopilot malfunctions with the tray in an unstable position, the aircraft can not be made stable immediately, and the safety pilot will not be able to retake control safely. However, both the positive feedback destabilisation and the autopilot can be disengaged instantly, allowing the safety pilot to retake control. Therefore this method of destabilising the aircraft is much safer than moving

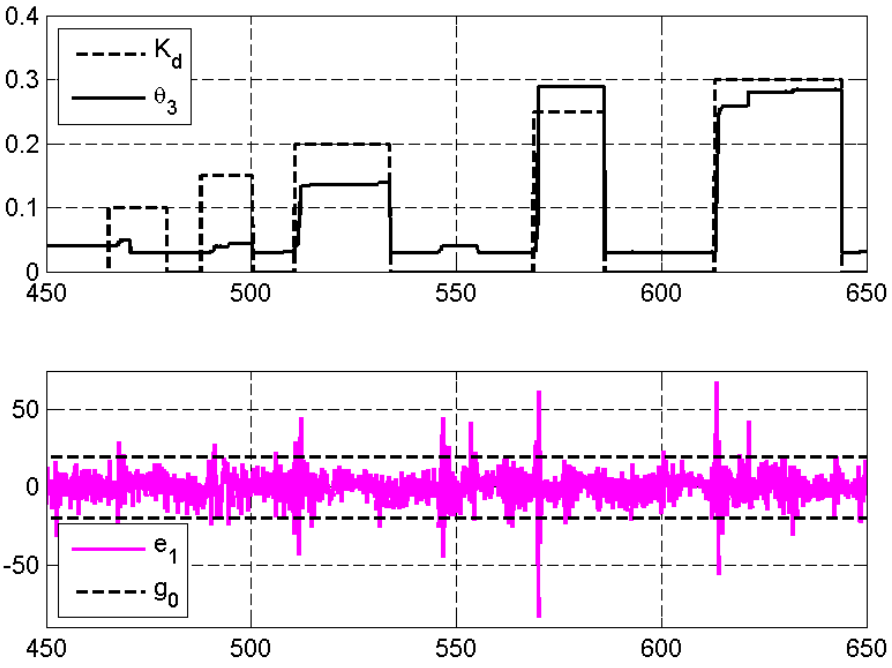

Figure 8.6.1: Response of the adaptive pitch rate controller to different steps in the destabilising gain K_d in the first fly-by-wire adaptation test

the CG in flight.

8.6 Fly-by-wire adaptation tests

The adaptive pitch rate controller was tested in flight by destabilising the aircraft using positive feedback, as described in the previous section. Initially, the controller was used in fly-by-wire mode in conjunction with the airspeed controller.

Since the output disturbance could not be eliminated completely, a dead zone had to be used in the adaptive law to prevent unnecessary adaptation. It was found that a dead zone width of 20°/s would prevent unnecessary adaptation without losing too much sensitivity to changes in the aircraft dynamics. Also, since it was seen that a feedback gain which is too large can cause instability, the adapted negative feedback gain was limited so that the net pitch rate feedback gain ($\theta_3 - K_d$) would not exceed 0.04, which was found to be a safe value.

Figure 8.6.1 shows the response of the adapted feedback gain θ_3 and the pitch rate error to different steps in the destabilising gain. When the destabilising gain was stepped to 0.1 and 0.15, the system remained stable without any significant adaptation of the feedback gain. When K_d was stepped from zero to 0.2, θ_3 quickly jumped from 0.03 to 0.134 and settled there when the output error re-entered the dead zone, resulting in net positive feedback with a gain of 0.066 after adaptation.

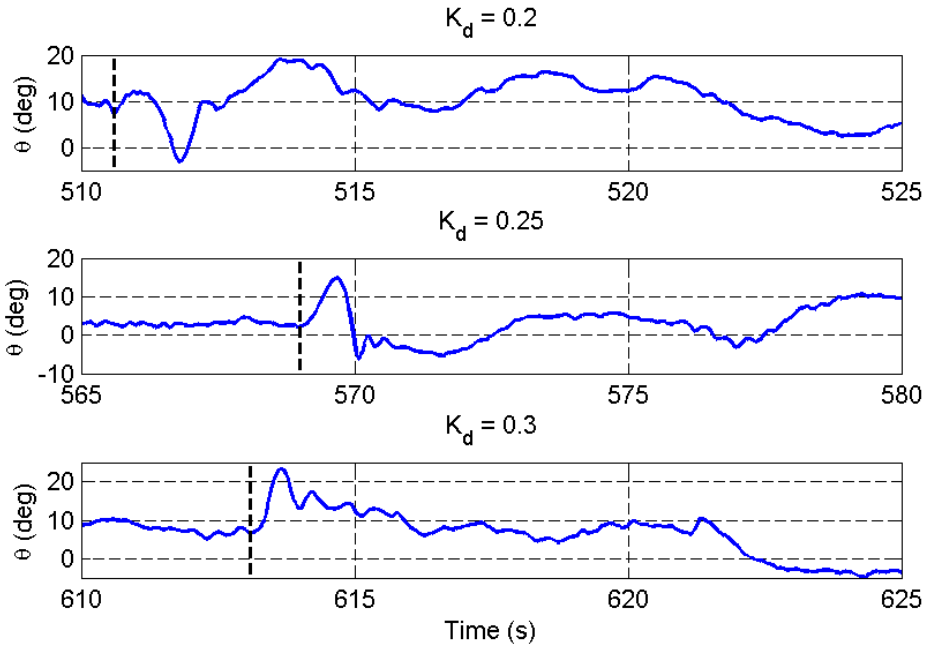

Figure 8.6.2: Pitch angle responses in the first adaptation test. The vertical dashed lines indicate when the steps in K_d took place.

When the destabilising gain was stepped to 0.25, the aircraft experienced a response of a much larger magnitude. The output error was large enough that the feedback gain adapted up to the limit within one second after the step. When K_d was stepped from zero to 0.3, θ_3 settled at a value slightly less than the destabilising gain, resulting an a small amount of net positive feedback.

Figure 8.6.2 shows the response of the pitch angle estimate to the last three steps in K_d. In each case, the aircraft experienced a large perturbation in pitch angle, which faded away after the aircraft was re-stabilised by the adaptation.

This flight test was repeated for a demonstration a week later. For the second flight, only the three destabilising gains that had caused significant adaptation in the first flight test were used. The response of the adaptive controller in this flight is shown in Figure 8.6.3.

The response of the adaptive controller when K_d was stepped to 0.2 is very similar to the previous flight, with the adaptation again resulting in net positive feedback. This time, however, the step to 0.25 also resulted in net positive feedback after adaptation, while the step to 0.3 caused the feedback gain to reach its limit.

These results show that, as expected, the adaptive law ensures stability of the closed-loop system, but does not ensure that the controller parameters converge to their ideal values. They also indicate that the behaviour of the adaptive control system can be slightly unpredictable in practice, depending on the exact conditions when the destabilising gain is stepped.

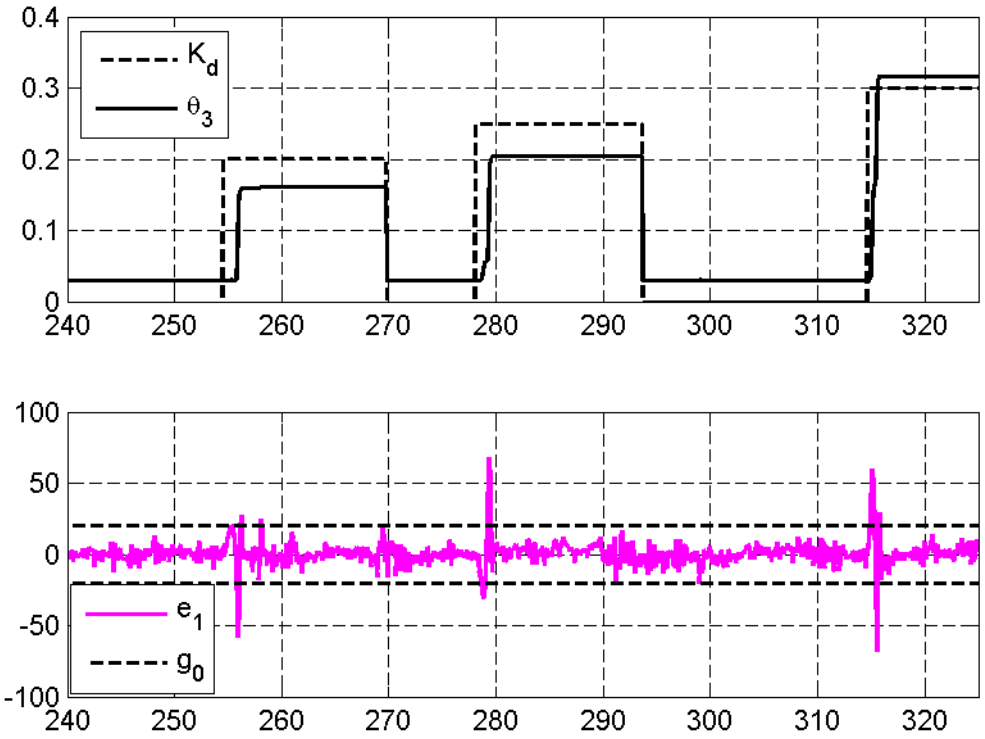

Figure 8.6.3: Response of the adaptive pitch rate controller to different steps in the destabilising gain K_d in the second fly-by-wire adaptation test

In both these flight tests, more positive feedback was required to destabilise the aircraft than the linear analysis had predicted. This indicates a difference in behaviour between the aircraft model and the actual aircraft. It appears that either the pitching moment caused by an elevator deflection ($C_{m_{\delta_e}}$) is less in practice than the value calculated by AVL, or the moment of inertia around the pitch axis (I_{yy}) is more than expected. The aircraft model was adjusted accordingly in subsequent simulations by decreasing the magnitude of $C_{m_{\delta_e}}$.

8.7 Adaptation test with outer loops

The fly-by-wire adaptation tests showed that the adaptive pitch rate controller can keep the aircraft stable, but the test results do not show clearly that the positive pitch rate feedback actually destabilises the aircraft, and therefore that the adaptive control system is able to re-stabilise an unstable system. In an effort to demonstrate this, the adaptive controller was also tested with the outer control loops enabled.

Figure 8.7.1 shows the root locus of the full longitudinal closed-loop system for positive feedback of the pitch rate to the elevator. This analysis shows that the short-period poles will be unstable for destabilising gains greater than about 0.1 – however, as mentioned previously,

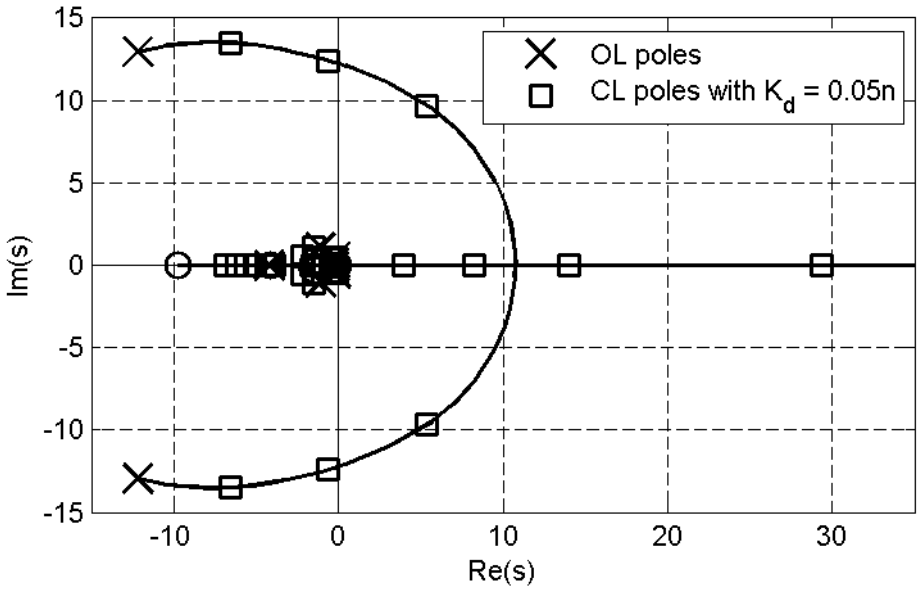

Figure 8.7.1: Root locus of the full closed-loop dynamics for positive pitch rate feedback

more positive feedback would probably be needed to destabilise the system in practice.

For this flight test, the adaptation dead zone was widened to 30°/s to delay adaptation and allow more visibly unstable oscillations before the aircraft is re-stabilised. Simulations and previous flight tests suggested that a destabilising gain around $K_d = 0.2$ could produce a visibly unstable oscillation before adaptation takes place, and therefore the destabilising gain was stepped to a number of values close to 0.2.

Figure 8.7.2 shows the response of the adaptive pitch rate controller when the destabilising gain was stepped from zero to 0.15, 0.175 and 0.2. The first two gains caused the aircraft to oscillate with a growing amplitude for about two seconds before the pitch rate error left the dead zone. In both cases, this caused the negative feedback gain to be adapted to a value where there was net positive feedback with a gain of about 0.06. These adaptations were just enough to re-stabilise the system, and the oscillations started to fade away at a relatively slow rate.

When the destabilising gain was stepped to 0.2, the aircraft entered a growing oscillation which quickly caused the output error to jump relatively far out of the dead zone. This caused significant adaptation of the negative feedback gain, which cancelled out the positive feedback almost exactly, and no poorly damped oscillations were visible after adaptation.

These results clearly show that the positive pitch rate feedback made the closed-loop system unstable, but that the adaptive pitch rate controller was able to re-stabilise the aircraft quickly.

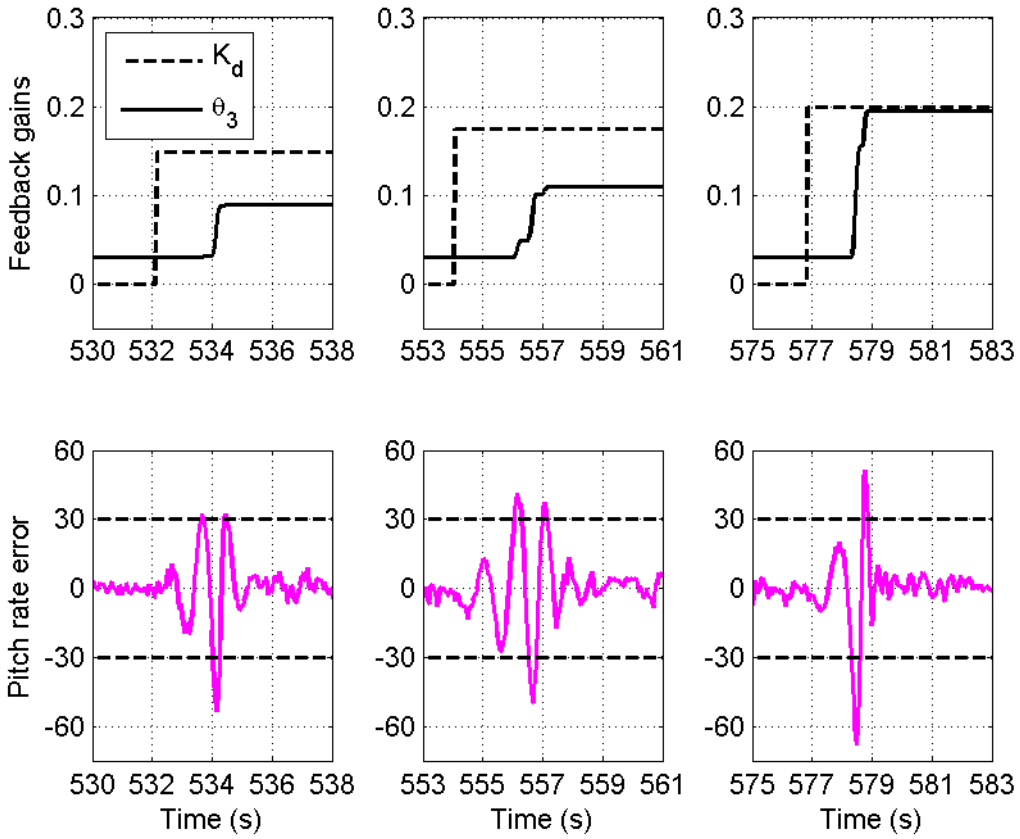

Figure 8.7.2: Response of the adaptive pitch rate controller to different steps in the destabilising gain K_d with outer loops enabled

8.8 Summary

In this chapter, results were given of flight tests that were used to test the adaptive control system in practice.

Flight tests of the pitch rate controller without adaptation showed that the aircraft can become unstable if the pitch rate feedback gain is too large. This was probably due to a combination of vibrations of the IMU relative to the aircraft, fluttering of the top cover of the aircraft, and the second-order Butterworth filter used by the pitch rate gyroscope. Therefore the adapted gains were limited to safe values when adaptation was enabled in flight.

The adaptive controller was tested in flight by destabilising the aircraft with positive pitch rate feedback, and allowing the control gains to be adapted to re-stabilise the system. Destabilising gains were used that linear analysis showed would make the aircraft unstable. In fly-by-wire operation, these destabilising gains caused large pitch rate and pitch angle responses, while with the outer loops enabled they caused visibly unstable oscillations. However, the adaptive control system quickly reacted to the unstable response and re-stabilised the closed-loop system within seconds.

These results do not provide direct insight into how the adaptive control system would handle a shift in the centre of gravity, which was the failure case chosen to demonstrate the fault-tolerant adaptive control system for this project. They do, however, show that the adaptive control system is able to re-stabilise an unstable system in practice, and so demonstrate its fault tolerance in a practical way.

One question mark over the validity of the flight test results is that the source of instability and the technique to address it are both based on pitch rate feedback to the elevators, and therefore can cancel each other out exactly. By contrast, if the Variable Stability UAV were to become unstable due to a CG shift in practice, the adaptive law would still increase the feedback gain θ_3, but this would not cancel the effect of the CG shift exactly. Therefore the total pitch rate feedback could be increased to a value which could aggravate the instability, as was seen in the early flight tests.

This extreme sensitivity to excessive negative feedback, however, is a problem specific to the aircraft that was used, and was caused by the factors discussed in Section 8.4. If the adaptive control system were implemented on an aircraft which does not suffer from the IMU and structural vibrations which affect the Variable Stability UAV, then the adaptive law would probably be able to increase the pitch rate feedback gain much further without causing instability.

Chapter 9

Conclusion

9.1 Summary

The goal of this thesis was to investigate the use of model reference adaptive control as part of a fault tolerant control system for a UAV. This was done by designing an adaptive control system to handle damage-induced longitudinal shifts in the centre of gravity of an aircraft, which were chosen as a suitable example situation to demonstrate the effectiveness of adaptive control. This control system was tested using linear analysis, non-linear simulations and flight tests to evaluate its fault tolerance.

A non-linear model of a fixed-wing aircraft was developed which includes the effect of CG shifts on the longitudinal aerodynamic parameters. Expressions were derived for these parameters as functions of their nominal values and the longitudinal position of the CG. These expressions were found to correspond well with the results of an AVL analysis.

The expressions were used in a linearised model of the longitudinal dynamics to analyse the effect of CG shifts on the behaviour of the aircraft. It was found that sufficiently large CG shifts will destabilise the short period mode of the aircraft, which indicated that an adaptive controller should be designed to control this mode of motion. If this controller could re-stabilise the short period mode when the CG shifts backwards, it could ensure that the full closed-loop system will remain stable.

This analysis, along with an investigation of adaptive control techniques based on stability theory, motivated the design of an adaptive pitch rate controller, with a fixed-gain longitudinal control system around it. The fixed-gain control system consisted of climb rate and altitude control loops closed successively around the adaptive pitch rate controller, as well as an airspeed controller parallel to it. These control loops could be designed with fixed parameters because the adaptive pitch rate controller would account for any changes to the aircraft dynamics due to in-flight damage. A linear closed-loop analysis of this control system confirmed that CG shifts can destabilise an autopilot which uses only fixed parameters.

The behaviour of the adaptive control system was investigated in non-linear simulation.

It was found that it is able to handle instantaneous CG shifts very well. When the adaptive control system was used, shifts that would destabilise a fixed-gain control system would cause the aircraft to experience a transient perturbation, which would quickly fade away as the adaptive law adjusted the parameters to re-stabilise the aircraft.

The basic adaptive control system was found to be quite sensitive to disturbances, such as the pitching moment disturbance caused by a CG shift, as well as measurement noise. A number of modifications were made to improve its robustness to these phenomena. An integral control law was added in parallel with the adaptive pitch rate controller to adjust the trim elevator setting in order to reject constant disturbances and prevent unwanted adaptation. Leakage and a dead zone were investigated as modifications to the adaptive law to improve its noise tolerance. It was found that both techniques prevented parameter drift due to noise, but that leakage negatively affected the response of the system to CG shifts.

As a secondary objective, the adaptive control system was also tested in simulation as a solution to the variable stability problem, where the CG is moved backwards intentionally and gradually to change the behaviour of the aircraft. The adaptive control system was found to be less effective in solving this problem than in providing fault tolerance. It was able to keep the aircraft stable during and after a gradual CG shift, but only barely so, leading to a very poorly damped response after the adapted controller parameters have settled.

A number of flight test were done to test the adaptive controller in practice. The tests were done using the Variable Stability UAV, which was designed and built with a moveable CG for a previous project at Stellenbosch University. However, necessary modifications to the aircraft prevented it from being made physically unstable in this way, and therefore the adaptive control system was tested by destabilising the aircraft using positive pitch rate feedback. When this was done in flight, the aircraft experienced large perturbations or visibly unstable oscillations, but the adaptive control system was able to re-stabilise the aircraft and restore control, preventing the aircraft from stalling or crashing.

The simulation and flight test results indicate that an adaptive control system, such as the one developed for this project, could be very effective as part of a fault-tolerant flight control system. The adaptive control system could regain stability immediately after a failure occurs, which would allow other components of the fault-tolerant system to identify the failure and reconfigure the control system to restore performance.

9.2 Recommendations

The adaptive control system developed for this project could be used as part of an integrated active fault-tolerant control (AFTC) system. It could also be subjected to a number of further tests to assess its performance, or different modifications could be investigated to improve it, and it could be applied to other problems besides restoring stability of a UAV after a failure.

9.2.1 Integration into an active fault-tolerant control system

As mentioned in the introduction, the role of adaptive control within an integrated AFTC system would be to provide a first line of defence against in-flight damage, quickly re-stabilising the aircraft and giving the other components time to identify the failure and reconfigure the control system to restore performance in an optimal way.

If a dead zone is used in the adaptive law, as was the case in this project, the output error leaving the dead zone could not only trigger the adaptation, but could also serve as an indication to the AFTC system that the aircraft dynamics have changed.

After a failure has occurred and the adaptive controller has re-stabilised the aircraft, the AFTC system would run some form of system identification to determine how exactly the behaviour of the aircraft has changed. If a sufficiently accurate model of the new aircraft dynamics could be determined, the controller parameters could be updated deterministically, and the adaptive law disabled.

Furthermore, a fault detection and isolation (FDI) algorithm could determine which part of the aircraft was damaged to cause the change in dynamics. If any actuators have been identified as damaged, a control re-allocation algorithm could be used to restore performance as closely as possible to what it was before the failure.

Future research could evaluate robust control as part of an AFTC system, and compare its effect to that of adaptive control. The two techniques could also be combined to create an adaptive robust control system.

9.2.2 Further testing of the adaptive control system

Only limited practical testing of the adaptive control system could be done for this project due to the physical limitations of the Variable Stability UAV. Implementing an adaptive control system on an aircraft with better sensors and structural rigidity could allow more in-depth tests of the response of the adaptive control system to changes in the aircraft behaviour.

If the variable stability capability of the aircraft could be restored, it could be used to test the response of the adaptive control system to actual shifts in the centre of gravity. Instant CG shifts could be simulated in flight by using knowledge of the CG position to update the controller parameters and keep the aircraft stable while the CG is moving backwards, and then switching back to the nominal controller parameters once the CG is in the backward position. Then the adaptive control system could be engaged to compensate for this instantaneous change in the closed-loop dynamics.

It could also be valuable for both research and demonstration purposes to create a system by which mass can be dropped from the aircraft in flight – either a payload attached to the front of the aircraft, which will cause an instant backward CG shift, or a part of the aircraft breaking off to replicate in-flight damage. The handling of such situations by the adaptive control system could then be tested in flight.

9.2.3 Improvements to the adaptive control system

Techniques could be investigated to improve the handling of gradual CG shifts by an adaptive control system. One possibility would be to estimate the CG position in real time, which would allow the autopilot to apply the control techniques of [4] without being given explicit information of the CG position.

Alternatives to the use of a dead zone and leakage as noise-tolerance modifications of the adaptive law could be investigated. For instance, a hybrid adaptive law can be used, which uses a continuous-time integral term in the update equation for a discrete-time adaptive law. Integrating the noise and slowing the response time of the adaptive control system in this way can improve its noise tolerance [12].

Another option, suggested by [10], could be to monitor the input signals to the adaptive control system to determine whether or not it is being sufficiently excited that the output error will contain useful information, and not just noise. This could provide a better criterion for switching adaptation on and off than the magnitude of the output error.

An alternative to ITEC in preventing adaptation caused by constant disturbances is the technique used in [15], where the output error is periodically reset to zero. Then, if there is an offset between the plant and model outputs, the adaptive law will effectively check for a change in the offset over the last period, rather than a difference between the output. Then the offset due to a constant pitching moment will not cause continued adaptation.

9.2.4 Other applications of adaptive control

The adaptive control system could also be used to restore the performance of the autopilot, rather than just ensuring stability. An adaptive autopilot could be designed for aggressive or aerobatic flight, and could ensure that manoeuvrability is maintained in the presence of actuator failures or other changes to the aircraft behaviour. The adaptive control system could also be expanded to the control of the lateral dynamics of the aircraft, which are much less likely to become unstable than the longitudinal dynamics.

Adaptive control can also be applied to other problems in the UAV field, besides fault tolerant control. For instance, the use of adaptive techniques to control an aircraft over a wide envelope or in different flight conditions such as take-off and landing could be investigated. Adaptive control algorithms could also be applied to other vehicles besides fixed-wing aircraft, such as autonomous helicopters, submarines and ground vehicles.

Research could also be done into the wide range of other adaptive control approaches, beyond the relatively simple techniques used in this project. Most of the recent adaptive control research has been around the use of neural networks and fuzzy logic, and an investigation into the application of these techniques to adaptive control of UAVs might be worthwhile.

Appendix A

The Variable Stability UAV

A.1 System description

This appendix describes the full aircraft system used to test the adaptive control system in practice, consisting of the aircraft, the ground station and the hardware-in-the-loop simulation setup.

The adaptive control system was tested in flight using the Variable Stability UAV built at Stellenbosch University. The aircraft was built by adding the avionics developed at the SU Electronic Systems Lab (ESL) and an E-Flite Power 25 motor [40] to a Queen Bee glider [41].

A.1.1 Airframe

The Queen Bee is a flying-wing glider made by Windrider Aviation. It is made out of expanded polypropylene (EPP) and has a wing span of 2.5 metres. The motor and the avionics were added to convert it from a RC glider to a powered UAV.

A.1.2 Power supply

The Variable Stability UAV is powered by two 3-cell lithium-polymer (LiPo) batteries: a 3300 mAh battery to power the motor, and a 1100 mAh battery to power the avionics. Both batteries generate about 12.6 V when fully charged, and have a discharge rating of 35C.

A 5 V nickel-cadmium (NiCad) battery was used as a backup battery. This battery can power the servo board and RC receiver if power from the main avionics battery is lost, which would allow the safety pilot to land the aircraft.

A.1.3 Avionics

A block diagram of the ESL Avionics is shown in Figure A.1.1. It is built around an onboard computer (OBC) with two PIC32 microcontrollers, one of which was used for this project, a uBlox GPS module, and a MaxStream RF module, which it uses to communicate

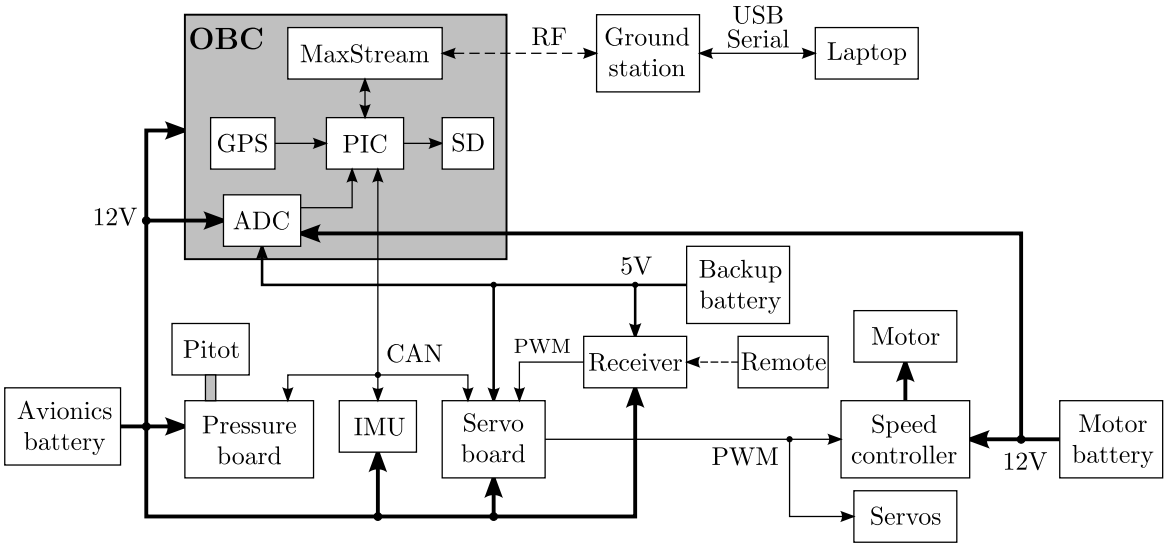

Figure A.1.1: Block diagram of the ESL avionics on board the Variable Stability UAV

with a ground station laptop. The OBC also contains connections for the analog-to-digital converters (ADCs) of the PIC, which are used in the Variable Stability UAV to measure the voltages of all the batteries, as well as the current drawn from the motor battery. Furthermore, the OBC contains a slot for a MicroSD card, which can be used to log data in-flight. The OBC is connected via a CAN bus to a servo board, an inertial measurement unit (IMU) and a pressure board.

The servo board receives signals from the safety pilot's remote control using a Spektrum AR9100 RC receiver, and sends PWM commands to the servos of the six control surfaces, as well as the speed controller which controls the motor. The servo board also includes a microcontroller which performs the mixing of virtual actuator commands to the physical actuators when the autopilot is disengaged; when the autopilot is armed, this mixing is performed by the OBC.

The IMU contains analog accelerometers and gyroscopes which measure the accelerations and rotation rates in the body axis system of the aircraft. The IMU performs analog-to-digital conversion and sends the ADC values of the measurements to the OBC via the CAN bus. It also includes analog second-order Butterworth filters with a cutoff frequency of 8 Hz for anti-aliasing.

The pressure board contains pressure sensors, which are connected through plastic tubes to the pitot tube mounted under the right wing. These sensors measure the static and total air pressure, which can be subtracted from each other to obtain the dynamic pressure. The static and dynamic pressure can in turn be use to calculate the altitude and airspeed respectively. The pressure board also includes a magnetometer, which can be used to determine the attitude of the aircraft.

A.1.4 Firmware

The standard OBC firmware developed in the ESL performs the following functions:

- Managing the PIC and the components of the OBC at a low level
- Managing communications with other components of the avionics through the CAN bus
- Communicating with the servo board – receiving RC commands and sending real or virtual actuator commands
- Receiving sensor data from the IMU, the pressure board and the ADC channels on the OBC
- Managing information from the GPS module
- An extended Kalman filter (EKF) which provides kinematic state estimation. It uses sensor information from the IMU, GPS and magnetometer to estimate the aircraft's velocity, position and attitude.
- Handling commands sent from the ground station through the RF link
- Sending telemetry to the ground station
- Logging flight data on the SD card

The firmware was modified to include the adaptive control system. All the control laws of Chapter 6 and the adaptive law were implemented in the firmware, using Euler integration to emulate the continuous-time controller dynamics. The control system firmware was written to allow control loops to be enabled and disabled and controller parameters to be set from the ground station.

A.1.5 Ground station

The ground station system consists of the ground station hardware and a laptop running the ground station software. The ground station hardware contains a MaxStream RF module which communicates with the MaxStream on-board the aircraft, and a serial connection to the laptop.

A screen shot of the ground station program is shown in Figure A.1.2. It is based on the standard ESL ground station software, developed in QT. The software includes controls to:

- Start and reset the OBC
- Start and stop data logging on the SD card
- Toggle the avionics to HIL simulation mode

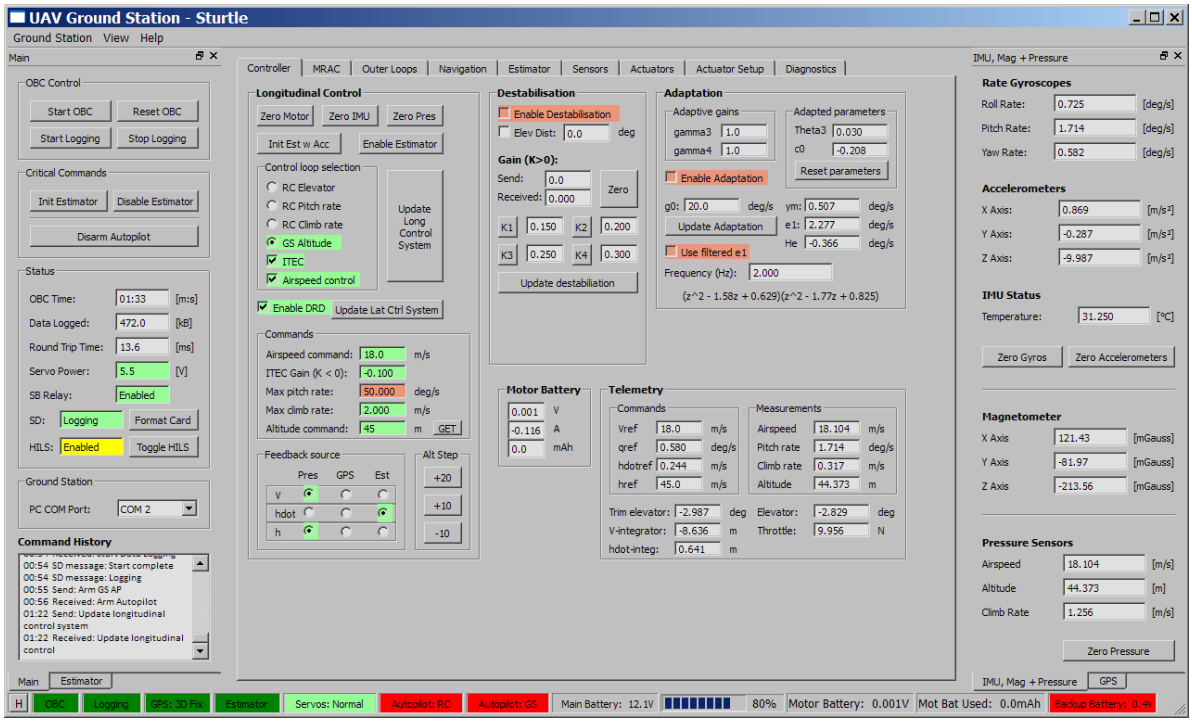

Figure A.1.2: Screen shot of the ground station software

- Manage the sensors of the aircraft (GPS, IMU, magnetometer and pressure sensors)
- Setup and arm the estimator
- Control the servos of the aircraft directly for servo calibration
- Display sensor, actuator, status and control telemetry sent by the OBC over the RF link

The ground station also stores all the telemetry data on the hard drive of the laptop. The standard ground station software was modified to allow the control loops of the adaptive control system to be enabled or disabled, and its parameters to be changed.

A.1.6 Hardware-in-the-loop simulation

The implementation of the control system on the avionics of the Variable Stability UAV can be tested in hardware-in-the-loop (HIL) simulations. In these simulations, the avionics and ground station operate in the same way as in flight, except that the aircraft behaviour is represented by a Simulink model. A command can be sent from the ground station which instructs the OBC to use sensor values from the simulator rather than those from the sensors themselves. The servo commands from the OBC are sent to the simulation to close the loop.

A HIL interface board connects the PC running Simulink to communicate the sensor and servo data. It is connected to the PC using a USB connection, and to the avionics using an extension of the CAN bus.

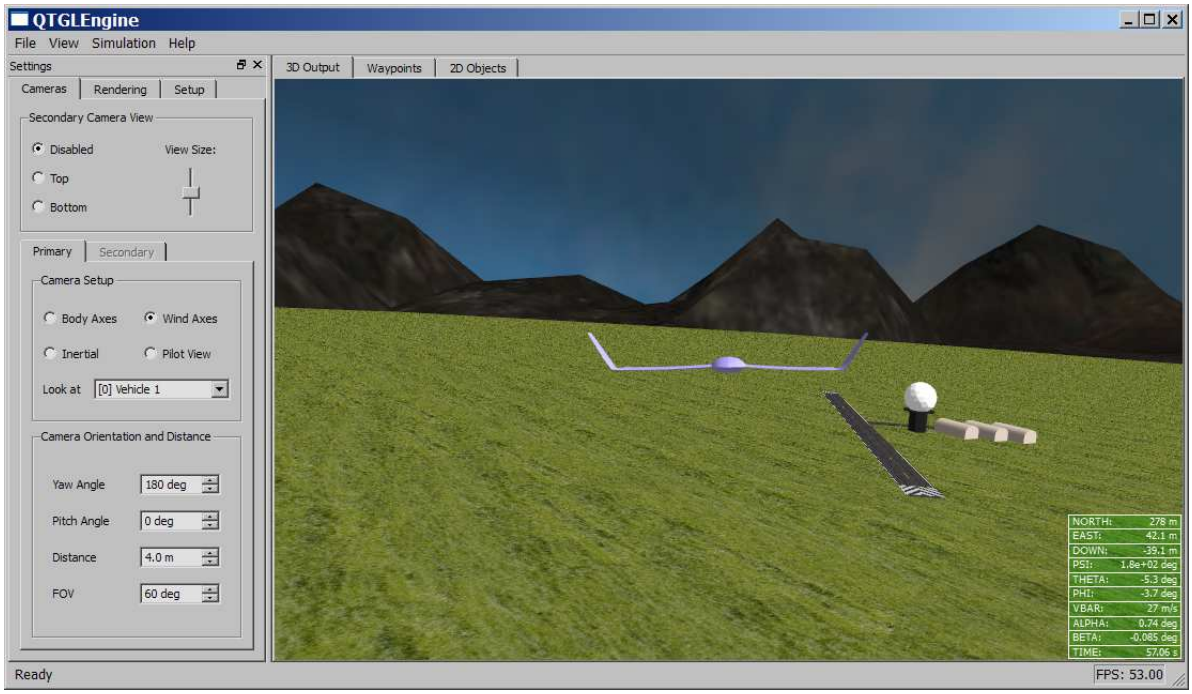

Figure A.1.3: The OpenGL engine displaying a HIL simulation

Both HIL and Simulink simulations of the control system can be visualised using an OpenGL display engine written at the ESL. A screen shot of the OpenGL engine is shown in Figure A.1.3.

A.2 Actuator definitions and mixing matrices

This appendix defines the physical actuators of the Variable Stability UAV, as well as the virtual actuators commanded by both the human pilot and the autopilot, and the relation between the two sets of actuators.

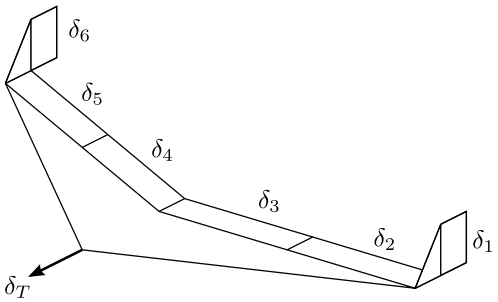

Figure A.2.1: The physical actuators of the Variable Stability UAV

A.2.1 Physical actuators

The Variable Stability UAV is controlled using seven actuators, depicted in Figure A.2.1. Actuators δ_1 to δ_6 are the aerodynamic control surfaces, namely a rudder and an outboard and inboard elevon on each wing, while δ_T is the thrust actuator.

Usually aerodynamic actuators are defined in such a way that a positive actuator deflection produces a negative moment. In keeping with this convention, the two rudders δ_1 and δ_6 were defined such that a positive deflection of either rudder will produce a negative yaw moment, and therefore a deflection to the left side of the aircraft is defined as positive. The four elevons δ_2 to δ_5 were defined such that a positive deflection of any elevon will produce a negative pitching moment, and therefore a downward deflection is defined as positive.

The servos of the Variable Stability UAV were calibrated so that each of the elevons has a maximum deflection of $\pm 24°$, and both rudders have a range of $\pm 15°$. The maximum thrust of the motor was determined in a thrust test to be 17 N.

A.2.2 Virtual actuators

Fixed-wing aircraft are normally modelled as having the four conventional actuators: throttle (δ_T), aileron (δ_A), elevator (δ_E) and rudder (δ_R). The six physical aerodynamic actuators of the Variable Stability UAV can be grouped together into virtual actuators which correspond to the three conventional aerodynamic actuators. This will simplify the aircraft model and the control system design.

The following virtual actuators are defined:

$$\delta_A = \frac{1}{4}\big(-\delta_2 - \delta_3 + \delta_4 + \delta_5\big) \tag{A.2.1}$$

$$\delta_E = \frac{1}{4}\big(\delta_2 + \delta_3 + \delta_4 + \delta_5\big) \tag{A.2.2}$$

$$\delta_R = \frac{1}{2}\big(\delta_1 + \delta_6\big) \tag{A.2.3}$$

Both the virtual aileron and elevator actuators are averages of the deflections of the four elevons. The left and right elevons contribute to the virtual aileron when they are deflected differentially, and contribute to the virtual elevator when they are deflected in the same direction. The virtual rudder actuator is the average of the deflections of the two rudders.

Furthermore, the physical actuators are constrained as follows:

$$\delta_1 = \delta_6 \tag{A.2.4}$$

$$\delta_2 = \delta_3 \tag{A.2.5}$$

$$\delta_4 = \delta_5 \tag{A.2.6}$$

These constraints imply that the two rudders will always be actuated together to have the same deflection, as will the two elevons on the left wing and the two elevons on the right wing.

Equations A.2.1 to A.2.6 can be expressed in matrix form as follows, with the thrust actuator also included:

$$\begin{bmatrix} \delta_T \\ \delta_A \\ \delta_E \\ \delta_R \\ 0 \\ 0 \\ 0 \end{bmatrix} = \begin{bmatrix} 0 & 0 & 0 & 0 & 0 & 0 & 1 \\ 0 & -\frac{1}{4} & -\frac{1}{4} & \frac{1}{4} & \frac{1}{4} & 0 & 0 \\ 0 & \frac{1}{4} & \frac{1}{4} & \frac{1}{4} & \frac{1}{4} & 0 & 0 \\ \frac{1}{2} & 0 & 0 & 0 & 0 & \frac{1}{2} & 0 \\ 1 & 0 & 0 & 0 & 0 & -1 & 0 \\ 0 & 1 & -1 & 0 & 0 & 0 & 0 \\ 0 & 0 & 0 & 1 & -1 & 0 & 0 \end{bmatrix} \begin{bmatrix} \delta_1 \\ \delta_2 \\ \delta_3 \\ \delta_4 \\ \delta_5 \\ \delta_6 \\ \delta_T \end{bmatrix} \tag{A.2.7}$$

or

$$\boldsymbol{\delta}^V = T^{VR}\boldsymbol{\delta}^R \tag{A.2.8}$$

where $\boldsymbol{\delta}^V$ is the virtual actuator vector, $\boldsymbol{\delta}^R$ is the real actuator vector and T^{VR} is the transformation matrix from real actuators to virtual actuators.

If the autopilot is designed to generate virtual actuator commands, then these commands must be transformed to real actuator commands using T^{RV}, the transformation matrix from virtual actuators to real actuators, also known as the mixing matrix, which is the inverse of T^{VR}. For the above values of T^{VR}, the transformation from virtual to real actuators will be as follows:

$$\begin{bmatrix} \delta_1 \\ \delta_2 \\ \delta_3 \\ \delta_4 \\ \delta_5 \\ \delta_6 \\ \delta_T \end{bmatrix} = \begin{bmatrix} 0 & 0 & 0 & 1 & \frac{1}{2} & 0 & 0 \\ 0 & -1 & 1 & 0 & 0 & \frac{1}{2} & 0 \\ 0 & -1 & 1 & 0 & 0 & -\frac{1}{2} & 0 \\ 0 & 1 & 1 & 0 & 0 & 0 & \frac{1}{2} \\ 0 & 1 & 1 & 0 & 0 & 0 & -\frac{1}{2} \\ 0 & 0 & 0 & 1 & -\frac{1}{2} & 0 & 0 \\ 1 & 0 & 0 & 0 & 0 & 0 & 0 \end{bmatrix} \begin{bmatrix} \delta_T \\ \delta_A \\ \delta_E \\ \delta_R \\ 0 \\ 0 \\ 0 \end{bmatrix} \tag{A.2.9}$$

Therefore the real aerodynamic actuators will have the following relation to the virtual actuators:

$$\delta_1 = \delta_6 = \delta_R \tag{A.2.10}$$

$$\delta_2 = \delta_3 = \delta_E - \delta_A \tag{A.2.11}$$

$$\delta_4 = \delta_5 = \delta_E + \delta_A \tag{A.2.12}$$

The deflection of both rudders is equal to the virtual rudder deflection. The elevons on the left wing are deflected positively for a positive virtual elevator deflection and negatively for a positive virtual aileron deflection, while the elevons on the right wing are deflected positively for both a positive virtual elevator deflection and a positive virtual aileron deflection.

The virtual actuators were defined for the Variable Stability UAV so that the virtual aileron and elevator would have a maximum deflection of $\pm 12°$, and the virtual rudder would have a range of $\pm 15°$. The virtual thrust actuator would have a maximum setting of 17 N.

A.3 Aircraft parameters

This appendix gives the parameters of the Variable Stability UAV that were used in modelling, analysis, control design and simulation, and describes how they were obtained.

A.3.1 Inertial and geometric properties

Table A.1 gives the inertial properties of the Variable Stability UAV. The moments of inertia were determined experimentally in [4], and it was assumed that the modifications to the aircraft did not change them significantly, since most of the mass that was added was located close to the centre of gravity. The mass was determined by weighing the aircraft midsection with the avionics installed, the two wings and the batteries separately, and the nominal position of the CG was determined by balancing the aircraft on its lateral axis.

Inertial property	**Value**
Mass (m)	3.9 kg
Distance from nose to CG	351 mm
Roll axis moment of inertia (I_{xx})	0.783 kg·m^2
Pitch axis moment of inertia (I_{yy})	0.188 kg·m^2
Yaw axis moment of inertia (I_{zz})	0.706 kg·m^2

Table A.1: Inertial properties of the Variable Stability UAV

The geometrical properties of the Variable Stability UAV, taken from [4], are given in Table A.2. As mentioned in Chapter 8, the mean aerodynamics chord $\bar{c}$ and the stability and control derivatives given in [4] were inconsistent. The value chosen for $\bar{c}$ is not important as long as it is used consistently, since it is merely used to make the aerodynamic parameters non-dimensional. A value of $\bar{c} = 0.33$ m was used consistently in analysis and modelling for this project.

Geometric property	Value
Wing area (S)	0.871 m^2
Wing span (b)	2.55 m
Aspect ratio (A)	7.18
Mean aerodynamic chord ($\bar{c}$)	0.33 m
Oswald efficiency factor (e)	0.75

Table A.2: Geometric properties of the Variable Stability UAV

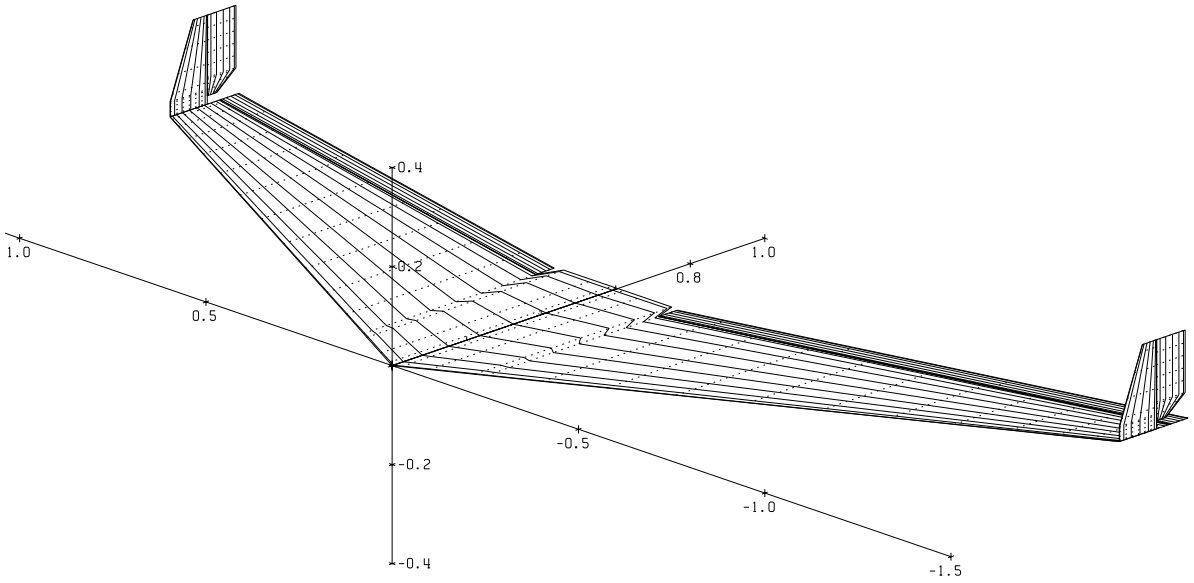

Figure A.3.1: AVL model of the Variable Stability UAV

A.3.2 AVL Analysis

The aerodynamics parameters of the Variable Stability UAV were determined by analysing the airframe using AVL, a vortex lattice analysis program. This program requires a geometrical model of the airframe, as well as the mass, moments of inertia, and CG position of the aircraft. It also requires the parasitic drag coefficient C_{D_0}, which is difficult to determine exactly. It was found, however, that using a value of $C_{D_0} = 0.055$ in simulation produced similar results to flight tests.

The geometrical model of the Variable Stability UAV that was used in the AVL analysis is shown in Figure A.3.1. Tables A.3 and A.4 give the longitudinal and lateral stability control derivatives calculated by AVL for the nominal CG position.

	α	q	δ_e
C_L	4.6149	4.3966	0.93435
C_m	-0.64237	-1.5964	-0.48838

Table A.3: Longitudinal non-dimensional stability and control derivatives of the Variable Stability UAV

The stability and control derivatives calculated by AVL depend on the CG position specified. Figures A.3.2 and A.3.3 show the parameters calculated by AVL if the CG is a number of distances behind the nominal position, 351 mm from the nose. The parameters that are not shown are unaffected by the CG shift.

These figures show that the longitudinal parameters are much more affected by the shift than the lateral parameters are.

	β	p	r	δ_a	δ_r
C_y	-0.1842	-0.0569	0.0465	-0.00768	0.0868
C_l	-0.0293	-0.48	0.0103	-0.1927	0.0165
C_n	0.0198	0.00883	-0.00725	0.00126	-0.0147

Table A.4: Lateral non-dimensional stability and control derivatives of the Variable Stability UAV

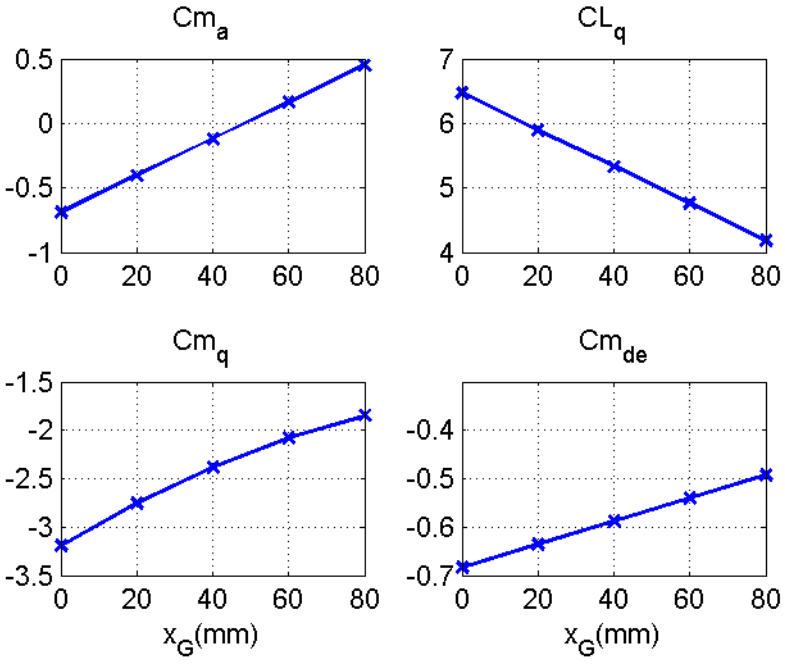

Figure A.3.2: Longitudinal parameters calculated by AVL for different CG positions, measured backwards from the nominal position of 351 mm

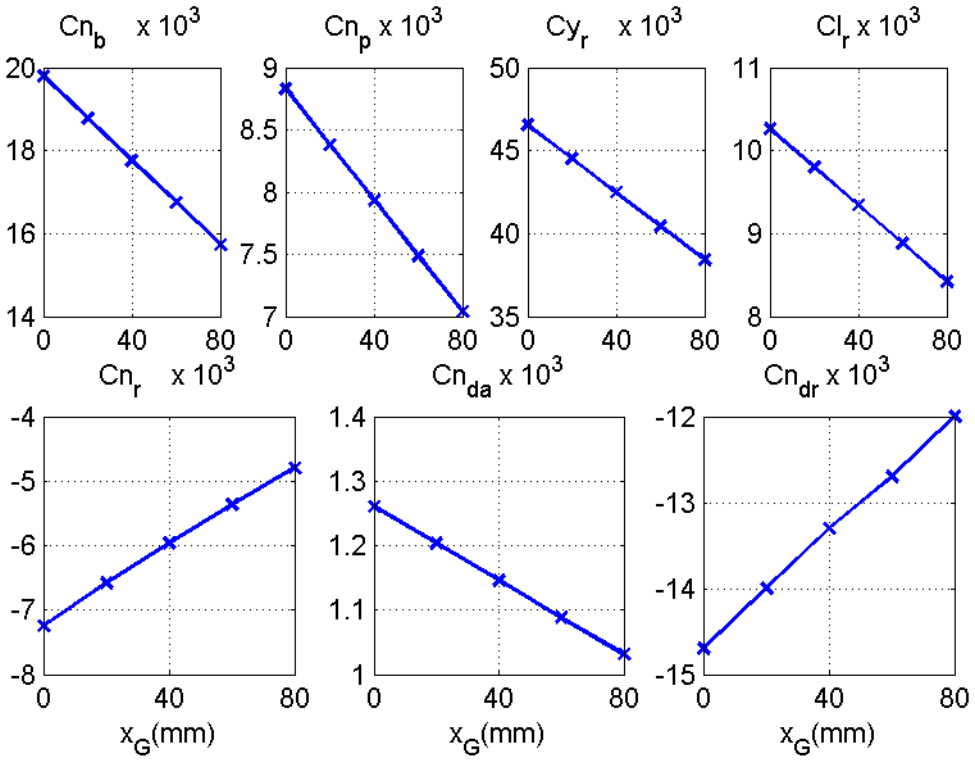

Figure A.3.3: Lateral parameters calculated by AVL for different CG positions, measured backwards from the nominal position of 351 mm

AVL also calculates the location of the neutral point of the aircraft. The neutral point of the Variable Stability UAV was calculated as 399 mm behind the nose of the aircraft, which is 48 mm behind the nominal CG. This correlates with the fact that $C_{m_\alpha} = 0$ when the CG shifts back by 48 mm, as found in Section 3.4.

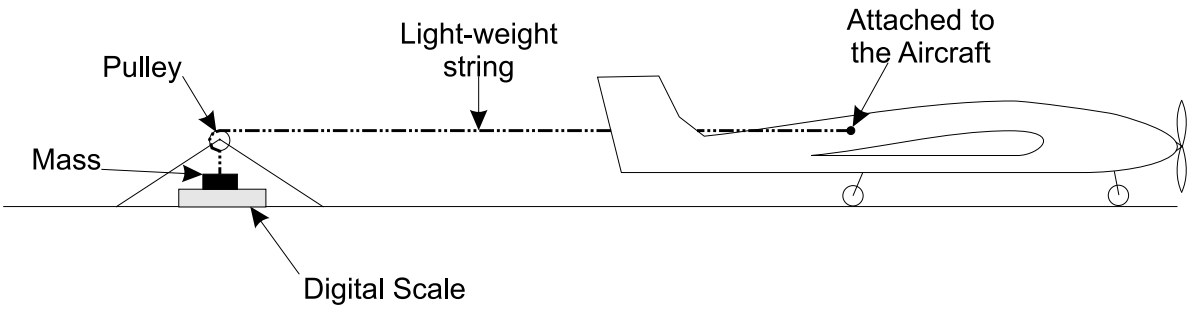

Figure A.3.4: Thrust test setup [4]

A.3.3 Thrust test

A thrust test was done using the setup shown in Figure A.3.4. A string was attached to the aircraft, taken around a pulley and attached to a weight on a digital scale. The throttle was opened to a number of settings, and at each setting the reading of the scale was noted, and current drawn from the motor battery and the throttle setting were logged on the on-board SD card.

The purpose of the thrust test is to determine the maximum thrust and the relation between the throttle setting and the thrust output, which can be used to calibrate the throttle setting for the autopilot, as well as to determine the maximum current that the motor will draw from its battery, which will determine whether or not the motor is in danger of burning out.

Figure A.3.5 shows the logged throttle setting and motor battery current measurement from the thrust test. The throttle setting is given in Aero units, where $+1$ represents the throttle being fully open and -1 represents the throttle being fully closed.

The throttle was stepped to a number of different values. At each value, the current measurement was allowed to settle and the mass reading was taken from the digital scale. This was first done for steps all the way up to full throttle. Then the throttle was closed and two more steps were done, but this time the throttle was not opened all the way, in order to minimise the risk of damaging the motor.

Figure A.3.6 shows the mass readings from the scale plotted against the throttle settings at the time the readings were taken, as well as the thrust calculated from the mass readings. The thrust can be calculated as the drop in the mass reading multiplied by gravity:

$$T = g(m_0 - m) \tag{A.3.1}$$

where $m_0 = 2.65$ kg is the mass of the weight that was used on the scale. Also shown in Figure A.3.6 is a linear curve fit performed on the five nonzero data points of the first thrust test. All five these points, as well as the two points of the second test, lie very closed to the line.

The data point where the throttle was closed does not lie near the line, since the engine

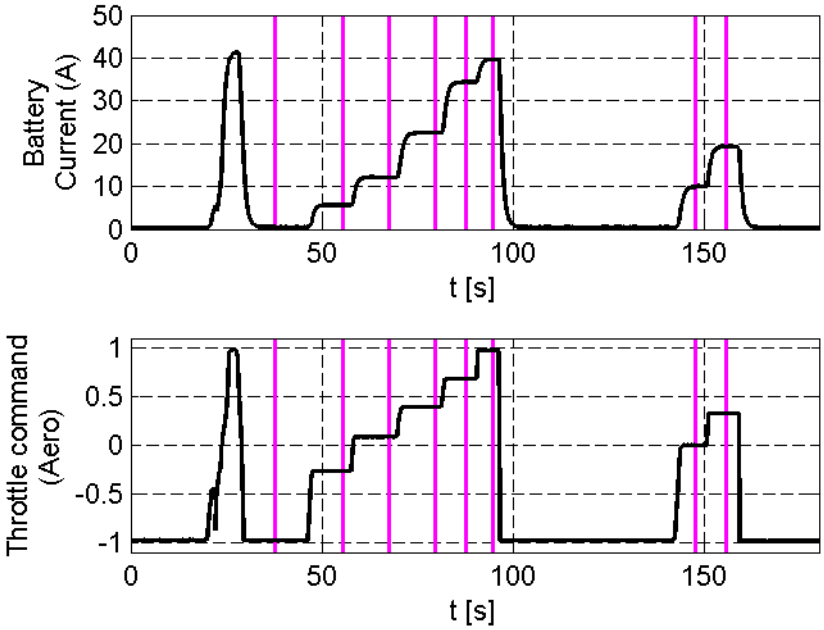

Figure A.3.5: Current drawn from the motor battery and throttle setting during the thrust test. The vertical lines indicate when the reading were taken from the digital scale.

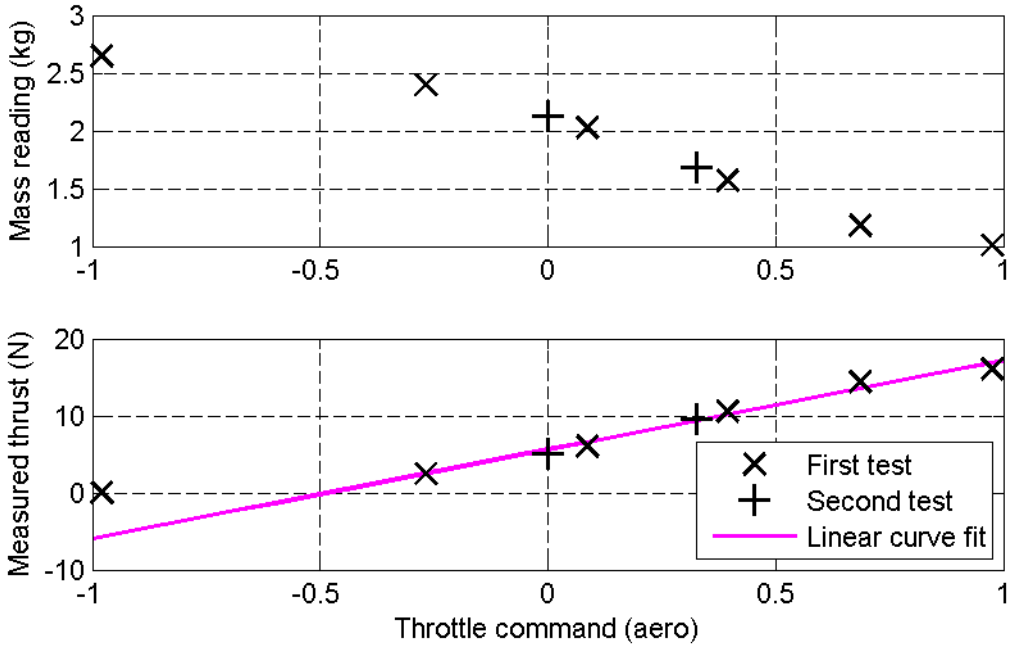

Figure A.3.6: Mass readings and corresponding thrust values from the thrust test, with a linear curve fit on the nonzero thrust points

does not produce any thrust if it is barely open. The straight line has a value of $T = 17.1$ N with the throttle fully open, and $T = -5.9$ N with the throttle fully closed. These values were used to calibrate the throttle commands from the autopilot.

The value of the engine time constant τ_T was assumed to be 0.2 seconds, since this is a typical value for this type of electric motor.

Appendix B

Stability theory

This appendix discusses some stability concepts which are relevant to the design of the adaptive control system. Sections B.1 and B.2 discuss the related concepts of strictly positive real systems and Lyapunov stability theory, while Section B.3 discusses the concept of stiffness in differential equations.

B.1 Strictly positive real transfer functions

In this section, we define a class of LTI systems known as *strictly positive real* (SPR) systems, which have useful properties in the design of adaptive control systems using Lyapunov stability theory. The class of systems is initially defined in the frequency domain using transfer functions, and then some properties are given of SPR systems in state space form.

The definitions and theorems in this section were taken from [12], and can also be found in other sources on adaptive and robust control such as [19].

B.1.1 Definitions and theorems

We begin by defining a class of transfer functions as *positive real*, and use this class of transfer functions to define a strictly positive real transfer function:

Definition B.1 *A transfer function $G(s)$ is **positive real** (PR) if:*

1. *$G(s)$ is real for real s*
2. *$\mathrm{Re}[G(s)] \geq 0$ for all $\mathrm{Re}[s] > 0$*

Definition B.2 *A transfer function $G(s)$, which is not identically zero for all s, is **strictly positive real** (SPR) if $G(s - \epsilon)$ is PR for some $\epsilon > 0$.*

The following theorem gives necessary and sufficient conditions for a transfer function to be SPR:

Theorem B.1 *Given a transfer function $G(s)$, which is not identically zero for all s, and has a relative degree n^* with $|n^*| \leq 1$. $G(s)$ is SPR if and only if:*

1. *$G(s)$ analytic in Re$(s) \geq 0$*
2. *Re$[G(j\omega)] > 0$ for all $\omega \in \mathcal{R}$*
3. *(a) When $n^* = 1$, $\lim_{|\omega|\to\infty} \left(\omega^2 \mathrm{Re}[G(j\omega)]\right) > 0$*

   (b) When $n^* = -1$, $\lim_{|\omega|\to\infty} \frac{G(j\omega)}{j\omega} > 0$

Having defined and shown the conditions for SPR transfer functions, we can now give the relevant properties of SPR systems. First we must define a *positive definite matrix*:

Definition B.3 *An $n \times n$ matrix A is **positive definite** if the inequality $\mathbf{x}^\mathsf{T} A\mathbf{x} > 0$ holds for every nonzero vector $\mathbf{x} \in \mathcal{R}^n$.*

Then we can state the Meyer-Kalman-Yakubovich (MKY) Lemma, a property of SPR systems which makes them very useful in Lyapunov stability theory:

Lemma B.1 (Meyer-Kalman-Yakubovich) *Given a state space representation of a SISO SPR system:*

$$\dot{\mathbf{x}} = A\mathbf{x} + Bu$$
$$y = C\mathbf{x} + du$$

with $d \geq 0$, then for any given symmetric positive definite matrix L, there exists a positive scalar ν, a vector q and a symmetric positive definite matrix P so that

$$A^\mathsf{T} P + PA = -qq^\mathsf{T} - \nu L$$
$$PB - C = \pm q\sqrt{2d}$$

B.1.2 Second-order SPR systems

For the design of the adaptive pitch rate controller, the reference model $W_m(s)$ must be chosen to be SPR, with two poles and one zero. The three requirements of Theorem B.1 can be simplified for this special case.

Point 1 in Theorem B.1 implies that $W_m(s)$ must be stable, while point 2 implies that the phase of the transfer function must be within the range $(-90^\circ,\ 90^\circ)$ for all frequencies. This places an upper bound on the frequency of the zero of $W_m(s)$, since the poles each contribute -90° of phase around their frequencies, and the zero must make its $+90^\circ$ contribution before the total phase exceeds -90°.

In order to apply point 3(a), we write $W_m(s)$ in the following form:

$$G(s) = \frac{k(s+b)}{s^2 + a_1 s + a_2} \tag{B.1.1}$$

Then it can be shown, by multiplying above and below the line with the complex conjugate of the denominator, that the real part of $W_m(j\omega)$ is:

$$\mathrm{Re}[W_m(j\omega)] = \frac{k(a_1 - b)\omega^2 + ka_2 b}{\omega^4 - (2a_2 - a_1^2)\omega^2 + a_2^2} \tag{B.1.2}$$

Therefore the limit in point 3(a) in Theorem B.1 evaluates as

$$\lim_{|\omega|\to\infty} \left(\omega^2 \mathrm{Re}[W_m(j\omega)]\right) = \lim_{|\omega|\to\infty} \left(\frac{k(a_1 - b)\omega^4 + ka_2 b\omega^2}{\omega^4 - (2a_2 - a_1^2)\omega^2 + a_2^2)}\right) \tag{B.1.3}$$

$$= k(a_1 - b) \tag{B.1.4}$$

$$\therefore k(a_1 - b) > 0 \tag{B.1.5}$$

Since all three constants must be positive, the inequality reduces to:

$$b < a_1 \tag{B.1.6}$$

If the poles of $W_m(s)$ are complex and of the form $s = -\sigma \pm j\omega_d$, then the denominator polynomial will be

$$s^2 + 2\sigma s + (\sigma^2 + \omega_d^2) \tag{B.1.7}$$

which implies that, for $W_m(s)$ to be SPR, the following relation must hold between the frequency of the zero and the real part of the poles:

$$b < 2\sigma \tag{B.1.8}$$

If $W_m(s)$ has two real poles $s = -p_1$ and $s = -p_2$, then the denominator polynomial will be

$$s^2 + (p_1 + p_2)s + p_1 p_2 \tag{B.1.9}$$

the following relation between the frequencies of the zero and the two real poles must hold for $W_m(s)$ to be SPR:

$$b < p_1 + p_2 \tag{B.1.10}$$

This places another upper bound on the frequency of the zero, along with the bound implied by point 2.

For example, consider the following two transfer functions, which both have the same denominator and unity DC gain:

$$G_1(s) = \frac{5(s + 5)}{s^2 + 7s + 25} \tag{B.1.11}$$

$$G_2(s) = \frac{2.5(s + 10)}{s^2 + 7s + 25} \tag{B.1.12}$$

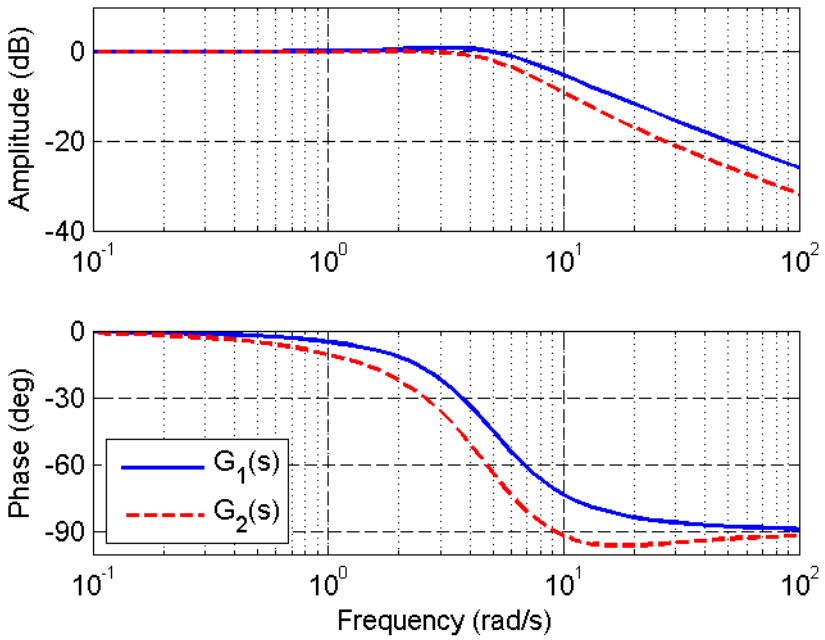

Figure B.1.1: Bode diagrams of the two example transfer functions

Both these transfer functions are stable, and therefore satisfy point 1 in Theorem B.1. In order to satisfy point 2, the phase of the transfer functions should never exceed $\pm 90°$. Figure B.1.1 shows that $G_1(s)$ satisfies this requirement, but $G_2(s)$ does not. Also, the frequency of the zero of $G_1(s)$ is less than the linear term in the denominator, while this is not true for $G_2(s)$. Therefore $G_1(s)$ is SPR, but $G_2(s)$ is not.

For this denominator polynomial, and for all others investigated, it was found that any transfer function which satisfies point 3 of Theorem B.1 also satisfies point 2. It is, however, beyond the scope of this project to prove this in general. Therefore transfer functions will be tested against point 2 directly and against point 3(a) using inequality B.1.6 to determine if they are SPR.

B.2 Lyapunov stability theory

Lyapunov stability theory can be used to design an adaptive control system. That is, given a plant and a control law, which uses a controller parameters vector $\boldsymbol{\theta}$, the theory can be used to find an adaptive law in the form of an expression for $\dot{\boldsymbol{\theta}}$ which will ensure that the output error goes to zero, and that all the signals in the system are bounded.

The aim of this section is not to provide a detailed discussion of Lyapunov stability theory. It only gives a qualitative overview of the principles behind the theory, which should provide insight into the mathematics behind the design of the adaptive control system. A detailed discussion of Lyapunov stability theory can be found in [12].

B.2.1 Definitions

Definition B.4 *A continuous function $\varphi : [0, r] \rightarrow \mathcal{R}$ is said to belong to* ***class $\mathcal{K}$****, i.e. $\varphi \in \mathcal{K}$ if*

- $\varphi(0) = 0$
- *φ is strictly increasing on $[0, r)$*

Definition B.5 *A function $V(t, \mathbf{x}) : \mathcal{R}^+ \times \mathcal{B}(r)$ with $V(t, \mathbf{0}) = 0 \; \forall \; t \in \mathcal{R}^+$ is* ***positive definite*** *if there exists a continuous function $\varphi \in \mathcal{K}$ such that $V(t, \mathbf{x}) \geq \varphi(|\mathbf{x}|) \; \forall \; t \in \mathcal{R}^+, \; \mathbf{x} \in \mathcal{B}(r)$ for some $r > 0$.*

Definition B.6 *A function $V(t, \mathbf{x}) : \mathcal{R}^+ \times \mathcal{B}(r)$ with $V(t, \mathbf{0}) = 0 \; \forall \; t \in \mathcal{R}^+$ is* ***positive semidefinite*** *if $V(t, \mathbf{x}) \geq 0$ for all $t \in \mathcal{R}^+$ and $\mathbf{x} \in \mathcal{B}(r)$ for some $r > 0$.*

Definition B.7 *$V(t, \mathbf{x})$ is* ***negative (semi)definite*** *if $-V(t, \mathbf{x})$ is positive (semi)definite.*

B.2.2 Choice of a Lyapunov-like function

In an ideal situation, the use of Lyapunov stability theory involves finding a positive definite function $V(\mathbf{x})$ of the state of a system, known as the *Lyapunov function*, which has a negative definite time derivative $\dot{V}$. If such a function can be found, the system is stable and will converge asymptotically to the equilibrium point $\mathbf{x} = 0$.

The Lyapunov function essentially represents a form of energy in the system, and therefore this type of function is often known as the *energy function* [42]. If there is any state or parameter error, the energy will be positive. Ensuring that the rate of change of the energy is negative will imply that the system will always dissipate energy, meaning that it will gravitate towards an equilibrium point where the energy is zero, and can not settle at any other point.

However, finding such a Lyapunov function is not always possible for practical systems. In the design of the adaptive control system, a *Lyapunov-like* function $V(\mathbf{e}, \tilde{\boldsymbol{\theta}})$ of the state and parameter errors can be chosen to be positive definite, but through the choice of adaptive law its time derivative can only be made negative semidefinite.

In Section 5.2.4, the following Lyapunov-like function, adaptive law and resulting time derivative of the Lyapunov-like function were obtained:

$$V = \frac{\mathbf{e}^\mathsf{T} P_c \mathbf{e}}{2} + \frac{\tilde{\boldsymbol{\theta}}^\mathsf{T} \Gamma^{-1} \tilde{\boldsymbol{\theta}}}{2} |\rho^*| \tag{B.2.1}$$

$$\dot{\boldsymbol{\theta}} = -\Gamma e_1 \boldsymbol{\omega} \, \mathrm{sgn}(\rho^*) \tag{B.2.2}$$

$$\dot{V} = -\frac{\mathbf{e}^\mathsf{T} q q^\mathsf{T} \mathbf{e}}{2} - \frac{\nu_c}{2} \mathbf{e}^\mathsf{T} L_c \mathbf{e} \tag{B.2.3}$$

where P_c, Γ and L_c are positive definite matrices, q is a vector and ν_c is a positive scalar. All the signals in these equations are defined in Chapter 5. It can be shown [12] that this expression for V is positive definite, and $\dot{V}$ is negative semidefinite.

As argued in Section 5.2.4, the properties of these functions imply that the plant output will track the reference model output asymptotically with zero error, and that all signals in the adaptive control system will be bounded. They do not, however, guarantee that the parameter error will go to zero, i.e. that the adapted parameters will go to their ideal values.

In the adaptive pitch rate controller, both the state error $\mathbf{e}$ and the adapted parameter vector $\boldsymbol{\theta}$ are four-dimensional vectors, which makes it difficult to visualise the operation of the adaptive control system. The following example, however, illustrates the principles in two dimensions, which can provide insight into the stability theory behind the adaptive control system.

B.2.3 Example: Adaptive regulation of a first-order plant

Consider a first-order plant and a proportional regulator with an adapted feedback gain. The plant is given by the differential equation:

$$\dot{x} = -ax + bu \tag{B.2.4}$$

where $b > 0$, and the proportional feedback control law is given by:

$$u = -\theta x \tag{B.2.5}$$

Then the closed-loop plant equation will be:

$$\dot{x} = -(a + b\theta)x \tag{B.2.6}$$

Since there is no reference command, the plant output x is equal to the output error e, and the plant equation can be rewritten as an error equation:

$$\dot{e} = -(a + b\theta)e \tag{B.2.7}$$

The regulator is to be designed so that the closed-loop error dynamics will have a pole at $s = -\alpha$, i.e.

$$\dot{e} = -\alpha e \tag{B.2.8}$$

Then the ideal feedback gain θ^* is can be calculated as follows if the plant parameters are known:

$$a + b\theta^* = \alpha \tag{B.2.9}$$

$$\therefore \theta^* = \frac{\alpha - a}{b} \tag{B.2.10}$$

and the parameter error is defined as $\tilde{\theta} = \theta - \theta^*$.

If the following positive definite Lyapunov-like function is chosen:

$$V = \frac{e^2}{2} + \frac{b\tilde{\theta}^2}{2\gamma} \tag{B.2.11}$$

then its time derivative will be:

$$\dot{V} = e\dot{e} + b\tilde{\theta}\frac{\dot{\theta}}{\gamma} \tag{B.2.12}$$

$$= -(a + b\theta)e^2 + b\tilde{\theta}\frac{\dot{\theta}}{\gamma} \tag{B.2.13}$$

$$= -\Big(a + b(\tilde{\theta} + \theta^*)\Big)e^2 + b\tilde{\theta}\frac{\dot{\theta}}{\gamma} \tag{B.2.14}$$

$$= -(\alpha + b\tilde{\theta})e^2 + b\tilde{\theta}\frac{\dot{\theta}}{\gamma} \tag{B.2.15}$$

$$= -\alpha e^2 + b\tilde{\theta}\left(\frac{\dot{\theta}}{\gamma} - e^2\right) \tag{B.2.16}$$

Therefore, if the following adaptive law is used:

$$\dot{\theta} = \gamma e^2 \tag{B.2.17}$$

then the derivative of the Lyapunov-like function reduces to:

$$\dot{V} = -\alpha e^2 \tag{B.2.18}$$

which is negative semidefinite.

Then the adaptive regulator becomes a second-order non-linear system described by the error equation and the adaptive law:

$$\dot{e} = -(a + b\theta)e \tag{B.2.19}$$

$$\dot{\theta} = \gamma e^2 \tag{B.2.20}$$

These two differential equations represent a vector field in a two-dimensional space. The Lyapunov-like function gives the energy in the system at any point in this space, and its derivative gives the rate at which energy is added to the system:

$$V = \frac{e^2}{2} + \frac{b\tilde{\theta}^2}{2\gamma} \tag{B.2.21}$$

$$\dot{V} = -\alpha e^2 \tag{B.2.22}$$

Since $\dot{V}$ is always negative, the system will dissipate energy at a rate αe^2.

In order to visualise this two-dimensional energy and vector field, let us consider the case where $a = b = \alpha = \gamma = 1$. Since $a = \alpha$, $\theta^* = 0$ and $\tilde{\theta} = \theta$.

Figure B.2.1 shows the vector field for this case, as well as contours of the energy function and a number of example trajectories from different initial conditions. Figure B.2.2 shows the response over time of the error, the feedback gain and the energy function for the same initial conditions.

These figures show a number of characteristics of this adaptive regulator system. Firstly, if the output error is initially zero, then nothing happens – the output error stays zero, and

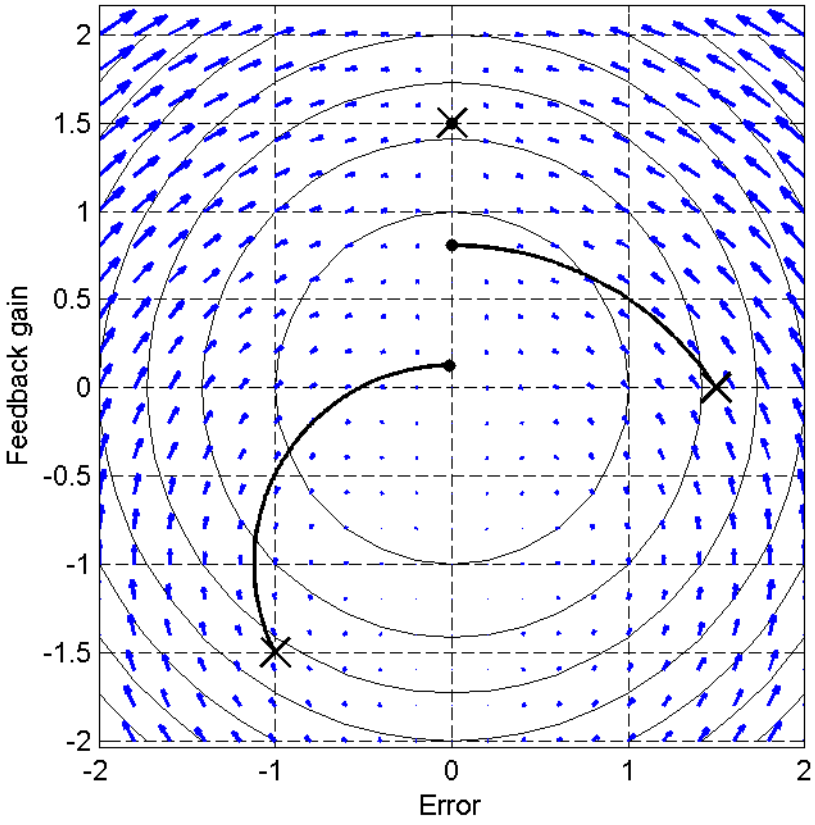

Figure B.2.1: Graph of the two-dimensional space showing the vector field of the state derivatives, contours of the energy function and trajectories for different initial conditions

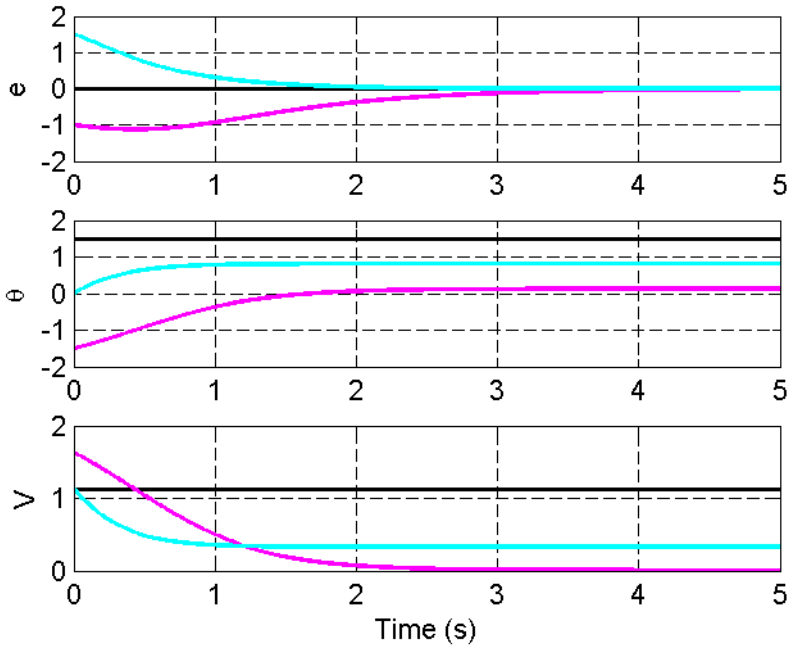

Figure B.2.2: Time responses of the output, parameter and energy for different initial conditions

the feedback gain remains constant. Secondly, the output error always tends asymptotically towards zero, but the parameter error does not – it merely settles at a constant value, which will usually be non-zero. Thirdly, if the system is initialised with the correct feedback gain but a non-zero output error, the feedback gain will be adapted away from its ideal value.

Finally, a constant feedback gain $\theta = -1.5$ would make the system unstable. If the adaptive regulator is initialised with this value and a non-zero output error, the magnitude of the output error will initially increase, as would be expected from an unstable system. However, the feedback gain will increase until the system becomes stable again, and the output error still goes to zero asymptotically. Also, even though the magnitude of the output error increases, it can be seen from the contours that the energy in the system still decreases.

In this example, the fact that the Lyapunov-like function is positive definite and dependent on the output and parameter errors, and that its derivative is negative semidefinite and dependent only on the output error, means that the output error will always tend to zero asymptotically, while the adapted parameter will be bounded, and will settle at some value.

The same applies to the multi-dimensional case, such as the design of the adaptive pitch rate controller. Furthermore, it can be shown [12] that the properties of the Lyapunov-like function imply that all signals in the closed-loop system are bounded, which is the objective of the adaptive control system.

B.3 Stiffness in differential equations

In Chapter 7, it was found that increasing the adaptive gain improves the convergence rate of an MRAC system, but that an adaptive gain which is too large can cause instability. This is due to the differential equation of the adaptive law becoming *stiff*. Stiffness is a phenomenon which can occur when continuous-time differential equations are solved through numerical integration, if the sample rate is slow and the derivatives in the differential equation depend strongly on the solution.

The concept of stiffness can best be explained using an example. Suppose the following differential equation is to be solved through numerical integration:

$$\dot{x} = f(x) = -ax, \qquad x(0) = 1 \tag{B.3.1}$$

The analytical solution to this equation is

$$x(t) = e^{-at} \tag{B.3.2}$$

The equation can be solved through Euler integration, with different values of the sampling period T:

$$x(k+1) = x(k) + Tf(x(k)) \tag{B.3.3}$$

$$= x(k) - aTx(k) \tag{B.3.4}$$

$$= (1 - aT)x(k) \tag{B.3.5}$$

The solutions of Equation B.3.1 with $a = 1$ and different values of T are shown in Figure B.3.1, along with the analytical solution. For a sample time of 0.5 seconds, the numerical solution is a reasonable approximation of the analytical solution. With $T = 1$ second, the solution reaches $x = 0$ after one time step and stays there. With $T = 1.5$ seconds, the solution overshoots the final value of $x = 0$ and oscillates around zero with a decaying magnitude. Using $T = 2$ seconds causes the solution to alternate between $x = 1$ and $x = -1$, while $T = 2.1$ seconds causes an unstable oscillation.

Since Equation B.3.1 is linear, the effect of the different sampling periods can be explained by analysing the discrete solution, Equation B.3.5, in the z-plane. Figure B.3.2 shows the poles of the discrete equation for each value of T. The five poles shown correspond to the responses seen in Figure B.3.1, with each sampling period yielding the response one would expect from the corresponding pole in the z-plane.

The response can, however, also be explained without using linear tools, which can provide insight into the stiffness of non-linear differential equations, such as the adaptive control system. The Euler integration method essentially assumes that the derivative in the differential equation is constant over the sampling period – that is, that the solution can be approximated as a straight line. Inspection of Figure B.3.1 shows that this is a reasonable approximation when $T = 0.5$ seconds, and therefore the solution with this sample time is good. For the

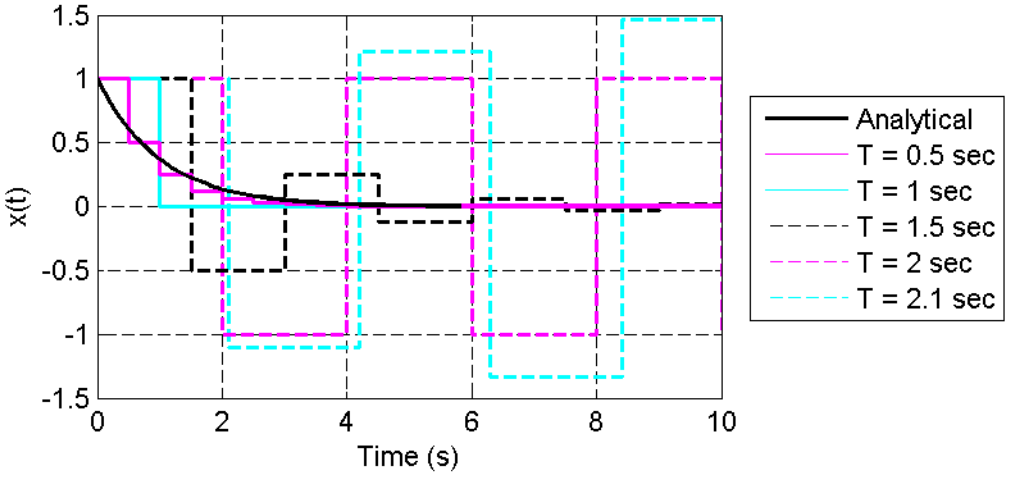

Figure B.3.1: Solutions of the continuous differential equation using Euler integration with different sampling times

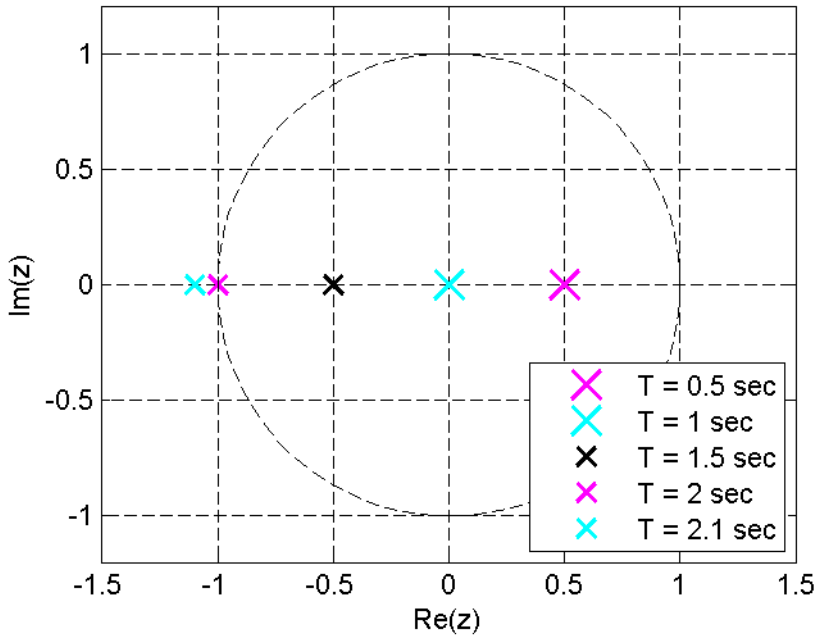

Figure B.3.2: Z-plane poles of the solutions using Euler integration with different sampling times

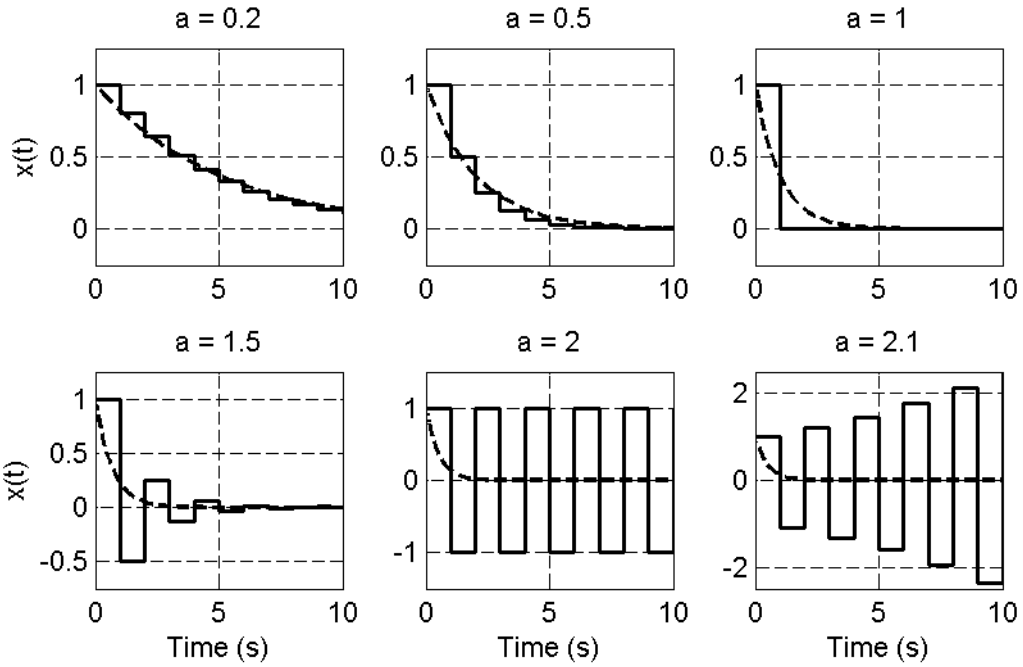

Figure B.3.3: Solutions of the continuous differential equation using Euler integration with $T = 1$ second and different values of a. The dotted lines show the analytical solution in each case.

larger time steps, however, this assumption is not valid, since the derivative of the analytical solution changes significantly during the sample period. This degrades the quality of the numerical solution, eventually making it unstable when the sample time exceeds 2 seconds.

This analysis of the effect of the sample time in the numerical solution of differential equations provides useful insight into the concept of stiffness. However, the issue in the design of the adaptive control system is not the choice of the sample time, but the choice of the adaptive gain. As an analogy for this, Figure B.3.3 shows the analytical solution to Equation B.3.1 with different values of a, which is effectively the gain of the system, and a sample time of $T = 1$ second.

Increasing a decreases the settling time of the analytical solution, just as increasing the adaptive gain improves the response of the adaptive control system. However, making a too large has the same effect as increasing the sample time, eventually causing instability.

In this example, a large value of a causes the solution in Equation B.3.1 to change very quickly, which implies that the derivative also changes significantly within one integration time step. Therefore the assumption of the Euler integrator that the derivative is constant over the time step is invalid, and the discrete integration performs poorly or even becomes unstable.

Similarly, in the adaptive law of Equation 5.2.39:

$$\dot{\boldsymbol{\theta}} = -\gamma e_1 \boldsymbol{\omega} \operatorname{sgn}(\rho^*) \tag{B.3.6}$$

a large value of the adaptive gain γ causes a large change in the controller parameter vector $\boldsymbol{\theta}$ within one sample period, which in turn can cause a large change in e_1 and $\boldsymbol{\omega}$, on which the derivative depends. Then the non-linear adaptive control system can become unstable, just as the linear example system did in this example.

A thorough discussion of the concept of stiffness in the context of simulations for computer animation can be found in [42]. Here the proposed solutions for stiffness are to increase the sampling rate of the Euler integrators, or to use a more accurate numerical integration method. In the adaptive control system, however, it was found that adequate performance could be achieved with adaptive gains which do not cause stiffness when Euler integrators are used at the 50 Hz sample rate of the ESL avionics.

Appendix C

Effect of CG shifts on the lateral dynamics

The lateral portion of the non-linear dynamics of Chapter 3 can be linearised to obtain the following state-space representation of the lateral dynamics of fixed-wing aircraft: [5]

$$\begin{bmatrix} \dot{\beta} \\ \dot{p} \\ \dot{r} \\ \dot{\phi} \end{bmatrix} = \begin{bmatrix} \frac{\bar{q}S}{m\bar{V}}C_{Y_\beta} & \frac{\bar{q}Sb}{2m\bar{V}^2}C_{Y_P} & \frac{\bar{q}Sb}{2m\bar{V}^2}C_{Y_R} - 1 & \frac{g}{\bar{V}} \\ \frac{\bar{q}Sb}{I_{xx}}C_{l_\beta} & \frac{\bar{q}Sb^2}{2I_{xx}\bar{V}}C_{l_P} & \frac{\bar{q}Sb^2}{2I_{xx}\bar{V}}C_{l_R} & 0 \\ \frac{\bar{q}Sb}{I_{zz}}C_{n_\beta} & \frac{\bar{q}Sb^2}{2I_{zz}\bar{V}}C_{n_P} & \frac{\bar{q}Sb^2}{2I_{zz}\bar{V}}C_{n_R} & 0 \\ 0 & 1 & 0 & 0 \end{bmatrix} \begin{bmatrix} \beta \\ p \\ r \\ \phi \end{bmatrix} + \begin{bmatrix} \frac{\bar{q}S}{m\bar{V}}C_{Y_{\delta_a}} & \frac{\bar{q}S}{m\bar{V}}C_{Y_{\delta_r}} \\ \frac{\bar{q}Sb}{I_{xx}}C_{l_{\delta_a}} & \frac{\bar{q}Sb}{I_{xx}}C_{l_{\delta_r}} \\ \frac{\bar{q}Sb}{I_{zz}}C_{n_{\delta_a}} & \frac{\bar{q}Sb}{I_{zz}}C_{n_{\delta_r}} \\ 0 & 0 \end{bmatrix} \begin{bmatrix} \delta_a \\ \delta_r \end{bmatrix} \tag{C.1}$$

The parameters of Appendix A.3 can be substituted into this state space to obtain the lateral open-loop poles of the Variable Stability UAV for different CG positions. The poles with the CG in the forward and backward ($x_G = -80$ mm) positions are shown in Table C.1 and Figure C.1.

x_G	0	-80 mm
Roll mode	$s = -19.1724$	$s = -19.1731$
Dutch roll mode	$s = -0.3748 \pm 3.518j$	$s = -0.3203 \pm 3.152j$
Spiral mode	$s = -0.542 \times 10^{-3}$	$s = -0.587 \times 10^{-3}$

Table C.1: Open-loop lateral poles of the Variable Stability UAV with the CG in the forward and backward positions

The complex pole pair and two real poles correspond to the three classical lateral modes of motion of a fixed-wing aircraft. The lightly-damped complex poles correspond to the

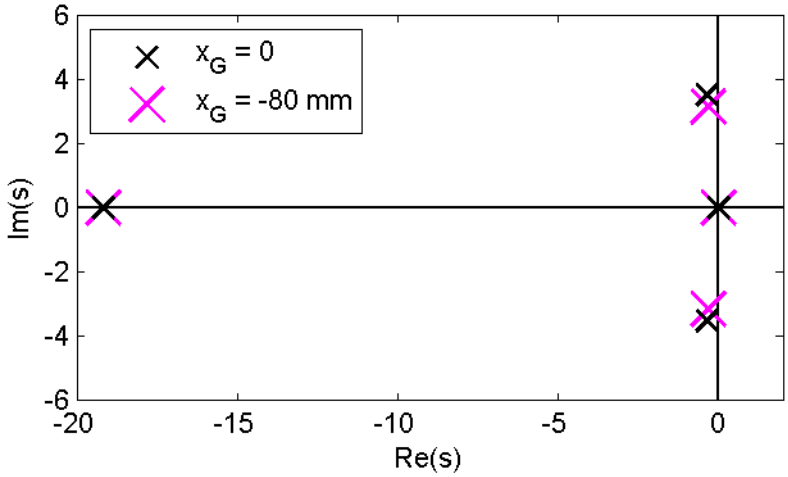

Figure C.1: Poles of the lateral dynamics of the Variable Stability UAV with the CG in the forward and backward positions

Dutch roll mode, which is the lateral equivalent of the short period mode. The slow real pole represents the spiral mode, which is the lateral equivalent of the phugoid mode. The fast real pole represents the roll mode.

The roll mode is virtually unaffected by the CG shift, which is to be expected since the CG shifts along the roll axis. The spiral and Dutch roll mode are affected by the CG shift, but not nearly as much as the longitudinal dynamics, which would be destabilised by an 80 mm backward shift.

This analysis shows that the lateral dynamics of an aircraft are not seriously affected by CG shifts along the X-axis. Therefore an adaptive lateral control system would not be required to keep the aircraft laterally stable if the CG shifts backwards, and the lateral dynamics were not discussed in much detail in this thesis.

References

[1] M. M. Basson, "Stall prevention control of fixed-wing unmanned aerial vehicles," Master's thesis, Stellenbosch University, March 2010.

[2] W. H. Pietersen, "System identification for fault tolerant control of unmanned aerial vehicles," Master's thesis, Stellenbosch University, March 2010.

[3] L. Basson, "Control allocation as part of a fault-tolerant control architecture for UAVs," Master's thesis, Stellenbosch University, March 2011.

[4] D. Blaauw, "Flight control system for a variable stability blended-wing-body unmanned aerial vehicle," Master's thesis, Stellenbosch University, March 2009.

[5] I. K. Peddle, "Autonomous flight of a model aircraft," Master's thesis, Stellenbosch University, April 2005.

[6] M. V. Cook, *Flight Dynamics Principles*. Elsevier Butterworth-Heinemann, second ed., 2007.

[7] B. Etkin and L. D. Reid, *Dynamics of Flight, Stability and Control*. John Wiley & Sons, 3rd ed., 1996.

[8] I. K. Peddle, *Acceleration Based Manoeuvre Flight Control System for Unmanned Aerial Vehicles*. PhD thesis, Stellenbosch University, 2008.

[9] K. J. Åström and B. Wittenmark, *Adaptive Control*. Addison-Wesley, 1989.

[10] S. Sastry and M. Bodson, *Adaptive Control - Stability, Convergence and Robustness*. Prentice Hall advanced reference series, 1989.

[11] R. Isermann, K.-H. Lachmann, and D. Matko, *Adaptive control systems*. Prentice-Hall, 1992.

[12] P. A. Ioannou and J. Sun, *Robust Adaptive Control*. Prentice Hall, Inc, 1996. (out of print in 2003), electronic copy at:
`http://www-rcf.usc.edu/~ioannou/Robust_Adaptive_Control.htm`.

[13] R. R. Costa, L. Hsu, A. K. Imai, and P. Kokotović, "Lyapunov-based adaptive control of MIMO systems," *Automatica*, vol. 39, pp. 1251–1257, 2003.

[14] X. Z. Jin and G. H. Yang, "Robust adaptive fault-tolerant compensation control with actuator failures and bounded disturbances," *Acta Automatica Sinica*, vol. 35, pp. 305–309, March 2009.

[15] D. W. Vos, *Nonlinear control of an autonomous unicycle robot: Practical issues*. PhD thesis, Massachusetts Institute of Technology, June 1992.

[16] M. Bodson and S. C. Douglas, "Adaptive algorithms for the rejection of sinusoidal disturbances with unknown frequency," *Automatica*, vol. 33, pp. 2213–2221, 1997.

[17] A. Ilchmann and E. P. Ryan, "On tracking and disturbance rejection by adaptive control," *Systems & Control Letters*, vol. 52, pp. 137–147, 2004.

[18] F. Pahlavanzadeh, H. Shandiz, and H. Khaloozadeh, "Noise behavior improvement of adaptive control systems with a filtering strategy," in *Electrical Engineering, Computing Science and Automatic Control (CCE), 7th International Conference on*, pp. 83 –86, September 2010.

[19] H. Kaufman, I. Barkana, and K. Sobel, *Direct adaptive control algorithms: theory and applications*. New York, NY: Springer, 2nd edition ed., 1998.

[20] B. Yao, *Adaptive Robust Control of Nonlinear Systems with Application to Control of Mechanical Systems*. PhD thesis, University of California at Berkeley, 1996.

[21] G. Gu and L. Qiu, "An $\mathcal{H}_\infty$ approach to robust adaptive control," in *Decision and Control, 46th IEEE Conference on*, pp. 903 –908, December 2007.

[22] J. Fisher, S. Smith, and J. Burken, "Adaptive robust control of an F-15 aircraft," in *American Control Conference, Proceedings of the 2004*, vol. 4, pp. 3191 –3196 vol.4, July 2004.

[23] R. Zbikowski and K. J. Hunt, eds., *Neural adaptive control technology*. World Scientific Publishing Co Pte Ltd, 1996.

[24] A. Calise and R. Rysdyk, "Nonlinear adaptive flight control using neural networks," *Control Systems Magazine, IEEE*, vol. 18, pp. 14 –25, December 1998.

[25] M. R. Napolitano, Y. An, and B. A. Seanor, "A fault tolerant flight control system for sensor and actuator failures using neural networks," *Aircraft Design*, vol. 3, pp. 103–128, 2000.

[26] A. Savran, R. Tasaltin, and Y. Beceriklic, "Intelligent adaptive nonlinear flight control for a high performance aircraft with neural networks," *ISA Transactions*, vol. 45, pp. 225–247, April 2006.

[27] N. Nguyen, K. Krishnakumar, J. Kaneshige, and P. Nespeca, "Flight dynamics and hybrid adaptive control of damaged aircraft," *Journal of Guidance, Control and Dynamics*, vol. 31, pp. 751–764, May-June 2008.

[28] G. C. Avenant, "Autonomous flight control system for an airship," Master's thesis, Stellenbosch University, March 2010.

[29] Y. Liu and Y. Lu, "Nonlinear fuzzy robust adaptive control of a longitudinal hypersonic aircraft model," in *Artificial Intelligence and Computational Intelligence, International Conference on*, vol. 4, pp. 31 –35, November 2009.

[30] G. Shi and S. Yang, "Intelligent control of UAV with neuron-fuzzy approach under hierarchical architecture," in *Intelligent Control and Automation. 7th World Congress on*, pp. 5238 –5243, June 2008.

[31] S. Toha and M. Tokhi, "Dynamic nonlinear inverse-model based control of a twin rotor system using adaptive neuro-fuzzy inference system," in *Computer Modeling and Simulation. Third UKSim European Symposium on*, pp. 107 –111, November 2009.

[32] K. Hentabli, O. Akhrif, and L. Saydy, "Robust longitudinal flight control system under weight and center of gravity uncertainty," in *Electrical and Computer Engineering, Canadian Conference on*, vol. 3, pp. 1743 – 1748 vol.3, May 2003.

[33] J. Zhang, L. Yang, and G. Shen, "Modeling and attitude control of aircraft with center of gravity variations," in *Aerospace conference, 2009 IEEE*, pp. 1 –11, March 2009.

[34] X. Yang, Y. Zhong, L. Yang, J. Zhang, and G. Shen, "Modeling and attitude control of aircraft with variations in mass and center of gravity," in *Intelligent Control and Automation, 8th World Congress on*, pp. 323 –329, July 2010.

[35] B. Nguyen, L. Hamilton-Jones, and D. Leggett, "Analysis of the VISTA longitudinal simulation capability for a cruise flight condition," in *Aerospace and Electronics Conference, Proceedings of the IEEE 1991 National*, pp. 501 –507 vol.2, May 1991.

[36] P. Blue, L. Guvenc, and D. Odenthal, "Large envelope flight control satisfying $\mathcal{H}_\infty$ robustness and performance specifications," in *American Control Conference, Proceedings of the*, vol. 2, pp. 1351 –1356 vol.2, 2001.

[37] G. Tao and P. Ioannou, "Necessary and sufficient conditions for strictly positive real matrices," in *IEE Proceedings*, vol. 137, October 1990.

[38] M. Polycarpou and P. Ioannou, "On the existence and uniqueness of solutions in adaptive control systems," in *IEEE Transactions on Automatic Control*, vol. 38, 1993.

[39] I. Bar Kana, "Rohrs' examples and robust stability of simple adaptive control," in *Transactions of ASME, Journal Dynamic Systems, Measurements and control*, pp. 721–728, 1991.

[40] E-Flite, "Power 25 bl outrunner motor, 870kv." Online: `http://www.e-fliterc.com/Products/Default.aspx?ProdID=EFLM4025A`. Retrieved April 8, 2011.

[41] Windrider R.S.B. Aviation Co. Ltd., "Queen Bee flying wing." Online: `http://www.windrider.com.hk/product.asp?id=165`. Retrieved April 8, 2011.

[42] M. Kass, *An Introduction to Physically Based Modeling*, ch. Energy Functions and Stiffness. Pixar, 1997. Online: `http://www.cs.cmu.edu/~baraff/pbm/energons.pdf`.